Biomimetic Active Chemical Separation

Yushi Zang

A dissertation

submitted in partial fulfillment of the

requirements for the degree of

Doctor of Philosophy

University of Washington

2023

Reading Committee:

Bruce J. Hinds, Chair

David S. Bergsman

Guozhong Cao

Program Authorized to Offer Degree:

Materials Science & Engineering

University of Washington

Abstract

Biomimetic Active Chemical Separation

Yushi Zang

Chair of the Supervisory Committee:
Prof. Bruce J. Hinds
Department of Materials Science & Engineering

This dissertation embarks on an exploration of nature's design principles in the realm of chemical separation and transfer, with the overarching goal of applying these insights to address pressing real-world challenges. Our journey begins with a comprehensive review of prevailing industrial chemical separation techniques, revealing their remarkable energy demands and the unfortunate squandering of unrecoverable energy. This realization serves as a catalyst for our quest to draw inspiration from the intricate, yet efficient solutions nature offers, particularly exemplified by the cell membrane's remarkable ability to discern among myriad compounds using a seemingly straightforward design.

The cell membrane in living organisms serves as an emblem of nature's ingenuity. Equipped with delicate membrane proteins, each devoted to specific functions vital for the cell's existence,

it operates with a sophistication that continues to elude our full understanding. Yet, our quest is not to replicate nature but to draw inspiration from it. We take the humble dialysis machine as an exemplary case, a technology characterized by its relatively simple design. This apparatus, functioning as an artificial kidney, relies on precision-controlled transmembrane separation facilitated by hollow fiber membranes with precise pore sizes, complemented by mechanical pumps and dialysate. Despite its apparent simplicity, this technology remains a lifeline for patients awaiting kidney transplants. Nevertheless, we acknowledge the imperative to enhance its long-term survival rates.

From a materials science perspective, our pursuit of advancement in these technologies hinges on the development of superior functional materials. For dialysis, this translates into better control of pore size distribution and porosity, a journey we embark upon through the development of hollow fiber membranes. However, the intrinsic limitation of passive diffusion in dialysis technology necessitates a shift towards biomimetic active high-selectivity functionalization. In response, we design, propose, synthesize, and validate selective surface chemistry modifications for serum albumin. This groundbreaking surface chemistry enhancement facilitates the adsorption and desorption cycling of albumin, concurrently removing protein-bound uremic toxins that defy conventional dialysis processes. Moreover, our journey extends to the scaling-up of this technology, underpinned by systematic design implementation and continuous refinements guided by computational models.

Likewise, in our pursuit of dialysis technology enhancement, we explore the modification of highly selective functional groups onto low-cost silica adsorbents. This endeavor aims to efficiently remove potassium ions enriched in dialysates during the development of mobile dialysis techniques. Despite the availability of various adsorbents and natural materials, we opt for silica

adsorbents due to their stability, cost-effectiveness, and ease of preparation. The modified crown ether-silica adsorbents exhibit remarkable potassium ion adsorption capacity, promising applications beyond conventional adsorbents.

Our expedition also ventures into the domain of carbon material-based membranes, particularly carbon nanotubes and reduced graphene oxide membranes. These materials hold the potential to revolutionize separation processes by compensating for membrane structure surface area limitations. Under nanoscale confinement, they achieve high-speed transmembrane fluid transport, outperforming conventional adsorbent-based methods. We make history by directly observing high-speed transmembrane electroosmotic transport within carbon nanotubes, marking a significant milestone in our journey.

The observations from this study underscore the promise of carbon nanotube membranes, especially when functionalized with high-selectivity functional groups. We validate the concept of transmembrane drug delivery on negatively modified carbon nanotube membranes, showcasing their potential in various applications.

In our exploration of graphene oxide membranes, we unearth a fascinating catalytic reaction, offering unique selectivity. However, this discovery comes with the challenge of reduced interlayer spacing, limiting transmembrane separation rates. We surmount this challenge by ingeniously reintroducing substances that reverse the catalytic reaction, enabling high-speed fluid passage and salvaging the potential of graphene oxide membranes in alcohol dehydration applications.

In conclusion, this dissertation's comprehensive exploration of materials science and biomimetic high-selectivity surface chemistry modification yields profound insights. Our research validates scientific theories and overcomes engineering constraints, heralding a promising future

for separation technologies. As we continue to draw inspiration from nature's design, the possibilities for addressing real-world challenges through biomimicry are vast and exciting.

TABLE OF CONTENTS

LIST OF FIGURES

LIST OF TABLES

ACKNOWLEDGEMENTS

I would like to express my heartfelt gratitude to all those who have been with me throughout my journey into this realm of scientific research. Your unwavering support and encouragement have been instrumental in making this journey possible.

First and foremost, I extend my deepest appreciation to my PI, professor Bruce Hinds, for his continuous guidance and mentorship throughout this research endeavor. His patience, wisdom, and unwavering support were pivotal in shaping this creative project.

To my esteemed committee members, Professor Buddy Ratner, Professor Guozhong Cao, and Professor David Bergsman, I extend my heartfelt thanks for their invaluable feedback, constructive criticism, and dedication to refining this dissertation. Your guidance and expertise greatly enriched the quality of this work.

I would like to acknowledge my fellow lab mates in Hinds' Lab and Gao's Lab for their camaraderie and support. Working alongside you has been both professionally rewarding and personally enjoyable. Together, we have worked tirelessly, throughout night and day, to ensure the success of the project. Your support and commitment were truly exceptional.

Last but certainly not least, I want to express my deepest appreciation to my family and friends for their unconditional support and patience throughout this journey. Your belief in me kept me motivated during the challenging times, and I am forever thankful for your unwavering encouragement.

My path to this point would not have been possible without the collective efforts of all those mentioned above. Each one of you played an essential role in this academic endeavor, and I am deeply grateful for your contributions.

Thank you all for being a part of this journey.

Chapter 1. INTRODUCTION

1.1 INDUSTRIAL CHEMICAL SEPARATION

How efficient the extraction of certain chemicals from their crude form is one of the direct measurements of the industrial capability of a society. To this day, the production of steel, petroleum products, and rare earth element of countries were still being closely tracked to predict the world's economic progression. And the production of aforementioned materials, even very well established, still came with extremely high costs on both fiscal and energy. In accordance with the suggestion provided by the US Energy Information Administration shown in Figure 1.1, it is noteworthy that among all major manufacturing sectors, the manufacture of chemical and petroleum products, which heavily relies on the separation of individual compounds, accounted for the consumption of over half of the total energy, amounting to 19.44 quadrillion BTUs, in the year 2018. [1] It was estimated that 45-55 % of energy consumption in the US was chemical separation. [2] The production of each ton of rare earth element consumes as high as 58.5 GJ and over 25 % of the energy was spent on chemical separation. [3] To put the data in reference, this power consumption for every ton of rare earth element is more than enough to cover the yearly electricity power consumption of over 1500 US households. [4] Therefore, rations for more energy-efficient chemical separation have long been called for.

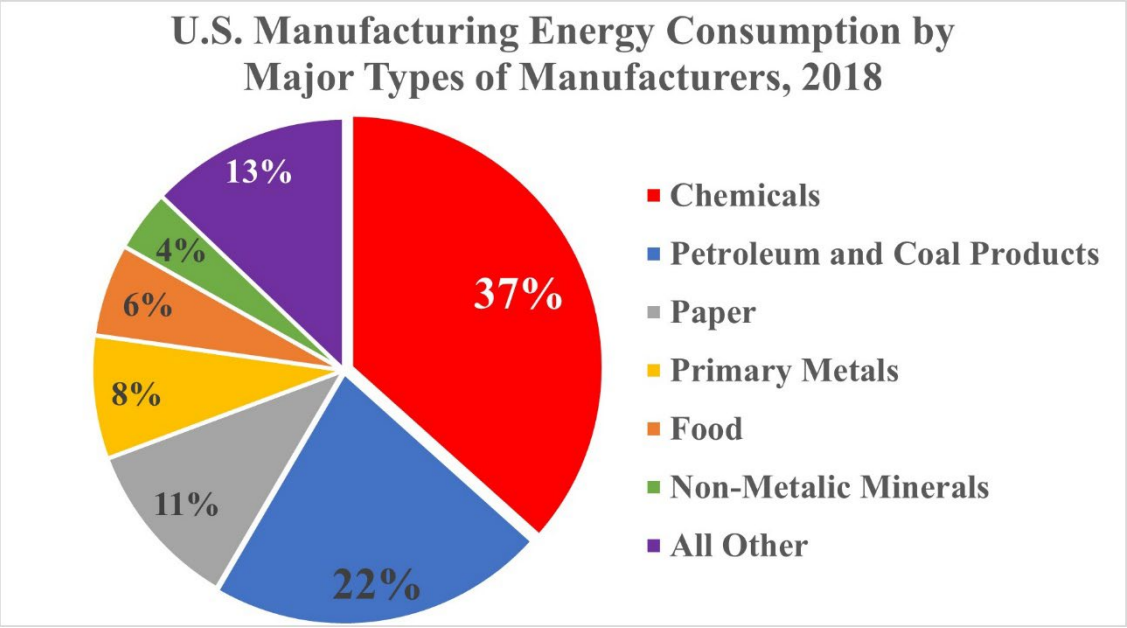

Figure 1.1. Pie chart of US manufacturing energy consumption by type of manufacturers. Data from US Energy Information Administration [1].

1.1.1 *Distillation*

Distillation undeniably stands as the most widely employed industrial separation technique, finding its extensive utility in fields such as petroleum product production, chemical manufacturing, desalination, and more. This method fundamentally separates chemicals with distinctive boiling points through the sequential condensation of the desired compound, either based on temperature or time. Distillation boasts scalability and proficiency in separating compounds with significant boiling point differences. However, it comes with the drawback of high energy costs, particularly during the initial heating of the chemical mixture. For instance, in crude oil refineries, the crude oil must be heated to temperatures exceeding 500 °C for effective fractionation. Nevertheless, the subsequent processes and the storage of fractionated crude oil do not necessitate or benefit from elevated temperatures. Consequently, a substantial portion of the energy consumed during distillation is wasted. To mitigate such energy losses, innovative applications like power generation and heating have been implemented to recover this thermal

energy. Furthermore, it's important to note that distillation has limitations in producing high-purity products and is ineffective in processing azeotropic mixtures, which consist of components that form constant-boiling mixtures. These challenges have spurred research into alternative separation techniques to address these shortcomings and enhance energy efficiency in the separation processes.

1.1.2 *Filtration and Membrane Separation*

The energy required for filtration processes is generally considered to be smaller than that for distillation. [2, 5] This is primarily because the majority of the energy in filtration is dedicated to pumping or pressurizing the system. In a filtration process, a mixture is forced through a porous filter or membrane, which separates the components based on factors such as particle size, charge, or affinity, without inducing a phase change in the mixture. This characteristic makes filtration particularly effective for separating mixtures with different phases, such as liquid from a liquid-solid mixture. The scalability of filtration and membrane separation depends on the properties of the filter or membrane and operational requirements such as flow rate, viscosity of the mixture, and pressure. The lifespan of the filter or membrane is of great importance due to its high cost. An illustrative application of membrane technology is in water treatment using reverse osmosis (RO) membranes to produce potable water by removing bacteria and salt ions. However, the lifetime of RO membranes and the energy required for pump operation have been subjects of criticism. [6] Additionally, separating mixtures with particles of similar sizes can pose a challenge for both filters and membranes. Therefore, significant efforts have been made to improve the tradeoff between selectivity and permeability of membranes to enhance separation efficiency.

1.1.3 *Solvent Extraction*

The extraction process manipulates the compound of interest based on its differing solubility in various solvents. A liquid phase containing the extractant is mixed with another solvent phase with a higher affinity. This encourages the solute compound to migrate and become enriched in the solvent phase. The extraction process itself is nearly energy cost-free, requiring only mechanical agitation and mixing unless pressurization or precise temperature control are needed. However, the extracted compound in the solvent phase must be recovered using energy-intensive methods such as evaporation or distillation. Furthermore, it's important to note that when dealing with complex mixtures with similar solubility properties, multiple-step extraction processes may be necessary. Additionally, the solvents used for extraction processes often pose environmental challenges. In an effort to address these drawbacks of the extraction processes, numerous innovations have been developed. These include the use of supercritical fluid or a solid phase instead of the conventional liquid matrix phase. [7] For instance, decaffeinated coffee is processed by caffeine extraction using pressurized supercritical carbon dioxide fluid.

1.1.4 *Chromatography*

Chromatography is a widely employed separation technique in the pharmaceutical, chemical, and biotechnology industries. Continuous operation of column chromatography allows the fractionation of individual components from a complex mixture based on their differing affinities for the stationary phase and the mobile phase. The resolution of such separation is fine-tuned by controlling this affinity difference. A variety of modifications can be made to fine-tune the affinity of the stationary phase. For instance, size exclusion chromatography can be adjusted using pore size and porosity to manipulate the retention time of molecules of the desired size. Ion exchange chromatography utilizes charged surface functionality on the resin to attract ions of the opposite

charge. Furthermore, selective surface chemistry can be applied to recognize and capture targets with high specificity. For example, fractionation of plasma proteins can be achieved using a Cibacron blue functionalized chromatography column, and selective capture of metal ions can be achieved through a crown ether functionalized resin. [8-11] It's important to note that chromatography separation is subject to real-world constraints. Affinity and selectivity are associated with higher costs of resin and eluent, and the operation often requires a higher level of expertise and longer processing times.

1.1.5 *General Remarks*

The industrial-level application of the aforementioned chemical separation techniques is a strong endorsement of their irreplaceable strengths in their respective fields. Furthermore, although these techniques have been discussed separately, successful separation procedures often involve a combination of these methods in various sequences and may include repetitions to compensate for their limitations and leverage their strengths.

For instance, in the production of lithium from brine, the process typically involves the evaporation of water, followed by extraction using ion exchange resin, membranes, or extraction with a kerosene-containing solvent phase. The engineering design of such processes depends on specific conditions and requirements. However, there are inherent limits to engineering's ability to fully exploit strengths and mitigate weaknesses.

In the realm of science, particularly in materials science, cutting-edge exploration is the path to pushing the limits of engineering. When reviewing scientific exploration, it becomes evident that the natural world possesses remarkable chemical separation capabilities. Even single-celled organisms can effectively control the recognition and transport of chemicals, both actively and passively, both within and outside the cell, through functional units such as numerous membrane

proteins that exists on the lipid bilayer cell membrane. This represents an engineering pinnacle that humans have yet to reach. In more complex tissues, organs, and organisms, there is an infinite amount of knowledge and engineering inspiration waiting for humans to explore, develop, and transfer into applications.

1.2 Biological Chemical Separation

When examining the showcases of chemical separation in nature, it is impossible to overlook the remarkable efficiency and elegance of the kidney's function. A healthy kidney consists of millions of functional nephrons operating with extraordinary efficiency. These nephrons actively excrete excessive salts and metabolic wastes while simultaneously reabsorbing nutrients, thanks to specialized cells and membrane structures, as well as membrane proteins.

Such membrane-regulated mass transfer can be active or passive, as illustrated in Figure 1.2. Passive mass transfer relies on chemical potential or concentration gradients, whereas active mass transfer defies concentration gradients with the assistance of membrane proteins or enzymes, incurring an associated energy cost. A classic example of active transport is the movement of sodium and potassium against their concentration gradients, regulated by sodium- and potassium-activated adenosine triphosphates (Na, K-ATPase). [12] Organic anion transporters (OATs) represent another category of membrane proteins responsible for picking up organic anions from the extracellular space and actively transporting them across the membrane. [13] In contrast to Na, K-ATPase and OATs, aquaporin-1 (AQP-1) serves as a conduit for water transport along osmotic gradients, whether intracellularly or extracellularly. [14] The regulation of water transport is achieved through coordination with other proteins that control the transmembrane osmotic gradient. It should be noted that AQP-1 is highly selective towards water, meaning the conduit is exclusively open to water molecules. It can be inferred from these mentioned membrane proteins

that, in contrast to most industrial separation processes, biological chemical separation is highly specific and selective towards target species, allowing for intricate and precise biochemical processes.

At a higher level, cells function through the collective interactions of various active and passive mass transfer mechanisms. And the function of organs introduces even greater complexity to these processes. Therefore, the review of biological mass transfer mechanisms must start with membrane proteins.

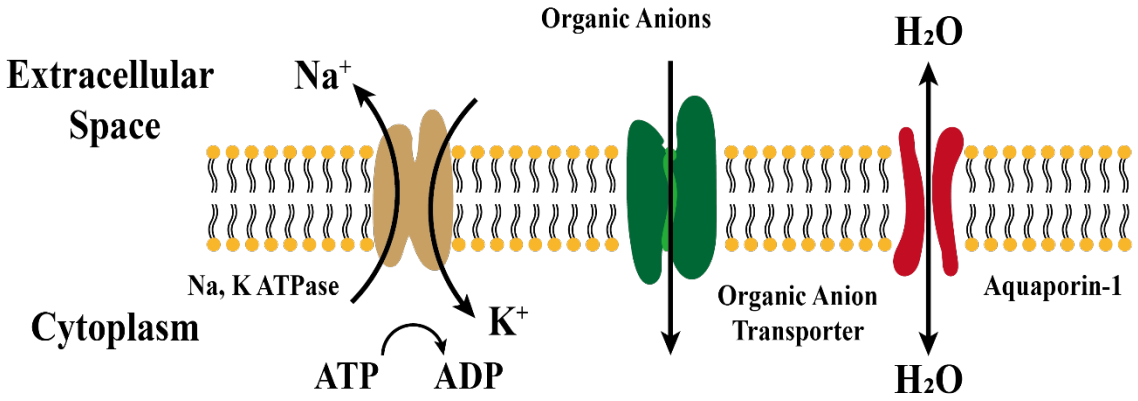

Figure 1.2. Schematic demonstration of mass transfer by membrane proteins.

1.2.1 *Na, K-ATPase*

What was commonly known as a "sodium-potassium pump" was first discovered in 1957 by Jens Christian Skou and formally named sodium- and potassium-activate adenosine triphosphates (Na, K-ATPase). [12] Na, K-ATPase is made of two subunits α and β, where the larger α-subunit is a transmembrane unit and has a binding site for both Na and K ions. [15, 16] The cross-membrane transportation of sodium and potassium was often done against their chemical potential/gradient at the cost of ATP hydrolysis. Establishing and maintaining cross-membrane Na and K gradients

is vital for most cells. So, as expected, this membrane protein is highly ubiquitous but found with higher concentration and activity in certain cells, like epithelia of kidney tubule, which were differentiated for transcellular transportation. [17-20]

The transportation of Na and K ions by Na, K-ATPase works in a cycle as follows: at activation of Na, K-ATPase by ATP, three cytoplasm sodium ions were captured. Then the hydrolysis of ATP to ADP supplies the energy for the transportation of cytoplasm sodium extracellular and capture of two extracellular potassium ions leaving the Na, K-ATPase phosphorylated. Finally, the phosphorylated Na, K-ATPase releases the attached phosphate and transports extracellular potassium to intracellular. [21] The turnover rate of such a cycle was limited by the conformational change from K affinity to Na affinity with the association of ATP. This process limited the turnover rate to ~10^1 /s level which is more than decent compared to most membrane separation turnover rates. [22] Considering that a single secretory epithelia cell has millions of Na, K-ATPase, it is no wonder that the kidney would handle electrolyte balance with such efficiency. [17-20]

1.2.2 *Organic Anion Transporters*

Larger than metal ions, organic anion (OA), such as indoxyl sulfate (IS), is another category of compounds that are excreted through the kidney. A family of proteins, organic anion transporters (OATs), specialized in transporting organic anions. Since the organic anions were excreted through the kidney, it is only logical to find all four main isomers (OAT 1, 2, 3, and 4) of OATs that exists in the kidney. But membranes of other organs were also found with OAT decorations. Such as the liver with OAT 2 and 3, and the brain with OAT 1. Because, unlike the Na, K-ATPase, the substrate selectivity spectrum of the OATs is rather wide and sometimes OATs are also responsible for transporting substrates like neurotransmitter metabolites. [13, 23, 24] However, it is important to note that, even with a wide selectivity spectrum, OATs are different

by their affinity toward specific compounds and distribution in nephrons to accommodate physiological function demands. [13, 24-26]

The structure of OAT1 was believed to be made of 12 transmembrane helices/domains linked by complex intracellular and extracellular loops. [24, 27, 28] OAT1 actively transport OAs across the membrane into the cell in exchange for dicarboxylates transported out of the cell while the gradient of the dicarboxylates was maintained by other transmembrane proteins. [24, 28, 29] While the total mechanism of the OA transport process is not entirely clear, it was noted that the presents of cross-membrane sodium gradient and abundance of ATP show a positive impact on the process. [13, 30]

1.2.3 *Aquaporins*

On one hand, similar to the transport proteins mentioned above, aquaporins (AQPs) are ubiquitously expressed but found in the kidney at higher concentrations. On the other hand, different from Na, K-ATPase, and OATs, the substrate of the aquaporins is not the solute but the solvent, water. A total of nine different AQPs were identified, among which four were found in the kidney, AQP 1-4. Although all the AQPs were associated with transmembrane water transport, the distribution of AQPs in the nephron is not even. AQP-1 was found in the proximal tubule and descending thin limb cells on both the apical and basolateral sides. AQP-2, -3, and -4 mostly locates at the distal convoluted tubule and are also responsible for water reabsorption. [31-33]

AQP-1 is one of the most studied AQPs. It has six transmembrane helices which were linked by five loops oriented on both sides of the membrane. The six transmembrane helices were believed to buddle up and form an hourglass-like geometry, where the neck of the “hourglass” is only 3 Å, marginally larger than the size of water molecules. [14, 34] Due to the extremely confined neck size, any larger molecules or ions were prohibited to pass through AQP-1, even protons. And it was believed that water molecules permeate through in a single-file formation.

However, at the neck of the “hourglass”, the hydrogen bond formed in the single-file water molecules was broken and the incident water molecule flipped 180 degrees while transporting to the other side of the membrane. Such a hydrogen bond-breaking phenomenon also explains prohibited proton transport. [34, 35] Hydrophobic residues at the inner pore surface promoted water permeation. The permeability of AQP-1 was estimated as 3×109 molecules/pore·second or higher. [34, 36, 37] Only with water permeability of AQPs, the kidney tubules were enabled to process over 100 L of water daily.

1.2.4 *When Kidney Fails*

Chronic renal disease or chronic kidney disease (CKD) is a progressive decrease of kidney function that is manageable, to some extent, until it reaches the end stage. Currently, end stage renal disease (ESRD) is only treated by hemodialysis and kidney transplant. Nephron loss, nephron hypertrophy, impaired glomerular filtration, and interstitial fibrosis were known to be the mechanism responsible for causing CKD. [38]

The management of sodium and potassium was found to be compromised in CKD patients. The excretion of both cations was found to decrease as the CDK progresses. The excretion of potassium is almost halved, to ~ 0.97 g/day, when CKD progresses to the G5 stage while recommended daily dietary intake of potassium is over 3 g/day leaving a 2 g excretion need unmet. [39, 40] At the G5 stage, the patient’s serum potassium level increased by ~ 20% which is prone to sliding to the hyperkalemia realm and can be deadly. [41] The worsening of chronic disease also directly influences the transporter proteins. Na, K ATPase was believed to be synthesized less than normal in many cells and tissues, including red blood cells and muscles, of CKD patients and causing higher than normal intracellular Na level. [42, 43] In polycystic kidney disease (gene-related

condition) epithelia, Na, K ATPase was found to mislocate to apical membranes with higher activity. [44]

Indoxyl sulfate is a metabolic waste that's excreted by the kidney mainly through tubule secretion. OAT-1 and -3 were found efficient in picking up IS from the extracellular environment. [45] When kidney function was reduced due to renal conditions, the tubule secretions became least efficient which results in increased serum IS (and other metabolic toxins) levels. Under normal conditions, OATs are effective in absorbing IS from the basolateral membrane and then actively secreting though luminal membrane OATs. However, increased serum IS level results in the accumulation of IS with epithelial cells. As IS level elevated, such epithelial cells were subjective to increasing oxidative radical concentration and decreasing OATs activity which eventually adds up to the loss of the remanent nephron. [45-47] And the loss of nephron in turn induces more stress on the kidney function. It was also noted that vascular epithelial cells were also the victim of the increased serum IS level due to similar OATs transportation mechanisms. [48] So, not surprisingly, the progress of CKD is associated with IS level in a self-actualizing or self-promoting fashion. [47, 49, 50]

Water transportation control is critical to maintaining osmotic balance. Since, as mentioned above, the transportation of metal cations and organic anions was subject to abnormality under the influence of CKD. It is reasonable to assume a similar observation of water transportation and the corresponding carrier protein, aquaporins. Expression of AQP-1 was normally found in proximal tubule cells but found at an increased level in glomeruli when the renal injury happens. [31, 51] AQP-2 was found closely associated with urine concentrations. Deficiency in activity or expression of AQP-2 results in diabetes insipidus while hyponatremia was found when AQP-2 function

increases. [33, 52] Other kidney conditions, such as polycystic kidney disease, were also found associated with abnormality of AQP functions.

1.2.5 *Current Challenges in Dialysis*

As previously mentioned, dialysis serves as the final option for patients experiencing deteriorating kidney function before receiving a transplant. The hemodialysis procedure closely *mimic*s the natural functioning of the kidneys by directing the patient's blood through a dialyzer for transmembrane mass exchange across the dialyzer membrane. In this process, uremic toxins are removed via diffusion along a concentration gradient. Nevertheless, current dialysis techniques aimed at mimicking kidney function still fall short in comparison to the capabilities of a healthy, functioning kidney.

*T*he capability of dialysis machines was limited by the efficiency of the dialysis membrane which normally allows permeance of compounds smaller than 500 Da. And the removal of these compounds relies on a huge amount of dialysate prescribed to the patient's need. Generally, over 100 L of dialysate would be used for a single hemodialysis session which lasts for over 4 hours. Because of the equipment required and the large amount of dialysate generated, dialysis sessions are normally held at special facilities with personnel trained for the operation. And as *renal* disease progresses, patients have no choice but to spend more time tied to such dialysis facilities. For substances that are hard to remove, such as indoxyl sulfate, which has a majority (over 90%) found bound to proteins, even longer dialysis sessions were often required. *[53, 54]* However, even with significant efforts made, the long-term survival rate of ESRD patients is still far from desirable. The five-year survival possibility is barely better than 40%. [55] And since these on-site dialysis sessions do not continuously manage the patient's condition, significant adverse effects take place

between the dialysis sessions. For instance, cardiac arrest, associated with hyperkalemia, is a major reason responsible for the mortality of patients between dialysis sessions.

Therefore, it is imperative to continuously manage plasma composition with greater efficiency. The continuous, at-home hemodialysis method presents significant challenges, primarily due to the substantial amount of dialysate required per session and the need for precise dialysate composition, as discussed earlier. The limited efficiency of dialysis can be attributed to its reliance on transmembrane diffusion driven by *solute* concentration differences. Drawing inspiration from functional nephrons, particularly in how membrane proteins collaborate, the optimal approach to addressing these challenges and achieving a more accurate mimicry of nephron function lies in the incorporation of active mass transfer mechanisms with molecule recognition and selectivity. This necessitates further exploration within the fields of materials science and surface chemistry.

1.3 Active Chemical Separation with Biomimicking Selective Chemistry

After a comprehensive review of the functions and operating mechanisms of healthy kidneys, industrial chemical separation methods, and dialysis mechanisms, it is logical to contemplate the utilization of the selective chemistry, mimicking highly selective biomembrane proteins, to imbue existing industrial chemical separation methods and dialysis devices with biomimetic principles. Nevertheless, numerous unknowns within the realm of materials science await exploration and investigation to bridge the gap between methodology and practical application. Therefore, the ensuing discussion will delve into topics pertaining to related materials and surface chemistry.

1.3.1 *Significance of Selective Chemistry*

Energy consumption is one major drawback of industrial thermal separation techniques. Distillation, for instance, is one of the most adopted processes constituting over 90% of total chemical and petroleum separation but costing as much energy as all the other separation processes combined. [5] Membrane separation with proper selectivity was believed to reduce such energy penalty by 90%. [2] Some substances, for example, proteins or pharmaceuticals, however, cannot be efficiently separated by thermal separation methods. For these substances, solid phase extraction methods, like chromatography, stand out as a better option. Solid phase absorbents commonly capture the substance of interest through van der Waal force, electrostatic interaction or hydrogen bonds. The selectivity of absorbent emerges from fine tuning these adsorption forces. For instance, plasma proteins were commonly fractionated with dye decorated chromatography and carefully designed eluent solution. [56-58] Appropriate affinity and selectivity are vital for delicate applications like protein fractionation because the complexity of the sample. Another good *example that* calls for high selectivity is isotope separation. Diluted sample processing also requires high selectivity and affinity chemistry. Enrichment of trace amount elements, like uranium in seawater, and removal or analysis of trace amount contaminants, such as pesticides in the water sample, benefits greatly from high selectivity solid phase absorbent. [2, 59]

1.3.2 *Solid Phase Support*

Solid-phase support for selective chemistry can be categorized into two main groups: high surface absorbents, such as chromatography columns, and porous membranes. These two categories have distinct merits and limitations due to their differing geometries.

Column chromatography offers a significant advantage in terms of a high surface area. When decorated with selective chemistry, this increased surface area directly translates into a higher

adsorption capacity, enabling the processing of larger sample volumes. In contrast, membrane separation is typically constrained by available surface area and porosity, resulting in lower processing capacity. However, innovative engineering can mitigate this limitation. For example, hollow fiber membranes used in hemodialysis treatments exhibit a favorable surface area-to-volume ratio. Similarly, reverse osmosis membranes employed in water purification are often spiral wound to optimize spatial geometry. Membrane geometry provides the advantage of high selectivity, primarily achieved through engineering the membrane to attain the desired pore size and surface chemistry.

In membrane separations, the two fundamental parameters controlled by membrane characteristics are selectivity and permeability. For instance, consider renal flux: the glomerular filtration rate is exceptionally high, allowing a wide spectrum of metabolic waste, electrolytes, and nutrients to pass through with limited selectivity. However, during the reabsorption process, specific transporter proteins actively reabsorb substances with high selectivity. Notably, certain segments of renal tubules are recognized as impermeable to water.

On the other hand, separation using high surface area absorbents like chromatography columns is subject to different considerations. As discussed in section 1.1.4, the affinity of chromatography resin or high surface area absorbent can be manipulated by surface functionality. While optimizing resin affinity leads to higher resolution in complex fractionation, a higher flow rate through the chromatography column can negatively impact the separation due to mechanical agitation. Tuning the affinity of the mobile phase used in column chromatography is another way to manipulate fractionation efficiency, but it falls outside the scope of our discussion on selective surface chemistry.

In industrial chemical separation, continuous operation is essential. As previously discussed, biochemical separation processes are continuous, making continuous operation in dialysis more desirable. To address this need for continuity, we propose a general workflow for regenerable solid-phase support, whether in the form of column chromatography or membrane geometry, as illustrated in Figure 1.3.

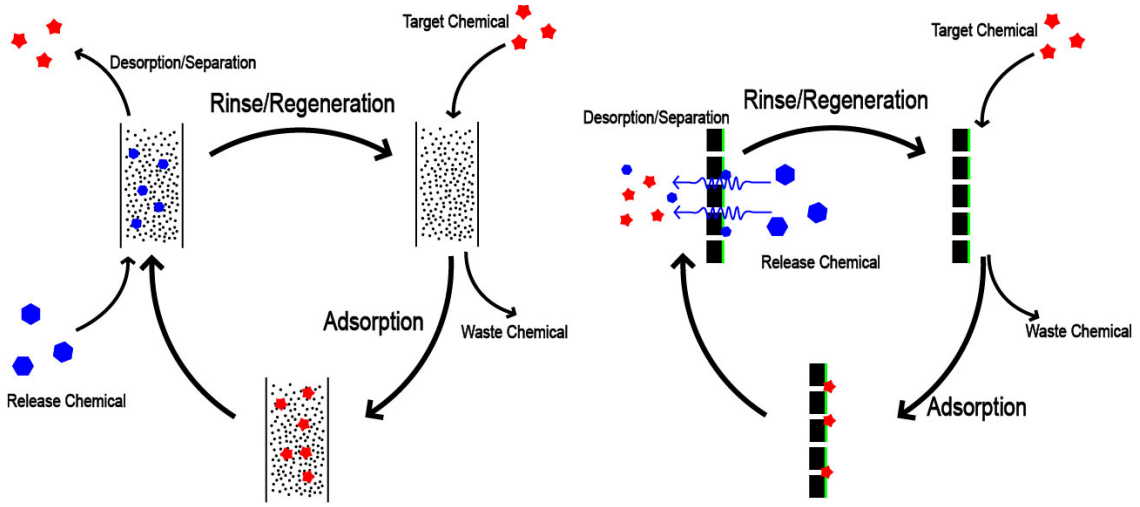

Figure 1.3. Schematic demonstration of regenerable solid phase absorbent workflow cycle.

1.3.3 *High Surface Area Absorbent*

Activated carbon (AC) is arguably the most renowned high surface area absorbent, albeit with limited selectivity. Specific areas of AC can be engineered to exceed 1000 m^2/g. [60, 61] Therefore, activated carbon finds widespread use in various industries. AC can be produced through either thermal or chemical activation of precursor materials such as peat, wood, coconut shells, and others. [62, 63] The activation process primarily involves carbonizing the precursor and eliminating volatile mass. Consequently, randomly distributed pores ranging in size from the angstrom level to the micrometer level are introduced to the activated carbon, significantly increasing its surface area. However, due to the inherent nature of the process, fine-tuning the pore geometry remains challenging. Moreover, the process only alters the material's nature to a limited extent, maintaining

graphitic layered structures as depicted in Figure 1.4. The adsorption behavior of activated carbon remains similar to that of other carbon absorbent materials unless modified otherwise. Adsorption on AC relies on its high surface area, employing a size-screening effect wherein smaller molecules have greater access to the smaller pores of the activated carbon, and the interaction between AC and the adsorbed substance occurs through Van der Waals forces. Therefore, achieving specific tasks with AC-based absorbents often necessitates specialized functionalization chemistry.

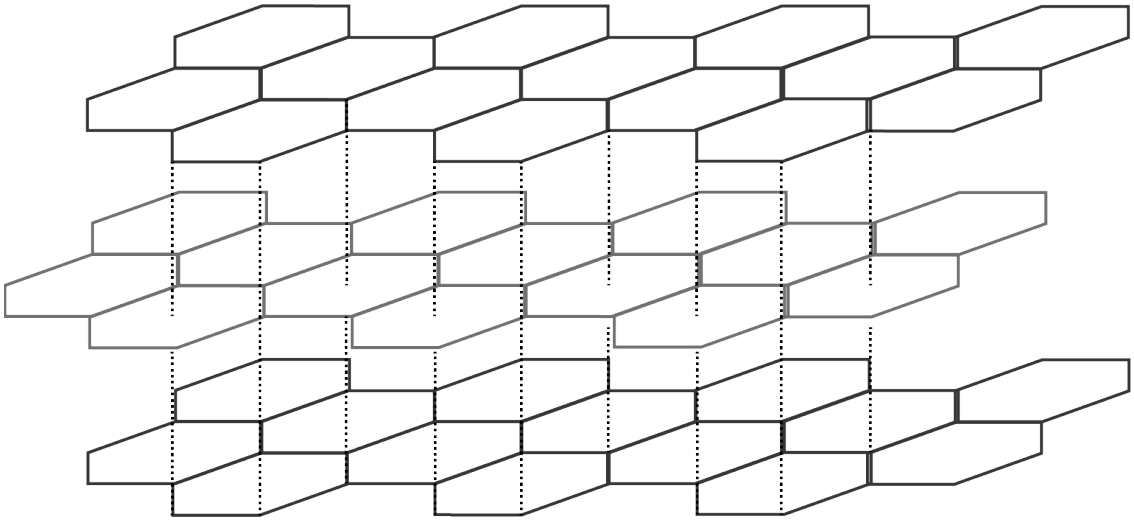

Figure 1.4. Scheme of layered graphite structure of activated carbon.

Zeolite is another category of high-surface-area absorbent material, comparable in surface area to activated carbon (AC), with over 255 unique framework structures that significantly impact its microstructure. [64] The material is general composed of $M_{x/n}^{n+}[Al_xSi_{1-x}O_2]\cdot yH_2O$, where M denotes different cations and x normally range from 0-0.5. [65] The porosity and pore structure of synthesized zeolite can be altered by manipulating the synthesis route, but natural zeolites exhibit less variability in microstructure. Similarly, the elemental composition of natural zeolites exhibits higher randomness. Similar to AC, zeolite exhibits Van der Waals adsorption due to its ordered nanoporous structure but has better size screen effect. As a result, molecular sieves made of zeolites find applications in various fields, such as solvent dehydration and gas separation. However, zeolite also displays another adsorption mechanism—cation exchange—in aqueous

solutions. In this mechanism, cations in the solution are believed to be exchanged for stoichiometric amounts of cations released into the solution by the zeolite. For example, this mechanism has been employed for treating wastewater to remove potassium and ammonia using naturally occurring zeolite, clinoptilolite. [66] Combining both adsorption mechanisms, zeolites were found with high capacity for ion adsorption. However, using zeolites in ion-sensitive scenarios may require additional engineering considerations due to the complexity of ion exchange interactions.

Metal-organic frameworks (MOFs) constitute a category of porous materials characterized by precisely engineered microstructures and porosity. They consist of metal coordination centers and linkers with desired geometries. By manipulating the metal coordination and linker shapes, the pore architecture of these materials can be finely engineered, resulting in surface areas reaching levels of up to 10,000 m^2/g. [67, 68] In general, longer linker molecules correspond to larger pore sizes (porosity), while the metal center determines the coordination and arrangement of the surrounding linker ligands. The microstructure of MOFs can be optimized by configuring the metal center and organic linker, enabling the recognition of guest species, including ions or large molecules. [69, 70] Because MOFs are synthetically designed materials and their structure is highly versatile, the selectivity of these porous materials can be finely tuned to meet the specific requirements of individual applications. Consequently, for applications targeting high-value objectives, such precision adsorption materials are highly desirable. However, it is important to note that, like the flip side of a coin, the high precision and selectivity of MOFs come with associated challenges, including high production costs, stringent synthesis process requirements, and the delicate nature of the material. These factors present obstacles to the widespread large-scale application of MOFs.

Silica xerogel (SG) is another category of absorbent with a surface area commonly found over 100x m^2/g level. Synthesis of silica xerogel was first done in the early 1900s. The hydrolysis of organic-orthosilicate initiates a polycondensation reaction by forming silanol and water or alcohol at the same time. Then, the produced silanol and organic orthosilicate form a network by condensation polymerization. Acid or base can be used to catalyze hydrolysis and polycondensation. It was believed that acid catalyst favors hydrolysis reaction while basic reaction favors polycondensation reaction. [71, 72] Therefore, acid catalyzed synthesis forms a large number of small particles before polycondensation into a more linear molecule compared to base catalyzed reaction, which yields silicate in a higher degree of polymerization (more branched) but with fewer starting nuclei. Thusly, the microstructure of silica gel was found to be controlled by the kinetics of hydrolysis and polycondensation. [71, 73-75] Properly designing the synthesis approach allows preparation of silica gel with well define microstructure such as narrow distribution of pore-size and desirable porosity. [76-78] During the drying process, after gelation and proper aging of polymerized silicate, the solvent was removed from the matrix. The capillary force of the leaving solvent causes micropores and microchannels of the silicate matrix to collapse. So, volume shrink was commonly observed during the drying of the gel. Once dried xerogel is obtained, a diversified surface function can be easily decorated to SG surface based on the residual silanol group at the surface allowing diversified separation applications. [77, 78]

1.3.4 *Silica Xerogel with Crown Ether Decoration for Potassium Control*

The excretion of potassium is mainly regulated by the kidney and excreted through urine. As mentioned in the previous section, imbalanced intake and excretion of potassium happen when kidney function was impaired. Loss of nephron function was believed to cause a decrease in urinal excretion of potassium. To this day, the definitive solution to potassium management, along with

other metabolic waste, is still hemodialysis. However, on-site dialysis treatment lacks continuity. Fluctuations of potassium levels were commonly observed between dialysis sessions, especially at longer intersession periods. [79, 80] In order to address the lack of continuity of on-site dialysis treatment, a portable continuously operating dialysis device is needed. High selectivity, towards potassium in this case, and regeneration capability are two vital criteria for efficient absorbent without utilizing an excessive amount of dialysate.

Crown ethers (CE) offer selectivity towards different metal ions and reversible adsorption. The cavity size of crown ether ranges according to the size of the crown ether molecule. For 18-crown-6-ether, the cavity size was found to be ~ 2.6-3.2 Å, which matches the size of the potassium ion. [81] Metal cations can be stabilized within the cavity of crown ether through the interaction between the positively charged cation and negative oxygen atoms of the CE ring. And selectivity arises from the matching of the cavity size and cation size. [81-86] Absorbents for chemical separation and specialized sensors based on the selectivity of CE were developed by incorporating CE with a proper supporting matrix. [87-91]

Among the high-surface-area materials discussed previously, silica gels emerge as a promising platform for the development of selective adsorbents for potassium management, taking into account factors such as complexity, cost, and stability. While zeolites exhibit desirable potassium adsorption capacity, their ion exchange mechanism carries potential risks to patients' electrolyte balance due to the release of cations like sodium or aluminum, which can disrupt homeostasis. MOFs, despite their versatility in microstructure and composition, fall short in terms of long-term stability and are generally more expensive to synthesize than other materials. Therefore, a rational approach for synthesizing a selective and regenerable absorbent for potassium level management in patients with CKD is to modify high-surface-area silica xerogel with 18-crown-6-ether.

1.3.5 *Agarose Gel with Albumin Selective Chemistry for Indoxyl Sulfate Removal*

Human albumin (HA) is the primary molecular transport protein in blood plasma for a variety of chemicals such as metal ions, fatty acids, and metabolism toxins. [92] The structure of HA is complex with three homologous helical domains (I–III) which can be further divided into subdomains A and B. [93] Protein-bound uremic toxins (PBUTs), such as indoxyl sulfate (IS), are responsible for causing a variety of fatal diseases of patients with kidney conditions. [94] While healthy kidneys have specialized molecular pumps to remove anionic-aromatic compounds from HA while avoiding healthy chemicals and pharmaceuticals captured in the S-II site, conventional kidney dialysis lacks the ability to selectively remove the PBUTs from HA. Because the protein-PBUT complex is too large (~66.5 kDa) to pass through conventional dialysis membranes with ~0.5 kDa molecular weight cut off (MWCO) and the strong binding of HA-IS. [54, 95] Some treatments allow a fraction of HA, with and without toxin, to be removed in dialysis using high MWCO (~70 kDa) to reduce toxin build-up when toxin-occupied albumin exceeds a certain level. But such practice suffers from the loss of healthy chemicals including pharmaceuticals and proteins. [96] Therefore, to address the dilemma between low PBUT removal rate and hypoalbuminemia caused by dialysis, a HA detoxification method needs to be developed.

Studies show that the Sudlow site II (S-II), where indoxyl sulfate (IS) mainly binds, also contains two fatty acid binding sites, and is capable of binding to a variety of molecules. [93, 97] Because the S-II site is capable of binding different molecules. It's possible to develop chemistry that competes with IS in binding to this shared binding site and simultaneously release bound IS. [98, 99] Hence, a series of covalently bonded surface functionalization, including long-chain alkanes, lipids, and charged aromatics, were investigated for their binding to HA using surface plasmon resonance (SPR). The desorption coefficients (Kd) of these examined ligands ranged from 0.9 to

3 μM, comparable to the binding of HA to the indoxyl sulfate (IS) toxin. Various release agents were also studied, spanning from physiologically toxic NaSCN and SDS to physiologically manageable NaCl, HCl, and fatty acids. Notably, plasma-compatible fatty acids, such as linoleic acid and a fatty acid mixture at physiological ratios, were found capable of releasing HA with approximately 30-40% surface coverage.

This process was scaled up using commercially available Cibacron blue-functionalized agarose beads, commonly used for plasma protein fractionation. It demonstrated binding capacities of 0.35 μmol HA/mL beads and release amounts of 0.23 μmol HA/mL beads when employing the plasma-compatible linoleic acid. Fluorescence studies of the released HA eluents indicated that the HA-IS complex had been effectively stripped of the protein-bound toxin, IS. It was then calculated that during a conventional 4-hour dialysis session with 2-minute binding release cycles, only 155 ml of CB-agarose beads would be required to process the 250 grams of HA typically present in a patient, thereby enabling a practical treatment strategy.

To further validate the albumin detoxification chemistry, a prototype add-on device was designed and constructed, with key components including a plasma fractionation membrane cartridge, a Cibacron blue functionalized detoxification column, and a linoleic acid filter. The design was meticulously assessed to ensure it met the operational requirements under physiological conditions.

Through a comprehensive evaluation of the albumin-Cibacron blue interaction in physiological conditions, it has been determined that the linoleic acid dissociation chemistry is functional but necessitates a linoleic acid solution concentration of 8 μl/10 ml buffer for optimal use. Further analysis indicated that structural differences among albumin variants do not significantly affect the efficiency of the linoleic acid release chemistry. Consequently, experiments involving artificial

plasma are deemed sufficient to demonstrate the efficacy of the add-on prototype. Therefore, the constructed prototype device was evaluated for its ability to remove indoxyl sulfate in comparison to the capabilities of a common dialyzer, with promising results anticipated.

1.3.6 *Carbon Nanotube Membrane*

As discussed in section 1.3.2, membrane geometry offers higher selectivity compared to simple high-surface-area absorbents. However, it also comes with limitations in terms of surface area and scalability. To overcome the constraint of limited surface area, engineering efforts aim to enhance the surface-to-volume ratio and improve porosity. Two examples discussed earlier illustrate these efforts: the use of hollow fiber membrane cartridges in dialysis applications and spiral-wound membrane modules for water treatment, both designed to improve the surface-to-volume ratio. Another avenue for enhancing membrane performance in these applications involves engineering the membrane materials themselves.

For instance, the first hollow fiber membrane used in dialyzers was synthesized through molten mixture extrusion in the 1960s. Nowadays, phase separation synthesis is employed to create polymer membranes with better control over pore structure. [100, 101] Materials like ceramics have also been transformed into porous membranes, with anodic aluminum oxide (AAO) being a notable example from the 1970s to the 1990s, characterized by a hexagonal arrangement of defined pore sizes. [102] Incorporating carbon nanotubes into membranes to serve as conduits for achieving smoother inner surfaces gained significant attention since the late 1990s.

The first reported observation of single-wall carbon nanotube (SWCNT) was made by Sumio Iijima's group through an arc discharge fabrication process back in 1993. [103] The observed CNTs were found with diameters ranging from 0.7 nm to 1.6 nm. Prior to the observation of SWCNT, multi-walled carbon nanotubes (MWCNT) were observed and studied by the mid-1900s. Chemical

vapor deposition (CVD) with transition metal nanoparticles acting as catalyst/deposition site is a conventional method for CNT fabrication. In fact, some of the early observations of CNTs were made during synthesis under similar conditions. [104, 105] Nowadays, with more precise control of the catalyst metal particle and synthesis conditions the parameters of synthesized CNT can be engineered with a diameter range from less than 1 nm to over 100 nm and a length over 100 μm. Microstructures of CNTs, such as vertically aligned arrays of CNTs can also be done by tuning the synthesis condition.

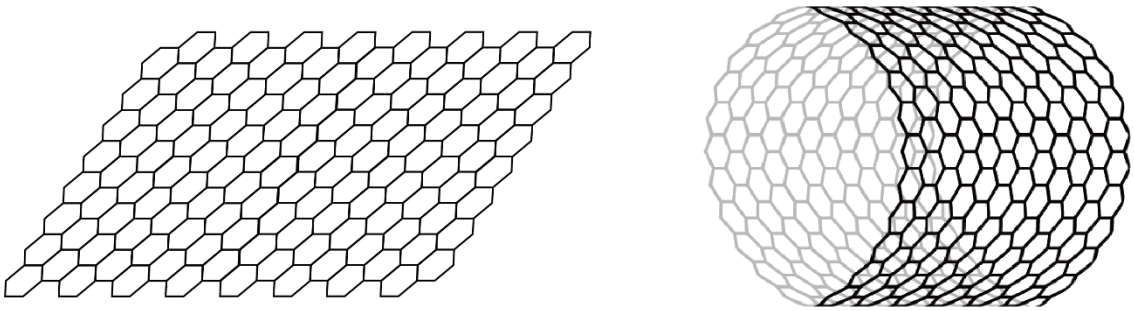

Figure 1.5. Scheme of graphene sheet structure and carbon nanotube structure.

The general structure of CNT can be simplified as a graphene sheet rolled up into a cylinder as shown in Figure 1.5, or multiple sheets of graphene rolled up in a concentrical fashion. With the same hexagonally arranged carbon atom structure "inherited" from the graphene, the pristine surface of CNTs was also believed to be smooth at the atom level. The ultra-smooth surface was also believed to promote fast water transport similar to the case in graphene capillary with increased slip length. [106, 107] Being different from graphene, CNT confines water molecules to transport in its core in a single file chain fashion with molecules connected by hydrogen bonds (H-bond). [106, 108] Due to the large slip length and nanoconfinement, liquid transport within the core of CNT was proven faster than prediction by conventional Hagen–Poiseuille equation. [106]

The inert chemical nature and hydrophobicity of CNT also arise from its carbon-only structure. One result of being hydrophobic is the difficulty in stably dispersing CNT with common solvents,

especially in an aqueous system. After dispersion, the dispersed CNTs tend to form aggregates to lower the surface energy even with loading as low as 1 wt%. One way to alter the hydrophobicity of CNT is chemical modification. Chemically treating CNT not only change the hydrophobicity but also give rise to other potential functionalization. Covalently functionalizing CNTs commonly starts with the introduction of oxygen-containing moieties as an anchor point for further chemical treatment. Such an oxidation process may be done with oxidizing acid mixtures (i.e. HNO_3/HCl), oxidizing plasma treatment, or an electrochemical process. [109-112] After the oxidation of CNT, the nanotube is decorated with hydroxyl, carbonyl, carboxyl, and occasionally epoxy groups. Such oxygen-containing groups, especially carboxyl groups, allow further grafting chemistry to be performed such as esterification, amination, etc. [109, 113, 114] Aside from oxidation, there is also other chemistry that grafts CNT in a covalent fashion such as halogenation, carbene addition, radical additions, etc. [115] Similarly, treated CNT can be further functionalized with a variety of molecules like dye molecules, polymers, macro-biomolecules, etc. [115-120] Granted that functionalization of CNT opens the potential for complex chemical grafting, it is also important to understand some of the harsh reaction condition also inevitably produces in defect site on the CNT, which lead to compromise in surface smoothness. Therefore, balancing the preservation of CNT integrity and functionalization of CNT becomes a challenge in engineering.

Carbon nanotube membrane fabricated by embedding CNTs into a polymer matrix is thought to preserve the smoothness of the CNT conduit core surface while allowing chemical functionalization of the CNT tips. In membrane form, the polymer matrix protects the outer shells of embedded nanotubes from harsh chemicals. But at the same time also covers the opening of the nanotubes in some cases. [111, 112] Therefore, an oxidizing process is commonly adopted to etch off the excess polymer layer revealing the embedded CNTs. Exposed CNTs, under oxidation, will be

etched as well to open the nanotube. Chemical treatment may be performed to functionalize the membrane once the membrane was processed to desired thickness or porosity. Membranes designed for certain practical applications ideally have limited functionalization to the surface of the membrane to preserve the smoothness of the CNT core allowing undisturbed flux. The diazonium grafting process with a solvent flux preventing diazonium molecules from entering the core of the nanotube was developed for functionalization selective to the surface of the membrane. [112]

1.3.7 *Carbon Nanotube Membrane for Electroosmosis Mass Transfer*

Carbon nanotubes are believed to promote the transportation of ions within their hollow cores. Concentration-induced ion diffusion within the core of CNT shows an order of magnitude higher velocity compared to the diffusion in bulk. [121] Under electric potential gradient, ion also demonstrates three times higher mobility when transporting within the CNT. [122] These electrophoretic motions have been found to induce flow of solvent molecules, as electroosmosis (EO) flow. [106, 122] The smooth core of carbon nanotube (CNT) conduits enables frictionless transport of water molecules, resulting in liquid transfer velocities predicted to exceed 1 m/s. [107, 108, 123] When compared to the thickness of a well-engineered CNT membrane, typically on the order of tens of micrometers, the liquid transfer velocity is exceptionally fast, almost instantaneous, occurring in mere microseconds. As a result, the transmembrane delivery of desired molecules can operate at a turnover rate on the order of 1 MHz, effectively compensating for the limitations imposed by membrane geometry in chemical separation applications. The rapid transport of ions and liquids inside carbon nanotubes has inspired researchers to translate these phenomena into practical applications, including drug delivery, desalination, ion/molecule pumps, ionic diodes, and more. [112, 124-127]

While numerous pilot studies have explored various applications using carbon nanotube (CNT) membranes, a substantial knowledge gap persists in the field of electroosmotic fluid flow under extreme nanoconfinement conditions. Our investigation into the factors affecting electroosmotic flow was conducted, utilizing a combination of silver chloride electrodes and robust CNT membranes measuring 10 μm in thickness with porosities ranging from 10^{-6} to 10^{-4}.

Fast electroosmotic flow was observed in 0.1 M KCl solution, with a velocity as high as 0.0196 ± 0.0017 cm/s or 0.233 ± 0.043 cm/sV when normalized for the applied potential. The smoothness of the CNT core emerged as the primary factor influencing electroosmotic flow, with ion size and valence demonstrating less impact when potential normalization was applied. Additionally, it was noted that lower ionic strength in the solution led to higher electroosmotic velocity due to the increased applied potential. The influence of hydrogen bonding structure was found to be insignificant, as demonstrated by the introduction of a chaotropic agent, NaSCN, to electroosmosis tests.

1.3.8 *Graphene and Graphene Oxide Membrane*

Investigations of graphene material can be traced back to as early as 1859 with Benjamin Brodie identifying what now is believed to be graphene oxide. [128] Then, it was till 2004 that isolation of graphene was done by the famous “scotch tape method”. [129] Observation of a single layer graphene sheet was made with the aid of Transmission electron microscopy (TEM) later in 2007. [130] It is now well known that the structure of a graphene sheet can be described as a 2-D crystal made of a single layer of hexagonally arranged carbon atoms. Graphene oxide (GO), a derivative of graphene, is commonly fabricated by methods involving the oxidation of graphite, such as Hummer’s method. [131] As can be expected, GO contains oxygen moieties such as hydroxyl, carbonyl, carboxyl, and epoxide groups covering, unevenly, over 20% of the graphene

sheet. [132], [133] With additional oxygen-containing moieties, GO shows improved hydrophilicity compared to graphene, giving ease in fabrication into membranes or other devices.

With well define interlayer space, or d-space, of about 0.8 nm in a dry state, and an overall atomically smooth surface, GO-based membranes show great potential for membrane separation applications. [132, 134] Membranes for separation applications commonly face the tradeoff between selectivity and efficiency. The selectivity of GO membranes was determined by the d-spacing of the membrane and chemical functionalization. To achieve chemical selectivity, the d-spacing of the GO membrane can be carefully engineered by intercalating a binder or spacer of small molecules, engineered nanoparticles, nanotubes, or polymers. [135-142] Small cations were also thought to be able to control the d-space of the GO membrane by screening repelling carboxylic acid anionic moieties of two adjacent GO sheets. [143] Such cation screen phenomena were also believed to stabilize GO membranes in aqueous solution as high hydrophilicity and inter-flake repulsion can sometimes lead to swelling or even redispersion of GO flakes. [132, 144] As mentioned before, the distribution of the oxygen-containing groups on the GO surface is not even leaving unoxidized graphene region remain atomically smooth. [133] Thanks to the atom-level smoothness induced large slip length, which is over 10 times the graphene interlayer space, such graphene region is hoped to form “frictionless channels” for fast water transport allowing GO membrane to show better efficiency performance. [145-148] It can be assumed that the engineering of GO membrane chemistry while utilizing the graphene fast fluidic channel of graphene would shift the selectivity-efficiency tradeoff to a more favorable balance.

Aside from the chemistry of GO membranes, the thickness is another key parameter that needs to be included in consideration for performance analysis. In general, studies have shown a trend that thinner membranes would show higher solvent permeance compared to thicker ones while

more prone to defect. Thus, pushing for higher permeance, GO membranes as thin as 8 nm, which was thought to be the critical thickness needed to not have major defects to introduce high flow artifacts. [149] However, more practical methods generally focus on fabricating much thicker GO membranes of (μm-scale) and also promote enhanced permeance performance by orienting GO flakes to form ordered and laminated 2-D channels. [134, 150] To account for thickness differences from different reports, permeability is proposed as a reference and defined as

$$permeability = membrane\ thickness \times permeance\ of\ solvent.$$ [135, 149, 151]

The fabrication method also shows a great impact on the performance of GO membranes. It was believed that a fabrication process that promotes the formation of laminated GO structure would greatly improve the permeability performance. [150] For instance, GO membrane fabricated by drop-casting, filtering, and slip-casting shows a difference in permeability of water ranges in 3 magnitudes. [152, 153]

1.3.9 *Graphene Oxide Membrane for Alcohol Dehydration*

Alcohol dehydration is one of the challenging industrial processes researchers trying to tackle in an attempt to resolve the dire energy situation nowadays. Membrane for alcohol dehydration application must be defect-free in large area and ordered in microstructure to ensure the selectivity of water and energy efficiency of the process. Recent advances in slip casting have led to the use of an optimized shear rate to align the GO grains in 5 μm thick GO membranes for ethanol dehydration via pervaporation. [134] Interestingly, in the pervaporation study, fluxes dropped dramatically for the water-alcohol mixture, but not for individual components. A similar flux decrease phenomenon was also observed in an attempt to separate water from ethanol and isopropyl alcohol. [152, 154] Proposed mechanisms include the formation of a water-GO complex at the GO channel entrance that reduces the effective hydrodynamic pore size of GO excluding

alcohol.[134, 154] Others propose that alcohol molecules disrupt the entrance of water molecules into the GO plane.[155-158] Our experiments show that the decreased flux was likely induced by decreased d-space from a partial reduction of GO through a catalytic reaction with the alcohol-water mixture.[151]

1.4 REFERENCES

[1] 2018 MECS Survey Data; Table 1.2 First Use of Energy for All Purposes (Fuel and Nonfuel), 2018. February 2021. https://www.eia.gov/consumption/manufacturing/data/2018/ (accessed Aug 2023).

[2] Sholl, D. S.; Lively, R. P. Seven chemical separations to change the world. *Nature* **2016**, *532* (7600), 435-437, Editorial Material. DOI: 10.1038/532435a.

[3] Peiro, L. T.; Mendez, G. V. Material and Energy Requirement for Rare Earth Production. *Jom* **2013**, *65* (10), 1327-1340, Article. DOI: 10.1007/s11837-013-0719-8.

[4] Administration, U. S. E. I. *How much electricity does an American home use?* 2022. https://www.eia.gov/tools/faqs/faq.php?id=97&t=3#:~:text=In%202021%2C%20the%20average%20annual,about%20886%20kWh%20per%20month (accessed.

[5] Oak Ridge National Laboratory (ORNL). Materials for Separation Technologies: Energy and Emission Reduction Opportunities. **2005**.

[6] Wade, N. M.; Hornsby, M. R. DISTILLATION AND REVERSE-OSMOSIS - ENERGY-CONSUMPTION AND COSTS. *Desalination* **1982**, *40* (3), 245-257. DOI: 10.1016/s0011-9164(00)88693-2.

[7] Raynie, D. E. Modern Extraction Techniques. *Anal. Chem.* **2010**, *82* (12), 4911-4916. DOI: 10.1021/ac101223c.

[8] Gianazza, E.; Arnaud, P. A GENERAL-METHOD FOR FRACTIONATION OF PLASMA-PROTEINS - DYE LIGAND AFFINITY-CHROMATOGRAPHY ON IMMOBILIZED CIBACRON BLUE F3GA. *Biochem. J.* **1982**, *201* (1), 129-136, Article. DOI: 10.1042/bj2010129.

[9] Gianazza, E.; Arnaud, P. CHROMATOGRAPHY OF PLASMA-PROTEINS ON IMMOBILIZED CIBACRON BLUE F3GA - MECHANISM OF THE MOLECULAR INTERACTION. *Biochem. J.* **1982**, *203* (3), 637-641, Article. DOI: 10.1042/bj2030637.

[10] Kim, D. W.; Kang, B. M.; Jeon, B. K.; Ryu, H. Adsorption and isotope effects by ion exchange with aqueous-2-aminomethyl-18-crown-6 bonded Merrifield resin. *Journal of Colloid and Interface Science* **2002**, *254* (1), 190-194. DOI: 10.1006/jcis.2002.8411.

[11] Lim, L. W.; Tokunaga, K.; Takeuchi, T. Development of chemically bonded crown ether stationary phases in capillary ion chromatography. *Chromatography* **2014**, *35* (2), 95-101.

[12] Skou, J. C. The influence of some cations on an adenosine triphosphatase from peripheral nerves. 1957. *Biochimica et biophysica acta* **1989**, *1000*, 439-446, Biography; Classical Article; Historical Article;.

[13] Sekine, T.; Cha, S. H.; Endou, H. The multispecific organic anion transporter (OAT) family. *Pflugers Arch.* **2000**, *440* (3), 337-350, Review. DOI: 10.1007/s004240000297.

[14] Walz, T.; Hirai, T.; Murata, K.; Heymann, J. B.; Mitsuoka, K.; Fujiyoshi, Y.; Smith, B. L.; Agre, P.; Engel, A. The three-dimensional structure of aquaporin-1. *Nature* **1997**, *387* (6633), 624-627, Article. DOI: 10.1038/42512.

[15] Morth, J. P.; Pedersen, B. P.; Toustrup-Jensen, M. S.; Sorensen, T. L. M.; Petersen, J.; Andersen, J. P.; Vilsen, B.; Nissen, P. Crystal structure of the sodium-potassium pump. *Nature* **2007**, *450* (7172), 1043-U1046, Article. DOI: 10.1038/nature06419.

[16] Shinoda, T.; Ogawa, H.; Cornelius, F.; Toyoshima, C. Crystal structure of the sodium-potassium pump at 2.4 angstrom resolution. *Nature* **2009**, *459* (7245), 446-U167, Article. DOI: 10.1038/nature07939.

[17] Katz, A. I. RENAL NA-K-ATPASE - ITS ROLE IN TUBULAR SODIUM AND POTASSIUM-TRANSPORT. *Am. J. Physiol.* **1982**, *242* (3), F207-F219, Review. DOI: 10.1152/ajprenal.1982.242.3.F207.

[18] Jorgensen, P. L. STRUCTURE, FUNCTION AND REGULATION OF NA,K-ATPASE IN THE KIDNEY. *Kidney International* **1986**, *29* (1), 10-20, Article. DOI: 10.1038/ki.1986.3.

[19] Doucet, A. FUNCTION AND CONTROL OF NA-K-ATPASE IN SINGLE NEPHRON SEGMENTS OF THE MAMMALIAN KIDNEY. *Kidney International* **1988**, *34* (6), 749-760, Review. DOI: 10.1038/ki.1988.245.

[20] Hamilton, K. L.; Devor, D. C. Basolateral membrane K+ channels in renal epithelial cells. *Am. J. Physiol.-Renal Physiol.* **2012**, *302* (9), F1069-F1081, Review. DOI: 10.1152/ajprenal.00646.2011.

[21] Post, R. L.; Kume, S.; Hegyvary, C. ACTIVATION BY ADENOSINE-TRIPHOSPHATE IN PHOSPHORYLATION KINETICS OF SODIUM AND POTASSIUM ION TRANSPORT ADENOSINE-TRIPHOSPHATASE. *J. Biol. Chem.* **1972**, *247* (20), 6530-&, Article.

[22] Lupfert, C.; Grell, E.; Pintschovius, V.; Apell, H. J.; Cornelius, F.; Clarke, R. J. Rate limitation of the Na+,K+-ATPase pump cycle. *Biophys. J.* **2001**, *81* (4), 2069-2081, Article. DOI: 10.1016/s0006-3495(01)75856-0.

[23] Ohtsuki, S.; Asaba, H.; Takanaga, H.; Deguchi, T.; Hosoya, K.; Otagiri, M.; Terasaki, T. Role of blood-brain barrier organic anion transporter 3 (OAT3) in the efflux of indoxyl sulfate, a

uremic toxin: its involvement in neurotransmitter metabolite clearance from the brain. *J. Neurochem.* **2002**, *83* (1), 57-66, Article. DOI: 10.1046/j.1471-4159.2002.01108.x.

[24] Nigam, S. K.; Bush, K. T.; Martovetsky, G.; Ahn, S. Y.; Liu, H. C.; Richard, E.; Bhatnagar, V.; Wu, W. THE ORGANIC ANION TRANSPORTER (OAT) FAMILY: A SYSTEMS BIOLOGY PERSPECTIVE. *Physiol. Rev.* **2015**, *95* (1), 83-123, Review. DOI: 10.1152/physrev.00025.2013.

[25] Breljak, D.; Ljubojevic, M.; Hagos, Y.; Micek, V.; Eror, D. B.; Madunic, I. V.; Brzica, H.; Karaica, D.; Radovic, N.; Kraus, O.; et al. Distribution of organic anion transporters NaDC3 and OAT1-3 along the human nephron. *Am. J. Physiol.-Renal Physiol.* **2016**, *311* (1), F227-F238, Article. DOI: 10.1152/ajprenal.00113.2016.

[26] Kojima, R.; Sekine, T.; Kawachi, M.; Cha, S. H.; Suzuki, Y.; Endou, H. Immunolocalization of multispecific organic anion transporters, OAT1, OAT2, and OAT3, in rat kidney. *Journal of the American Society of Nephrology* **2002**, *13* (4), 10, Article.

[27] Janaszkiewicz, A.; Toth, A.; Faucher, Q.; Martin, M.; Chantemargue, B.; Barin-Le Guellec, C.; Marquet, P.; Di Meo, F. Insights into the structure and function of the human organic anion transporter 1 in lipid bilayer membranes. *Scientific Reports* **2022**, *12* (1), 15, Article. DOI: 10.1038/s41598-022-10755-2.

[28] Burckhardt, G.; Wolff, N. A. Structure of renal organic anion and cation transporters. *Am. J. Physiol.-Renal Physiol.* **2000**, *278* (6), F853-F866, Review. DOI: 10.1152/ajprenal.2000.278.6.F853.

[29] Anzai, N.; Kanai, Y.; Endou, H. Organic anion transporter family: Current knowledge. *J. Pharmacol. Sci.* **2006**, *100* (5), 411-426, Review. DOI: 10.1254/jphs.CRJ06006X.

[30] Pritchard, J. B.; Miller, D. S. MECHANISMS MEDIATING RENAL SECRETION OF ORGANIC-ANIONS AND CATIONS. *Physiol. Rev.* **1993**, *73* (4), 765-796, Review. DOI: 10.1152/physrev.1993.73.4.765.

[31] Bedford, J. J.; Leader, J. P.; Walker, R. J. Aquaporin expression in normal human kidney and in renal disease. *Journal of the American Society of Nephrology* **2003**, *14* (10), 2581-2587, Article. DOI: 10.1097/01.asn.0000089566.28106.f6.

[32] Maunsbach, A. B. Aquaporin-1 water channel expression in human kidney (vol 8, pg 1, 1997). *Journal of the American Society of Nephrology* **1997**, *8* (2), 358-360, Correction, Addition.

[33] Su, W.; Cao, R.; Zhang, X. Y.; Guan, Y. F. Aquaporins in the kidney: physiology and pathophysiology. *Am. J. Physiol.-Renal Physiol.* **2020**, *318* (1), F193-F203, Review. DOI: 10.1152/ajprenal.00304.2019.

[34] Murata, K.; Mitsuoka, K.; Hirai, T.; Walz, T.; Agre, P.; Heymann, J. B.; Engel, A.; Fujiyoshi, Y. Structural determinants of water permeation through aquaporin-1. *Nature* **2000**, *407* (6804), 599-605, Article. DOI: 10.1038/35036519.

[35] de Groot, B. L.; Frigato, T.; Helms, V.; Grubmuller, H. The mechanism of proton exclusion in the aquaporin-1 water channel. *Biophys. J.* **2004**, *86* (1), 628A-628A, Meeting Abstract.

[36] de Groot, B. L.; Grubmuller, H. Water permeation across biological membranes: Mechanism and dynamics of aquaporin-1 and GlpF. *Science* **2001**, *294* (5550), 2353-2357, Article. DOI: 10.1126/science.1062459.

[37] Zhu, F. Q.; Tajkhorshid, E.; Schulten, K. Theory and simulation of water permeation in aquaporin-1. *Biophys. J.* **2004**, *86* (1), 50-57, Article. DOI: 10.1016/s0006-3495(04)74082-5.

[38] Romagnani, P.; Remuzzi, G.; Glassock, R.; Levin, A.; Jager, K. J.; Tonelli, M.; Massy, Z.; Wanner, C.; Anders, H. J. Chronic kidney disease. *Nat. Rev. Dis. Primers* **2017**, *3*, 24, Article. DOI: 10.1038/nrdp.2017.88.

[39] Ueda, Y.; Ookawara, S.; Ito, K.; Miyazawa, H.; Kaku, Y.; Hoshino, T.; Tabei, K.; Morishita, Y. Changes in urinary potassium excretion in patients with chronic kidney disease. *Kidney research and clinical practice* **2016**, *35* (2), 78-83. DOI: 10.1016/j.krcp.2016.02.001.

[40] Supplements, N. I. o. H. O. o. D. *Potassium Fact Sheet for Health Professionals*. 2022. https://ods.od.nih.gov/factsheets/Potassium-HealthProfessional/ (accessed.

[41] Kraft, M. D.; Btaiche, I. F.; Sacks, G. S.; Kudsk, K. A. Treatment of electrolyte disorders in adult patients in the intensive care unit. *Am. J. Health-Syst. Pharm.* **2005**, *62* (16), 1663-1682, Review. DOI: 10.2146/ajhp040300.

[42] Cheng, J. T.; Kahn, T.; Kaji, D. MECHANISM OF ALTERATION OF NA-K PUMP IN ERYTHROCYTES FROM PATIENTS WITH CHRONIC-RENAL-FAILURE (CRF). *Kidney International* **1982**, *21* (1), 228-228, Meeting Abstract.

[43] Kaji, D.; Kahn, T. NA+-K+ PUMP IN CHRONIC-RENAL-FAILURE. *Am. J. Physiol.* **1987**, *252* (5), F785-F793, Review. DOI: 10.1152/ajprenal.1987.252.5.F785.

[44] Wilson, P. D.; Sherwood, A. C.; Palla, K.; Du, J.; Watson, R.; Norman, J. T. REVERSED POLARITY OF NA+-K+-ATPASE - MISLOCATION TO APICAL PLASMA-MEMBRANES IN POLYCYSTIC KIDNEY-DISEASE EPITHELIA. *Am. J. Physiol.* **1991**, *260* (3), F420-F430, Article. DOI: 10.1152/ajprenal.1991.260.3.F420.

[45] Enomoto, A.; Takeda, M.; Tojo, A.; Sekine, T.; Cha, S. H.; Khamdang, S.; Takayama, F.; Aoyama, I.; Nakamura, S.; Endou, H.; et al. Role of organic anion transporters in the tubular

transport of indoxyl sulfate and the induction of its nephrotoxicity. *Journal of the American Society of Nephrology* **2002**, *13* (7), 10, Article. DOI: 10.1097/01.asn.0000022017.96399.b2.

[46] Niwa, T. UREMIC TOXICITY OF INDOXYL SULFATE. *Nagoya J. Med. Sci.* **2010**, *72* (1-2), 1-11, Review.

[47] Enomoto, A.; Niwa, T. Roles of organic anion transporters in the progression of chronic renal failure. *Ther. Apher. Dial.* **2007**, *11*, S27-S31, Article; Proceedings Paper. DOI: 10.1111/j.1744-9987.2007.00515.x.

[48] Niwa, T. Indoxyl Sulfate Is a Nephro-Vascular Toxin. *J. Renal Nutr.* **2010**, *20* (5), S2-S6, Article; Proceedings Paper. DOI: 10.1053/j.jrn.2010.05.002.

[49] Cheng, T. H.; Ma, M. C.; Liao, M. T.; Zheng, C. M.; Lu, K. C.; Liao, C. H.; Hou, Y. C.; Liu, W. C.; Lu, C. L. Indoxyl Sulfate, a Tubular Toxin, Contributes to the Development of Chronic Kidney Disease. *Toxins* **2020**, *12* (11), 15, Review. DOI: 10.3390/toxins12110684.

[50] Wu, I. W.; Hsu, K. H.; Lee, C. C.; Sun, C. Y.; Hsu, H. J.; Tsai, C. J.; Tzen, C. Y.; Wang, Y. C.; Lin, C. Y.; Wu, M. S. p-Cresyl sulphate and indoxyl sulphate predict progression of chronic kidney disease. *Nephrology Dialysis Transplantation* **2011**, *26* (3), 938-947, Article. DOI: 10.1093/ndt/gfq580.

[51] Feraille, E.; Sassi, A.; Olivier, V.; Arnoux, G.; Martin, P. Y. Renal water transport in health and disease. *Pflugers Arch.* **2022**, *474* (8), 841-852, Review. DOI: 10.1007/s00424-022-02712-9.

[52] He, J. Z.; Yang, B. X. Aquaporins in Renal Diseases. *Int. J. Mol. Sci.* **2019**, *20* (2), 16, Review. DOI: 10.3390/ijms20020366.

[53] Sakai, T.; Yamasaki, K.; Sako, T.; Kragh-Hansen, U.; Suenaga, A.; Otagiri, M. Interaction mechanism between indoxyl sulfate, a typical uremic toxin bound to site II, and ligands bound to

site I of human serum albumin. *Pharmaceutical Research* **2001**, *18* (4), 520-524, Article. DOI: 10.1023/a:1011014629551.

[54] Devine, E.; Krieter, D. H.; Rüth, M.; Jankovski, J.; Lemke, H. D. Binding affinity and capacity for the uremic toxin indoxyl sulfate. *Toxins (Basel)* **2014**, *6* (2), 416-429. DOI: 10.3390/toxins6020416.

[55] United States Renal Data System (USRDS) 2021 Annual Data Report. https://adr.usrds.org/2021/chronic-kidney-disease/6-healthcare-expenditures-for-persons-with-ckd (accessed.

[56] Subramanian, S. DYE-LIGAND AFFINITY-CHROMATOGRAPHY - THE INTERACTION OF CIBACRON BLUE F3GA WITH PROTEINS AND ENZYMES. *Crc Critical Reviews in Biochemistry* **1984**, *16* (2), 169-205, Review. DOI: 10.3109/10409238409102302.

[57] Denizli, A.; Kokturk, G.; Yavuz, H.; Piskin, E. Albumin adsorption from aqueous solutions and human plasma in a packed-bed column with Cibacron Blue F3GA-Zn(II) attached poly(EGDMA-HEMA) microbeads. *React. Funct. Polym.* **1999**, *40* (3), 195-203, Article. DOI: 10.1016/s1381-5148(98)00043-1.

[58] Yavuz, H.; Duru, E.; Genc, O.; Denizli, A. Cibacron Blue F3GA incorporated poly(methylmethacrylate) beads for albumin adsorption in batch system. *Colloids and Surfaces a-Physicochemical and Engineering Aspects* **2003**, *223* (1-3), 185-193, Article. DOI: 10.1016/s0927-7757(03)00153-5.

[59] Zwir-Ferenc, A.; Biziuk, M. Solid phase extraction technique - Trends, opportunities and applications. *Pol. J. Environ. Stud.* **2006**, *15* (5), 677-690, Review.

[60] Sudaryanto, Y.; Hartono, S. B.; Irawaty, W.; Hindarso, H.; Ismadji, S. High surface area activated carbon prepared from cassava peel by chemical activation. *Bioresour. Technol.* **2006**, *97* (5), 734-739, Article. DOI: 10.1016/j.biortech.2005.04.029.

[61] Hu, Z. H.; Srinivasan, M. P. Mesoporous high-surface-area activated carbon. *Microporous Mesoporous Mat.* **2001**, *43* (3), 267-275, Article. DOI: 10.1016/s1387-1811(00)00355-3.

[62] Allen, S.; Whitten, L.; McKay, G. The production and characterisation of activated carbons: a review. *Developments in Chemical Engineering and Mineral Processing* **1998**, *6* (5), 231-261.

[63] McDougall, G. J. THE PHYSICAL NATURE AND MANUFACTURE OF ACTIVATED CARBON. *Journal of the South African Institute of Mining and Metallurgy* **1991**, *91* (4), 109-120.

[64] Database of Zeolite Structures. http://www.iza-structure.org/databases/ (accessed Aug 2023).

[65] Baile, P.; Fernandez, E.; Vidal, L.; Canals, A. Zeolites and zeolite-based materials in extraction and microextraction techniques. *Analyst* **2019**, *144* (2), 366-387. DOI: 10.1039/c8an01194j.

[66] Guo, X.; Zeng, L.; Li, X. M.; Park, H. S. Ammonium and potassium removal for anaerobically digested wastewater using natural clinoptilolite followed by membrane pretreatment. *Journal of Hazardous Materials* **2008**, *151* (1), 125-133. DOI: 10.1016/j.jhazmat.2007.05.066.

[67] Furukawa, H.; Cordova, K. E.; O'Keeffe, M.; Yaghi, O. M. The chemistry and applications of metal-organic frameworks. *Science* **2013**, *341* (6149), 1230444.

[68] Ding, S.-Y.; Wang, W. Covalent organic frameworks (COFs): from design to applications. *Chem. Soc. Rev.* **2013**, *42* (2), 548-568.

[69] Xu, T. T.; Shehzad, M. A.; Yu, D. B.; Li, Q. H.; Wu, B.; Ren, X. M.; Ge, L.; Xu, T. W. Highly Cation Permselective Metal-Organic Framework Membranes with Leaf-Like Morphology. *Chemsuschem* **2019**, *12* (12), 2593-2597. DOI: 10.1002/cssc.201900706.

[70] Han, L.; Zhou, J.; Li, X.; Sun, C. Y.; Zhao, L.; Zhang, Y. T.; Zhu, M.; Wang, X. L.; Su, Z. M. Recognition of harmful fused aromatic hydrocarbons via a metal-organic framework with hydrophobic pores. *Inorganic Chemistry Communications* **2017**, *86*, 200-203. DOI: 10.1016/j.inoche.2017.10.015.

[71] Assink, R. A.; Kay, B. D. SOL-GEL KINETICS .1. FUNCTIONAL-GROUP KINETICS. *J. Non-Cryst. Solids* **1988**, *99* (2-3), 359-370, Article. DOI: 10.1016/0022-3093(88)90441-3.

[72] Livage, J.; Sanchez, C.; Henry, M.; Doeuff, S. THE CHEMISTRY OF THE SOL-GEL PROCESS. *Solid State Ion.* **1989**, *32-3*, 633-638, Article. DOI: 10.1016/0167-2738(89)90338-x.

[73] Hench, L. L.; West, J. K. THE SOL-GEL PROCESS. *Chem. Rev.* **1990**, *90* (1), 33-72, Review. DOI: 10.1021/cr00099a003.

[74] Livage, J.; Sanchez, C. SOL-GEL CHEMISTRY. *J. Non-Cryst. Solids* **1992**, *145* (1-3), 11-19, Article; Proceedings Paper. DOI: 10.1016/s0022-3093(05)80422-3.

[75] Bryans, T. R.; Brawner, V. L.; Quitevis, E. L. Microstructure and porosity of silica xerogel monoliths prepared by the fast sol-gel method. *J. Sol-Gel Sci. Technol.* **2000**, *17* (3), 211-217, Article. DOI: 10.1023/a:1008711921746.

[76] Takahashi, R.; Sato, S.; Sodesawa, T.; Kawakita, M.; Ogura, K. High surface-area silica with controlled pore size prepared from nanocomposite of silica and citric acid. *J. Phys. Chem. B* **2000**, *104* (51), 12184-12191, Article. DOI: 10.1021/jp002662g.

[77] Brinker, C. J.; Brow, R. K.; Tallant, D. R.; Kirkpatrick, R. J. SURFACE-STRUCTURE AND CHEMISTRY OF HIGH SURFACE-AREA SILICA-GELS. *J. Non-Cryst. Solids* **1990**, *120* (1-3), 26-33, Article; Proceedings Paper. DOI: 10.1016/0022-3093(90)90187-q.

[78] Vong, M. S. W.; Bazin, N.; Sermon, P. A. Chemical modification of silica gels. *J. Sol-Gel Sci. Technol.* **1997**, *8* (1-3), 499-505, Article; Proceedings Paper. DOI: 10.1007/bf02436889.

[79] Yamada, S.; Inaba, M. Potassium Metabolism and Management in Patients with CKD. *Nutrients* **2021**, *13* (6), 19, Review. DOI: 10.3390/nu13061751.

[80] Bansal, S.; Pergola, P. E. Current Management of Hyperkalemia in Patients on Dialysis. *Kidney Int. Rep.* **2020**, *5* (6), 779-789, Review. DOI: 10.1016/j.ekir.2020.02.1028.

[81] Frensdorff, H. K. STABILITY CONSTANTS OF CYCLIC POLYETHER COMPLEXES WITH UNIVALENT CATIONS. *J. Am. Chem. Soc.* **1971**, *93* (3), 600-+. DOI: 10.1021/ja00732a007.

[82] Tsurubou, S.; Mizutani, M.; Kadota, Y.; Yamamoto, T.; Umetani, S.; Sasaki, T.; Le, Q. T. H.; Matsui, M. IMPROVED EXTRACTION SEPARATION OF ALKALINE-EARTHS AND LANTHANIDES USING CROWN-ETHERS AS ION SIZE-SELECTIVE MASKING REAGENTS - A NOVEL MACROCYCLE APPLICATION. *Anal. Chem.* **1995**, *67* (8), 1465-1469, Article. DOI: 10.1021/ac00104a025.

[83] Izatt, R. M.; Terry, R. E.; Haymore, B. L.; Hansen, L. D.; Dalley, N. K.; Avondet, A. G.; Christensen, J. J. Calorimetric titration study of the interaction of several uni- and bivalent cations with 15-crown-5, 18-crown-6, and two isomers of dicyclohexo-18-crown-6 in aqueous solution at 25.degree.C and .mu. = 0.1. *J. Am. Chem. Soc.* **1976**, *98* (24), 7620-7626. DOI: 10.1021/ja00440a028.

[84] Lamb, J. D.; Izatt, R. M.; Swain, C. S.; Christensen, J. J. A systematic study of the effect of macrocycle ring size and donor atom type on the log K, .DELTA.H, and T.DELTA.S of reactions at 25.degree.C in methanol of mono- and divalent cations with crown ethers. *J. Am. Chem. Soc.* **1980**, *102* (2), 475-479. DOI: 10.1021/ja00522a005.

[85] Bradshaw, J. S.; Izatt, R. M. Crown ethers: The search for selective ion ligating agents. *Accounts Chem. Res.* **1997**, *30* (8), 338-345, Review. DOI: 10.1021/ar950211m.

[86] Dang, L. X. MECHANISM AND THERMODYNAMICS OF ION SELECTIVITY IN AQUEOUS-SOLUTIONS OF 18-CROWN-6 ETHER - A MOLECULAR-DYNAMICS STUDY. *J. Am. Chem. Soc.* **1995**, *117* (26), 6954-6960, Article. DOI: 10.1021/ja00131a018.

[87] Alexandratos, S. D.; Stine, C. L. Synthesis of ion-selective polymer-supported crown ethers: a review. *React. Funct. Polym.* **2004**, *60*, 3-16, Review. DOI: 10.1016/j.reactfunctpolym.2004.02.006.

[88] Escobar, E. C.; Sio, J. E. L.; Bendoy, A. P.; Torrejos, R. E. C.; Fissaha, H. T.; Kim, H.; Chung, W. J.; Nisola, G. M. Removal of Cs+ in water by dibenzo-18-crown-6 ether tethered on mesoporous SBA-15 as a reusable and efficient adsorbent. *J. Water Process. Eng.* **2021**, *39*, 13, Article. DOI: 10.1016/j.jwpe.2020.101716.

[89] You, N.; Song, Y. X.; Wang, H. R.; Kang, L. X.; Fan, H. T.; Yao, H. Sol-Gel Derived Benzo-Crown Ether-Functionalized Silica Gel for Selective Adsorption of Ca2+ Ions. *J. Chem. Eng. Data* **2019**, *64* (4), 1378-1384, Article. DOI: 10.1021/acs.jced.8b00955.

[90] Zhang, H. X.; Huang, Z. X.; Zhao, P. Y.; Hou, Y.; Guo, J. J.; Wu, Y. C. Crown ether functionalized graphene oxide as ultrasensitive electrochemical sensor for detection of potassium ions. *Mater. Res. Express* **2019**, *6* (12), 6, Article. DOI: 10.1088/2053-1591/ab5d65.

[91] Lindner, E.; Toth, K.; Jeney, J.; Horvath, M.; Pungor, E.; Bitter, I.; Agai, B.; Toke, L. NOVEL BIS(CROWN ETHER)-BASED POTASSIUM SENSOR FOR BIOLOGICAL APPLICATIONS. *Mikrochim. Acta* **1990**, *1* (3-4), 157-168, Article.

[92] Theodore, P. All about albumin: biochemistry, genetics, and medical applications; 1995.

[93] Roberto, A. A molecular dynamics study of human serum albumin binding sites. Gabriella, B., Ed.; Elsevier: Il Farmaco, 2005; Vol. Volume 60, pp 485-495.

[94] Leong, S. C.; Sirich, T. L. Indoxyl Sulfate-Review of Toxicity and Therapeutic Strategies. *Toxins* **2016**, *8* (12), 13, Review. DOI: 10.3390/toxins8120358.

[95] Niwa, T.; Takeda, N.; Tatematsu, A.; Maeda, K. Accumulation of indoxyl sulfate, an inhibitor of drug-binding, in uremic serum as demonstrated by internal-surface reversed-phase liquid chromatography. *Clin Chem* **1988**, *34* (11), 2264-2267.

[96] Ward, R. A.; Beck, W.; Bernardo, A. A.; Alves, F. C.; Stenvinkel, P.; Lindholm, B. Hypoalbuminemia: a price worth paying for improved dialytic removal of middle-molecular-weight uremic toxins? *Nephrol Dial Transplant* **2019**, *34* (6), 901-907. DOI: 10.1093/ndt/gfy236.

[97] Curry, S. Lessons from the crystallographic analysis of small molecule binding to human serum albumin. *Drug Metab Pharmacokinet* **2009**, *24* (4), 342-357. DOI: 10.2133/dmpk.24.342.

[98] Birkett, D. J.; Myers, S. P.; Sudlow, G. Effects of fatty acids on two specific drug binding sites on human serum albumin. *Mol Pharmacol* **1977**, *13* (6), 987-992.

[99] Tao, X.; Thijssen, S.; Kotanko, P.; Ho, C. H.; Henrie, M.; Stroup, E.; Handelman, G. Improved dialytic removal of protein-bound uraemic toxins with use of albumin binding competitors: an in vitro human whole blood study. *Scientific Reports* **2016**, *6*. DOI: 10.1038/srep23389.

[100] Guillen, G. R.; Pan, Y. J.; Li, M. H.; Hoek, E. M. V. Preparation and Characterization of Membranes Formed by Nonsolvent Induced Phase Separation: A Review. *Ind. Eng. Chem. Res.* **2011**, *50* (7), 3798-3817. DOI: 10.1021/ie101928r.

[101] Sargent, J. A. Dialysis in the 1960s and the first hollow fiber dialyzer. *International Journal of Artificial Organs* **2007**, *30* (11), 953-963. DOI: 10.1177/039139880703001103.

[102] Masuda, H.; Fukuda, K. ORDERED METAL NANOHOLE ARRAYS MADE BY A 2-STEP REPLICATION OF HONEYCOMB STRUCTURES OF ANODIC ALUMINA. *Science* **1995**, *268* (5216), 1466-1468. DOI: 10.1126/science.268.5216.1466.

[103] Iijima, S.; Ichihashi, T. SINGLE-SHELL CARBON NANOTUBES OF 1-NM DIAMETER. *Nature* **1993**, *363* (6430), 603-605, Article. DOI: 10.1038/363603a0.

[104] Hofer, L. J. E.; Sterling, E.; McCartney, J. T. STRUCTURE OF THE CARBON DEPOSITED FROM CARBON MONOXIDE ON IRON, COBALT AND NICKEL. *J. Phys. Chem.* **1955**, *59* (11), 1153-1155, Article. DOI: 10.1021/j150533a010.

[105] Lieberman, M. L.; Hills, C. R.; Miglioni, C. GROWTH OF GRAPHITE FILAMENTS. *Carbon* **1971**, *9* (5), 633-+, Article. DOI: 10.1016/0008-6223(71)90085-6.

[106] Majumder, M.; Chopra, N.; Andrews, R.; Hinds, B. J. Nanoscale hydrodynamics - Enhanced flow in carbon nanotubes. *Nature* **2005**, *438* (7064), 44-44, Editorial Material. DOI: 10.1038/43844a.

[107] Joseph, S.; Aluru, N. R. Why are carbon nanotubes fast transporters of water? *Nano Lett.* **2008**, *8* (2), 452-458, Article. DOI: 10.1021/nl072385q.

[108] Hummer, G.; Rasaiah, J. C.; Noworyta, J. P. Water conduction through the hydrophobic channel of a carbon nanotube. *Nature* **2001**, *414* (6860), 188-190, Article. DOI: 10.1038/35102535.

[109] Andersson, C. H.; Grennberg, H. Reproducibility and Efficiency of Carbon Nanotube End-Group Generation and Functionalization. *Eur. J. Org. Chem.* **2009**, *2009* (26), 4421-4428, Article. DOI: 10.1002/ejoc.200900534.

[110] Jun, L. Y.; Mubarak, N. M.; Yon, L. S.; Bing, C. H.; Khalid, M.; Abdullah, E. C. Comparative study of acid functionalization of carbon nanotube via ultrasonic and reflux mechanism. *J. Environ. Chem. Eng.* **2018**, *6* (5), 5889-5896, Article. DOI: 10.1016/j.jece.2018.09.008.

[111] Majumder, M.; Chopra, N.; Hinds, B. J. Effect of tip functionalization on transport through vertically oriented carbon nanotube membranes. *J. Am. Chem. Soc.* **2005**, *127* (25), 9062-9070, Article. DOI: 10.1021/ja043013b.

[112] Gulati, G. K.; Hinds, B. J. Electrically controlled nicotine delivery through Carbon nanotube membranes via electrochemical oxidation and nanofluidically enhanced electroosmotic flow. *Biomed. Microdevices* **2021**, *23* (4), 14, Article. DOI: 10.1007/s10544-021-00580-1.

[113] Banerjee, S.; Kahn, M. G. C.; Wong, S. S. Rational chemical strategies for carbon nanotube functionalization. *Chem.-Eur. J.* **2003**, *9* (9), 1899-1908, Article. DOI: 10.1002/chem.200204618.

[114] Kahn, M. G. C.; Banerjee, S.; Wong, S. S. Solubilization of oxidized single-walled carbon nanotubes in organic and aqueous solvents through organic derivatization. *Nano Lett.* **2002**, *2* (11), 1215-1218, Article. DOI: 10.1021/nl025755d.

[115] Tasis, D.; Tagmatarchis, N.; Bianco, A.; Prato, M. Chemistry of carbon nanotubes. *Chem. Rev.* **2006**, *106* (3), 1105-1136, Review. DOI: 10.1021/cr050569o.

[116] Majumder, M.; Zhan, X.; Andrews, R.; Hinds, B. J. Voltage gated carbon nanotube membranes. *Langmuir* **2007**, *23* (16), 8624-8631, Article. DOI: 10.1021/la700686k.

[117] Eskandari, P.; Abousalman-Rezvani, Z.; Roghani-Mamaqani, H.; Salami-Kalajahi, M. Polymer-functionalization of carbon nanotube by in situ conventional and controlled radical polymerizations. *Adv. Colloid Interface Sci.* **2021**, *294*, 34, Review. DOI: 10.1016/j.cis.2021.102471.

[118] Spitalsky, Z.; Tasis, D.; Papagelis, K.; Galiotis, C. Carbon nanotube-polymer composites: Chemistry, processing, mechanical and electrical properties. *Prog. Polym. Sci.* **2010**, *35* (3), 357-401, Review. DOI: 10.1016/j.progpolymsci.2009.09.003.

[119] Derycke, V.; Auvray, S.; Borghetti, J.; Chung, C. L.; Lefevre, R.; Lopez-Bezanilla, A.; Nguyen, K.; Robert, G.; Schmidt, G.; Anghel, C.; et al. Carbon nanotube chemistry and assembly for electronic devices. *C. R. Phys.* **2009**, *10* (4), 330-347, Article. DOI: 10.1016/j.crhy.2009.05.006.

[120] Shiraki, T.; Miyauchi, Y.; Matsuda, K.; Nakashima, N. Carbon Nanotube Photoluminescence Modulation by Local Chemical and Supramolecular Chemical Functionalization. *Accounts Chem. Res.* **2020**, *53* (9), 1846-1859, Review. DOI: 10.1021/acs.accounts.0c00294.

[121] Buchsbaum, S. F.; Jue, M. L.; Sawvel, A. M.; Chen, C. T.; Meshot, E. R.; Park, S. J.; Wood, M.; Wu, K. J.; Bilodeau, C. L.; Aydin, F.; et al. Fast Permeation of Small Ions in Carbon Nanotubes. *Adv. Sci.* **2021**, *8* (3), 7, Article. DOI: 10.1002/advs.202001802.

[122] Wu, J.; Gerstandt, K.; Zhang, H. B.; Liu, J.; Hinds, B. J. Electrophoretically induced aqueous flow through single-walled carbon nanotube membranes. *Nat. Nanotechnol.* **2012**, *7* (2), 133-139. DOI: 10.1038/nnano.2011.240.

[123] Guo, S. R.; Meshot, E. R.; Kuykendall, T.; Cabrini, S.; Fornasiero, F. Nanofluidic Transport through Isolated Carbon Nanotube Channels: Advances, Controversies, and Challenges. *Adv. Mater.* **2015**, *27* (38), 5726-5737. DOI: 10.1002/adma.201500372.

[124] Fang, C.; Lv, F. J.; Huang, D. C.; Su, J. Y. Coupling transport of water and ions through a carbon nanotube: A novel desalination phenomenon induced by tuning the pressure direction. *Desalination* **2020**, *492*. DOI: 10.1016/j.desal.2020.114656.

[125] Rabinowitz, J.; Cohen, C.; Shepard, K. L. An Electrically Actuated, Carbon-Nanotube-Based Biomimetic Ion Pump. *Nano Lett.* **2020**, *20* (2), 1148-1153. DOI: 10.1021/acs.nanolett.9b04552.

[126] Peng, R.; Pan, Y. Y.; Liu, B. W.; Li, Z.; Pan, P.; Zhang, S. L.; Qin, Z.; Wheeler, A. R.; Tang, X. W.; Liu, X. Y. Understanding Carbon Nanotube-Based Ionic Diodes: Design and Mechanism. *Small* **2021**, *17* (31). DOI: 10.1002/smll.202100383.

[127] Tunuguntla, R. H.; Henley, R. Y.; Yao, Y. C.; Pham, T. A.; Wanunu, M.; Noy, A. Enhanced water permeability and tunable ion selectivity in subnanometer carbon nanotube porins. *Science* **2017**, *357* (6353), 792-796, Article. DOI: 10.1126/science.aan2438.

[128] Collins, B. B. On The Atomic Weight Of Graphite. Royal Society: Philosophical Transactions, 1859; Vol. volume 149, pp 249-259.

[129] Novoselov, K. S.; Geim, A. K.; Morozov, S. V.; Jiang, D.; Zhang, Y.; Dubonos, S. V.; Grigorieva, I. V.; Firsov, A. A. Electric field effect in atomically thin carbon films. *Science* **2004**, *306* (5696), 666-669, Article. DOI: 10.1126/science.1102896.

[130] Meyer, J. C.; Geim, A. K.; Katsnelson, M. I.; Novoselov, K. S.; Booth, T. J.; Roth, S. The structure of suspended graphene sheets. *Nature* **2007**, *446* (7131), 60-63, Article. DOI: 10.1038/nature05545.

[131] Hummers, W. S.; Offeman, R. E. PREPARATION OF GRAPHITIC OXIDE. *J. Am. Chem. Soc.* **1958**, *80* (6), 1339-1339, Article. DOI: 10.1021/ja01539a017.

[132] Dreyer, D. R.; Park, S.; Bielawski, C. W.; Ruoff, R. S. The chemistry of graphene oxide. *Chem. Soc. Rev.* **2010**, *39* (1), 228-240, Review. DOI: 10.1039/b917103g.

[133] Liu, Z. L.; Norgaard, K.; Overgaard, M. H.; Ceccato, M.; Mackenzie, D. M. A.; Stenger, N.; Stipp, S. L. S.; Hassenkam, T. Direct observation of oxygen configuration on individual graphene oxide sheets. *Carbon* **2018**, *127*, 141-148, Article. DOI: 10.1016/j.carbon.2017.10.100.

[134] Shin, Y.; Taufique, M. F. N.; Devanathan, R.; Cutsforth, E. C.; Lee, J.; Liu, W.; Fifield, L. S.; Gotthold, D. W. Highly Selective Supported Graphene Oxide Membranes for Water-Ethanol Separation. *Scientific Reports* **2019**, *9*, 11, Article. DOI: 10.1038/s41598-019-38485-y.

[135] Boffa, V.; Etmimi, H.; Mallon, P. E.; Tao, H. Z.; Magnacca, G.; Yue, Y. Z. Carbon-based building blocks for alcohol dehydration membranes with disorder-enhanced water permeability. *Carbon* **2017**, *118*, 458-466, Article. DOI: 10.1016/j.carbon.2017.03.077.

[136] Hua, D.; Rai, R. K.; Zhang, Y.; Chung, T. S. Aldehyde functionalized graphene oxide frameworks as robust membrane materials for pervaporative alcohol dehydration. *Chem. Eng. Sci.* **2017**, *161*, 341-349, Article. DOI: 10.1016/j.ces.2016.12.061.

[137] Hung, W. S.; Tsou, C. H.; De Guzman, M.; An, Q. F.; Liu, Y. L.; Zhang, Y. M.; Hu, C. C.; Lee, K. R.; Lai, J. Y. Cross-Linking with Diamine Monomers To Prepare Composite Graphene Oxide-Framework Membranes with Varying d-Spacing. *Chem. Mat.* **2014**, *26* (9), 2983-2990, Article. DOI: 10.1021/cm5007873.

[138] Hu, M.; Mi, B. X. Enabling Graphene Oxide Nanosheets as Water Separation Membranes. *Environ. Sci. Technol.* **2013**, *47* (8), 3715-3723, Article. DOI: 10.1021/es400571g.

[139] Chen, L.; Li, N.; Wen, Z. Y.; Zhang, L.; Chen, Q.; Chen, L. N.; Si, P. C.; Feng, J. K.; Li, Y. H.; Lou, J.; et al. Graphene oxide based membrane intercalated by nanoparticles for high performance nanofiltration application. *Chem. Eng. J.* **2018**, *347*, 12-18, Article. DOI: 10.1016/j.cej.2018.04.069.

[140] Jia, M. M.; Feng, Y.; Liu, S. C.; Qiu, J. H.; Yao, J. F. Graphene oxide gas separation membranes intercalated by UiO-66-NH2 with enhanced hydrogen separation performance. *J. Membr. Sci.* **2017**, *539*, 172-177, Article. DOI: 10.1016/j.memsci.2017.06.005.

[141] Han, Y.; Jiang, Y. Q.; Gao, C. High-Flux Graphene Oxide Nanofiltration Membrane Intercalated by Carbon Nanotubes. *ACS Appl. Mater. Interfaces* **2015**, *7* (15), 8147-8155, Article. DOI: 10.1021/acsami.5b00986.

[142] Chen, X. F.; Qiu, M. H.; Ding, H.; Fu, K. Y.; Fan, Y. Q. A reduced graphene oxide nanofiltration membrane intercalated by well-dispersed carbon nanotubes for drinking water purification. *Nanoscale* **2016**, *8* (10), 5696-5705, Article. DOI: 10.1039/c5nr08697c.

[143] Chen, L.; Shi, G. S.; Shen, J.; Peng, B. Q.; Zhang, B. W.; Wang, Y. Z.; Bian, F. G.; Wang, J. J.; Li, D. Y.; Qian, Z.; et al. Ion sieving in graphene oxide membranes via cationic control of interlayer spacing. *Nature* **2017**, *550* (7676), 415-418, Article. DOI: 10.1038/nature24044.

[144] Zheng, S. X.; Tu, Q. S.; Urban, J. J.; Li, S. F.; Mi, B. X. Swelling of Graphene Oxide Membranes in Aqueous Solution: Characterization of Interlayer Spacing and Insight into Water Transport Mechanisms. *ACS Nano* **2017**, *11* (6), 6440-6450, Article. DOI: 10.1021/acsnano.7b02999.

[145] Radha, B.; Esfandiar, A.; Wang, F. C.; Rooney, A. P.; Gopinadhan, K.; Keerthi, A.; Mishchenko, A.; Janardanan, A.; Blake, P.; Fumagalli, L.; et al. Molecular transport through

capillaries made with atomic-scale precision. *Nature* **2016**, *538* (7624), 222-+. DOI: 10.1038/nature19363.

[146] Kannam, S. K.; Todd, B. D.; Hansen, J. S.; Daivis, P. J. Slip length of water on graphene: Limitations of non-equilibrium molecular dynamics simulations. *J. Chem. Phys.* **2012**, *136* (2). DOI: 10.1063/1.3675904.

[147] Abraham, J.; Vasu, K. S.; Williams, C. D.; Gopinadhan, K.; Su, Y.; Cherian, C. T.; Dix, J.; Prestat, E.; Haigh, S. J.; Grigorieva, I. V.; et al. Tunable sieving of ions using graphene oxide membranes. *Nat. Nanotechnol.* **2017**, *12* (6), 546-+, Article. DOI: 10.1038/nnano.2017.21.

[148] Borges, D. D.; Woellner, C. F.; Autreto, P. A. S.; Galvao, D. S. Insights on the mechanism of water-alcohol separation in multilayer graphene oxide membranes: Entropic versus enthalpic factors. *Carbon* **2018**, *127*, 280-286, Article. DOI: 10.1016/j.carbon.2017.11.020.

[149] Yang, Q.; Su, Y.; Chi, C.; Cherian, C. T.; Huang, K.; Kravets, V. G.; Wang, F. C.; Zhang, J. C.; Pratt, A.; Grigorenko, A. N.; et al. Ultrathin graphene-based membrane with precise molecular sieving and ultrafast solvent permeation. *Nat. Mater.* **2017**, *16* (12), 1198-+, Article. DOI: 10.1038/nmat5025.

[150] Tsou, C. H.; An, Q. F.; Lo, S. C.; De Guzman, M.; Hung, W. S.; Hu, C. C.; Lee, K. R.; Lai, J. Y. Effect of microstructure of graphene oxide fabricated through different self-assembly techniques on 1-butanol dehydration. *J. Membr. Sci.* **2015**, *477*, 93-100, Article. DOI: 10.1016/j.memsci.2014.12.039.

[151] Zang, Y. S.; Peek, A.; Shin, Y.; Gotthold, D.; Hinds, B. J. Catalytic Reduction of Graphene Oxide Membranes and Water Selective Channel Formation in Water-Alcohol Separations. *Membranes* **2021**, *11* (5), 18, Article. DOI: 10.3390/membranes11050317.

[152] Aher, A.; Cai, Y. G.; Majumder, M.; Bhattacharyya, D. Synthesis of graphene oxide membranes and their behavior in water and isopropanol. *Carbon* **2017**, *116*, 145-153. DOI: 10.1016/j.carbon.2017.01.086.

[153] Akbari, A.; Sheath, P.; Martin, S. T.; Shinde, D. B.; Shaibani, M.; Banerjee, P. C.; Tkacz, R.; Bhattacharyya, D.; Majumder, M. Large-area graphene-based nanofiltration membranes by shear alignment of discotic nematic liquid crystals of graphene oxide. *Nat. Commun.* **2016**, *7*. DOI: 10.1038/ncomms10891.

[154] Akbari, A.; Meragawi, S. E.; Martin, S. T.; Corry, B.; Shamsaei, E.; Easton, C. D.; Bhattacharyya, D.; Majumder, M. Solvent Transport Behavior of Shear Aligned Graphene Oxide Membranes and Implications in Organic Solvent Nanofiltration. *ACS Appl. Mater. Interfaces* **2018**, *10* (2), 2067-2074, Article. DOI: 10.1021/acsami.7b11777.

[155] Talyzin, A. V.; Hausmaninger, T.; You, S. J.; Szabo, T. The structure of graphene oxide membranes in liquid water, ethanol and water-ethanol mixtures. *Nanoscale* **2014**, *6* (1), 272-281, Article. DOI: 10.1039/c3nr04631a.

[156] Gravelle, S.; Yoshida, H.; Joly, L.; Ybert, C.; Bocquet, L. Carbon membranes for efficient water-ethanol separation. *J. Chem. Phys.* **2016**, *145* (12). DOI: 10.1063/1.4963098.

[157] You, S. J.; Yu, J. C.; Sundqvist, B.; Belyaeva, L. A.; Avramenko, N. V.; Korobov, M. V.; Talyzin, A. V. Selective Intercalation of Graphite Oxide by Methanol in Water/Methanol Mixtures. *J. Phys. Chem. C* **2013**, *117* (4), 1963-1968, Article. DOI: 10.1021/jp312756w.

[158] Dharupaneedi, S. P.; Anjanapura, R. V.; Han, J. M.; Aminabhavi, T. M. Functionalized Graphene Sheets Embedded in Chitosan Nanocomposite Membranes for Ethanol and Isopropanol Dehydration via Pervaporation. *Ind. Eng. Chem. Res.* **2014**, *53* (37), 14474-14484, Article. DOI: 10.1021/ie502751h.

Chapter 2. PROTEIN BOUND UREMIC TOXIN REMOVAL WITH ALBUMIN REGENERATION

Adapted from Yushi Zang, Jeremy L. Fredricks, Yuehan Chen, Dan Shea, Bruce J Hinds "Protein Bound Uremic Toxin Removal with Albumin Regeneration" Submitted to ACS BioMaterials

2.1 INTRODUCTION

In-center hemodialysis is lifesaving treatment for 85% of patients with end stage renal disease (ESRD) with an annual cost of $28 billion in the United States or about $90,000 per patient. [1] However even with this large expense, the five-year survival rate is only 35-42% (2005 to 2015 data), with cardiac failure and infections being the leading causes of mortality. [1] Conventional kidney hemodialysis is effective for small molecule toxin removal using ~0.5 kDa molecular weight cutoff (MWCO) membranes. However, protein-bound uremic toxins (PBUTs) are hard to remove since the protein-toxin complex is too large (~66.5 kDa) to pass through dialysis membranes. [2-5] PBUTs have a low unbound fraction which proportionately lowers their removal efficiency with respect to other small molecule solutes. For instance, indoxyl sulfate (IS), which is associated with cardiovascular disease, was found with 95% bound to albumin at equilibrium. [6-10] Some current treatments allow a fraction of HA, with and without toxins, to be removed in dialysis using high MWCO (~70 kDa) membrane but the approach suffers from potential malnutrition and hypoalbuminemia. [3, 4] Modest improvements (2x) in PBUT removal was demonstrated with the addition of activated carbon to the hemodialyzer cartridge, but PBUT levels remain far above non-uremic levels. [11] Thus, PBUT removal during hemodialysis remains an unmet therapeutic need.

Human albumin (HA) is a heart-shaped protein made of three homologous helical domains (I–III) that can be further divided into subdomains A and B. [12-15] Fatty acids bind to multiple binding sites spread over all three domains. [14, 16-18] PBUT molecules such as IS and p-cresyl sulfate, associated with cardiorenal syndrome [19], are made of an ionic portion and an aromatic portion that make it strongly bind to hydrophobic cavities with cationic entrances in subdomain II-A and III-A. [20, 21] The Sudlow site II (S-II), where indoxyl sulfate mainly binds to, is located at subdomain III-A and also contains two fatty acid binding sites. [18] Thus, IS and fatty acids may compete in binding to the S-II site. [14, 22, 23] While healthy kidneys have specialized molecular pumps to selectively remove anionic-aromatic compounds from the S-II site, conventional kidney dialysis lacks the same ability. Strategies such as the Molecular Adsorbents Recycling System, MARS system, employs an albumin-containing dialysate system to promote removal of PBUTs. [24, 25] The externally supplied HA is in a dialysate loop and carries PBUTs from the blood loop to an activated carbon (AC) "sink" for removal. However, such process is costly due to added HA and lacks improvement in toxin selectivity. An absorbent, AST 120, was developed to target food sourced toxin precursors that exist in the digestive system. [26, 27] It was reported that AST lowers the patient's serum IS level by 40% after 12 weeks treatment. However, an undesirable amount of absorbent (30 capsules daily) needs to be administrated orally. Metal organic framework (MOF) was proposed as a better toxin-selective absorbent. [28, 29] Studies showed high removal rates of plasma toxin with high selectivity. But since the majority of toxin was still bound to proteins the toxin removal efficiency was found to be similar to conventional dialysis. Other approaches directly focus on HA cleansing by using cyclic electromagnetic field or PBUT binding competitor into conventional dialysis system shows improved efficiency but still have technical challenges or limitation. [5, 23, 30, 31] For conventional protein separation processes, HA is typically purified from

blood plasma by use of chromatography columns functionalized with aromatic and charged Cibacron blue dye that binds to S-II sites and released by highly concentrated thiocyanate. [32-36] Extensive ion exchange rinsing to remove thiocyanate is needed for a physiologically safe product. Ideally a material system can be developed to bind to HA S-II sites to release PBUTs, then release cleaned HA back into the blood stream *with a physiologically safe release agent*.

Here we demonstrated a 2-step albumin regeneration process with HA-selective binding and release for selective removal of PBUTs from S-II site of HA as shown in Figure 2.1. We explored a variety of surface chemistries that selectively bind to HA and simultaneously forces the release of IS from S-II sites. Then a series of plasma-safe release agents for releasing cleansed HA from the surfaces was studied. Cibacron Blue and physiological fatty acid mixtures were found to be optimal binding and release agents. The albumin regeneration chemistry was then applied to agarose bead support showing binding and release which can be scaled to regenerate 250 g of HA daily while using only 155 ml of agarose/CB resin with 2-minute cycles.

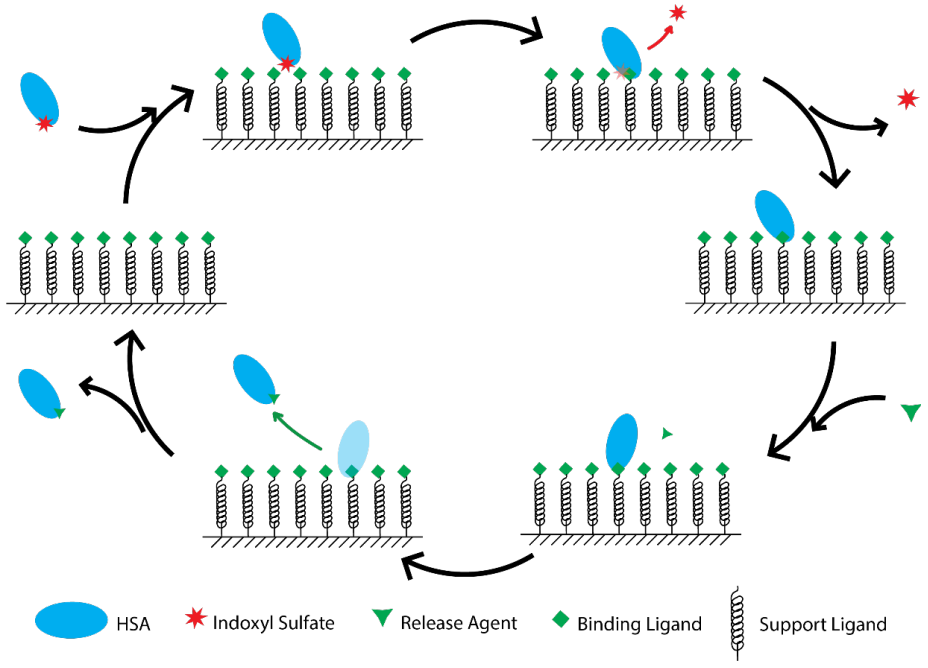

Figure 2.1. Schematic demonstration of detoxification process of human albumin with designed surface chemistry and biocompatible release agent.

2.2 MATERIALS AND METHODS

2.2.1 *Surface Plasmon Resonance (SPR) Sensor Chip Cleaning*

As-received SPR sensor chips were rinsed with de-ionized (DI) water and ethanol followed by Ar drying. Dried chips were then treated with oxygen plasma in a plasma cleaner (Model PDC-001-HP, Harrick Plasma) and stored under Ar.

2.2.2 *Ligand Grafting onto SPR Sensor Chips*

The general ligan grafting strategy was demonstrated in Figure 2.2. MUDA grafting: 10 mM 11-mercaptoundecanoic acid (MUDA) was dissolved in Ar-purged dry ethanol. Clean SPR chips were immersed in prepared solution, and then set on an orbital shaker overnight under Ar protection, then twice rinsed and sonicated in ethanol followed by drying and storage in an Ar atmosphere. H_2N-PEG-NH_2 grafting: 19.8 mg bis(3-aminopropyl) terminated PEG ($M_n \sim 1500$), 4 mg 1-(3-dimethylaminopropyl)-3-ethylcarbodiimide hydrochloride (EDC), and 3 mg N-hydroxy succinimide (NHS) were dissolved via sonication in 20 mL dry DMF. SPR chips were immersed in this solution and left on a shaker overnight in an Ar atmosphere. Cibacron Blue grafting: In 70 mL of Milli-Q water, 51.3 mg Cibacron Blue and 2.336 g NaCl were dissolved with aid of bath sonication. This solution was heated to 60 °C while stirring and tuned to pH 10-11 with NaOH for reaction for 4 hr. Concentration change due to evaporation was compensated with DI water. Functionalized chips were rinsed with water and ethanol then stored in an Ar atmosphere. Decanoic acid grafting: PEG-modified SPR chips were treated with 20 ml DMF solution with 8.9 mg sebacic acid bis(N-succinimidyl) ester overnight in an Ar atmosphere on an orbital shaker. Yielded chips were rinsed with DMF and ethanol followed by drying and storage in Ar before use. Tryptophan grafting: Tryptophan was grafted onto PEG-modified SPR chips by two different

mechanisms to produce different spatial orientations (C or N terminus). A coupling solution was made by dissolving 3.1 mg EDC, 2.3 mg NHS, and 4.1 mg tryptophan in 20 mL dry DMF. i) Tryptophan was coupled by its –COOH group with the $–NH_2$ groups on a PEG-modified chip surface by immersing chips in the coupling solution overnight on an orbital shaker. ii) Tryptophan was attached by its $–NH_2$ group to the chip surface. This process includes an additional disuccinimidyl carbonate (DSC) activation step, 30 min. in 51.2 mg DSC 20 mL DMF solution, prior to the EDC coupling mentioned above. Tryptophan-grafted chips were rinsed with DMF and ethanol and stored in inert gas. Direct Blue 71 grafting: DSC activated PEG-modified SPR chips were treated with DB71 solution made of 193.2 mg Direct Blue 71 in 20 mL dry DMF. After grafting, the SPR chips were rinsed with DMF and ethanol and then dried and stored in an Ar atmosphere. Stearic Acid grafting: Thiol PEG (M.W. 3400 Da) with a stearic acid terminus was purchased and used as-is. SPR chips were immersed in solutions of 25.5 mg stearic acid thiol PEG in 15 mL Ar-purged chloroform overnight on an orbital shaker. The resultant grafted SPR chips were rinsed with chloroform and IPA and then dried and stored in Ar. Thiol azide PEG grafting: Thiol PEG (M.W. 3400 Da) with an azide terminus was purchased and used as-is. Cleaned SPR chips were immersed in a solution of 20 mg thiol-azido-PEG in 20mL Ar-purged DMF for over 6 hr. The reaction was protected from light and the solution and chips were shaken on an orbital shaker. The resultant SPR chips were rinsed with DMF and stored in Ar. Alkane chain grafting: Alkane chains with different chain lengths, 1-hexyne to 1-dodecyne, were grafted via click chemistry on the azide PEG grafted chips. The desired alkyne, $CuSO_4$, and ascorbic acid were dissolved in a 1:1:1 molar ratio in a 4:1 v/v DMF:water solvent to make a 1 mM alkyne solution. The thiol azide PEG grafted chips were immersed in such solution overnight in an Ar atmosphere

and protected from light. Yielded chips were rinsed with DMF and ethanol prior to drying and storage before use.

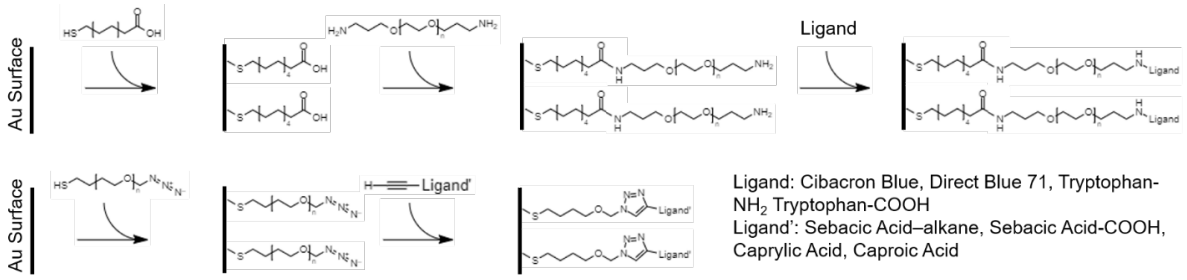

Figure 2.2. Scheme of chemical grafting process for SPR chips using carboimide coupling (Ligand) and click chemistry coupling (Ligand').

2.2.3 *SPR Test*

A temperature controlled NanoSPR8 Model 481 device with a 4-channel flow cell was used and calibration and warm up were performed (2 hr) prior to tests. Two flow cell channels were set as reference in all tests. Basic solution with surfactant (0.1 M NaOH and 1% SDS), acidic solution (0.1 M HCl), and water were used to clean the testing flow cell and tubing system.

A phosphate buffer solution (PB) for SPR studies was prepared by dissolving 21.48 g Na_2HPO_4 and 3.11 g KH_2PO_4 in 1 L Milli-Q water for SPR tests. With this buffer a variety of solutions were prepared: NaCl, Na_2SO_4 and NaSCN was dissolved in the PB to prepare a 2 M solution. Sodium dodecyl sulfate (SDS) solution of 1 wt% (~35 mM) was prepared by dissolving SDS in PB with aid of bath sonication. Fatty acid solutions were made by pipetting fatty acid into PB and bath sonicating. Linoleic acid solution (LA) consisted of 1.8 µL of LA and 10 mL PB. Fatty acid mix solution (FA mix) was prepared by dispersing 1.8 µL linoleic acid, 1.05 µL oleic acid and 1.08 µL palmitic acid in 10 mL PB. FA mix was an inhomogeneous emulsion due to the limited solubility of fatty acids even with aid of bath sonication.

2.2.4 *Langmuir Isotherm*

HA was dissolved in PB to make solutions with concentration range from 0.1 mg/mL to 2.0 mg/mL for adsorption study. Such HA solutions were pumped through the flow cell in low to high sequence with 20 min. adsorption time for each solution. Between each HA adsorption session, buffer was used to rinse off unbound protein residue for 20 min. PB signal from selected reference channels was used as baseline.

Prior to further analysis, the raw SPR data, absolute maximum absorption angle versus time, was referenced to a baseline reading. A 3-point running average was applied to reduce noise.

The values of SPR signal shift (in degrees) induced by HA solutions of different concentrations were manually identified. For Langmuir adsorption model fitting, the SPR signal shifts were converted to fractional occupancy of adsorption sites (θ) by assuming 0% and 100% site occupancy under 0 mg/mL and 2 mg/mL HA solution treatment, respectively. After plotting the concentration on x-axis and θ on y-axis, the data was fitted to a Langmuir isotherm model with equation

$$\theta = \frac{K_a \times Conc.}{1 + K_a \times Conc.} \qquad (2.1)$$

where the adsorption constant, K_a, was obtained under the best fitting condition. The desorption constant, K_d, reported in Table 2. 1 was calculated by $K_d = 1/ K_a$.

2.2.5 *Adsorption and Desorption Cycles*

Cyclic tests were performed with functionalized SPR sensor chips and 2 mg/mL HA solutions. The test was carried out in sequence of HA solution, buffer rinse, releasing agent rinse, buffer rinse, in cycles after an initial PB rinse. Three absorption and desorption cycles were performed on each sample for repeatability/stability. The first two cycles used the same release agents of interest and the third cycle used a reference release agent, usually 2 M NaSCN.

Percentage of HA released by different release agents was calculated by dividing the value difference between the SPR peak shift value using

$$Release\ Percentage = \frac{Ad-Rel}{Ad} \times 100\% \qquad (2.2)$$

where Ad is the value corresponds to albumin adsorption ('Adsorb' in Figure 2.5) and Rel is the value of post-release SPR signal ('Release' in Figure 2.5).

2.2.6 *Adsorption Column Setup*

Devcon 5-minute epoxy in Dev-tube (ITW Polymer Adhesives, USA) was used on all epoxied parts of the column and was allowed to cure for an hour before use. Agarose beads functionalized with Cibacron Blue dye and suspended in 20% ethanol and 0.1 M KH_2PO_4 (Blue Sepharose Fast Flow 6, GE Healthcare, USA) was obtained and used as-is.

As diagrammed in Figure 2.3 (A) a glass tube (inner diameter = 4 mm) was cut to 4.1 cm (0.52 ml volume). Two sheets of 10.0 μm pore size Teflon membrane filters (Sterlitech Corp., USA) covered the eluent end of the tube and were sealed around the edge with larger diameter elastic tubing (Tygon SE-200, Saint-Gobain Corp., USA) with excess membrane trimmed by knife. The tubing was secured to the tube via glass-compatible glue (Loctite, Henkel AG & Co. KGaA, Germany) and then epoxied to prevent air leakage. The beads in their suspension fluid (0.739 mL total slurry) were pipetted into the tube on top of the membrane seal and drained to form a bed of beads. The other end of the tube was sealed with membrane filters and tubing in a similar manner. Figure. 2.3 (B) shows both ends of the bead bed tube were connected to a Luer lock needle assembly that were epoxied to input tubing to prevent fluid leakage. Figure. 2.3 (C)shows the solution reservoir consisting of a syringe and a Luer lock connection. The column was suspended vertically and syringe pump (Model NE 300, New Era Pump Systems, Inc., USA) set to 4.0 mL/min with 125-250 μL samples collected at time points with lag time experimentally accounted

for. Replacing of solutions occurred by switching out the syringe at the base of the Luer lock needle assembly in (B), ensuring no air bubbles were introduced.

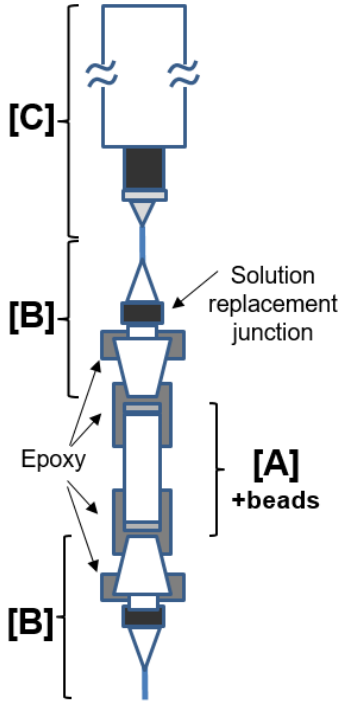

Figure 2.3. Schematic of adsorption column. A: glass tube holding agarose beads functionalized with human albumin binding chemistry Cibacron Blue dye. B: Barbed inlet/outlet with Luer lock and needle tip to flow solution in and out of glass tube. C: Interchangeable solution reservoir feed.

A phosphate buffer (PB) (pH 7.4) for the adsorption column was prepared to mimic the salt composition of human blood serum. [37-39] 144.3 mg/L $CaCl_2$, 4.26 g/L Na_2HPO_4, 612.4 mg/L KH_2PO_4, 85.7 mg/L $MgCl_2$, and 4.68 g/L NaCl were dissolved in HPLC-grade submicron filtered water under stirring and heat, then filtered through a 10.0 µm membrane filter. NaCl was purchased from EMD Chemicals Inc. (Germany); all other chemicals were obtained from Sigma-Aldrich (USA). NaSCN, indoxyl sulfate, and HA solutions were prepared by simple dissolution in PB. 0.58 mM linoleic acid (LA) solution was prepared by pipetting liquid LA into phosphate buffer and sonicating in 10 minute increments until micelles were formed and evenly distributed,

indicated by the solution becoming uniformly cloudy. Solutions of micro BCA protein assay were prepared as instructed in a kit obtained from Thermo Scientific (USA).

2.2.7 *Absorption and Fluorescence Measurements*

Absorbance and fluorescence measurements were taken with a UV-Vis spectrophotometer (Molecular Devices SpectraMax i3x). Eluent solutions from the absorption column were collected in fluorescence plates (Thermo Scientific Nunc, USA). Fluorescence spectrum scans from 320-410 nm were recorded for each sample with an excitation wavelength of 270 nm and bandwidth of 15 nm. For absorbance measurements, each sample was then transferred and diluted to its 1/8 strength in absorbance plates (Corning, USA). For BCA analysis, absorbance samples were further diluted to 1/533 in a new absorbance plate. A 6-point calibration curve was used and data normalized to known maximum and minimum values. Binding capacities were measured by trapezoidal integration of eluent concentration as a function of time during release/rinse periods. Free volume was calculated from bead volume of 0.38 mL and spherical packing density of 0.64.

2.3 RESULTS AND DISCUSSION

HA selective ligand was grafted onto SPR chips with a three-layer structure: Thiol-gold chemistry, as the bottom layer, immobilized thiol-azido PEG or MUDA (and PEG) onto the chips while PEG provide anti-fouling layer in the middle. HA selective ligands, targeting S-II sites and fatty acid binding sites, were grafted on top of the MUDA or PEG layer. Fig. 2.4 (left) shows a representative adsorption of HA onto the modified chip surface monitored by SPR signal shift as a function of increased concentration. The binding behavior signal (binding 1 & 2) was fit to the Langmuir isotherm model (isotherm 1 & 2) and plotted in Fig. 2.4 (right) with adsorption coefficient calculated accordingly.

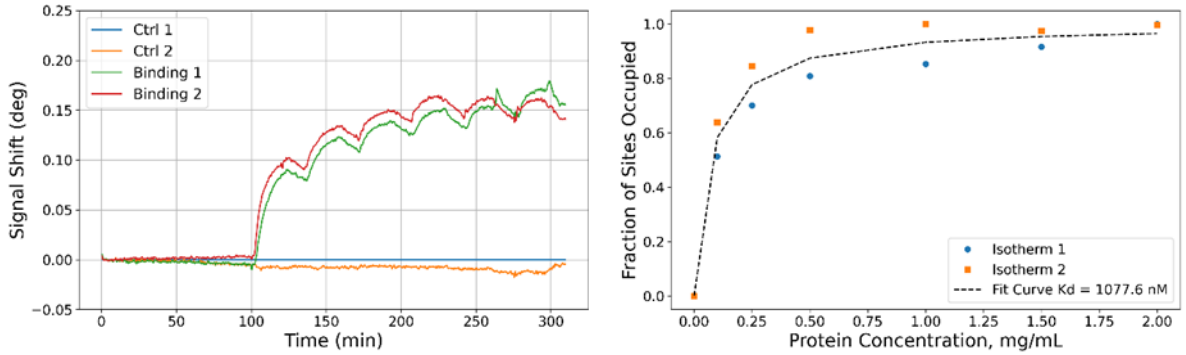

Figure 2.4. A representative SPR absorption curve of albumin on functionalized (Direct Blue 71) SPR sensor chip (left) and corresponding Langmuir isotherm curve (right).

Table 2.1. K_d of HA on SPR sensor modified with different ligands

Surface Ligand	**K_d**
Cibacron Blue	3.0 μM
Direct Blue 71	1.1 μM
Tryptophan	0.9 μM
Octadecane (C18;Alkane)	2.0 μM
Decane (C10;Alkane)	1.1 μM
Capric Acid (C10;COOH)	0.9 μM
Hexane (C6;Alkane)	1.6 μM

The K_ds of various surfaces show in a narrow range of 0.9 to 3.0 μM, which is comparable to the K_d of HA-IS of 0.6-1.1 μM. [6, 8] For the application of binding HA to remove PBUTs, the binding affinity between surface modification ligand and HA should be comparable to the affinity between HA and IS, leading to competition between surface ligand and IS for binding to HA. [5, 23]

Significantly different albumin binding behavior is seen at different stages of chemical functionalization of the SPR chip. Unmodified chips show a binding signal as high as 0.29° because of albumin fouling onto Au. Chips functionalized with PEGs (with terminus of -NH_2, -

COOH, or -N_3) shows signal levels around 0.05° due to the anti-fouling nature of PEG. Fully functionalized chips show absorption signals around 0.2° when fully occupied by HA. This lower shift (0.2°), compared to a bare Au signal (0.29°), is expected due to the increased distance of binding ligands from the Au plasmon surface when a PEG layer is present and limited density of binding sites.

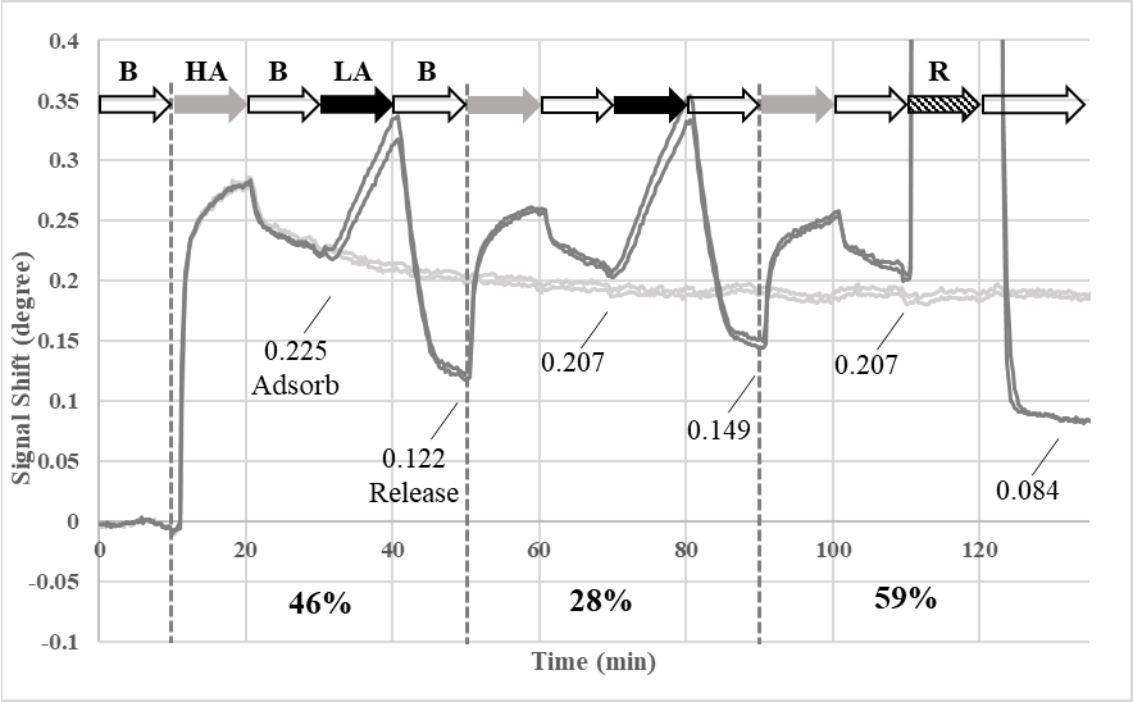

Figure 2.5. A representative SPR signal response for HA adsorption and desorption (in cycles). Light gray curves represent control channels with continuous buffer rinse after initial HA adsorption. Dark gray curves represent the signal shift as HA is adsorbed/desorbed as different solutions are flowed through. The adsorption/desorption test was done in repeating sequence with different solutions indicated by different colored arrows and notations (B: phosphate buffer; HA: human albumin; LA: linoleic acid; R: NaSCN). Labeled numbers are SPR signal shift value. Calculated release of bound albumin by release agent is shown in percentage.

Figure 2.5 shows the reversible HA adsorption and desorption on functionalized SPR chips with 2 LA cycles and a final thiocyanide release cycle. SPR shift has a strong dependence on solution conditions, thus one can only compare shift signals after a buffer rinse. [40, 41] The initial sensor baseline is set to zero. For the first cycle, after initial HA exposure and buffer rinse a shift of 0.225 is seen corresponding to full HA coverage. After LA exposure and buffer rinse a drop in shift 0.122 is seen instead of the ideal zero if HA is completely released to initial state. The percent released is calculated as (0.225-0.122)/0.225 or ~46%. The signal corresponding to protein adsorption was found to be similar over cycles which is an indication of stable binding affinity, which leads to similar amount of captured protein over cycles. Even though the total amount of captured protein remains stable, an increasing amount of un-released protein over cycles was observed. Un-releasable protein was expected due to fouling onto unprotected surface of desorbed surface chemistry and practical limitations of buffer rinse times. Thiol-gold is known to be unstable under oxidative conditions, therefore, functionalized SPR chips were found to have reduced release capacity after long storage time or testing with more than five adsorption/desorption cycles. [42, 43] SPR angle shifts and releasability percent as a function of surface functionalization and release chemical are summarized in Table 2.2.

Table 2.2. Summary of albumin absorption and desorption on SPR chips as a function of surface terminus functionalization and release agent

Surface ligand	SPR Signal with HA Bound (°)	Release Percentage (highest observed, in %)							
		NaSCN 2M	NaCl 2M	Na_2SO_4 2M	pH 3.6	SDS 35mM	LA 0.6mM	FA mix	Ibp 0.1mM
Cibacron Blue (CB)	**~0.25**	**78.0**	**34**	**12.7**	**0**	**93.0**	**44.1**	**49.5**	**0**
Direct Blue 71	~0.19	0	-	-	-	0	-	-	-
Tryptophan NH_2 term	~0.17	15.0	-	-	0	0	-	-	-
COOH term	~0.19	0	-	-	0	-	-	-	-
Octadecane (C18;Alkane)	~0.24	42.0	-	-	-	0	-	-	-
Decane (C10;Alkane)	~0.15	0	-	-	-	38.1	-	-	-
Capric Acid (C10;COOH)	**~0.18**	**65.0**	**37.1**	**0**	**18.7**	**72.5**	**52.3**	**36.1**	**-**
Octane (C8;Alkane)	~0.11	51.4	-	-	-	29.5	-	-	-
Hexane (C6;Alkane)	~0.05	0	-	-	-	0	-	-	-

Fatty acid-like ligands and ligands of longer hydrocarbon chain length show stronger binding affinity as octadecane (C18) shows a SPR signal 0.24°, which is comparable to our set reference of 0.25° representing full-surface coverage, while hexane (C6) shows a signal of 0.05°, which is near the detection limit. Octane and decane ligands show intermediate signals of 0.11° and 0.15°. Capric acid has same chain length compared to decane but shows higher binding signal of 0.18° due to its carboxyl terminus which further stabilizes the binding through electrostatic interaction. Longer alkane chain length is desirable for better protein binding stability but undesirable for dissociation of protein from bound ligand. For instance, the octadecane surface shows significant binding to HA but the release agents proved to have limited effects. Balancing the binding and dissociation ability, capric acid was thought to be the best performing fatty acid-like ligand.

Another set of ligands, including Cibacron Blue (CB), Direct Blue 71 (DB71), and tryptophan, that specifically target the S-II site of HA has large aromatic rings and charged side groups. [12, 32-36, 44] The surface chemistry ligands were stabilized in the S-II cavity by hydrophobic-hydrophobic and electrostatic interactions and π-stacking between aromatic rings and surrounding moieties. The HA binding signal was found to be 0.25°, 0.19°, 0.17° and 0.19° for CB, DB71, tryptophan of -NH2 and -COOH terminus respectively. Compared to fatty acid-targeting ligands, S-II site-targeting ligands showed a more stable binding of albumin. However, only CB showed feasible release ability for HA regeneration.

Previous studies have proven that it is difficult to remove albumin bound to a CB chromatography column. Only NaSCN solutions with high concentrations near 2 M were found to sufficiently strip absorbed albumin from CB chromatography columns [32-36], which would be unacceptable for direct contact with blood plasma. As is shown in Table 2.2, a variety of chemicals were chosen to release albumin by different mechanisms. NaSCN works as a chaotropic agent disrupting H-bonds, protein-ligand interactions, and protein conformation. NaCl and Na_2SO_4 of high ionic strength shields the electrostatic interaction between ligand and albumin. The pH 3.6 buffer protonates the albumin therefore altering its charge in order to release it from the surface. Fatty acids and SDS target fatty acid binding sites to competitively replace surface ligands attached to albumin to initiate release. [17, 18, 22] Ibuprofen (ibp) competes with surface ligands to occupy the S-II site, causing release. [5] Despite showing the best albumin release ability, SCN^- is not a viable choice for HA regeneration because of its toxicity and that large volumes of ion exchange solution are needed downstream. SDS effectively releases albumin but also denatures it. In order to demonstrate the feasibility of a portable albumin regeneration device, the release chemical used must be biocompatible or easy to remove in downstream processes. High ionic strength and pH-

altering buffer solutions were considered for ease of downstream reversal. However, both failed to provide satisfying release capacity, as shown in Table 2.2. Biocompatible fatty acids were then examined. Plasma-prevalent linoleic acid (LA) and the LA-containing fatty acid mixture showed great albumin release capacity of 44.1% and 49.5% on CB surface even at limited concentrations of about 0.5 μg/ml. [45]

In Table 2.3, the optimal albumin binding chemistry and release conditions were measured. The release capacity was calculated with respect to their monolayer averaged SPR signal shift (Cibacron Blue: 0.23°, n=76; Capric Acid: 0.14°, n=50). From fatty acid binding ligands, capric acid was found to have the best adsorption/desorption capacity. CB is the best for albumin regeneration among the S-II targeting binding ligands. On both types of treated sensor surface, linoleic acid and fatty acid mix was able to release approximately 1/3 of a monolayer-worth of bound protein, which allows the cleaned albumin and the release agent to be returned to plasma without further treatment.

Table 2.3. Human serum albumin desorption percent as a function of release agent on capric acid and Cibacron Blue functionalized chips.

Release Agent / Surface Ligand	Linoleic Acid	Fatty Acid Mix	NaSCN
Capric Acid	27.5±15.5% (n=14)	38.9±9.9% (n=15)	49.5±20.4% (n=20)
Cibacron Blue	31.0±18.9% (n=12)	37.4±14.2% (n=18)	65.0±12.3% (n=45)

Values reported are in percentage with respect to a monolayer protein binding signal strength.

There is a risk that HA carrying PBUT in a S-II site will not bind to the functionalized surfaces. The primary hypothesis is that binding HA-PBUT complex to a surface will release the PBUT. However, as shown in Figure 2.6, the HA-IS binding-induced SPR signal shifts are comparable to

those of the tests that used albumin with unoccupied S-II sites. This indicates the HA binding affinity to CB-grafted surface does not change with pre-occupied S-II site. The captured HA-IS complex can be desorbed with the same fatty acid release chemistry.

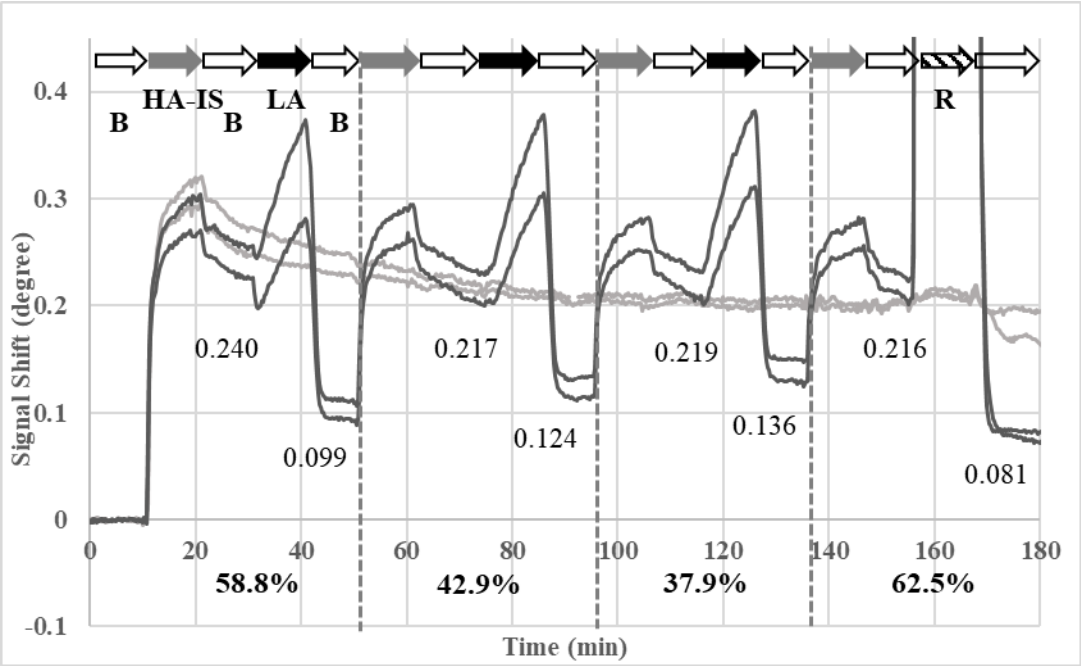

Figure 2.6. A representative SPR curve of HA-IS complex adsorption and desorption in cycles on a CB-functionalized SPR chip. Dark gray curve represents the absorption/desorption test done with indicated release chemicals while light gray are buffer reference channels after HA-IS adsorption. The test was done in repeating sequence with different solutions indicated by different colored arrows and notation (B: phosphate buffer; HA-IS: human albumin indoxyl sulfate complex; LA: linoleic acid; R: NaSCN). Labeled numbers are SPR signal shift representing the amount of stably adsorbed albumin and the amount of unreleased albumin after release agent rinse. Calculated releasability of bound albumin is shown in percentage.

To demonstrate practical application for clinically relevant amounts of HA-PBUT cleansing, commercially available CB-functionalized agarose beads were purchased and built into an adsorption column as described in the Materials and Methods section. In cycles, phosphate buffer, HA-IS complex solution, phosphate buffer, and then release agents (linoleic acid or NaSCN) were pumped through the column and the eluent was collected. CB-functionalized beads were expected

to adsorb HA-IS and cause the dissociation of IS from the captured HA. Release agents were expected to cause desorption of captured IS-free HA from the adsorption column. These adsorption and desorption behaviors were studied by optical absorbance at 280 nm of the eluent proportional to HA-IS concentration. As Figure 2.7 shows, with low initial eluent concentration rising to the feed concentration, HA-IS complex quickly binds to and saturates CB-agarose beads. Then both LA and NaSCN release HA from the adsorption column. However, the release behavior is different between LA and NaSCN. On one hand, NaSCN shows fast release immediately upon introduction which corresponds to a sharp peak in Figure 2.7. On the other hand, LA shows most release occurs at the buffer rinse after LA flow. We hypothesized that the delayed LA release was caused by LA micelles dissolving at the buffer solution exchange front where concentration drops below the critical micelle concentration (0.1 mM) giving more free-floating molecules of LA capable of release. [45, 46] This release profile may be optimized by multiple shorter buffer/LA cycles. Even though it is clear from the absorption measurements that HA or HA-IS is bound by the CB chemistry and then eventually released when a release agent is flowed through, it remains unclear whether IS was removed from HA upon binding as the absorbance include contributions from both IS and HA and so they cannot be distinguished from this data alone.

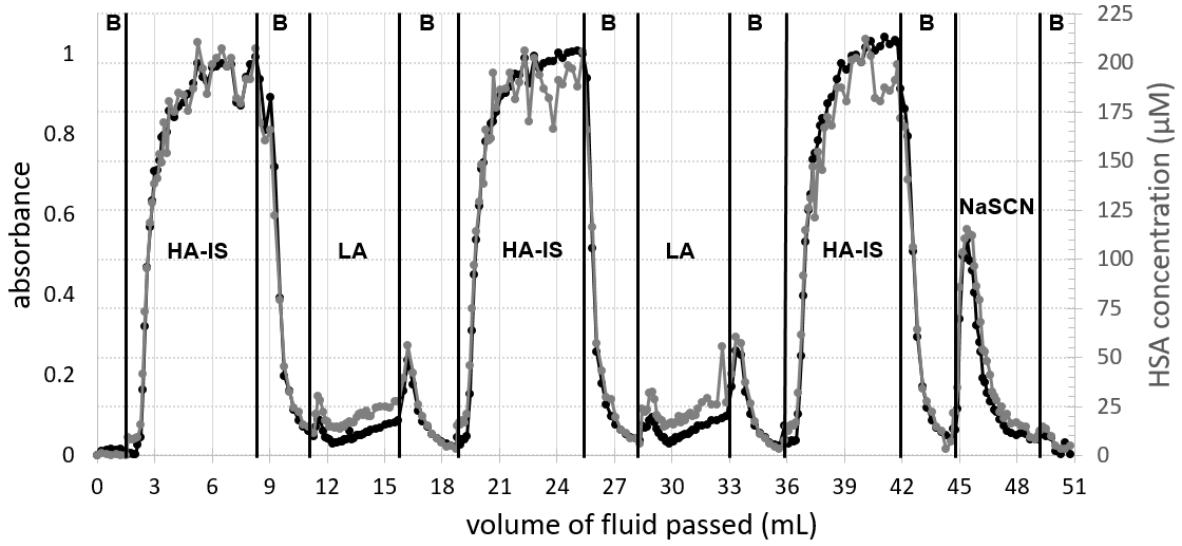

Figure 2.7. UV-vis absorbance 280 nm (dark curve) and BCA assay (light curve) for eluent solutions with respect to cumulative volume of eluent passing through 0.52 mL CB-agarose beads. Vertical black lines demarcate eluent regions while acronyms indicate eluent composition: 'B' for buffer, "LA" for linoleic acid, "HA-IS" for 200 μM human serum albumin with 200 μM indoxyl sulfate in buffer, and "NaSCN" for 2 M NaSCN in buffer. Lines are guides to the eye.

BCA assay is a protein sensitive quantification method which was used here to measure the concentration of HA. From the BCA assay curves we were able to calculate binding capacity of the column, which was 0.371, 0.304, 0.371 μmol HA/mL beads corresponding to three cycles of adsorption/desorption shown in Figure 2.7. Similarly, release capacities were measured to be: 0.177 (LA), 0.232 (LA), 0.292 (NaSCN) μmol HA/mL beads for the three cycles. Specifications for the CB-functionalized beads have 0.271 μmol/mL beads, so the experimental release capacities are close to expected values. Binding capacity can be easily over-estimated because it is hard to precisely determine the dead volume and starting time of flow across an adsorption column. From these calculations, LA releases at least 60% (or up to 79%) as well as commercially used NaSCN. Comparing binding capacity to release capacity, LA and NaSCN release at least 47% and 79% of HA bound to the column, respectively. Both values corroborate SPR results (31% and 65%,

respectively). LA shows a promising release capacity, though lower than NaSCN, for a CB-based HA regeneration system because, unlike NaSCN, LA is plasma-compatible.

Even though we demonstrated that HA capture and release was achieved with the plasma-compatible CB-LA chemistry, the absorption and BCA assay studies do not prove that binding of HA causes IS release, which is important for toxin separations in treatment. Theoretically, it is possible to calculate IS concentration from subtraction of BCA-derived HA concentration from total solution absorbance and using known optical absorption coefficients. However, the system proved too noisy to produce conclusive results in an analysis that subtracts between two measurements. Addressing this problem, fluorescence measurements were used to distinguish HA from IS. HA fluorescence is based on the tryptophan residue in S-II binding site which can be influenced by its surrounding chemical environment, such as the bound IS, release agent and composition of buffer solution. Spectra measurements were taken of HA-IS solutions with and without LA (Figure 2.8).

In the case of simple HA-IS mixture solutions, going from 1:0 to 1:1 ratio, there is a linear peak shift of a single fluorescence peak wavelength from 354 to 367 nm consistent with a coupled IS in S-II site. While in the presence of LA, the HA-IS fluorescence spectrum consists of two independent peaks with the HA peak shifted down to 342 nm and IS peak appearing at 380 nm as IS concentration increases. This behavior is consistent with the hypothesis that HA forms an HA-LA complex at the S-II site, causing a shift in HA fluorescence peak wavelength and formation of an independent IS peak. Importantly, we can prove that released HA is cleaned and contains no IS (<10 μM detection limit) with an observed fluorescence peak at 342 nm.

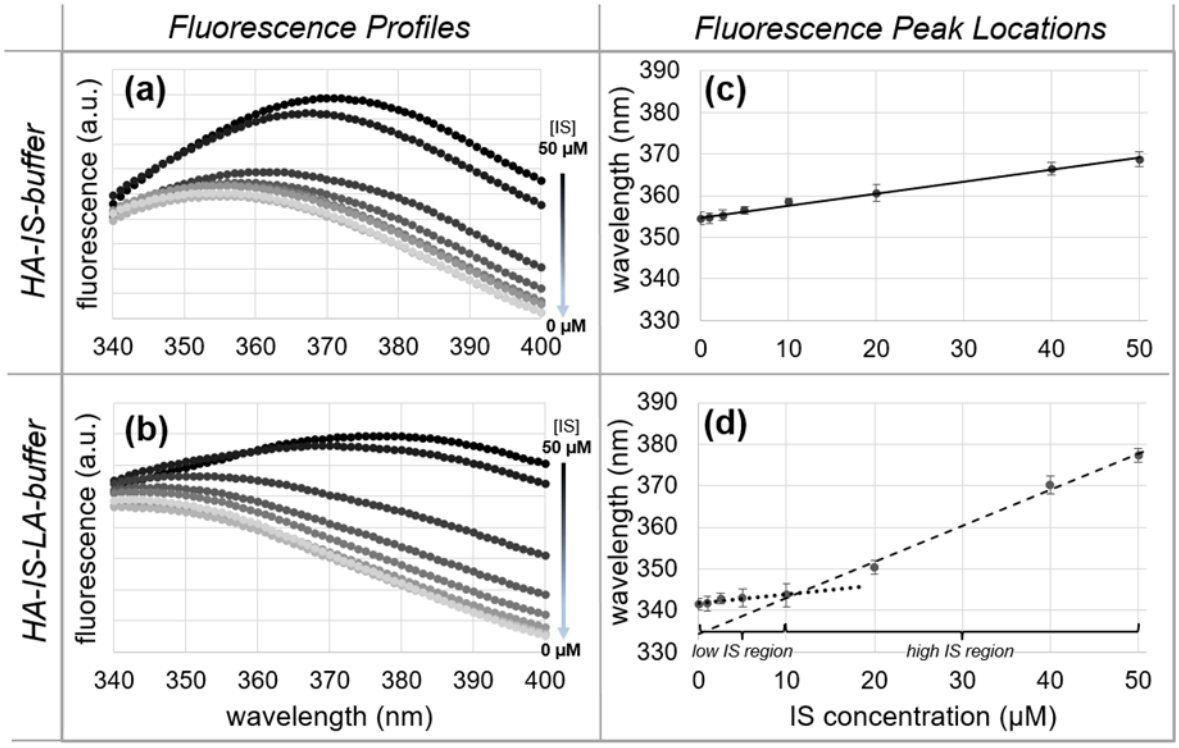

Figure 2.8. HA-IS solution fluorescence signal profiles (a,b) and fluorescence signal peak locations at constant HA (50 µM) and varying IS concentrations (50, 40, 20, 10, 5, 2.5, 1, 0 µM) (c,d). HA-IS is dissolved in buffer (a,c) and HA-IS is dissolved in buffer containing LA micelles (b,d). Due to dilution needed for assay, 50 µM corresponds to a feed solution concentration sample of 200 µM used for adsorption studies..

Figure 2.9 shows the fluorescence peak wavelength as a function of volume of solution eluted through the column. At initial HA-IS introduction, there is a temporary shift to ~380 nm consistent with free IS released as HA is bound to beads. This behavior indicates that the IS was removed from HA when the CB-chemistry captured the HA-IS complex. The peak then shifts to the 1:1 wavelength of 367 nm for the feed solution flowing over saturated beads. The second rinse also causes a jump to ~380 nm, presumably rinsing off loosely bound IS on other HA sites. Notably, when LA is added the peaks shifted to 342 nm, showing that IS-free HA was released. Thus, IS was removed from HA and HA was regenerated.

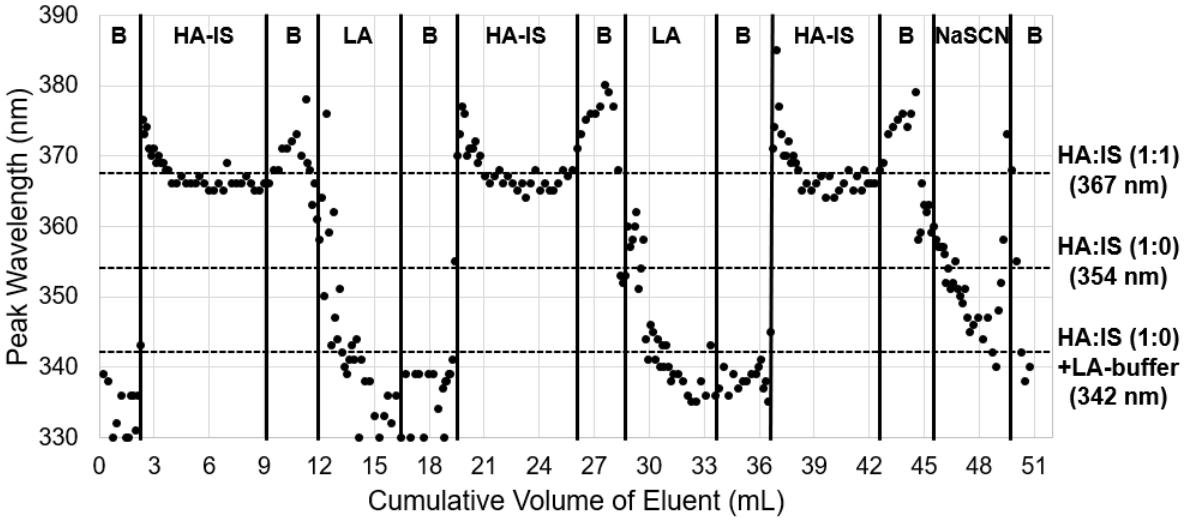

Figure 2.9. Fluorescence peak wavelength vs.cumulative eluent volume. Dark gray points indicate measured fluorescence peak locations. Horizontal dashed lines indicate peak values of solutions containing indicated species (50 μM).

BCA protein analysis was used to quantify HA concentration while fluorescence peak shift analysis showed that the released HA was cleaned of IS. These analyses showed that LA has ~60% of the release capacity of the NaSCN standard. Release capacity was measured to be ~0.2 μmol HA/mL beads (13.5 mg/mL). In our system, flow rate was set to 4.0 mL solution/min. Based on our data, a column is saturated with bound HA in ~1 min. and full release could take as little as 1 min. if LA and buffer cycles were optimized to maximize release. Given 2 min. binding/release cycles, 120 cycles would be possible in a 4-hour conventional dialysis treatment session. To calculate the volume of chromatography resin required for such processing we can use the simple relationship $Resin\ volume = A/PC$ where A is the amount of HA to process per session (250 g), P is the processing capacity per cycle (13.5 mg/ml), and C is the number of cycles (120). To process the typical adult amount of HA in blood plasma (250 g) in one 4-hour hemodialysis session, only 155 mL chromatography resin is needed, enabling a practical dialysis treatment design.

2.4 CONCLUSIONS

Presently there are no treatment options to reduce protein bound toxins to non-uremic levels. A possible approach is to bind HA-PBUT complexes to a surface, release toxin to a waste stream/dialyzer, and then release HA back into the plasma stream. Currently used HA purification methods use toxic levels of NaSCN requiring extensive ion exchange volumes not compatible with dialysis treatments. Here we found that plasma compatible fatty acids (linoleic acid and fatty acid mixture at physiological ratios) can release cleaned HA and be returned to a plasma stream for potential dialysis treatment. SPR studies showed Cibacron Blue and capric acid to be suitable surface functionalization for HA capture and release, while long chain alkanes bind too strongly resulting in low release yield. The process was scaled to commercially available Cibacron Blue-functionalized agarose beads commonly used for HA purification by chromatography. Binding capacities of 0.35 μmol HA/mL beads and release amounts of 0.23 μmol HA/mL beads were seen using the plasma compatible linoleic acid. Fluorescence studies of the released HA eluents showed the HA-IS complex had been stripped of the protein bound toxin indoxyl sulfate. During a conventional 4-hour dialysis session with 2-minute binding release cycles, only 155 ml of CB-agarose beads would be needed to process the 250 g of HA in a typical patient. This new process can enable more effective dialysis treatments and positively impact mortality rates associated with heart disease in hemodialysis patients.

2.5 REFERENCES

[1] United States Renal Data System (USRDS) 2021 Annual Data Report. https://adr.usrds.org/2021/chronic-kidney-disease/6-healthcare-expenditures-for-persons-with-ckd (accessed.

[2] Sirich, T. L.; Fong, K.; Larive, B.; Beck, G. J.; Chertow, G. M.; Levin, N. W.; Kliger, A. S.; Plummer, N. S.; Meyer, T. W.; Frequent Hemodialysis Network Trial, G. Limited reduction in uremic solute concentrations with increased dialysis frequency and time in the Frequent Hemodialysis Network Daily Trial. *Kidney international* **2017**, *91* (5), 1186-1192, Clinical Trial; Comparative Study; ; Research Support, N.I.H., Extramural; Research Support, U.S. Gov't, Non-P.H.S. DOI: 10.1016/j.kint.2016.11.002.

[3] Ward, R. A.; Beck, W.; Bernardo, A. A.; Alves, F. C.; Stenvinkel, P.; Lindholm, B. Hypoalbuminemia: a price worth paying for improved dialytic removal of middle-molecular-weight uremic toxins? *Nephrol Dial Transplant* **2019**, *34* (6), 901-907. DOI: 10.1093/ndt/gfy236.

[4] Brettschneider, F.; Toelle, M.; von der Giet, M.; Passlick-Deetjen, J.; Steppan, S.; Peter, M.; Jankowski, V.; Krause, A.; Kuehne, S.; Zidek, W.; et al. Removal of Protein-Bound, Hydrophobic Uremic Toxins by a Combined Fractionated Plasma Separation and Adsorption Technique. *Artificial Organs* **2013**, *37* (4), 409-416. DOI: 10.1111/j.1525-1594.2012.01570.x.

[5] Tao, X.; Thijssen, S.; Kotanko, P.; Ho, C. H.; Henrie, M.; Stroup, E.; Handelman, G. Improved dialytic removal of protein-bound uraemic toxins with use of albumin binding competitors: an in vitro human whole blood study. *Scientific Reports* **2016**, *6*, 9, Article. DOI: 10.1038/srep23389.

[6] Sakai, T.; Yamasaki, K.; Sako, T.; Kragh-Hansen, U.; Suenaga, A.; Otagiri, M. Interaction mechanism between indoxyl sulfate, a typical uremic toxin bound to site II, and ligands bound to

site I of human serum albumin. *Pharmaceutical Research* **2001**, *18* (4), 520-524, Article. DOI: 10.1023/a:1011014629551.

[7] Leong, S. C.; Sirich, T. L. Indoxyl Sulfate-Review of Toxicity and Therapeutic Strategies. *Toxins* **2016**, *8* (12), 13, Review. DOI: 10.3390/toxins8120358.

[8] Devine, E.; Krieter, D. H.; Ruth, M.; Jankovski, J.; Lemke, H. D. Binding Affinity and Capacity for the Uremic Toxin Indoxyl Sulfate. *Toxins* **2014**, *6* (2), 416-429, Article. DOI: 10.3390/toxins6020416.

[9] Niwa, T.; Takeda, N.; Tatematsu, A.; Maeda, K. Accumulation of indoxyl sulfate, an inhibitor of drug-binding, in uremic serum as demonstrated by internal-surface reversed-phase liquid chromatography. *Clin Chem* **1988**, *34* (11), 2264-2267.

[10] Meijers, B. K. I.; De Loor, H.; Bammens, B.; Verbeke, K.; Vanrenterghem, Y.; Evenepoel, P. p-Cresyl Sulfate and Indoxyl Sulfate in Hemodialysis Patients. *Clinical Journal of the American Society of Nephrology* **2009**, *4* (12), 1932-1938, Article. DOI: 10.2215/cjn.02940509.

[11] Pavlenko, D.; van Geffen, E.; van Steenbergen, M. J.; Glorieux, G.; Vanholder, R.; Gerritsen, K. G. F.; Stamatialis, D. New low-flux mixed matrix membranes that offer superior removal of protein-bound toxins from human plasma. *Scientific Reports* **2016**, *6*. DOI: 10.1038/srep34429.

[12] Peters Jr, T. All about albumin: biochemistry, genetics, and medical applications; Academic press, 1995.

[13] Fasano, M.; Curry, S.; Terreno, E.; Galliano, M.; Fanali, G.; Narciso, P.; Notari, S.; Ascenzi, P. The extraordinary ligand binding properties of human serum albumin. *IUBMB Life* **2005**, *57* (12), 787-796, Review. DOI: 10.1080/15216540500404093.

[14] Curry, S. Lessons from the crystallographic analysis of small molecule binding to human serum albumin. *Drug Metab Pharmacokinet* **2009**, *24* (4), 342-357. DOI: 10.2133/dmpk.24.342.

[15] He, X. M.; Carter, D. C. ATOMIC-STRUCTURE AND CHEMISTRY OF HUMAN SERUM-ALBUMIN. *Nature* **1992**, *358* (6383), 209-215. DOI: 10.1038/358209a0.

[16] Ghuman, J.; Zunszain, P. A.; Petitpas, I.; Bhattacharya, A. A.; Otagiri, M.; Curry, S. Structural basis of the drug-binding specificity of human serum albumin. *Journal of Molecular Biology* **2005**, *353* (1), 38-52. DOI: 10.1016/j.jmb.2005.07.075.

[17] Curry, S.; Mandelkow, H.; Brick, P.; Franks, N. Crystal structure of human serum albumin complexed with fatty acid reveals an asymmetric distribution of binding sites. *Nat. Struct. Biol.* **1998**, *5* (9), 827-835, Article. DOI: 10.1038/1869.

[18] Bhattacharya, A. A.; Grune, T.; Curry, S. Crystallographic analysis reveals common modes of binding of medium and long-chain fatty acids to human serum albumin. *Journal of Molecular Biology* **2000**, *303* (5), 721-732. DOI: 10.1006/jmbi.2000.4158.

[19] Lekawanvijit, S.; Kompa, A. R.; Krum, H. Protein-bound uremic toxins: a long overlooked culprit in cardiorenal syndrome. *Am. J. Physiol.-Renal Physiol.* **2016**, *311* (1), F52-F62, Article. DOI: 10.1152/ajprenal.00348.2015.

[20] Sudlow, G.; Birkett, D. J.; Wade, D. N. FURTHER CHARACTERIZATION OF SPECIFIC DRUG BINDING-SITES ON HUMAN-SERUM ALBUMIN. *Mol. Pharmacol.* **1976**, *12* (6), 1052-1061, Article.

[21] Sakai, T.; Takadate, A.; Otagiri, M. Characterization of binding site of uremic toxins on human serum albumin. *Biol. Pharm. Bull.* **1995**, *18* (12), 1755-1761, Article.

[22] Birkett, D. J.; Myers, S. P.; Sudlow, G. Effects of fatty acids on two specific drug binding sites on human serum albumin. *Mol Pharmacol* **1977**, *13* (6), 987-992.

[23] Tao, X.; Thijssen, S.; Levin, N.; Kotanko, P.; Handelman, G. Enhanced Indoxyl Sulfate Dialyzer Clearance with the Use of Binding Competitors. *Blood Purif.* **2015**, *39* (4), 323-330, Article. DOI: 10.1159/000381008.

[24] Mitzner, S. R.; Stange, J.; Klammt, S.; Peszynski, P.; Schmidt, R. Albumin dialysis using the molecular adsorbent recirculating system. *Current Opinion in Nephrology and Hypertension* **2001**, *10* (6), 777-783. DOI: 10.1097/00041552-200111000-00008.

[25] Kobashi-Margain, R. A.; Gavilanes-Espinar, J. G.; Gutierrez-Grobe, Y.; Gutierrez-Jimenez, A. A.; Chavez-Tapia, N.; Ponciano-Rodriguez, G.; Uribe, M.; Mendez Sanchez, N. Albumin dialysis with molecular adsorbent recirculating system (MARS) for the treatment of hepatic encephalopathy in liver failure. *Annals of hepatology* **2011**, *10 Suppl 2*, S70-76, ; Review.

[26] Schulman, G.; Agarwal, R.; Acharya, M.; Berl, T.; Blumenthal, S.; Kopyt, N. A multicenter, randomized, double-blind, placebo-controlled, dose-ranging study of AST-120 (Kremezin) in patients with moderate to severe CKD. *American Journal of Kidney Diseases* **2006**, *47* (4), 565-577. DOI: 10.1053/j.ajkd.2005.12.036.

[27] Schulman, G.; Berl, T.; Beck, G. J.; Remuzzi, G.; Ritz, E.; Arita, K.; Kato, A.; Shimizu, M. Randomized Placebo-Controlled EPPIC Trials of AST-120 in CKD. *Journal of the American Society of Nephrology* **2015**, *26* (7), 1732-1746. DOI: 10.1681/asn.2014010042.

[28] Abdelhameed, R. M.; Rehan, M.; Emam, H. E. Figuration of Zr-based MOF@cotton fabric composite for potential kidney application. *Carbohydrate Polymers* **2018**, *195*, 460-467. DOI: 10.1016/j.carbpol.2018.04.122.

[29] Kato, S.; Otake, K.; Chen, H. Y.; Akpinar, I.; Buru, C. T.; Islamoglu, T.; Snurr, R. Q.; Farha, O. K. Zirconium-Based Metal-Organic Frameworks for the Removal of Protein-Bound

Uremic Toxin from Human Serum Albumin. *J. Am. Chem. Soc.* **2019**, *141* (6), 2568-2576, Article. DOI: 10.1021/jacs.8b12525.

[30] Jankowski, J.; Zidek, W.; Brettschneider, F.; Jankowski, V. Method of dialysis for removing protein-bound toxins from the blood of patients using high-frequency electromagnetic fields. 2022.

[31] Tschulena, U.; Jankowski, J.; Fabig, A. Apparatus for removing protein-bound toxins from blood plasma. 2020.

[32] Gianazza, E.; Arnaud, P. A GENERAL-METHOD FOR FRACTIONATION OF PLASMA-PROTEINS - DYE LIGAND AFFINITY-CHROMATOGRAPHY ON IMMOBILIZED CIBACRON BLUE F3GA. *Biochem. J.* **1982**, *201* (1), 129-136, Article. DOI: 10.1042/bj2010129.

[33] Gianazza, E.; Arnaud, P. CHROMATOGRAPHY OF PLASMA-PROTEINS ON IMMOBILIZED CIBACRON BLUE F3GA - MECHANISM OF THE MOLECULAR INTERACTION. *Biochem. J.* **1982**, *203* (3), 637-641, Article. DOI: 10.1042/bj2030637.

[34] Subramanian, S. DYE-LIGAND AFFINITY-CHROMATOGRAPHY - THE INTERACTION OF CIBACRON BLUE F3GA WITH PROTEINS AND ENZYMES. *Crc Critical Reviews in Biochemistry* **1984**, *16* (2), 169-205, Review. DOI: 10.3109/10409238409102302.

[35] Denizli, A.; Kokturk, G.; Yavuz, H.; Piskin, E. Albumin adsorption from aqueous solutions and human plasma in a packed-bed column with Cibacron Blue F3GA-Zn(II) attached poly(EGDMA-HEMA) microbeads. *React. Funct. Polym.* **1999**, *40* (3), 195-203, Article. DOI: 10.1016/s1381-5148(98)00043-1.

[36] Yavuz, H.; Duru, E.; Genc, O.; Denizli, A. Cibacron Blue F3GA incorporated poly(methylmethacrylate) beads for albumin adsorption in batch system. *Colloids and Surfaces a-Physicochemical and Engineering Aspects* **2003**, *223* (1-3), 185-193, Article. DOI: 10.1016/s0927-7757(03)00153-5.

[37] Besarab, A.; Deguzman, A.; Swanson, J. W. EFFECT OF ALBUMIN AND FREE CALCIUM CONCENTRATIONS ON CALCIUM-BINDING INVITRO. *J. Clin. Pathol.* **1981**, *34* (12), 1361-1367, Article. DOI: 10.1136/jcp.34.12.1361.

[38] Kim E. Barrett, S. M. B., Scott Boitano, Heddwen Brooks. *Ganong's Review of Medical Physiology, 23rd Edition*; McGraw-Hill Medical, 2009

[39] Hall, A. C. G. J. E. *Textbook of Medical Physiology (11th edition)*; Saunders Co., 2004.

[40] Liedberg, B.; Nylander, C.; Lundstrom, I. SURFACE-PLASMON RESONANCE FOR GAS-DETECTION AND BIOSENSING. *Sensors and Actuators* **1983**, *4* (2), 299-304, Article. DOI: 10.1016/0250-6874(83)85036-7.

[41] Homola, J.; Yee, S. S.; Gauglitz, G. Surface plasmon resonance sensors: review. *Sens. Actuator B-Chem.* **1999**, *54* (1-2), 3-15, Review. DOI: 10.1016/s0925-4005(98)00321-9.

[42] Bhatt, N.; Huang, P. J. J.; Dave, N.; Liu, J. W. Dissociation and Degradation of Thiol-Modified DNA on Gold Nanoparticles in Aqueous and Organic Solvents. *Langmuir* **2011**, *27* (10), 6132-6137, Article. DOI: 10.1021/la200241d.

[43] Xue, Y. R.; Li, X.; Li, H. B.; Zhang, W. K. Quantifying thiol-gold interactions towards the efficient strength control. *Nat. Commun.* **2014**, *5*, 9, Article. DOI: 10.1038/ncomms5348.

[44] McMenamy, R. H.; Oncley, J. L. SPECIFIC BINDING OF L-TRYPTOPHAN TO SERUM ALBUMIN. *J. Biol. Chem.* **1958**, *233* (6), 1436-1447, Article.

[45] Mabrouk, A. F.; Dugan, L. R. SOLUBILITY OF LINOLEIC ACID IN AQUEOUS SOLUTIONS AND ITS REACTION WITH WATER. *J. Am. Oil Chem. Soc.* **1961**, *38* (1), 9-13, Article. DOI: 10.1007/bf02633110.

[46] Shen, Z. H.; Zhang, Q.; Li, X. B.; Chen, Q. L. Adsorption Behavior and Wettability of Rhodochrosite Surface: Effect of C-18 Fatty Acid Unsaturation. *Minerals* **2020**, *10* (10), 17, Article. DOI: 10.3390/min10100905.

Chapter 3. PROTOTYPE ADD-ON DEVICE DESIGN FOR CONVENTIONAL DIALYZER MACHINE WITH SELECTIVE PROTEIN BOUND UREMIC TOXIN REMOVAL CHEMISTRY

3.1 INTRODUCTION

The importance of protein bound uremic toxins (PBUTs) removal had been repeatedly emphasized in previous chapters. Simply put, despite the tremendous efforts made by the medical community and researchers, this unmet challenge is still tolling thousands of lives and billions of dollars every year. With albumin-centered PBUTs removal strategy established and emphasized in previous chapter, this chapter will focus on the transformation of this scientific finding into a prototype device that cooperates with conventional hemodialysis devices and demonstrate its albumin detoxification-PBUT removal efficacy.

Clinical operations, hemodialysis (HD) and hemodiafiltration (HDF), relays on the hollow fiber membranes to sieve uremic toxin smaller than membrane pore size. Hemodialysis operates with blood and dialysate flowing in opposite direction at a prescribed flow rate, with over 200 ml/min of blood and higher for dialysate. [1, 2] While HD operates solely through cross-membrane diffusion, HDF utilizes pressure-induced convection flow to promote cross-membrane transportation. However, limited by the nature of pore size-based screening and the fact that only a small free fraction of PBUT is available, even HDF does not efficiently manage plasma PBUTs, especially over the long term. [3-5] The clearance of marker PBUT, indoxyl sulfate (IS), was found to be around 60 mg per HD or HDF session unless enhanced by other improvements. The removal of PBUT was indeed improved by convection flow through the membrane, but the cost associated with such improvements is an additional loss of albumin for over 2 gram per session compared to

HD. [3, 6] Carefully expanding the membrane's molecular weight cut off (MWCO) improved diffusion and flow across membrane for removal of uremic toxins. [7] But larger pore size of hollow fibers are often accompanied by the leakage of plasma solutes. Interestingly, sometimes membranes are designed to be intentionally leaky for the albumin and PBUT to be circulated into a designed loop where absorbents are introduced to pick up toxins through selective chemistry or a high surface area. [8-11] A similar plasma manipulation strategy was adopted to fractionate albumin-containing fluid for processing. However, in contrast to previous studies with absorbents aiming for toxin uptake, the withdrawn plasma is circulated with absorbents targeting the binding of albumin in the presented design of this chapter.

The fractionation of whole blood for processing is actually nothing new to the realm of artificial liver and kidney support. [12, 13] Plasma exchange therapy, in which a portion of plasma is extracted from the patient's body and replaced with donor plasma or substitute fluid, is prescribed for patients with acute hepatic failure to supplement the lost liver function. In this procedure, a limited (volume) fraction, typically around 20% but possibly higher per cycle, of blood is continuously extracted until the target exchange volume is reached. [12, 14-16] The reason for limiting the fraction of plasma extraction is to avoid a severe interruption of blood cells. Hemolysis, which refers to the destruction of blood cells, particularly red blood cells, is associated with a range of adverse symptoms. Electrolyte concentration is another factor associated with management of hemolysis as it influences the osmotic pressure imposed on blood cells. [17] Hemolysis caused by mechanical disturbance, such as the actions of pumps, tubing, and dialysis/filtration membranes, to a certain extent, cannot be completely avoided but should be minimized as much as possible. [18]

Guided by the reviewed considerations and parameters of dialysis and plasma exchange procedures, a prototype device was designed to complement conventional hemodialysis for the removal of PBUTs. The system loop begins with plasma separation from blood with designed filter cartridge. Extracted plasma was then treated with albumin detoxification chemistry and release chemistry established in previous chapter for removal of PBUTs. Another filter cartridge was set to screen chemical utilized for albumin release. All aforementioned setup operates in a close loop with conventional dialyzer.

3.2 EXPERIMENTAL

3.2.1 *Materials and Chemicals*

Human Serum Albumin (HSA, fraction V) was acquired from EMD Millipore Corp and used as is. Bovine Serum Albumin (BSA, lyophilized powder), Linoleic acid (LA, ≥ 95%), Sodium Thiocyanate and other phosphate salts were acquired from Sigma Aldrich and used as is. Cibacron blue functionalized agarose bead, Blue Sepharose 6 Fast Flow, was CytivaLifeScience. Peristaltic pumps used for tests were Cole-Palmer MasterFlex, tubing is from the same source. Sonicator was built from custom made power board and transducer (43kHz, 35W). SwitchEZ™ solenoid pinch valves were acquired from PreciGenome. Dialyzer used are Optiflux F16NR and Femoflow F3 from Fresenius. Hollow fiber membranes, PlasmaPhan P1LX and MicroPES TF10 were kindly supplied by 3M free of charge. Artificial plasma was made with 40 g/L bovine serum albumin and 30 mg/L indoxyl sulfate in dialysate (Naturalyte, Fresenius Medical Care) to mimic solute concentration in hemodialysis patient body. [11, 19]

3.2.2 *Cibacron Blue Functionalized Bead Column*

In Figure 3.1, the Cibacron Blue Functionalized Bead Column (referred to as the CB column hereafter) was fashioned using acquired Blue Sepharose 6 Fast Flow beads (referred to as CB beads) and a custom-made housing. The housing was constructed from a plastic tube, a PTFE filter with a pore size of 20 µm, and a nylon mesh support of 255 µm. For column assembly, medical-grade alcohol-compatible epoxy (Loctite EA M-31CL) was employed. A predetermined quantity of CB beads in suspension was carefully pipetted into the custom-made housing and subsequently rinsed with an ample amount of phosphate buffer (containing 21.48 g Na_2HPO_4, 3.11 g KH_2PO_4 in 1 L of water) or dialysate from Fresenius Medical Care. The packed column was stored in a refrigerator until its use.

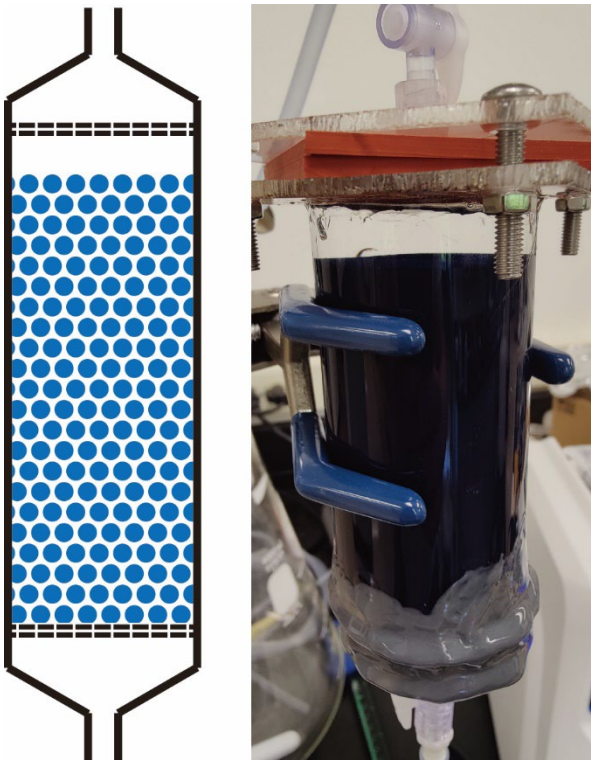

Figure 3.1. Scheme (left) and picture (right) of Cibacron blue functionalized bead column.

The adsorption efficacy and release chemistry were examined using the assembled CB column, as illustrated in Figure 3. 1. The adsorption and desorption cycles of albumin were tested in the following sequence while collecting and subjecting the eluent to UV-Vis spectroscopy: 1. A physiological concentration of albumin solution (40 mg/ml in phosphate buffer) was introduced into the CB column after it had been rinsed with buffer, and the process was continued until saturation was achieved. 2. Phosphate buffer was subsequently passed through the CB column to cleanse any unbound albumin residue. 3. A carefully selected release agent solution was then flushed through the CB column until complete release was attained. 4. Phosphate buffer was once again utilized to clear the CB column. The absorbance of the eluent was measured at λ=278 nm to quantitatively determine the concentration of albumin.

3.2.3 *Plasma Filter and Linoleic Acid Filter*

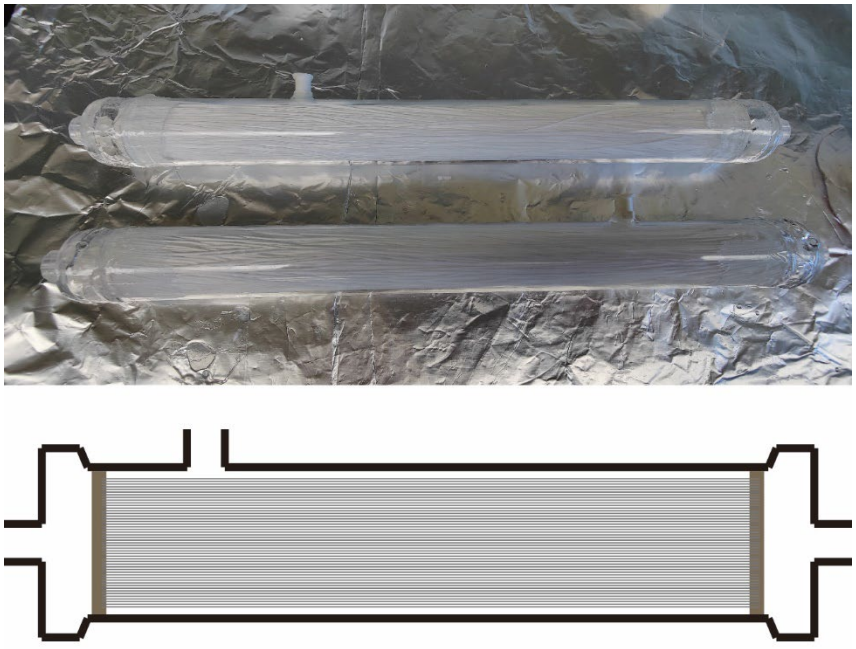

Figure 3.2. Picture (top) and scheme (bottom) of assembled plasma/linoleic acid filter.

As shown in figure 3.2, a plasma filter and linoleic acid filter were assembled using a set amount of PlasmaPhan hollow fiber membranes from 3M. These membranes were potted with epoxy in a designed barrel. Once the epoxy was properly cured, the excess length of the hollow fiber was trimmed using a scalpel to expose the potted hollow fibers. Subsequently, a Luer lock connector was attached to the filter cartridge. After the assembly process, the hollow fibers were wetted with ethanol and rinsed with a generous amount of water. An adequate quantity of dialysate was employed to flush the cartridge before its use.

The effectiveness of the linoleic acid filter was evaluated by intentionally obstructing the filter with a linoleic acid suspension (8 µl/10 ml buffer), while observing changes in both the volume of the feed solution and the clarity of the eluent. To investigate the regeneration of the filter, various solutions were employed to flush the filter in different directions.

3.2.4 *Sonicator*

For linoleic acid dispersion, a sonicator was constructed using a custom-made power supply and frequency generator. The sonication bath was comprised of a ceramic plate transducer (43 kHz, 35W) attached beneath a stainless-steel bowl using cyanoacrylate glue. A 20 ml glass vial was then securely positioned in the center of the sonication bath with tubing arrangement outlined in Figure 3.3.

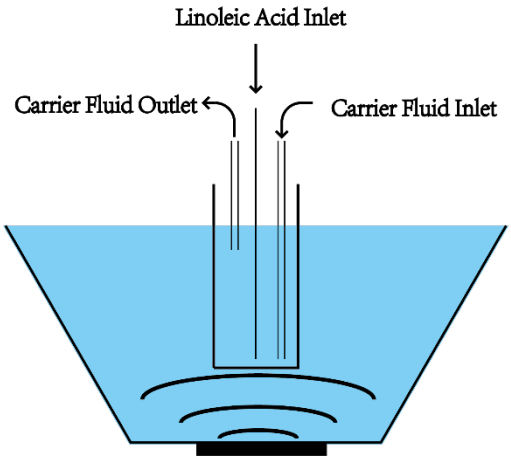

Figure 3.3. Scheme of sonicator with carrier flow and linoleic acid flow.

Linoleic acid was introduced into the bottom of the glass vial via a syringe pump and stainless-steel needle. Carrier fluid was introduced through tubes, set at varying heights to promote convection flow. The sonicator was evaluated under operational conditions to assess its capability for dispersing linoleic acid before use.

3.2.5 *Prototype Assembly and Control*

The prototype dialysis addon device was assembled with aforementioned modules connected by tubing and peristaltic pumps. Inert materials were selected for tubing and connections used. The control of assembled prototype was achieved through programed Arduino micro controller unit and programed peristaltic pumps.

3.3 RESULT AND DISCUSSION

The efficiency of the Cibacron blue functionalized column (referred to as the CB column hereafter) in adsorbing and detoxifying albumin was demonstrated in the previous chapter. Using an albumin solution with a concentration of 200 μM (1.32 mg/ml), the adsorption capacity and release capacity of the CB column were determined to be 0.35 μmol HA/mL beads and 0.23 μmol

HA/mL beads, respectively. This translates to approximately 1 ml of CB beads being capable of processing around 15.3 mg of human serum albumin (HSA). Consequently, the application of albumin detoxification was considered feasible, with 155 ml of CB beads being able to process 250 grams of HSA during a 4-hour dialysis session. However, in practical applications, further examination and validation of additional operational parameters and physiological/hematological considerations are necessary before proceeding with device design.

3.3.1 *Blood Fractionation Membrane Cartridge*

The composition of human blood is very complex compared to the simple albumin-indoxyl sulfate system studied in previous chapter. And the blood composition is subject to change under different health conditions. Generally, an adult body contains approximately 5 liters of blood, with around 55% being plasma and the remaining portion constituting blood cells. [20] This plasma, composed of water, sugars, fats, proteins, and salts, serves as the arena for interactions between albumin and indoxyl sulfate. Hence, in order to simplify the process and prevent hemolysis due to mechanical stress and chemical environments, it is desirable to fractionate blood for plasma. And as reviewed in previous section, blood flow rates during dialysis commonly exceed 200 ml/min. [1, 2] And 20%, in volume, extraction from blood flow for plasma is safe for most operations. [12, 14-16] The blood fractionation flow rate was therefore set to be 40 ml/min.

The selection of hollow fiber membranes was based on considerations of pore size and permeability. Given that the dimensions of albumin are approximately 15 nm in length and 4 nm in diameter, with slight variations observed between human serum albumin and bovine serum albumin, the minimum pore size permitting the passage of albumin is over 15 nm. [21, 22] However, effective transport generally necessitates a larger pore size to achieve higher flux without inducing protein fouling or denaturation. Therefore, MicroPES and PlasmaPhan hollow fiber membrane

was selected for sub-micron meter sized pores. Another major serum protein category is globulins, which are larger than albumin but hard to distinguish solely by this pore size. This might induce unexpected interactions on the designed Cibacron blue functionality.

Table 3.4. Specifications of MicroPES TF10 and PlasmaPhan P1LX hollow fiber membranes, surface area calculated of single strand fiber membrane and required number of fibers to accommodate 40 ml/min of fractionation flow. [23]

Type	MicroPES	PlasmaPhan	Unit
Permeance	35	9.3	ml/min cm bar
Pore Size	0.5	0.47	μm
Thickness	100	150	μm
Diameter, Inner	300	330	μm
Diameter, Outer	400	480	μm
Fiber Length	269	277	mm
Surface Area, Inner	2.54	2.87	cm^2
Surface Area, Outer	3.38	4.18	cm^2
Average	2.96	3.52	cm^2
Strand of Fiber Need for Fractionation Flow, 40 ml/min	5.60	17.70	/psi

The number of hollow fiber membranes required to accommodate a blood fractionation flow rate of 40 ml/min was calculated based on the membrane specifications provided in Table 3.1. The surface area of the hollow fiber membranes was first calculated by averaging the inner and outer surface areas of the hollow fiber. Then, the required number of fibers was determined by dividing the set flow rate by the surface area multiplied by the permeance of the fiber membrane. As demonstrated in Table 3.1, only 6 or 18 hollow fibers were needed for MicroPES and PlasmaPhan, respectively, thanks to high permeability of chosen membranes. The results of these calculations are presented in units of /psi. Therefore, as long as the applied cross-membrane pressure exceeds 1 psi, the estimated fiber requirement should prove adequate. Consequently, the peristaltic pump was assessed for its operational pressure, which surpasses 5 psi.

As cross-membrane requirement was easily handled by less than 20 fibers, the axial flow requirement was examined by Hagen–Poiseuille equation as follows:

$$\Delta p = \frac{8\mu l Q}{\pi r^4} \tag{3.3}$$

where Δp is the required pressure to drive a liquid with dynamic viscosity of μ through a tube, with length of l and radius of r, at a volumetric flow rate of Q. While the other parameters are predetermined by design, the dynamic viscosity of blood in this calculation remains a variable. It is understood that blood cells undergo some degree of deformation, consequently altering the blood viscosity. The viscosity of blood, which typically ranges from 3.5 to 5.5 cP, was found to be negatively correlated with the shear rate of blood. [24] To estimate the viscosity of blood, the shear rate was calculated using the fiber geometry and the designed blood flow rate of 200 ml/min. As depicted in Figure 3.4, the estimated shear rate consistently exceeds 100/s for blood fractionation bundle sizes ranging from 1 to 10,000 fibers. Under such shear rate of blood, a conservative estimation of blood viscosity should be about 4.5 cP, or 0.0045 Pa·s. [24] The extracted plasma is a Newtonian fluid with viscosity of 1.2 to 1.3 cP.

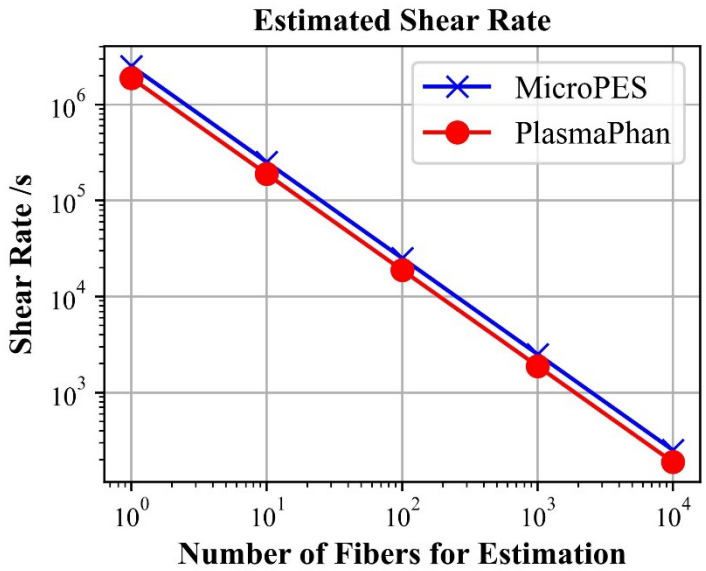

Figure 3.4. Estimated shear rate of blood versus number of fibers used for estimation.

Upon incorporating the estimated dynamic viscosity of blood, hollow fiber specifications, and a conservative pressure drop estimation (1 psi) into the Hagen–Poiseuille equation, the equivalent tube radius necessary for axial flow was determined to be approximately 1.23 mm. Subsequently, this equivalent radius was translated into the number of hollow fibers required to sustain the designated blood flow rate. This estimation was achieved by dividing the cross-sectional area of the 'equivalent tube' by the cross-sectional area of individual fibers. The estimation rounds up to 67 and 56 fibers needed for MicroPES and PlasmaPhan. The number of fibers needed to accommodate a 40 ml/min cross-membrane flow was determined to be fewer than the number of fibers required for supporting axial blood flow. As a result, the design of the plasma fractionation filter must adhere to the higher requirement. In fact, blood fractionation filters comprising more than 90 fibers was constructed for the prototype in order to compensate for potential damaged or closed fibers during fabrication.

Prior to prototype demonstrations, such blood fractionation filters were examined with buffer solutions under extended flow rate evaluate the permeability and fabrication quality. All of the blood filters demonstrated stable permeance of liquid across the hollow fiber membrane under designed flow rate. It should be noted that the prototype device demonstration experiment used artificial plasma instead of blood. But the filter was still integrated into the prototype to demonstrate filter stability.

3.3.2 *Reevaluate Adsorption and Desorption of Albumin on Cibacron Blue Functionality*

Among all proteins, human serum albumin (HSA) is the most abundant with a concentration about 40 g/L. [25, 26] Furthermore, HSA is known for its strong affinity for indoxyl sulfate (IS), resulting in a small fraction of IS, about 5%, being unbound by HSA. However, as chronic kidney disease progresses, albumin is believed to undergo mutations and partially lose its IS binding

capacity, while the IS accumulates about a hundredfold in concentration to 30-40 mg/L from 0.1-0.6 mg/L. [19, 25, 27-30] Given that the concentrations of both HSA and IS employed in the previous study differ from the physiological conditions described above, it is anticipated that the processes of albumin adsorption and desorption on the CB column will exhibit differences.

In the prior investigation, HSA at a concentration of 200 μM (1.32 mg/ml) was combined with the stoichiometric quantity of IS, specifically 42.64 mg/L. Subsequently, this mixture was subjected to assessment for its adsorption onto the CB column and subsequent desorption through the utilization of a linoleic acid (LA) solution, with a concentration of 1.8 μl LA per 10 ml of buffer. The tested IS level is comparable to serum level of patient with stage five chronic kidney disease while the tested HSA concentration is only about 1/30 of serum level. Considering that the interaction between HSA and the Cibacron blue functionality could be affected by the heightened concentration of HSA in serum, the adsorption and desorption procedures that were previously established must be reevaluated.

The initial experiments involved BSA solution of 40 mg/ml and a LA solution of 2 μl LA per 10 ml buffer (hereafter referred to as x μl/10 ml for conciseness). The investigation focused on the adsorption of BSA onto the CB column and the desorption through LA solution, following cycles of solution purging through the CB column as outlined in Section 3.2.2. Essentially, the CB column was initially saturated with the BSA solution and then rinsed using the LA solution for dissociation. Phosphate buffer (PB) was employed to separate the adsorption and desorption sessions, as well as to rinse off any unbound BSA. The rinse eluent was collected and quantified using UV-Vis spectroscopy. Surprisingly, no substantial desorption/release was observed with the LA solution rinsing during these initial explorations, as indicated in Figure 3.5 (left). Any suspicion that the Uv-Vis adsorption peak might shift due to association with LA was disproven

by the adsorption spectrum of the eluent, as depicted in Figure 3.5 (right), where no significant shift in the absorbance peak was observed. Therefore, other possible explanation of this observation was put to test.

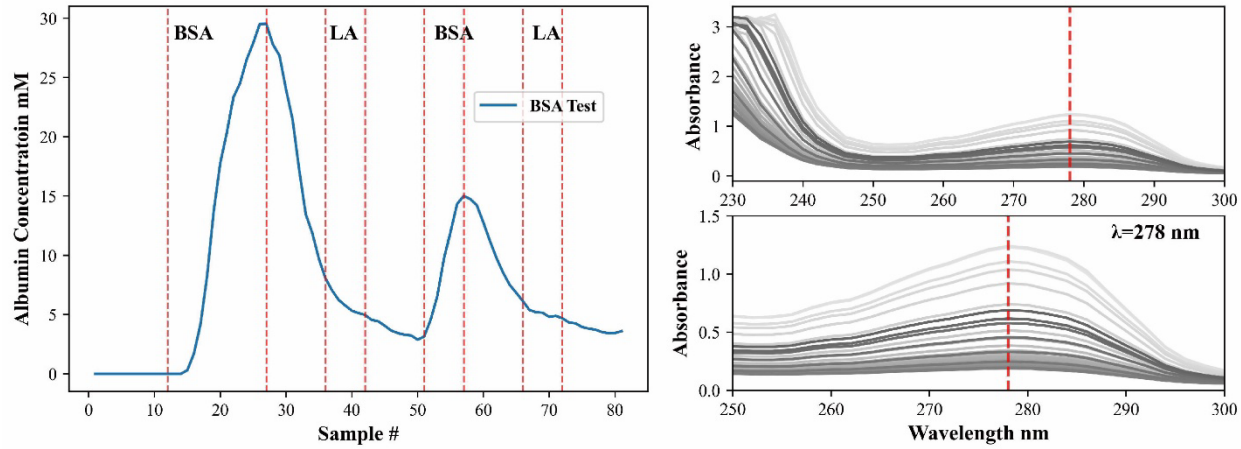

Figure 3.5. Adsorption and desorption cycles of BSA on CB column with feed solution labeled (Left) and Absorbance spectrum of eluent samples with the light-to-dark color gradient denoting sample numbers from 27 to 57 (Right).

The interaction between albumin and Cibacron blue was initially investigated using a 2M NaSCN solution to assess the strength of BSA adsorption on the CB column, as depicted in Figure 3.6. In contrast to another test using LA as the release agent, shown by the blue curve, the results of the adsorption-desorption test with NaSCN as the release agent, represented by the red curve, exhibited a distinct peak at the intended position. Subsequently, numerical analysis of the test cycle curve, tabulated in Table 3.2, unveiled the stability of albumin adsorption across all listed cycles, while the release agent NaSCN showcased a consistent ability to induce albumin desorption from the CB column over cycles. This pattern indicates that the albumin-Cibacron blue interaction is both stable and reversible, aligning with expectations.

Conversely, the blue curve representing LA release displayed a limited response to the release agent. Additionally, the albumin desorption peak from the last cycle using NaSCN was observed

to be higher than the release peak from the red curve. This observation is likely attributable to albumin accumulation from prior adsorption sessions. As the albumin-Cibacron blue interaction has demonstrated stability and reversibility, it is hypothesized that the lack of successful BSA release by LA may be attributed to the higher concentration of albumin employed, compared to the previous study. Another possible explanation for the limited response of LA release is the structural differences between BSA and HSA, which was used in the previous study.

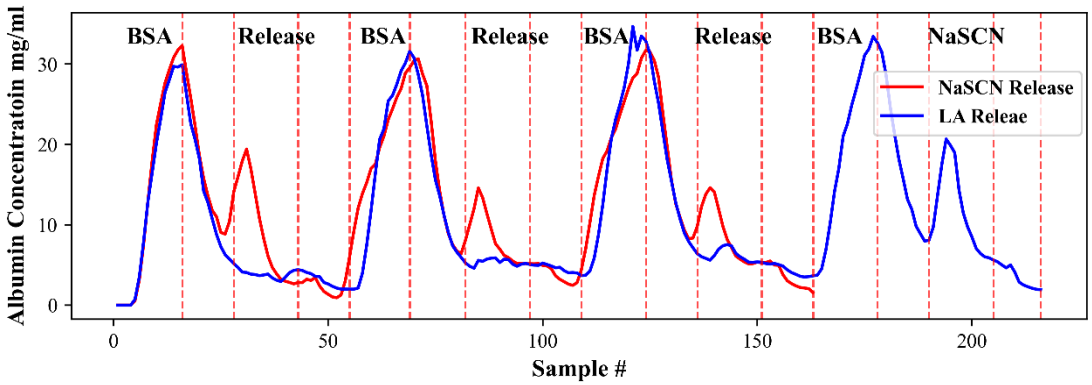

Figure 3.6. Adsorption and desorption cycles of BSA onto a Cibacron blue column using different release agents. The red curve represents test cycles with NaSCN (2M) as the release agent, while the blue curve corresponds to test cycles where LA is employed as the release agent for the initial three cycles and NaSCN is utilized as the release agent for the final cycle.

Table 3.5. Amount of albumin adsorption onto the CB column and desorption induced by buffer rinse and NaSCN as release agent.

(mg)	Cycle 1	Cycle 2	Cycle 3	Ave
BSA	47.82	47.87	46.92	47.54±0.54
PB	26.41	27.38	32.18	28.66±3.08
NaSCN	21.98	19.79	20.17	20.65±1.17
PB	3.64	6.35	6.64	5.54±1.66

To test the aforementioned hypotheses, a series of experiments were conducted using LA solutions of varying concentrations and HSA solutions with a concentration of 40 mg/ml. As depicted in Figure 3.7, these experiments were carried out with a slight operational modification.

The first adsorption-desorption cycle was executed with phosphate buffer serving as a mock release agent to reveal the actual desorption strength of the release agent.

Through a comparison between the release session with buffer and linoleic acid (LA) shown in Figure 3.7, it was evident that even a small addition of LA, as little as 2 µl/10 ml, induced the desorption of HSA from the CB column, although with a minor release effect. Increasing the LA solution concentration to 4 µl/10 ml did not exhibit significant improvements in release capability. However, when the LA solution concentration was further elevated to 6-8 µl/10 ml, a linear enhancement in HSA desorption performance was observed.

The amount of HSA released by LA was quantified by integrating the area beneath the release session curve and subtracting the baseline corresponding to the phosphate buffer rinse. This value represents the fraction of HSA that can be manipulated by the LA solution in a reversible manner. In this context, the adsorption of this fraction of HSA onto the Cibacron blue functionalized beads (CB beads) was considered reversible by LA. Subsequently, the reversible adsorption capacity of CB beads and the albumin release peak height, from Figure 3.7, were plotted against the LA solution concentration, as shown in Figure 3.8.

It is easy to deduce a linear relationship between LA solution concentration and the reversible adsorption capacity of CB beads or the release peak height after the LA solution concentration surpasses 4 µl/10 ml level. Notably, the threshold for significant HSA desorption is lower at 2 µl/10 ml, which is in alignment with the previous study. However, it was only through the increase of the LA solution concentration to 8 µl/10 ml that an HSA desorption capacity of 19.44 mg/ml beads was achieved, surpassing the value from the previous study, which stood at 15.3 mg/ml beads. This number is also in good agreement of manufacturers estimation of 18 mg/ml. The need for higher LA concentrations to achieve effective HSA release is likely a consequence of the

elevated HSA concentration used in these tests. This is because the association between HSA and CB beads becomes stronger under these conditions.

Further improving the release capability of linoleic acid by increasing its concentration is desirable. However, the LA “solution” was actually a micelle suspension acquired by ultrasonication. Such suspension of micelle is subject to stability challenges with increased concentration over long term. Furthermore, the previously used concentration of LA was physiologically equivalent. Increasing the use of LA can indeed enhance protein elution efficiency, but it also complicates the subsequent removal of LA. Therefore, considering that the demonstrated albumin desorption capability has already met the design requirements and aligns with manufacturer's specification, and further elevating the LA concentration would complicate subsequent removal steps, further exploration into increasing the LA concentration is deemed unnecessary.

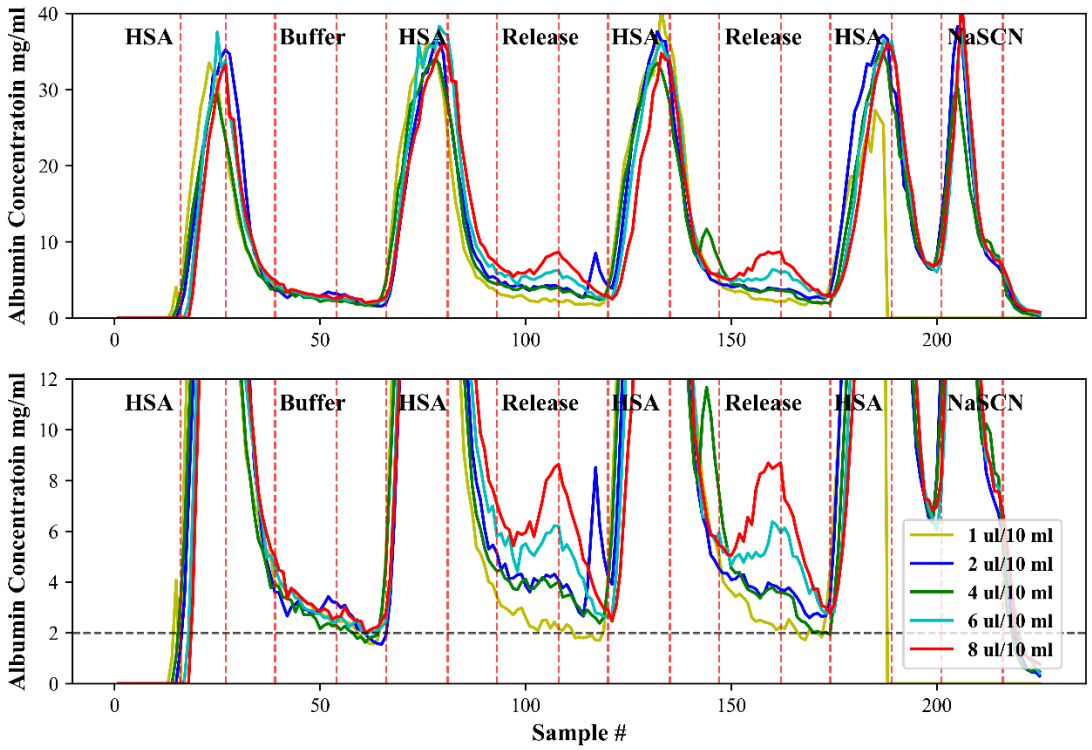

Figure 3.7. Adsorption and desorption cycles of HSA onto a Cibacron blue column using linoleic acid of different concentration.

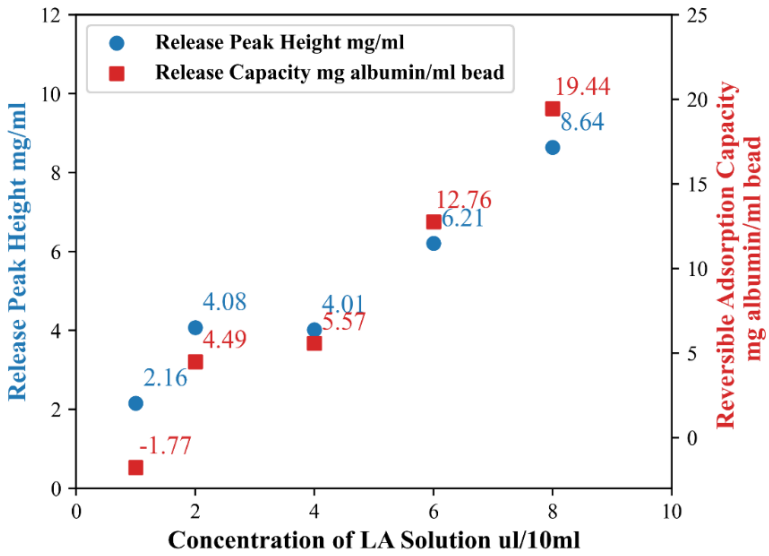

Figure 3.8. Release peak height and calculated reversible adsorption capacity versus concentration of linoleic acid solution.

Another series of experiments was devised to investigate whether differences between BSA and HSA influenced dissociation via the LA solution. As illustrated in Figure 3.9, a direct comparison of the release peak heights between the BSA curve (shown in green) and the HSA curve (in blue) reveals that the linoleic acid solution of 8 µl/10 ml is equally capable of inducing albumin dissociation from the CB column, regardless of the albumin's structure. However, there is a minor distinction in dissociation behavior that merits attention. The release peak position of BSA is observed to shift to the left when referenced against the peak position of HSA. This could suggest that BSA is more sensitive to the effects of LA.

Extending the adsorption session and desorption rinse by twice, a further test was conducted to delve deeper into the BSA-Cibacron blue interaction. The results are summarized in Figure 3.10 and are consistent with the findings shown in Figure 3.9. Indeed, BSA is more responsive to the LA solution in comparison to HSA. Upon closer examination of the curve and peak positions, it was determined that BSA adsorption reached 80% of its saturation capacity after the feed solution was introduced at a volume equal to 4.5 times the CB column volume. Additionally, the dissociation of BSA from the CB column was found to peak at volumes equivalent to 1.5 times and 2.5 times the column volume for NaSCN and LA solutions, respectively.

Given that the release peaks of BSA exhibit a bell-shaped curve, the release peak width is double the peak position volume. Consequently, the necessary volume of BSA solution for achieving 80% saturation in adsorption matches the required volume of LA solution for inducing desorption at an approximate 1:1 ratio. Consequently, in prototype demonstrations artificial plasma, employing a 1:1 ratio for adsorption-desorption session length is anticipated to prompt sufficient albumin detoxification.

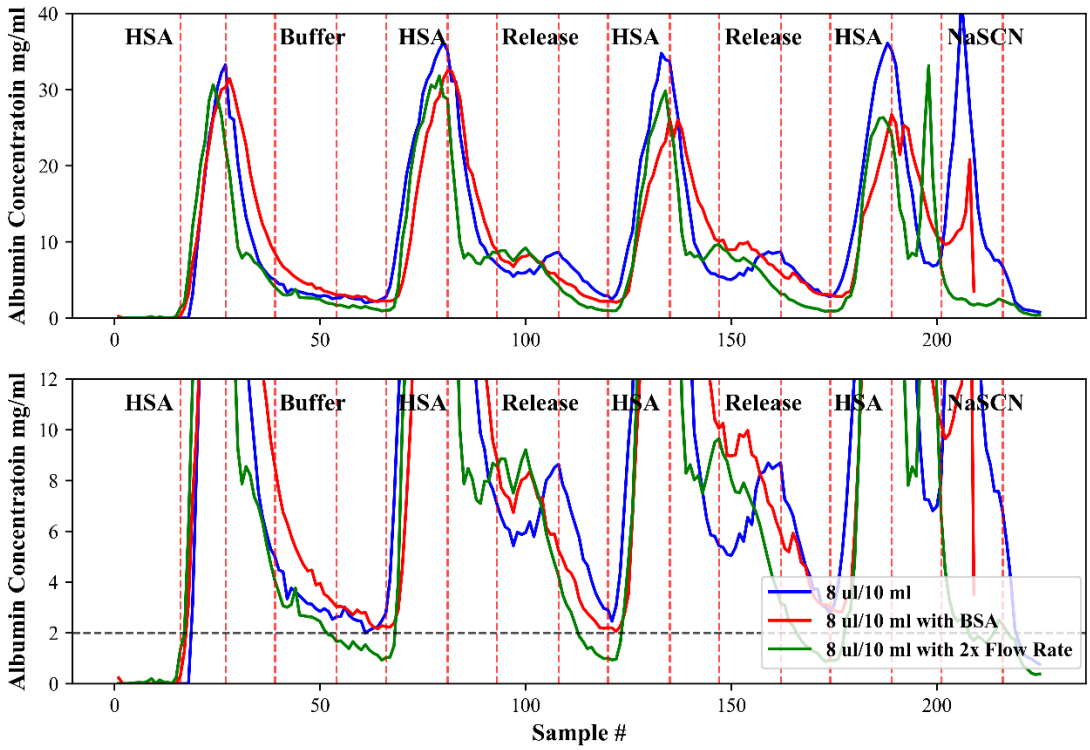

Figure 3.9. Adsorption and desorption cycles of albumin onto a Cibacron blue column under different setting of release agent rinse.

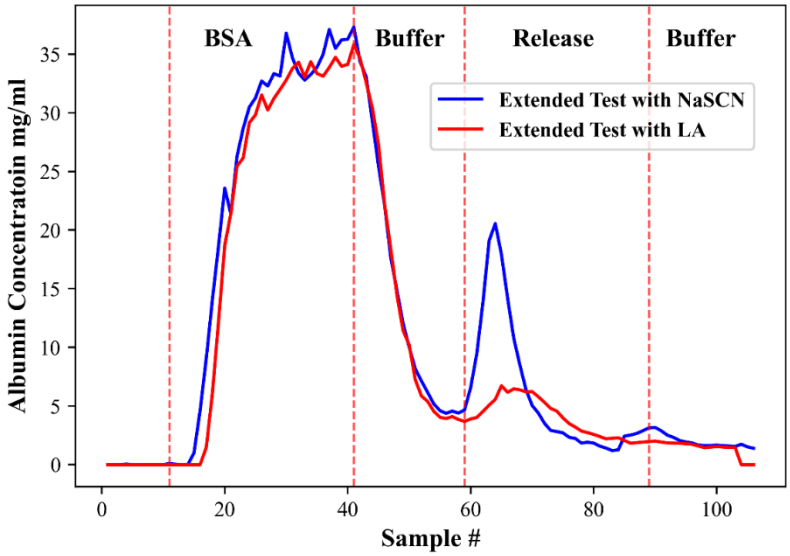

Figure 3.10. Extended adsorption and desorption cycle of BSA onto CB column with release agent of NaSCN (2M) and LA solution (8 µl/10 ml).

Another dataset presented in Figure 3.9, denoted by the green curve, represents the test outcomes obtained by doubling the flow rate during the LA desorption session while keeping other parameters constant. Referring to Figure 3.8, it can be observed that the release of albumin actually peaked at the transition point from the release agent to the buffer solution. This signifies an incomplete release of albumin, which is undesirable for prototype operation where no phosphate buffer rinse will be employed. With the consideration that further increasing the concentration of the LA solution is deemed unfeasible, a solution was proposed involving the manipulation of flow rate to introduce a larger amount of release agent per unit time.

Evidently, the increased flow rate facilitated the dissociation of albumin from the CB column, as indicated by the lower albumin concentrations in the eluent at the end of the release session compared to the results of the normal flow rate. Even the buffer rinse with the increased flow rate was more effective in mechanically washing off albumin. Notably, the position of the albumin release peak was also found to shift to the left due to the heightened flow rate. Therefore, the challenge of incomplete albumin dissociation from the CB column can be addressed by raising the flow rate, ensuring the effectiveness of the intended 1:1 adsorption-desorption cycle for prototype operation.

3.3.3 *Design of Cibacron Blue Functionalized Column*

The adsorption parameter, or albumin processing capability, of the Cibacron blue functionalized column was determined to be 19.44 mg albumin/ml beads with an 8 µl/10 ml LA solution. For simplicity in calculation and conservativeness in estimation, an albumin processing capability of 18 mg albumin/ml beads was used for the design of the Cibacron blue column. Since the albumin concentration in blood is 40 mg/ml, it was estimated that approximately 2.2 ml of

Cibacron blue functionalized beads is capable of completely removing albumin from 1 ml of plasma.

With this 2.2 ml CB beads/ml of plasma ratio in mind, the required amount of dry CB beads was calculated and plotted in Figure 3.11 against the plasma flow rate. The turnover rate, which is twice the adsorption session time, was also considered by factoring in the influence of the adsorption session time in the figure. As shown in Figure 3.11, the volume of CB beads required for a plasma flow rate of 40 ml/min ranges from 44.4 ml to 133.3 ml, depending on the binding session time, which varies from 0.5 min to 1.5 min. It is easy to understand that with a shorter adsorption session time, less albumin will be fed to the CB column, resulting in a lower requirement for CB beads. This is desirable, especially considering that the cost of Blue Sepharose 6 Fast Flow is approximately $10 per ml.

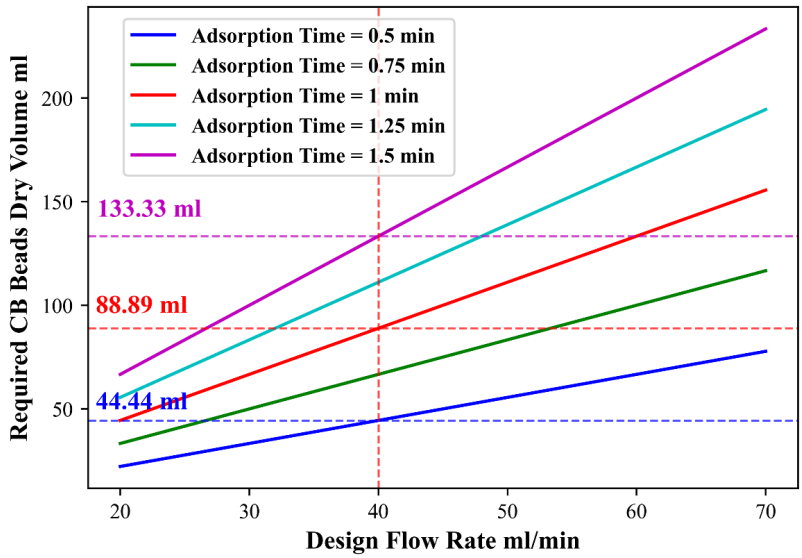

Figure 3.11. Required CB beads dry volume to accommodate various flow rate and adsorption session time.

However, engineering design involves more than just the cost of a single component. A hexagonal close packing factor of 0.74 was used to estimate the void space volume of a densely

packed CB column. This factor indicates that approximately 26% of the total column volume, excluding the CB beads, is the gap or void volume between densely packed beads, regardless of the column size. This represents the fraction of a CB column that will be occupied by plasma during operation. The dead volume of the column, tubes, and connectors is another important consideration for the turnover rate. To simplify the estimation, all the tubes and connectors were approximated as a 40 cm long tube with a diameter of 5.1 mm, which is commonly used in hemodialysis, resulting in a volume of approximately 8.1 ml.

By comparing the estimated total dead volume with the flow volume (set flow rate of 40 ml/min multiplied by adsorption session time), it was determined that adsorption session times shorter than 1 minute would result in incomplete rinsing, as suggested in Table 3.3. Therefore, the minimum volume required for the prototype design is 88.9 ml, rather than 44.4 ml.

Table 3.6. Comparison between estimated total bead volume and flow volume of set time.

	Adsorption Time min				
	0.5	0.75	1	1.25	1.5
Dry Beads Volume ml	44.44	66.67	88.89	111.11	133.33
Column Void Volume ml	15.62	23.42	31.23	39.04	46.85
Total Dead Volume ml	23.72	31.52	39.33	47.14	54.95
Volume Flow of Set Time ml	20.00	30.00	40.00	50.00	60.00

3.3.4 *Linoleic Acid Filter*

Linoleic acid is inherently insoluble in water. The previously mentioned linoleic acid solution was, in fact, a suspension of LA micelles. The increased concentration of LA (8 µl/10 ml), in contrast to the previous study that used physiological concentrations (1.8 µl/10 ml), necessitates its removal. Given that the size of LA micelles far exceeds 100 nm level, the hollow fiber membranes, specifically PlasmaPhan and MicroPES, with pore sizes not exceeding 500 nm, should be capable of capturing a substantial portion of LA micelles. [31]

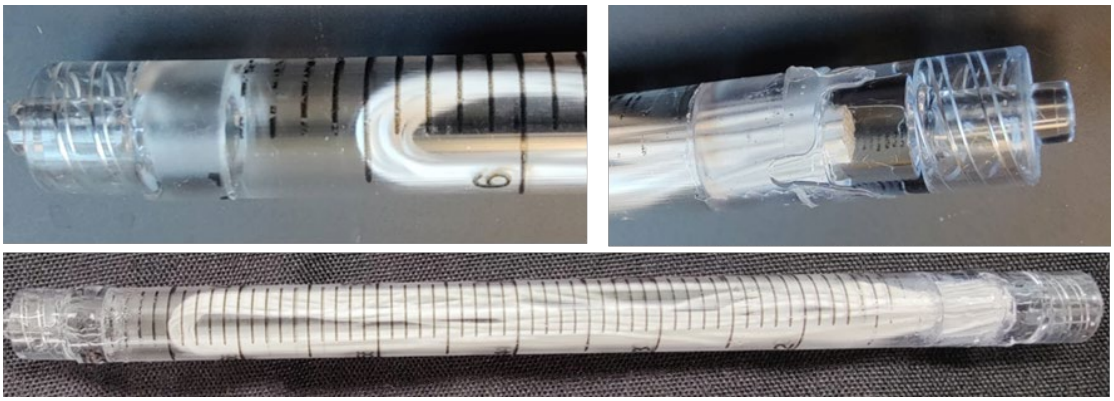

Figure 3.12. Picture of dead-end linoleic acid filter with zoom-in demonstration pictures of the filter cartridge openings.

Through multiple experiments using a dead-end filter configuration, as depicted in Figure 3.12, it was determined that 15 strands of PlasmaPhan (and MicroPES) hollow fiber membrane could filter 30 ml of an 8 µl/10 ml LA solution before becoming completely obstructed. This translates roughly to a LA removal capability of 2 ml of LA solution per hollow fiber. Therefore, considering the designed prototype operation of a 4-hour session, during which half of the time is allocated for LA desorption, the volume of LA solution to be processed would be 4800 ml, and the required amount of hollow fiber membrane would be 2400, unless the LA filter can be regenerated during operation. While industrial production of hollow fiber cartridges easily incorporates thousands of hollow fibers, creating a filter cartridge with high fiber count presents challenges in laboratory settings. Consequently, the potential for regenerating the LA filter was explored.

The intentionally blocked LA filter was found to impede the flow of liquid in any direction. However, when the flow was reversed (opposite to the filtration direction), it loosens the blockage to some extent. At this point, the addition of alcohols, IPA and ethanol, has been discovered to effectively alleviate the obstruction. And the reversed flow was observed to wash out fiber-shaped precipitates. Under this circumstance, the blockage was attributed to the accumulation of such

precipitates. The precipitate was hypothesized to be the result of linoleic acid oxidation in ambient air, although this has not been confirmed through characterization. [32, 33]

To allow easier access to remove the LA precipitate, the design of the blood fractionation filter was adopted as the linoleic acid (LA) filter. Illustrated in Figure 3.2, the filter enables cross-membrane flow when one end (outlet) of the filter cartridge is closed and allows axial flow when both ends of the filter cartridge are open. This mechanism facilitates LA precipitate removal by the axial flow.

More fiber-shaped precipitate was observed during axial rinsing of ethanol-water in sequence through the hollow fibers. Interestingly, this resulted in the relief of blockage, allowing unimpeded axial flow. However, when LA solution was subsequently filtered through the unblocked filter, it became blocked again after passing only 18 ml of LA solution, whereas the initial blockage required 30 ml of LA solution. Subsequent unblocking and LA filtering revealed an even earlier blockage at 13 ml of LA solution but stabilized for 5 unblock-block cycles. This phenomenon was hypothesized to be a consequence of liquid passing through the opened fibers while the blocked fibers remained obstructed.

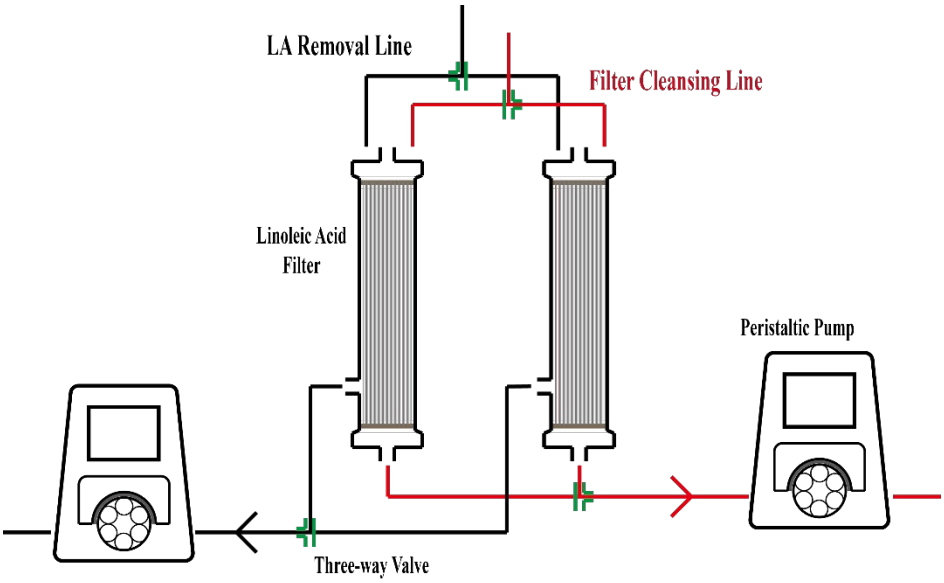

Figure 3.13. Schematic demonstration of proposed linoleic acid filter configuration for operation and inline cleansing.

For prototype device operation spanning 4 hours with regeneration every 20 minutes, each cartridge would be required to process 400 ml of linoleic acid solution, hence necessitating 462 hollow fibers of PlasmaPhan or MicroPES. To prevent the loss of filter capacity, as discussed above, it's essential not to saturate the filtering capacity. Consequently, the LA filter cartridge was designed with 600 hollow fibers. Given the need for continuous prototype operation, a parallel operation-cleansing line design was proposed, as illustrated in Figure 3.13. In this configuration, one LA filter cartridge would be in operation while the other undergoes cleansing by axial flow.

3.3.5 *Prototype Design and Test*

Taking into consideration all the components discussed above, the proposed design for the prototype device is depicted in Figure 3.14. The device features three loops distinguished by red, green, and black colors: the blood circulating loop, the dialysate loop, and the albumin detoxification loop. The red and green loops resemble conventional dialyzer devices, with the

exception of the plasma fraction membrane cartridge. The central component of the albumin detoxification prototype device is the black loop, housing the Cibacron blue column responsible for processing albumin carrying PBUTs.

The coordination between the various components of the prototype device was managed by a preprogrammed Arduino microcontroller unit (MCU), as illustrated in Figure 3.15. Solenoid pinch valves were employed to control the flow path of plasma fractionated from the blood loop, while the peristaltic pumps operated at a constant speed. Other components of the prototype device were controlled through power regulation as well.

The operation of the proposed prototype device is divided into two modes: adsorption and desorption of albumin. During the adsorption session, the two-way valve (A), shown in Figure 3.14, remains open while valve (B) is closed. Plasma is then extracted from the blood loop (red) at a rate of 40 ml/min. Albumin present in the extracted plasma is adsorbed onto the detoxification column, while its cargo, indoxyl sulfate, is dissociated. The unbound IS is subsequently dialyzed out using dialyzers.

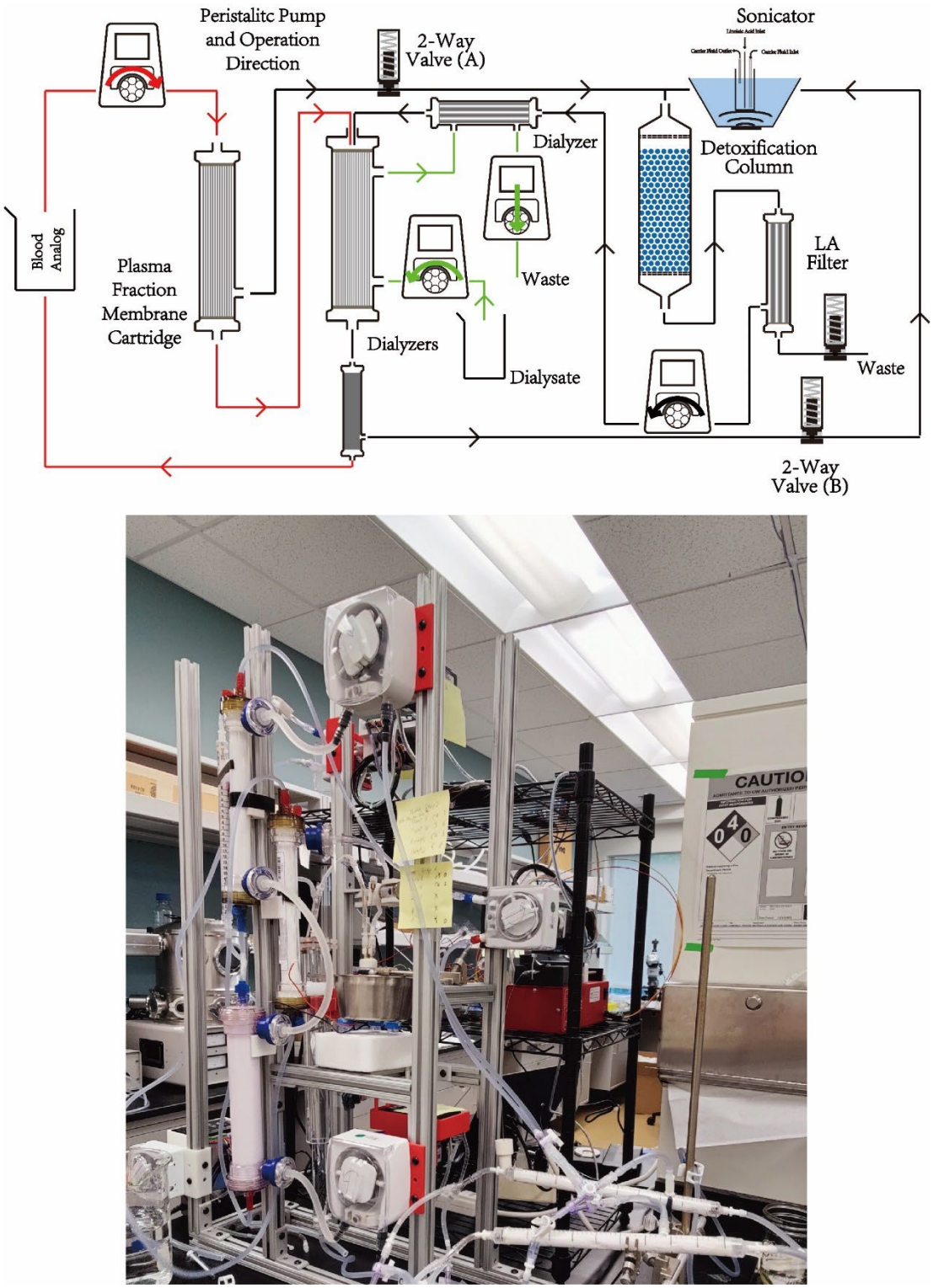

Figure 3.14. Schematic demonstration of proposed prototype design with flow direction denoted with arrows and loops distinguished by color (top) and picture of prototype built based on the design (bottom).

During the desorption session, valve (A) is closed, and valve (B) is opened. A portion of the blood flow is fractionated and extracted through a dialyzer at the same flow rate of 40 ml/min. It is important to note that dialyzers do not permit protein permeance. A protein-free carrier fluid is then employed to deliver linoleic acid to the albumin-bound detoxification column. The dissociation of the albumin-Cibacron blue column caused by the LA solution is followed by LA removal through the designed filter. At this LA filter, toxin-free albumin is allowed to transport across the membrane and is sequentially returned to the blood loop, while LA micelles are trapped.

By cycling between the adsorption and desorption cycles, both free and albumin-bound indoxyl sulfate are expected to be removed from the blood loop. A control experiment was conducted using the same setup, only without the Cibacron blue functionalized detoxification column.

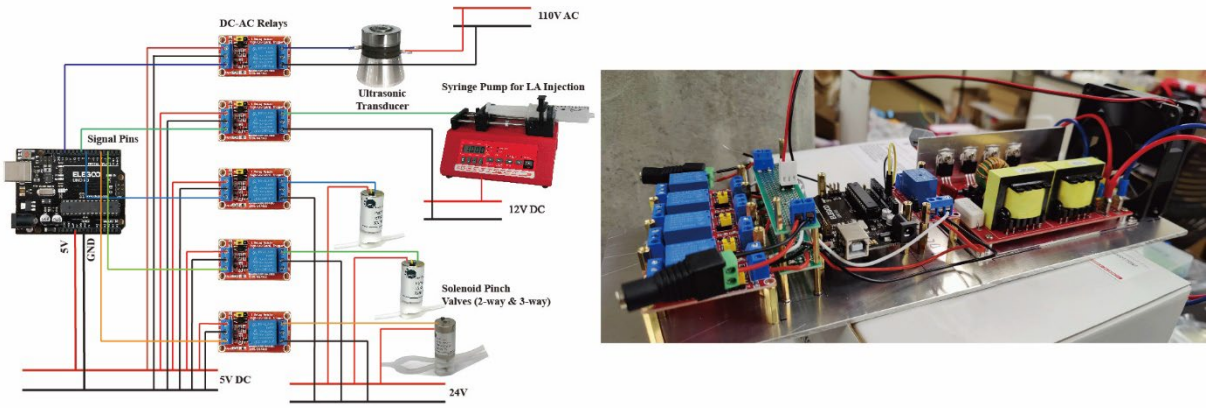

Figure 3.15. Schematic control circuit coordinated by Arduino microcontroller unit (left) and picture of control circuit built according to the design (right).

3.4 CONCLUSION

The project presented in this chapter primarily focuses on the scaling up of the previously established albumin detoxification chemistry. The aim is to develop a prototype add-on device for conventional dialysis machines, with the intention of enhancing the removal limit of PBUTs during a 4-hour dialysis session.

Through a comprehensive reevaluation of the albumin-Cibacron blue interaction under physiological conditions, it has been determined that the linoleic acid dissociation chemistry remains functional. However, its effectiveness is somewhat reduced compared to the previous study due to a strengthened association between albumin and Cibacron blue. It was observed that increasing the concentration of linoleic acid solution linearly enhances the albumin desorption capability, particularly after the threshold concentration of 4 µl/10 ml. Taking into account factors such as release capacity, micelle stability, and sequential removal, a linoleic acid solution concentration of 8 µl/10 ml was identified as the optimal release agent for promoting albumin dissociation.

Further analysis indicated that structural differences between albumin variants do not significantly influence the efficiency of the linoleic acid release chemistry. Therefore, experiments with bovine blood/plasma are considered sufficient to demonstrate the efficacy of the add-on prototype. Additionally, it was found that increasing the flow rate of the release agent positively impacts the dissociation of albumin from Cibacron blue. By incorporating all feasible improvements, it was concluded that employing a 1:1 ratio for the adsorption-desorption session should effectively enhance PBUT removal, which aligns well with the findings of the previous study.

After conducting systematic calculations and in-depth discussions on the key components of the prototype, namely the plasma fractionation membrane cartridge, the Cibacron blue functionalized column, and the linoleic acid filter, a well-rounded design for the prototype has been proposed. The operation, settings, and parameters of the prototype device have also undergone rigorous validation processes.

3.5 FUTURE OUTLOOK

The prototype device developed in this study is not limited to the removal of indoxyl sulfate alone. In fact, it is anticipated that similar protein-bound uremic toxins with aromatic-anion structures can be effectively removed through the same albumin targeting mechanism. Consequently, future research endeavors should focus on the removal of other PBUTs, including but not limited to p-cresol sulfate, hippuric acid, bilirubin, and other indole derivatives, with the expectation of fruitful outcomes. It is also imperative to explore the interplay within complex toxin systems.

The operation of such a prototype device was designed to showcase the capability of the albumin detoxification process in a proof-of-concept fashion. Therefore, future work should prioritize the optimization of the fluid system, albumin treatment kinetics, and enhancements in the control system, all of which have the potential to significantly enhance the efficacy of albumin detoxification.

3.6 REFERENCES

[1] PRC, N. H. C. o. Blood Purification Standard Operating Procedures 2021 - 血液净化标准操作规程 2021; 2021.

[2] Chang, K. Y.; Kim, S. H.; Kim, Y. O.; Jin, D. C.; Song, H. C.; Choi, E. J.; Kim, Y. L.; Kim, Y. S.; Kang, S. W.; Kim, N. H.; et al. The impact of blood flow rate during hemodialysis on all-cause mortality. Korean Journal of Internal Medicine **2016**, 31 (6), 1131-1139. DOI: 10.3904/kjim.2015.111.

[3] Duval-Sabatier, A.; Burtey, S.; Pelletier, M.; Laforet, M.; Dou, L. T. T.; Sallee, M.; Lorec, A. M.; Knidiri, H.; Darbon, F.; Berland, Y.; et al. Systematic Comparison of Uremic Toxin Removal Using Different Hemodialysis Modes: A Single-Center Crossover Prospective Observational Study. Biomedicines **2023**, 11 (2). DOI: 10.3390/biomedicines11020373.

[4] Krieter, D. H.; Kerwagen, S.; Ruth, M.; Lemke, H. D.; Wanner, C. Differences in Dialysis Efficacy Have Limited Effects on Protein-Bound Uremic Toxins Plasma Levels over Time. Toxins **2019**, 11 (1). DOI: 10.3390/toxins11010047.

[5] Meert, N.; Waterloos, M. A.; Van Landschoot, M.; Dhondt, A.; Ledebo, I.; Glorieux, G.; Goeman, J.; Van der Eycken, J.; Vanholder, R. Prospective Evaluation of the Change of Predialysis Protein-Bound Uremic Solute Concentration With Postdilution Online Hemodiafiltration. Artificial Organs **2010**, 34 (7), 580-585. DOI: 10.1111/j.1525-1594.2010.01005.x.

[6] Cuvelier, C.; Tintillier, M.; Migali, G.; Van Ende, C.; Pochet, J.-M. Albumin losses during hemodiafiltration: all dialyzers are not created equal-a case report. BMC nephrology **2019**, 20, 1-5.

[7] Krieter, D. H.; Wanner, C. Comparison of four medium cut-off dialyzers. Clinical Kidney Journal **2023**. DOI: 10.1093/ckj/sfad002.

[8] Kobashi-Margain, R. A.; Gavilanes-Espinar, J. G.; Gutierrez-Grobe, Y.; Gutierrez-Jimenez, A. A.; Chavez-Tapia, N.; Ponciano-Rodriguez, G.; Uribe, M.; Mendez Sanchez, N. Albumin dialysis with molecular adsorbent recirculating system (MARS) for the treatment of hepatic encephalopathy in liver failure. Annals of hepatology **2011**, 10 Suppl 2, S70-76, ; Review.

[9] Lee, S. L. Y.; Sirich, T. L.; Meyer, T. W. Improving Solute Clearances by Hemodialysis. Blood Purif. **2022**. DOI: 10.1159/000524512.

[10] Brettschneider, F.; Toelle, M.; von der Giet, M.; Passlick-Deetjen, J.; Steppan, S.; Peter, M.; Jankowski, V.; Krause, A.; Kuehne, S.; Zidek, W.; et al. Removal of Protein-Bound, Hydrophobic Uremic Toxins by a Combined Fractionated Plasma Separation and Adsorption Technique. Artificial Organs **2013**, 37 (4), 409-416. DOI: 10.1111/j.1525-1594.2012.01570.x.

[11] Meyer, T. W.; Lee, S.; Whitmer, L. C.; Blanco, I. J.; Suba, J. K.; Sirich, T. L. Increasing the Clearance of Protein-Bound Solutes by Recirculating Dialysate through Activated Carbon. Kidney360 **2023**, 4 (6), 744-750. DOI: 10.34067/kid.0000000000000155.

[12] Madore, F.; Lazarus, J. M.; Brady, H. R. Therapeutic plasma exchange in renal diseases. Journal of the American Society of Nephrology **1996**, 7 (3), 367-386.

[13] Rifai, K. Fractionated plasma separation and adsorption: current practice and future options. Liver international : official journal of the International Association for the Study of the Liver **2011**, 31 Suppl 3, 13-15. DOI: 10.1111/j.1478-3231.2011.02595.x.

[14] AiMin, Z.; ShaoLi, Y.; ZhiHong, W.; YiHui, R.; Bing, Z.; Hong, Z.; ShaoJie, X. Combination therapy of plasma perfusion, plasma exchange, and entecavir in patients with hepatitis B acute-on-chronic liver failure. 临床肝胆病杂志 **2012**, 28 (10), 744-747.

[15] Ipe, T. S.; Marques, M. B. Vascular access for therapeutic plasma exchange. Transfusion **2018**, 58, 580-589. DOI: 10.1111/trf.14479.

[16] Basic-Jukic, N.; Kes, P.; Glavas-Boras, S.; Brunetta, B.; Bubic-Filipi, L.; Puretic, Z. Complications of therapeutic plasma exchange: Experience with 4857 treatments. Ther. Apher. Dial. **2005**, 9 (5), 391-395. DOI: 10.1111/j.1744-9987.2005.00319.x.

[17] Akeson, S. P.; Mel, H. C. OSMOTIC HEMOLYSIS AND FRAGILITY - A NEW MODEL BASED ON MEMBRANE DISRUPTION, AND A POTENTIAL CLINICAL-TEST. Biochimica Et Biophysica Acta **1982**, 718 (2), 201-211. DOI: 10.1016/0304-4165(82)90220-3.

[18] Kohne, I. Haemolysis induced by mechanical circulatory support devices: unsolved problems. Perfusion-Uk **2020**, 35 (6), 474-483. DOI: 10.1177/0267659120931307.

[19] Sirich, T. L.; Funk, B. A.; Plummer, N. S.; Hostetter, T. H.; Meyer, T. W. Prominent Accumulation in Hemodialysis Patients of Solutes Normally Cleared by Tubular Secretion. Journal of the American Society of Nephrology **2014**, 25 (3), 615-622. DOI: 10.1681/asn.2013060597.

[20] HEMATOLOGY, A. S. O. Blood Basics. AMERICAN SOCIETY OF HEMATOLOGY, https://www.hematology.org/education/patients/blood-basics#:~:text=Blood%20is%20a%20specialized%20body,white%20blood%20cells%2C%20and%20platelets (accessed 2023.

[21] Wright, A. K.; Thompson, M. Hydrodynamic structure of bovine serum albumin determined by transient electric birefringence. Biophys. J. **1975**, 15 (2), 137-141.

[22] Tojo, A.; Kinugasa, S. Mechanisms of glomerular albumin filtration and tubular reabsorption. International journal of nephrology **2012**, 2012, 481520. DOI: 10.1155/2012/481520.

[23] 3M. Healthcare Documents - Products for New Therapies - Data Sheets. https://www.3m.com/3M/en_US/membrana-us/resources/documents/ (accessed.

[24] Nader, E.; Skinner, S.; Romana, M.; Fort, R.; Lemonne, N.; Guillot, N.; Gauthier, A.; Antoine-Jonville, S.; Renoux, C.; Hardy-Dessources, M. D.; et al. Blood Rheology: Key Parameters, Impact on Blood Flow, Role in Sickle Cell Disease and Effects of Exercise. Frontiers in Physiology **2019**, 10. DOI: 10.3389/fphys.2019.01329.

[25] Lin, C. J.; Chen, H. H.; Pan, C. F.; Chuang, C. K.; Wang, T. J.; Sun, F. J.; Wu, C. J. p-Cresylsulfate and Indoxyl Sulfate Level at Different Stages of Chronic Kidney Disease. Journal of Clinical Laboratory Analysis **2011**, 25 (3), 191-197. DOI: 10.1002/jcla.20456.

[26] 5 Human Albumin. Transfus Med Hemother **2009**, 36 (6), 399-407. PubMed.

[27] Watanabe, H.; Noguchi, T.; Miyamoto, Y.; Kadowaki, D.; Kotani, S.; Nakajima, M.; Miyamura, S.; Ishima, Y.; Otagiri, M.; Maruyama, T. Interaction between Two Sulfate-Conjugated Uremic Toxins, p-Cresyl Sulfate and Indoxyl Sulfate, during Binding with Human Serum Albumin. Drug Metabolism and Disposition **2012**, 40 (7), 1423-1428. DOI: 10.1124/dmd.112.045617.

[28] Rueth, M.; Lemke, H. D.; Preisinger, C.; Krieter, D.; Theelen, W.; Gajjala, P.; Devine, E.; Zidek, W.; Jankowski, J.; Jankowski, V. Guanidinylations of albumin decreased binding capacity of hydrophobic metabolites. Acta Physiologica **2015**, 215 (1), 13-23. DOI: 10.1111/apha.12518.

[29] Vanholder, R. C.; Uremic Toxin Mapping, P. Review on uremic toxins: Classification, concentration and interindividual variability. Journal of the American Society of Nephrology **2002**, 13, 521A-521A.

[30] Meijers, B. K. I.; De Loor, H.; Bammens, B.; Verbeke, K.; Vanrenterghem, Y.; Evenepoel, P. p-Cresyl Sulfate and Indoxyl Sulfate in Hemodialysis Patients. Clinical Journal of the American Society of Nephrology **2009**, 4 (12), 1932-1938, Article. DOI: 10.2215/cjn.02940509.

[31] Degrand, L.; Garcia, R.; Urion, K. C.; Guiga, W. Dynamic light scattering for the determination of linoleic acid critical micelle concentration. Effect of pH, ionic strength, and ethanol. Journal of Molecular Liquids **2023**, 388. DOI: 10.1016/j.molliq.2023.122670.

[32] Pryor, W. A.; Kaufman, M. J.; Church, D. F. AUTOXIDATION OF MICELLE-SOLUBILIZED LINOLEIC-ACID - RELATIVE INHIBITORY EFFICIENCIES OF ASCORBATE AND ASCORBYL PALMITATE. J. Org. Chem. **1985**, 50 (2), 281-283. DOI: 10.1021/jo00202a028.

[33] Ponginebbi, L.; Nawar, W. W.; Chinachoti, P. Oxidation of linoleic acid in emulsions: Effect of substrate, emulsifier, and sugar concentration. J. Am. Oil Chem. Soc. **1999**, 76 (1), 131-138. DOI: 10.1007/s11746-999-0059-6.

Chapter 4. SILICA XEROGEL WITH CROWN ETHER DECORATION FOR REVERSIBLE POTASSIUM ADSORPTION

4.1 INTRODUCTION

Patients with renal disease suffer from loss, partially to completely, of kidney function, which includes the ability to maintain electrolyte balance, as the disease progresses to later stages. Normally, two general mechanism is responsible for potassium homeostasis, hormonal regulation of intracellular and extracellular potassium level and potassium excretion though renal system. [1, 2] While healthy kidney is capable of handling 90% of potassium excretion, diseased kidney with lowered glomerular filtration rate (GFR), which is associated with defective glomerulus, does not handle the secretion of potassium as needed, which often leads to a higher chance of hyperkalemia. [3-5] Such break of potassium homeostasis was known to cause serious adverse effects on the patient. For instance, one of the outcomes of hyperkalemia is cardiac arrhythmia or cardiac arrest in more severe cases, which are responsible for approximately 30% or higher of death of patients on hemodialysis. [6-10] Therefore, it's of critical importance to carefully monitor patients' serum potassium level and contain the progression of hyperkalemia.

Current measurement for hyperkalemia prevention, control and management starts with patient education and dietary restriction. Limiting ingestion of potassium, at the source, relieves the patients from excretion bourdons with impaired kidney function. Such dietary restriction was commonly recommended because evidence suggests the restriction of potassium intake improves patients' overall mortality rate. However, evidence for slowing the progression of kidney disease is lacking. [2, 11, 12] Additionally, strictly following such restriction poses long-term challenge to patients and might be disrupted by unforeseeable intake of potassium. Acute, short-term,

hyperkalemia can be quickly and effectively treated by administrating calcium gluconate, sodium bicarbonate, insulin, b-agonists, etc. to the patient individually or in combination as needed. [13-15] But treatment of chronic hyperkalemia, which is often associated with chronic kidney disease (CKD), are not so promising compared to treatment for short-term symptoms.

4.1.1 *Treatment for Chronic Kidney Diseases Associated Chronic Hyperkalemia*

It is not controversial that, currently, dialysis remains the definitive solution for the control of body fluids and components. For the purposes of managing serum potassium level, dialysis is capable of removal of the needed amount of potassium from the patients' body within a 4-hours normal dialysis session. Thus, for both acute and chronic hyperkalemia, dialysis is recommended especially when the patient is in more dire situation. However, due to the nature of only about 2% of potassium resides extracellularly, a post-dialysis serum potassium level rebound is more likely to happen. [13, 14, 16, 17] And such fluctuations of serum potassium level are associated with risk for adverse effect on patients' long-term survival. [7, 8, 18] To lower the magnitude of such fluctuations, potassium management strategy turned to focus on continuity/consistency and potassium binders were introduced.

Sodium Polystyrene Sulfonate (SPS), also known as Kayexalate, is a polymer-based potassium binder introduced in 1950s. It has the longest history of clinical use and great controversial for its efficacy. [14, 19] SPS is normally orally or rectally administrated into the gastrointestinal (GI) tract to reduce the potassium intake and promote elimination of potassium in feces. This is achieved through a cation exchange mechanism without selectivity. Potassium along with calcium and magnesium was absorbed in exchange for sodium and/or ammonium. Studies suggests that the serum potassium level can be lowered by up to about 1 mmol/L by SPS in a dosage dependent fashion. [20-24] And oral administration was found more effective compared to

rectal administration. While such potassium lowering effects may appears promising, there are adverse effects associated with use of SPS. The most pronounced adverse effect associated with SPS is disturbance of GI tract causing obstruction, disease, and, in worst cases, colonic necrosis, which is fatal if not promptly treated. [13, 14, 19, 25, 26] Another potential adverse effect of SPS is electrolyte disorder. This was believed to be caused by the non-selective adsorption of cations. Thus, calcium and magnesium may be depleted by SPS while extra sodium introduced, potentially causing hypocalcemia, hypomagnesemia and hypersomnia. [26-28] The dosage required, 15-60 g daily, for SPS also burdens the patient greatly especially through rectal administration. Considering its efficacy and associated serious adverse effects, nowadays' studies and researchers advocate for use and development of potassium binder options other than SPS.

Patiromer was introduced as an alternative to SPS. Similar to SPS, Patiromer is polymer potassium binder functions mostly in colon through exchange of potassium for calcium without selectivity. As all adsorbed cations will be excreted through feces, similar side effects of depletion of cations other than potassium are expected. [17, 27, 29] Patiromer is also associated with adverse effects on the GI tract, but the incidence of these effects is relatively low, ranging from 10% to 30%. Moreover, these GI issues, such as constipation and diarrhea, are generally milder in severity compared to the adverse effects caused by SPS, i.e., colonic necrosis. [29-32] Such enhancements achieved in managing adverse effects was made possible by improving the stability of the binder polymer resin. It was reported that Patiromer has better swelling performance and are not adsorbable under physiological conditions within GI tract. [33] Also, since the calcium cation was utilized instead of sodium cation, which was used by SPS, the cation exchange is more efficient mass-wise. In vitro potassium binding capacity of Patiromer was found to be about 8.5 mmol/g under physiological condition. This value is considerable better than the performance of SPS at

about 5 mmol/g. [33] Clinical studies have demonstrated the effectiveness of Patiromer in managing hyperkalemia and maintaining patients' serum potassium levels. The serum potassium lowering effect are positively correlated with Patiromer dosage. With a daily dosage of approximately 17 grams, the serum potassium level decreased by about 1 mmol/L. Moreover, through long-extension studies spanning over 52 weeks, Patiromer was shown to effectively suppress the progression of hyperkalemia. [30-32] The time required for this new potassium binder to take action is within hours range. Therefore, there is also potential for Patiromer to be used in combination with other medications for fast serum control. [14, 29]

Figure 4.1. Schematic demonstration of cation stabilized in Sodium Zirconium Cyclosilicate adapted from Wikipedia with permission. [34] Copyright 2014, Wikipedia.

Even though the aforementioned potassium binders, namely SPS and Patiromer, show impressive improvements and efforts have been made for hyperkalemia treatment, one fundamental defect of these binders remains untouched: selectivity. Therefore, ***Sodium Zirconium Cyclosilicate*** **(SZC)** was purposed as a better replacement. Superior selectivity towards potassium of SZC arise from its microporous structure (of 3 Å) which matches the size of dehydrated potassium ions (of 2.98 Å). [35, 36] Cations were believed to experience a dehydration process with associated energy penalty before entering the micropore of SZC. Such dehydration energy penalty was then compensated by stabilizing the cation, which has entered the micropores, through

interaction with the adjacent oxygen of SZC cavity. [35] As shown in Figure 4.1 Other cations such as sodium, calcium, and magnesium, does not benefit as much from such interactions expect ammonium. Therefore, only potassium and ammonium are effectively removed by SZC. In vitro study indicates that SZC shows improved potassium adsorption capacity at 2.8 mmol/g while having 25x selectivity over calcium making rare observations of unintended depletion of other cations. [35, 37-40] Studies conducted over long term, up to 1 year, demonstrated the efficacy of SZC in managing hyperkalemia in a dosage dependent fashion, with most patients maintaining normokalaemia without severe adverse effects. [14, 37, 39-41] However, since the binder administration does not differ from the others, orally, GI tract disorder are still observed. SZC shows great potential as a hyperkalemia management method, given its demonstrated efficacy in serum potassium level management and mild adverse effects, despite having lower in vitro potassium binding capacity compared to Patiromer.

In clinical trials and studies, the three aforementioned potassium binders share a common attribute: the mechanism responsible for potassium binding, known as cation exchange. Among them, Patiromer stands out due to its significant lead in terms of potassium exchange/adsorption capacity. However, when considering other performance aspects, SZC appears to have a slight edge, showcasing better selectivity and safety performance.

Conclusively determining the best potassium binder among these options is challenging. But it is evident that future explorations and studies for new potassium binding materials are necessary.

4.1.2 *Porous Absorbents*

In light of exploration for new potassium binding materials, existing porous materials, for instance, zeolite, metal-organic frameworks (MOF), and silica gel, must be reviewed first.

Zeolites is a crystalline material with a variety of structure often used as specialized absorbent and/or catalyst. There are 255 registered types of unique zeolite framework structure with assigned code name from International Zeolite Association (IZA) Structure Commission. [42] Unique framework of zeolite is associated with unique structures properties such as pore or cavity shape and size. Aside from its composition, the stability of zeolite is also influenced by its framework structure. The general composition of zeolite follows the formula of $M_{x/n}^{n+}[Al_xSi_{1-x}O_2]\cdot yH_2O$, where M denotes different cations and x normally range from 0-0.5. [43, 44] The building unit of TO_4 tetrahedral, where T can be Al and Si, coordinates together through shared oxygen atoms to form complex zeolite structure. [43, 45, 46] As Al and Si has different valance structure, the corresponding TO_4 units was believed to introduce localized negative charge to the zeolite framework which is normally compensated by insertion of cations. Such cations may be exchanged with cations from environment. Therefore, the composition of zeolite, especially natural zeolite, is not fixed. Based on ions exchange mechanisms, zeolite-based materials were widely used as ion exchanger. For instance, natural zeolite clinoptilolite are commonly used as an ion exchanger in varies field such as agronomy, wastewater treatment, medical, etc. [47-51] Through the strategic manipulation of zeolite composition and the optimization of the synthesis pathway, it becomes feasible to fine tuning its microstructural attributes, such as the size and shape of pores and cavities, as well as the density of charges within the zeolite. [52-57] This precise modulation capability consequently produced higher surface area zeolite materials exhibiting heightened size-based selectivity for specialized absorbent application.

Metal-Organic Frameworks (MOFs) is a distinct class of porous materials characterized by precisely defined pore architectures, boasting an exceptionally elevated surface area range in 1000-10000 m^2/g while, in contrast, conventional materials like zeolites exhibit a surface area at 100

m^2/g level. [58, 59] The optimization of absorbent application, concerning the tradeoff between efficiency and selectivity of MOFs, is managed by engineering the organic linker geometry and the metal cation coordinate centers. The linker size, shape and flexibility determine the pore size and structure. In general, longer the linker molecule bigger the pore size (porosity) and flexible linker allow easier intercalation of guest molecule. [58, 60-62] metal-based coordinate centers, on the other hand determines the coordination and arrangement of surrounding linker ligand. Together, size-selectivity of guest molecules/ions by MOFs was demonstrated. Selective adsorption and storage of desired gas molecules is a major application for MOF-based materials. [60, 63-65] And since gas molecules are known to have small size and high physical activity, such adsorption was only made possible by the high porosity (surface area) and angstrom level precision pore size manipulation of MOFs. Similarly, selective adsorption of ions can be achieved through manipulation of MOF structures as well. Studies have shown that MOF-base materials are capable of distinguishing ions by charge and size allowing applications like water desalination, wastewater treatment, mineral exaction, etc. [66-68] Further, MOF recognition of large molecules, such as aromatic compounds, was also demonstrated through managing the linker guest interaction and MOF structure. [69, 70] In short, because of the complex interplay between effect of organic linker molecules and metal coordinate centers, MOFs exhibit a wide range of microstructures and porosities, making them promising materials for selective absorbent.

Silica gel (SG) or ***silica xerogel (SXG)*** is another category of well-studied porous material. When compared to the previously mentioned materials, zeolites and MOFs, silica-based materials made through the sol-gel process are simple in composition—consisting solely of SiO_2. However, this compositional simplicity does not necessarily translate to simplicity in microstructure, as it is influenced by multiple factors including precursors, catalysts, solvents, gelation conditions,

drying, and more. [71-73] The sol-gel process can be generalized into two steps, hydrolysis and polycondensation of precursors. In solution, sols, the precursor, normally silicon alkoxide, such as tetramethyl orthosilicate (TMOS) and tetraethyl orthosilicate (TEOS), are dispersed and hydrolyzed to form intermediate with hydroxyl group as shown in reaction for hydrolysis. And, simultaneously, such intermediates interact in condensation reaction, simplified as following reaction of condensation, forming polymerized molecules.

$$Si(OR)_4 + n\,H2O \rightarrow Si(OR)_{4-n}(OH)_n + n\,ROH \qquad \text{Hydrolysis}$$

$$2\,(OR)_xSiOH \;\rightarrow\; (OR)_xSiOSi(OR)_{x'} + H_2O \text{ or } ROH \qquad \text{Condensation}$$

With time, the polymerized molecules in the sol gradually develop into a highly crosslinked 3-D network, the gel. It was believed that the nature of the catalyst, whether acidic or basic, influences the natures of gel network structure during this process. The acidic catalyst induces protonation of the alkoxide oxygen atom forming a Si-OHR structure. This is followed by a slow, rate-limiting nucleophilic attack by water molecules at the silicon atom. And condensation under acidic environment preferentially happens at the end silanol resulting in linear molecule. [71, 72, 74-76] Base catalyzed hydrolysis and condensation reaction starts with nucleophilic attack of hydroxide ion on precursor silicon atom. In the condensation step, this yields water and a siloxide ion, which then attacks another silanol's silicon atom, forming a siloxane linkage while regenerating a hydroxide ion. [71, 72, 75, 76] Base catalyzed polycondensation are faster compared acid catalyzed reaction. Therefore, product of base catalyzed sol-gel process is highly branched polymer with coarser structure but higher surface area. [71, 73] Aging of the gel is the process where localized residue reactant continues to react with gel network further strengthening the network. Such strengthening process is desirable to maintain the microstructure during drying. Dyring the gel of solvent from the porous gel network opens the network, allowing inclusion of guest molecule

or ions. However, the solvent residing in the micropores exerts significant capillary forces upon leaving the pores, causing the microstructure of the silica gel to collapse and shrink in volume during drying. The product yield from such uncontrolled drying is called xerogel which has surface up to 100-1000 m^2/g level and pores of 10 nm level size. [71, 73, 77] The combination of high surface area and large accessible pores makes xerogels efficient absorbents. Nonetheless, since the composition of SG or SXG is solely SiO2, pristine silica-based absorbents lack selectivity for delicate chemical separations. As a result, researchers have integrated silica gel with various selective chemistries for dedicated applications.

In summary, zeolites, MOFs, and silica gel each possess distinct attributes that cater to different absorption and selectivity needs. Zeolites offer flexibility through precise composition modulation, MOFs exhibit complex microstructures for targeted absorption, and silica gel provides a straightforward yet efficient porous structure. However, upon carefully examining criteria required for the application of potassium management, these materials still have hidden risks to be managed or may not be completely competent. Indeed, zeolites exhibit desirable potassium adsorption capacity. But the corresponding ion exchange mechanism poses potential risk to the application because the released cation, sodium or aluminum, also burdens the patients' electrolyte homeostasis. Also, naturally occurring zeolite does not have fixed composition, which translates into regulatory risk. Medical application of synthesized zeolite in contact with body fluid is still in exploratory stage. MOFs are more versatile in microstructure and compositions. The drawback for its' application in potassium management is lack in stability. Complex physiological condition challenges such delicate materials for long-term applications. Additionally, the synthesis of MOFs is costly compared to the other materials discussed. Lastly, silica gel-based absorbent does not have disadvantages as zeolites and MOFs do. Yet, lack in selectivity is the Achilles' heel of silica

gels. Even with surface area up to hundreds of square meters per gram, adsorption of cation solely with electrostatic interaction leads to inadequate adsorption capacity. Moreover, all of aforementioned materials lack regeneration ability. For application in potassium binder as a supplementation to regular dialysis, regeneration ability is key to manageable per-session cost and ensuring continuous operation. In this case, a chemistry that selectively facilitates the reversible capture of potassium ions seems to be a suitable complement to these porous materials. Considering the combined factors of synthetic complexity, cost considerations, and material stability, silica gels were deemed as suitable platform for the development of selective adsorbents aimed at potassium management. As a result, forthcoming discussions pertaining to surface chemistry and functionalization will center around silica-gel based materials.

4.1.3 *Selective Chemistry & Functionalization of Porous Silica Gels*

As mentioned above, porous silica gels are highly capable in adsorption with high surface area. And modification of functional group with high selectivity is undoubtedly an advantageous complement to SG materials. Review of cation selective chemistry must start with appreciation of magnificent Na, K-ATPase designed by nature. This ion pump protein is regulated by ATPs tuning between affinity towards Na^+ or K^+ for pumping extracellular or intracellular. [78-80] And the recognition of different ions for different pumping direction is the pedestal of its function. In attempts to mimic the recognition of cations done by nature, cyclic polyether, crown ether (CE), is one of the most promising candidates. CE is capable of recognizing cations based on size and reversibly stabilize the cation within its cavity through electrostatic interactions like SZC mentioned before. Such selectivity and reversibility are essential for emulating the function cycles of Na,K ATPases by synthetic materials.

Crown ethers got its name from crown-shaped molecule structure made of ethylene oxide repeating units. It was known to form stable complex with cation that matches their cavity size as early as 1967. [81] Then, extensive study regarding on the cation affinity of crown ether provided in depth knowledge size-based cation selectivity in different media. [82, 83] It was demonstrated that among various monovalent cations, 18-crown-6 ether (18C6E) possesses a cavity size that best complements the potassium ion. And slightest mismatch in cavity-cation size can cause day and night difference in complex stability. For instance, ammonium ion is of similar size of potassium ion. But their complex stability differs by almost 10-fold. [82, 84] Aside from simple size exclusion induced selectivity, cation recognition by CE is also associated with dehydration energy penalty upon hydrated cation entering the CE cavity, which further explains the selectivity of K+ over Na+ of 18C6E. [85, 86] Because of distinguished selectivity difference of crown ethers among different cations, various delicate applications was made possible. For example, polymer membranes doped with CE shows high efficiency in sieving K^+. [87] For sensor application, graphene oxide was functionalized with 18C6E for detection of potassium at 10-15 M level. [88] By attaching crown ethers to different substrates such as nanopores, liquid phase membranes, and conventional wire electrodes, researchers can create materials with cation-selective properties for applications in ion sensing, separation, and electrochemical processes. [89-91] Aside from selectivity, the reversibility of cation capture is critical for regenerating the absorbent and releasing the captured ion to collection in ion extraction application. Because of that, multiple studies showcased reversible adsorption to target cation by crown ether with distinguish pH dependence. [92-95] So it is safe to conclude that reversible and size-based selective cation adsorption can be realized through functionalization of crown ether of proper size.

However, pristine crown ether with ethylene oxide units is normally hard to covalently immobilize. Therefore, silica gel encapsulation of crown ether was explored. Through manipulating the microstructure of synthesized SGs, different crown ethers were trapped in matrix, thereby showcasing discerning adsorption capability for specific cations. [92, 96, 97] But, because of limited interaction between CE and SG surface, the leaching of crown ether from matrix remains potential risk to be managed. In effort to remedy the leaching of crown ether, heterocyclic crown ether was used in place of pristine CE for better chemical activity. Aminomethyl and aza crown ethers was demonstrated to covalently bond to Merrifield resin via chlorine substitute reaction. [98, 99] Decorated resin exhibited ion adsorption capacity over 2 meq/g. Similar chlorine substitute reaction can also be employed to affix aza or aminomethyl crown ether onto chlorine-decorated silica gels, leveraging the enhanced surface area for potential advantages. [100-102] For epoxy functionalized silica gels, immobilization of heterocyclic crown ether was achieved through epoxy-ring opening reaction. [103, 104] Capillary ionic chromatography demonstrated significant retention time differences among cations of different affinity to designed CE-decorated stationary phase. [105, 106] Multitude of viable methods to incorporate crown ethers into crown ether-free silica gel materials. Additionally, it should not be overlooked that synthesizing crown ether-functionalized silica gel using precursors containing crown ethers is also a feasible approach. [95] Given the endless array of chemical modification and synthesis strategies and the constrained space, we shall refrain from further delving into further discussion of plausible CE introduction strategies.

4.2 EXPERIMENTAL

4.2.1 *Materials and Chemicals*

Solid supports, Acid washed glass beads (≤106 μm), Silica gel 60 (63-100 μm), Merrifield Resin HL (75-150 μm, 1.0 - 1.6 mmol/g active chemistry loading) are acquired from Sigma-Alderich and used as is. Zeolite absorbents, ZK-1 and ZK-2 are acquired from Tosoh Corp. Japan. Clinoptilolite powder sample (≤3 μm) from Todicamp® Products was acquired from Amazon. Chemicals, includes 1-aza-18-crown-6-ether (1a18C6E) and 18-crown-6-ether (18C6E), and solvents are acquired from Sigma-Alderich and used as is unless otherwise specified.

4.2.2 *Crown Ether Immobilization and Corresponding Synthesis*

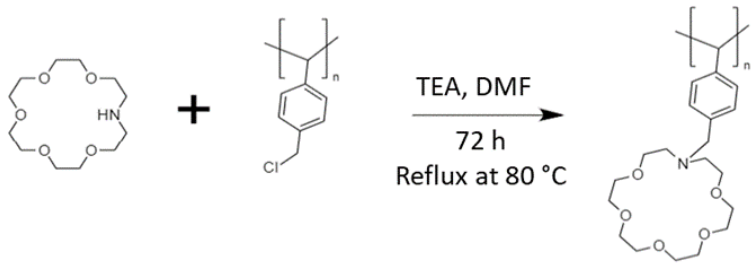

Figure 4.2. Scheme of addition reaction of 1a18C6E onto Merrifield resin.

1-aza-18-crown-6-ether (1a18C6E) on Merrifield resin immobilization was done with designed synthesis based on references from reported recipe as shown in Figure 4.2. [98, 99] Slurry of 1.5 g Merrifield Resin in 28 ml dimethylformamide (DMF) was first added in a three-neck flask. A condenser and two dropping funnels were connected to the three-neck flask for synthesis (as shown in figure 4.3). Solution of 1 ml triethylamine (TEA) in 10 ml DMF and solution of 0.0394 g of 1a18C6E in 100 ml of DMF was set in aforementioned dropping funnels. After thoroughly purging the reactor chamber with argon, the three-neck bottle was heated in oil bath to 80 °C under constant Ar flow. Then TEA solution was added to reaction followed by drop-wise addition of

1a18C6E solution. The mixture was stirred and refluxed at 80 °C for 72 hrs. After reaction, the mixture was cooled in refrigerator. The filtered solid was then washed by water, ether and methanol before drying. A yellow powder was yielded after the process.

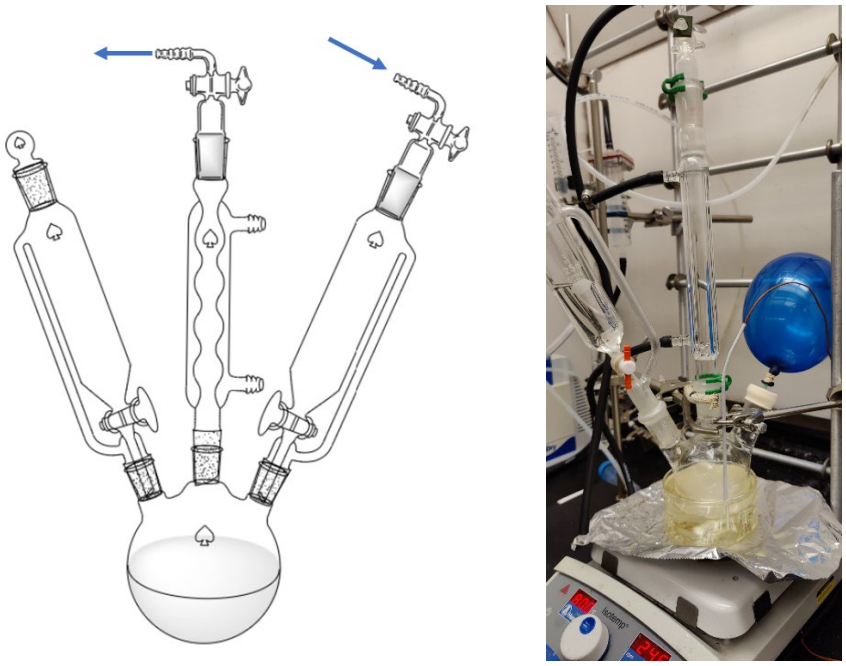

Figure 4.3. Scheme of synthesis setup with arrow indication of protective gas flow for purging (left) and experiment setup with Ar protection gas maintained by balloon (right).

For synthesis concerning silica-based materials, ***glassware passivation*** was performed to avoid reaction on glassware surface based on references from reported procedure. [107] Needed glassware was first treated piranha solution (H_2SO_4: H_2O_2 = 3:1) for 30 min then rinsed with DI water prior to treatment. Passivation solution of isobutyl-methyloxysilane (2 vol%) was prepared by mixing with ethanol (10 vol%) and 0.1 M HCl (3.3 vol%) in water and allow to stir for 1.5 hr for proper hydrolysis prior to use. The treatment was allowed for 24 hr followed by ethanol rinsing. Treated glassware was then transferred to oven for drying overnight at 110 °C.

Synthesis of silica gel with epoxy moieties was achieved through sol-gel process of 3-glycidoxypropyltrimethoxysilane (GPTMS) following reported recipe as shown in Figure 4.4. [108] GPTMS sol was prepared by mixing 15 ml of GPTMS with 6 ml of aqueous solution containing 0.272 g of NaOH. The sol was left at room temperature for 10 days till gelation happened and dried sequentially under vacuum. Yield solid was grinded into powder and rinsed with DI followed vacuum drying. The final product is a white powder.

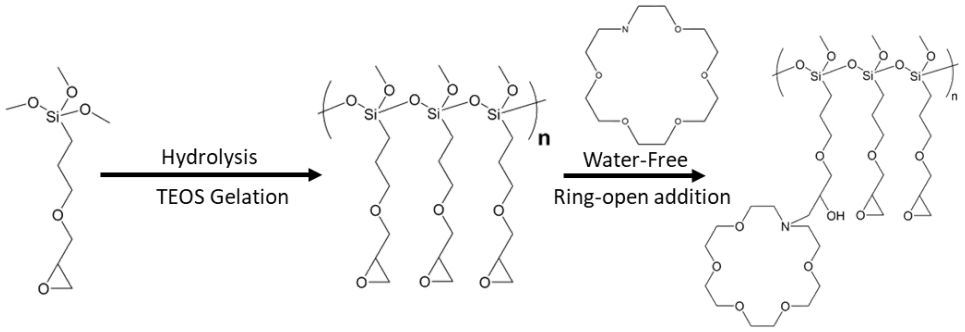

Figure 4.4. Scheme of GPTMS gelation reaction and epoxy ring-opening reaction for 1a18C6E addition.

Silica base materials, namely, ***glass beads, silica gel 60, and synthesized GPTMS gel was decorated with 1-aza-18-crown-6-ether*** through similar reaction inspired by previous studied. [100, 105, 106] For these materials expect GPTMS gel, epoxy decoration was first done by refluxing 5ml GPTMS with 5 g of selected solid material in 30 ml of dry toluene at 110 °C for 20 hr. The epoxy functionalized solid support, include GPTMS gel, was then rinsed with methanol and dried at 70 °C for 6 hr. Then, 54 mg of 1a18C6E was tethered to 1.2 g of selected solid support material in 27.6 ml of toluene-acetonitrile mixture (7/3 v/v). The mixture was refluxed at 90 °C for 18 hr. After reaction, the filter product was rinsed and dried prior to use.

4.2.3 *Crown Ether Encapsulation in Silica Gel*

CE encapsulated silica gel was synthesized with procedure and recipe adopted from previous studies with modifications. [92, 96, 97, 109] All of products yield from following process are silica xerogel because of uncontrolled drying condition. However, for the concision of discussion, the term silica gel or SG will be used.

Acid catalyzed CE silica gel was synthesized by mixing 18C6E of desired amount into solution of 2 ml water, 4 ml methanol, 1 ml of 0.5 M HCl (aq), and 4 ml of tetramethyl orthosilicate (TMOS). The mixture was stirred for mixing then let rest for extended time (over 20 days) till gelation complete. Then the acid catalyzed CE silica gel was dried under vacuum at 45 °C for two days then grinded to powder with mortar and pestle form before use.

Base catalyzed CE silica gel was synthesized by mixing 18C6E of desired amount in solution of 2.427 ml methanol, 7 ml water, 0.028 ml 30% NH_4OH (aq) with solution of 3.328 ml TMOS in 2.771 ml methanol. The mixture gelation was found to happen within few minutes. The gel was then allowed to age for 3 days followed by drying 45 °C for two days and grinding before use. Similar recipe was also used to encapsulate polyethylene glycol (PEG). Instead of 18C6E, PEG with molecular weight of 4000 g/mol was mixed into aforementioned solutions with added potassium chloride. The yield silica PEG gel was also dried and grinded to powder with mortar and pestle before use.

Other exploration for CE encapsulation was done with agar as well. 18C6E was mixed with 1% agar aqueous suspension with heat till thickened followed by cooling to form bulk agarose hydrogel. The agarose hydrogel was stored in water prior to use.

4.2.4 *Cation Adsorption Tests*

The synthesized CE loaded absorbent was tested with static adsorption and flow-through continuous adsorption test. Static adsorption test was done by mixing set amount of dry absorbent with potassium chloride solution for 10 minutes. The supernatant was collected and examined for ion concentration. For continuous adsorption test, the absorbent was first pack into chromatography column as shown in Figure 4.5. The column was made with syringe barrels and 0.2 μm filters on both sides. 20 ml of water as flown through the column before experiment. During test, 5 mM KCl (aq) was fed through the column while the eluent being collected for concentration quantification by AU680 Clinical Chemical Analyzer from Beckman Coulter.

Figure 4.5. Picture of absorbent column for continuous adsorption test.

4.3 RESULT AND DISCUSSION

As discussed previously, current studies acknowledge the importance of continuity of serum potassium management. But the most effective solution to hyperkalemia is still maintenance hemodialysis (HD) normally with three 4-hr-sessions per week. And pre- and post- session potassium level fluctuations must be carefully managed while intersession potassium control relies on dietary restriction and potassium binders. Such combination therapy indeed increased the patients' survival rate, but it is not the optimal solution. Ideally, continuous at-home dialysis treatment is the proper replacement of in-center dialysis. However, the vast amount of dialysate required for treatment, 120 L for a 4-hr HD session, is a major challenge. Therefore, dialysate regeneration was brought to consideration for conquering this issue.

Suggested daily intake of potassium is 3.4 g/day and 2.6 g/day for male and female adult while real average intake was found to be 3 g/day (male) and 2.3 g/day (female). [110] Considering 80-90% of potassium excretion were done through healthy kidney and conventional HD removes 70-100 mmol potassium per session, conservative estimation of dialysate regeneration requirement is potassium removal capacity of 50 mmol/day. [18, 111, 112] Under this estimation, for an absorbent with 0.1 mmol/g potassium adsorption capacity, 500 g of absorbent is needed. And if the absorbent is regenerable for 10 times/day, the required absorbent is then reduced to merely 50 g. This line of reasoning then led to the conclusion that an increased number of regeneration cycles per day results in reduced absorbent requirements, potentially causing expensive chemicals to become more cost-effective. Under this premises, crown ether chemistry of proper reversible and selective cation capture ability emerges as a promising candidate for the application.

4.3.1 *Crown Ether Selectivity*

Crown ethers of six ethylene oxide units, 18-crown-6-ether (18C6E) and its variant 1-aza-18-crown-6-ether (1a18C6E), has the best size-based selectivity towards potassium ions. The association constant for 1:1 complex between 18C6E and potassium and other cations are summarized in table 4.1. [81, 82] As can be seen, the selectivity of K^+ is superior compared to Na^+ and other ions. For instance, calculation of K_{K^+}/K_{Na^+} suggests the association of 18C6E with K^+ is over 10 times more stable comparing to Na^+.

Table 4.7. Association constant of cation and 18-crown-6-ether for 1:1 complex, data summarized from reference [82].

Cation	Log K
Na^+	0.80 ± 0.10
K^+	2.03 ± 0.10
NH_4^+	1.23 ± 0.06
Ca^{2+}	<0.5

However, the concentration of sodium ion and potassium ion in dialysate is vastly different. Commercially available dialysate sodium level is about 140 mM while potassium level ranges from 0-4 mM. Since serum potassium level is often higher than 5 mM for patients with hyperkalemia, the potassium level in waste dialysate is expected to be higher than its initial value especially when a smaller dialysate volume is desirable for at-home application. Similar logic is also applicable to sodium. Therefore, serum level cation concentration, 5mM for K^+ and 145 mM for Na^+, can be used to examine the efficacy of CE selectivity.

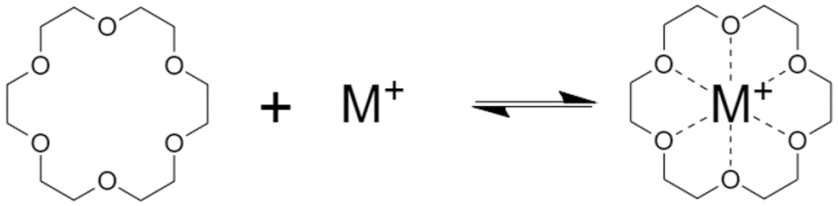

Figure 4.6. Scheme of monovalent cation stabilized in 18C6E.

For a 1:1 association reaction between CE and a monovalent cation as shown in Figure 4.6, the reaction can be described as follows,

$$[CE] + [M^+] \leftrightarrow [CE - M^+]$$

where [CE] is the concentration of available crown ether cavity, $[M^+]$ is the concentration monovalent cation and $[CE\text{-}M^+]$ is the concentration of CE-cation complex. Then the corresponding association constant can be described as follows.

$$K_{M^+} = \frac{[CE - M^+]}{[CE][M^+]}$$

In the assumed application scenario, where the adsorption capacity of absorbent CE was exhausted by Na^+ and K^+ in the spent dialysate with residue, the reaction and association constant can be described as follows,

$$[CE] + [K^+] + [Na^+] \leftrightarrow [CE - K^+] + [CE - Na^+] + [K^+]' + [Na^+]'$$

$$K_{K-Na} = \frac{[CE - K^+][CE - Na^+][K^+]'[Na^+]'}{[CE][K^+][Na^+]}$$

where $[K^+]'$ and $[Na^+]'$ is the residue concentration of potassium and sodium. Assuming the interaction kinetic between CE and cation does not change when multiple cations are in the system, the association constant description can be rearranged into following equation.

$$K_{K-Na} = K_{K^+}\frac{[CE - Na^+][K^+]'[Na^+]'}{[Na^+]} = K_{Na^+}\frac{[CE - K^+][K^+]'[Na^+]'}{[K^+]}$$

The ratio between $[CE\text{-}Na^+]/[CE\text{-}K^+]$ is an important information for the absorbent selectivity efficacy analysis as it describes the occupation of CE by sodium and potassium. Therefore, equation above was rearranged to the following form,

$$\frac{[CE - Na^+]}{[CE - K^+]} = \frac{K_{Na^+}}{K_{K^+}}\frac{[Na^+][K^+]'[Na^+]'}{[K^+][K^+]'[Na^+]'} = \frac{10^{0.8}}{10^{2.03}}\frac{145\ mM}{5\ mM} \approx 1.7$$

where the $[CE\text{-}Na^+]/[CE\text{-}K^+]$ ratio was found to be approximately 1.7. This suggests an extra 170% of absorbent in volume is needed to compensate the adsorption of sodium ion. For example, taking 0.1 mmol/g adsorption capacity with 10 regeneration cycle/day for calculation, instead of 50 g, 135 g of absorbent is needed of effective dialysate regeneration. A subtle side effect for this dialysate regeneration is that sodium and other cation was deprived as well. But replenish of cations can be easily managed by adding corresponding salt.

4.3.2 *Adsorption Performance of Covalently Immobilized CE Absorbents*

The first attempt for developing CE absorbent was through coupling of 1-aza-18-crown-6-ether (1a18C6E) to Merrifield resin. Synthesized CE functionalized resin was dried and setup for static adsorption test with 10 mg of synthesized resin and 1.8 ml of 5 mM KCl solution for 10 mins. Because of the hydrophobicity of polystyrene backbone, the mixing of synthesized absorbent into potassium solution was accomplished with aid of centrifuge mixer. Unfortunately, crown ether

functionalized Merrifield resin did not show significant adsorption of potassium. Control resin without CE chemistry also lacks in potassium adsorption capability. Inferred (IR) spectroscopy, Figure 4.7, analysis confirmed decoration of 1a18C6E by a peak a 1260 cm^{-1} which corresponds to C-O-C and C-N-C bond. However, both the functionalized and the control resin shows stronger peak of C-Cl at 700 cm^{-1}. Therefore, it was suspected that the majority of chloromethyl group on Merrifield resin was unaffected. This explains the lack of potassium uptake capacity in CE functionalized resin.

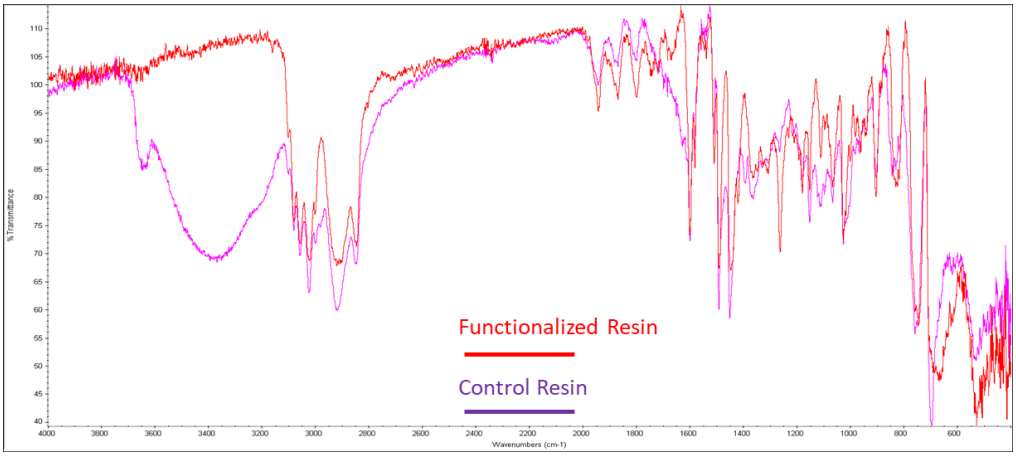

Figure 4.7. IR Spectrum of crown ether functionalized Merrifield resin and control resin without decoration.

Acid-washed glass beads was another candidate for CE decoration. Instead of chlorine substitute addition with 1a18C6E, epoxy ring-opening reaction was designed to immobilize CE onto the beads' surface. Since the glass bead samples were acid-washed, DI water, at 5 ml/g of absorbent, was used to rinse the sample prior to testing. After drying, static adsorption tests were conducted with 1 g of glass beads and 1 ml of 1 mM KCl. Both CE-functionalized glass beads and untreated glass beads were found to have 0.2 μmol/g. For continuous adsorption tests, 5 g of absorbent were packed into a column for the adsorption of 1 mM KCl solution at a flow rate of 0.5 ml/min. Similarly, for both functionalized glass beads and untreated glass beads, the adsorption

capacity was found to be approximately 0.5 μmol/g. Since there was no distinguishable difference in adsorption capacity between samples with and without CE functionality, the grafting of CE was assumed to be unsuccessful. Additionally, the observed adsorption capacity of the tested absorbents is two orders of magnitude off from the dialysate regeneration requirement. The lack of CE functionality was suspected to be the reason for the insufficient surface area or the loss of epoxy moieties during the synthesis process.

Silica gel 60 (SG60), with a surface area of approximately 500 m^2/g, was used in synthesis to replace glass beads for higher surface area. In similar static adsorption tests, SG60 with or without CE functionalization were found to reach potassium adsorption capacity at around 10^{-2} mmol/g level. The adsorption capacity indeed increased thanks to improved surface area, but it still fell short of the estimated value. Interestingly, the observed potassium uptake capacity of untreated SG60 was found to be 9.76×10^{-3} mmol/g, which is higher than CE functionalized SG60 with a capacity of 7.66×10^{-3} mmol/g. This counterintuitive observation can be explained by the hypothesis that the GPTMS grafting onto SG60 was successful, while the CE tethering failed. The grafted alkane chains were thought to reduced effective surface area of SG 60 and disrupted stabilization of cation through electrostatic interaction.

GPTMS gel was synthesized aimed to resolve the unsuccessful CE ether grafting. Following reported recipe, the synthesized GPTMS gel was believed to have epoxide moieties available for CE immobilization at 2 mmol/g level, which is comparable to commercial Merrifield resin. [108] After CE grafting and proper rinsing, CE decorated GPTMS gel demonstrated potassium adsorption capacity as high as 4.5×10^{-2} mmol/g, which is about half of the target capacity of 0.1 mmol/g. The enhancement of potassium adsorption capability was believed to be the combined result of a denser surface epoxy group and crown ether decoration. However, adsorption

performance varies greatly due to sample-to-sample differences. And reason responsible for such differences was not thoroughly studied due to complexity in materials and lack of access to analytical instruments. Other GPTMS-based gels were synthesized with modification of recipe and procedure, yet results were unsatisfactory.

4.3.3 *Adsorption Performance of Silica Gel with CE Encapsulated*

As an alternative to covalent binding of CE, immobilization of CE through matrix encapsulation was explored and turned out fruitful. Acid and base catalyzed CE silica gel (CE-SG) was synthesized following reported procedures with modifications. [92, 96, 109] As can be expected, difference in catalyst results in different adsorption capacity. Acid catalyzed CE silica gel exhibited adsorption capacity in 4.4-4.9×10^{-2} mmol/g range with different CE loading (1:20-1:50 crown ether to silicate molar ratio), which is comparable to the performance of CE decorated GPTMS gel.

However, due to the undesirably long synthesis time, approximately a month, associated with the acid catalyst, a base catalyst was employed instead, which shortened the synthesis time to less than one week. Surprisingly, from the first attempt of base catalyzed CE encapsulation, yield product exhibited potassium adsorption capacity of 0.1 mmol/g, which meets the requirements designed for dialysate regeneration applications.

A comparison between this sample and control silica gel sample, which exhibited adsorption capacity of 3.7±0.8×10^{-2} mmol/g without CE loading, indicates that the CE functionalization is of vital importance for potassium adsorption. However, upon examining the synthesis recipe, the molar ratio between crown ether and silicate (CE:Si), which is 1:7.9, indicates that the synthesized CE-SG should possess a crown ether loading over 0.8 mmol/g. From the contrast between calculated CE loading (0.8 mmol/g) and observed adsorption capacity (0.1 mmol/g), it was

speculated that a fraction of crown ether might be leached out of matrix during pre-test rinsing or inaccessible to potassium ion during adsorption test. This hypothesis was examined by evaporating and weighing the eluent of pre-test rinse solution. It was found that, indeed, over 80% of crown ether was leached out prior to test. Another potential explanation for this contrast between estimation and observation is the inefficiency of cation adsorption by crown ether, despite suggestions in the literature to the contrary.

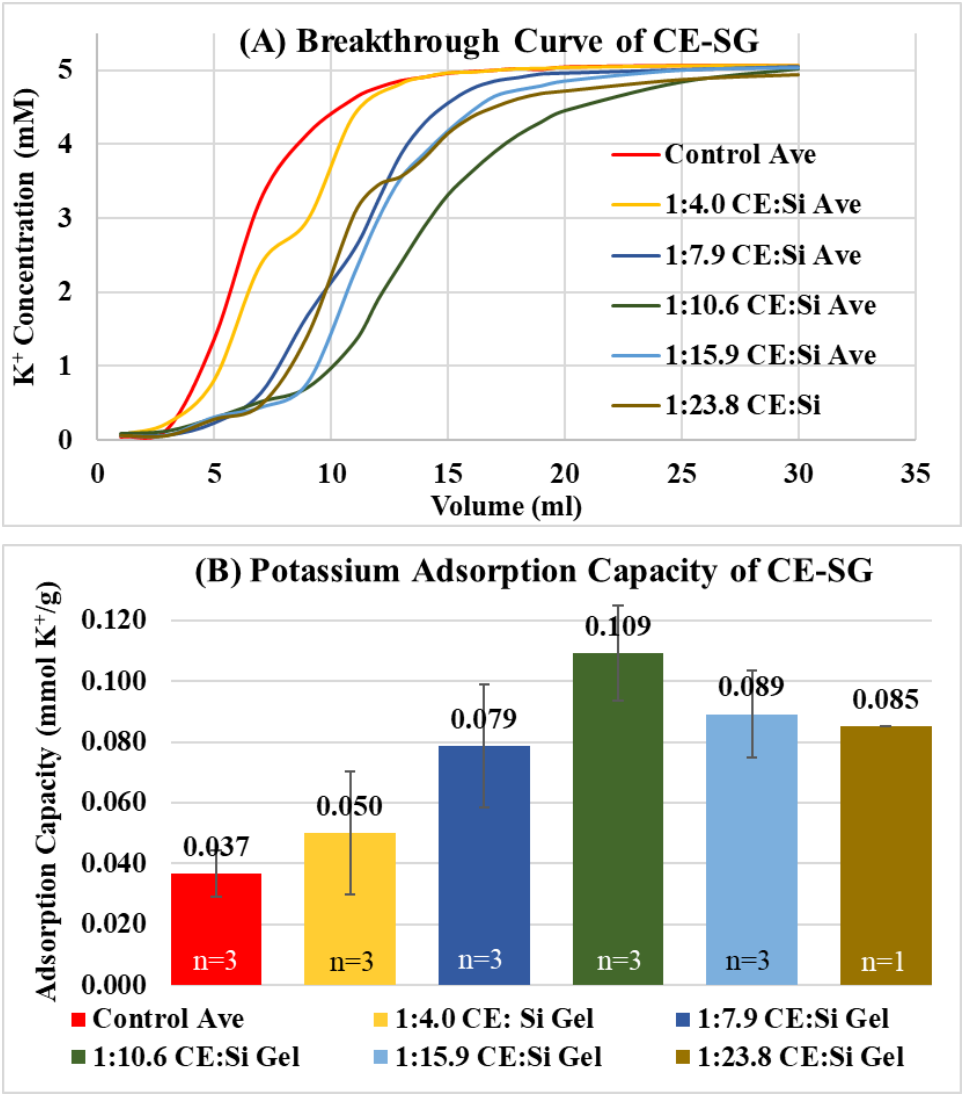

Figure 4.8. Averaged Breakthrough Curves of CE silica gels with different CE:Si ratio in potassium adsorption test (A) and Bar Chart of average potassium adsorption capacity of CE silica gels with different CE:Si ratio (B), error bar indicates the standard deviation.

Table 4.8. Average potassium adsorption capacity of CE silica gel with different CE:Si ratio.

Potassium Adsorption Capacity (mmol K^+/g adsorbent)						
Adsorption Capacity (mmol/g)	Control Gel	1:4.0 CE:Si Gel	1:7.9 CE:Si Gel	**1:10.6 CE:Si Gel**	1:15.9 CE:Si Gel	1:23.8 CE:Si Gel
Average	0.037	0.050	0.079	**0.109**	0.089	0.085
Std	0.008	0.020	0.025	**0.016**	0.014	NA

The CE:Si ratio is considered a critical factor influencing the immobilization and absorption efficiency of crown ether. This can be explained by considering two extreme scenarios. On one hand, if the CE:Si ratio is excessively high, it implies that a substantial amount of CE cannot be encapsulated and immobilized by the silica gel. On the other hand, in the case of an extremely low CE:Si ratio, the crown ether is entirely encapsulated within the SG, rendering it inaccessible to cations. Therefore, an optimal CE:Si ratio must exist balancing CE immobilization and accessibility. With all hypotheses considered, CE-SG with CE:Si ratio range from 1:4 to 1:23.8 was synthesized for optimization.

Continuous adsorption tests with 5 mM KCl solution were done with synthesized CE-SG samples. The averaged breakthrough curves from these tests were shown in Figure 4.8 (A), and numerical results were visualized in Figure 4.8 (B) and tabulated in table 4.2. As can be seen, all of the breakthrough curves of CE-SGs, except for the one with a CE:Si ratio of 1:4, showed distinctive differences compared to control sample which has not CE loading. This is a clear demonstration of efficacy of CE adsorption. Difference in silica gel microstructure was believed to be the reason responsible for the curve pattern difference among results from CE-SG with a CE:Si of 1:7.9 or lower. It is not difficult to deduce from Figure 4.8 (B) that there is likely an optimal CE:Si ratio around 1:10.6 as this ratio exhibits the highest potassium adsorption capacity among all CE-SGs, measuring at $1.09\pm0.16\times10^{-1}$ mmol/g. Furthermore, the correlation between

adsorption capacity and the CE:Si ratio aligns with the model described above, in which adsorption capacity is negatively influenced by both excessively high and extremely low CE:Si ratios. Because the potassium adsorption capacity of CE-SG with CE:Si of 1:10.6 satisfies the target capacity design for dialysate regeneration applications, no further recipe optimization was done.

4.3.4 *Particle Size Examination*

Absorbent particle size may subtly influence its adsorption performance as well. Since the mortar and pestle grinding method used is relatively primitive, an examination of the particle size of the synthesized powders is necessary. As shown in Figure 4.9 (A)-(E), the particle size of prepared control SG and CE-SGs, with CE:Si ratio ranging from 1:7.9 to 1:23.8, falls in 1-100 μm level. In terms of particle size ranges, these samples do not show significant differences. However, the particle size distribution of these synthesized absorbents has not been quantified, introducing uncertainties regarding its influence on the cation adsorption capacity of these materials. It is noticeable from Figure 4.9 that larger particles, which is unfavorable for adsorption, are more frequently found in samples with better adsorption performance. This suggests that despite the differences in particles size distribution, CE:Si ratio remains a more dominant factor that influences the cation adsorption capacity.

One interesting observation is that, from Figure 4.9 (F), the particles size distribution of CE-GPTMS gel is visually tighter compared to other SGs. This is probably because of the difference in silicate precursors used.

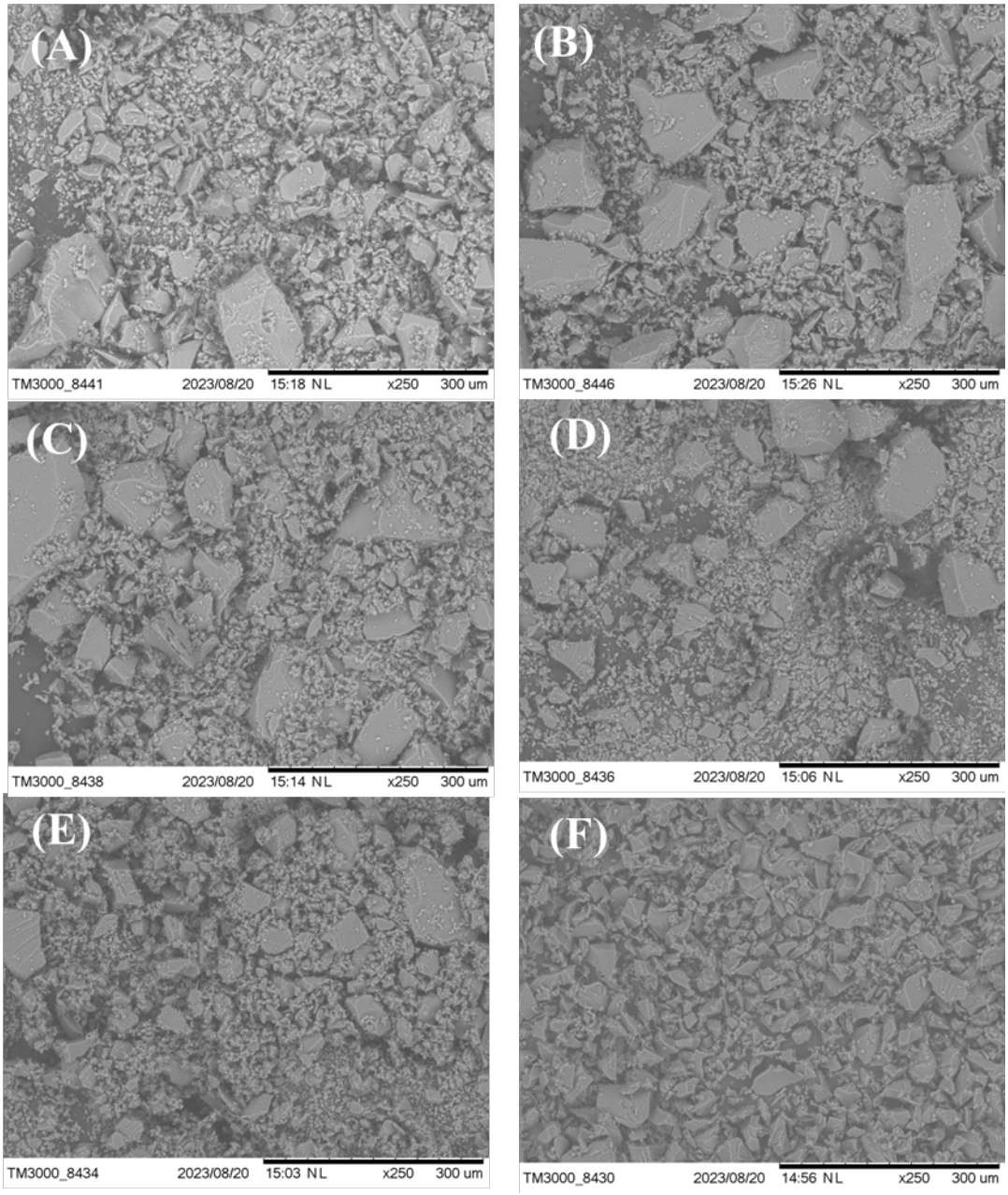

Figure 4.9. SEM image of Control Gel (A), SEM image of CE-SG with CE:Si of 1:7.9 (B), 1:10.6 (C), 1:15.9 (D), 1:23.8 (E) and SEM image of CE-GPTMS Gel (F).

4.3.5 *Reversibility of Potassium Adsorption by Crown Ether*

As previously discussed, simple encapsulation of CE in SG matrix enabled low-cost fabrication of CE-SG with potassium adsorption capacity at $1.09\pm0.16\times10^{-1}$ mmol/g. When compared with

other potassium binders, Patiromer with adsorption capacity of 8.5 mmol/g and SZC with adsorption capacity of 2.8 mmol/g, the synthesized CE-SGs has inferior adsorption capacity. However, this does not diminish the value of synthesized CE-SGs, because it was designed for cyclic adsorption and desorption application while the desorption/regeneration of Patiromer and SZC will be challenging due to their cation ion exchange mechanism. Similarly, lack in regeneration ability also renders zeolites and MOFs unfavorable for application requiring cyclic adsorption and desorption.

Therefore, the feasibility of releasing captured potassium ion from CE-SG was examined. It was previously reported that the dissociation of K^+ from CE cavity is possible by changing the environment pH. [92, 93, 95] Similar to continuous adsorption tests, hydrochloric acid solution of different pH was set to protonate crown ether and force release of potassium in continuous desorption tests as shown in Figure 4.10. And it was observed that, with relative mild condition of pH 5, a significant amount of K^+ was rinsed off from previously saturated CE-SG column with CE:Si of 1:7.9. However, the eluent's potassium concentration quickly equilibrated at 1.3 mM throughout the experiment. This is a possible indication that the potassium dissociation was achieved through proton replacement as the molarity of pH 5 HCl solution is 1 mM. By the end of experiment, 32% of previously captured potassium was removed from the absorbent. This demonstrated the reversibility of cation capture by crown ether but also indicated a lack in efficiency. Therefore, lowering the pH of HCl solution was considered to amplify the potassium dissociation. Not surprisingly, with 0.1 M HCl of pH 1, a significant concentration peak of potassium release was observed followed by a rapid dropped of eluent concentration to near-zero level. Integration of peak area suggests over 90% of previously bound potassium was successfully removed from the column. Thus, it can be concluded that the adsorption of potassium by crown

ether can be efficiently reversed by 0.1 M hydrochloric acid, enabling the regeneration of crown ether-based absorbents.

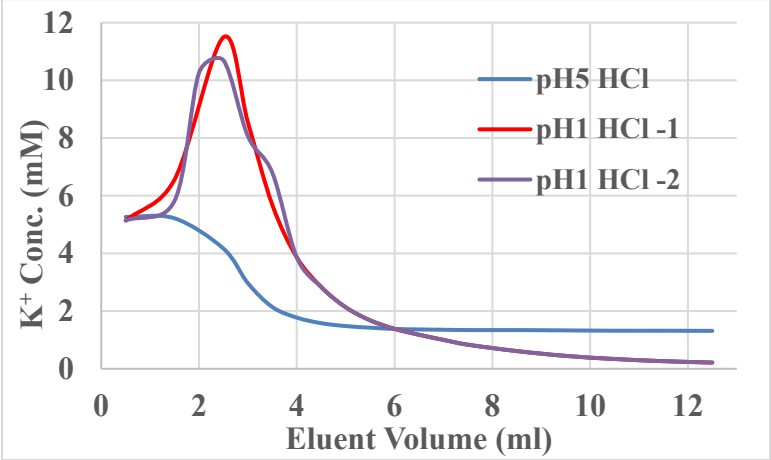

Figure 4.10. Desorption of potassium from previously saturated CE-SG.

4.3.6 *Continuous Potassium Adsorption and Desorption in Cycle*

As the adsorption capacity was demonstrated with good reversibility, the last step proof of concept demonstration is continuous potassium adsorption and desorption in cycles. Three tests were done on CE-SG with CE:Si of 1:10.6 as shown in Figure 4.11. The test was done in sequence of adsorption-rinse-desorption-rinse by switching feed solution and collecting eluent for quantification. During the first cycle of all three tests, the adsorption capacity was found to be approximately 9.5×10^{-1} mmol/g which is in good alignment with previous tests. Using a pH 1 HCl solution, about 69% of the bound potassium was removed from the absorbent, while the pH 5 HCl solution resulted in a release of 18%. The released amount potassium is less than previous test due to shortened release session. However, the adsorption and desorption behavior changed dramatically after the first cycle. In short, both adsorption of potassium by CE-SG decayed to the strength of control gel level. Consequently, the amount of dissociated potassium was also observed to decrease.

It was believed that the crown ether retained within the SG matrix remained stable under neutral conditions since all samples were thoroughly rinsed with an excessive amount of water prior to experiments. However, after undergoing acid treatment, the residual potassium adsorption capacity of the tested CE-SG samples decreased to a level comparable to that of silica gel without any crown ether functionality. Interestingly, it is observed that with a less acidic solution, specifically in the pH 5 desorption test, the potassium adsorption capability of CE-SG is better maintained. Therefore, this unexpected decline in the adsorption performance of CE-SG was hypothesized to result from acid-induced leaching of the crown ether.

Crown ether-functionalized silica gels synthesized through other approaches were also tested for their tolerance to acidic environments. Both acid-catalyzed silica gel encapsulating CE and CE-GPTMS gel demonstrated modest adsorption and desorption capabilities. However, they were also found to experience a decrease in performance due to exposure to acidic conditions.

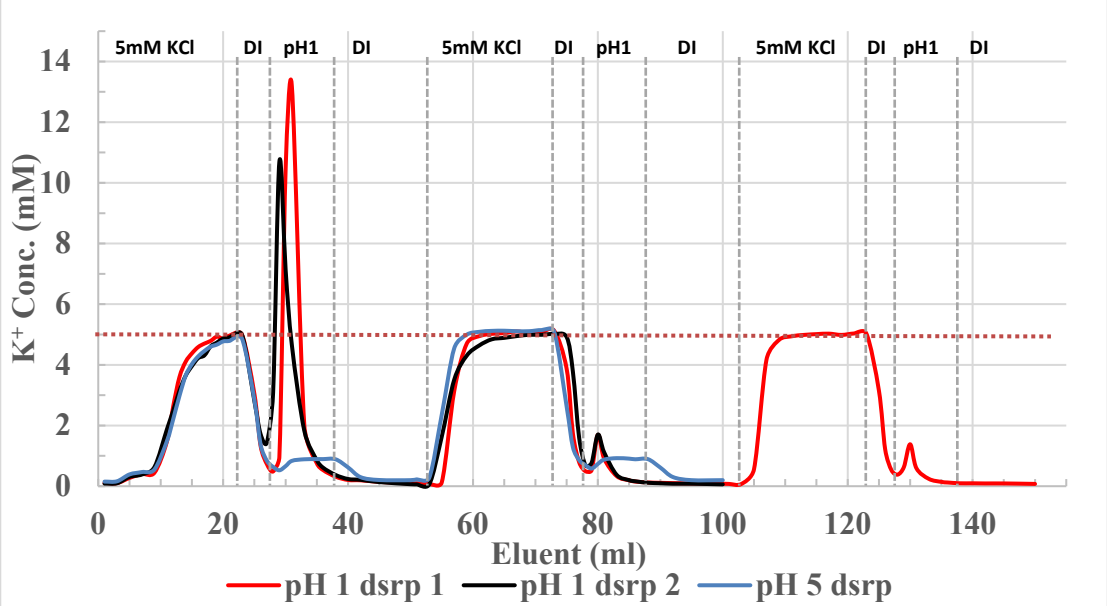

Figure 4.11. Continuous adsorption and desorption in cycles of potassium by CE-SG.

4.4 CONCLUSION

The research project presented here delves into the development and assessment of crown ether-based absorbents for the purpose of potassium adsorption and desorption in the context of dialysate regeneration for development of at-home dialysis machine. The investigation began with an exploration of the selectivity properties of crown ethers to capture potassium ions over other cations. And literature review revealed the promising selectivity of the 18-crown-6-ether showing excellent size-based discrimination for potassium ions. A series of mathematical validations was done to confirm the efficacy of 18-crown-6-ether.

Then, various support materials, such as Merrifield resin, glass beads, and silica gel, were examined with crown ether immobilization chemistry. While initial attempts to functionalize these materials encountered limitations, the encapsulation of crown ethers within a silica gel matrix emerged as a successful approach. The base-catalyzed encapsulation demonstrated remarkable potential, achieving the desired potassium adsorption capacity of $1.09\pm0.16\times10^{-1}$ mmol/g for effective dialysate regeneration. Additionally, the synthesis of crown ether functionalized GPTMS gel showcased advancements in enhancing adsorption capability via modified grafting strategies.

The investigation of synthesis recipe in CE:Si ratio and particle size analysis provided further insights of these materials. The particle size analysis revealed consistent ranges across the synthesized absorbents, highlighting the role of the CE:Si ratio as a more influential factor in determining adsorption capacity. After this, the feasibility of releasing captured potassium ions from the CE-SG absorbent through controlled pH adjustments was validated, enabling efficient desorption for cyclic adsorption applications.

Crucially, the presented research demonstrated the capability of crown ether-functionalized silica gel for potassium adsorption and desorption. The successful proof-of-concept demonstration

affirmed the potential utility of these absorbents in dialysate regeneration scenarios. However, it was also noted that long-term stability and the impact of acidic environments on the leaching of crown ethers need to be further explored and optimized.

4.5 FUTURE OUTLOOK

There are several foreseeable directions for future research that could significantly enhance the current study. Firstly, it is essential to investigate the potential factors responsible for crown ether leaching. This investigation should focus on exploring the interactions between the acidic environment and the microstructure of the synthesized silica gel and crown ether. Understanding these interactions will be crucial in mitigating crown ether leaching and improving the overall performance.

Secondly, it is worth exploring potassium-crown ether dissociation mechanisms beyond pH adjustments. Infrared beam and electromagnetic field are two potential candidates. [113, 114] Research should delve into identifying physical triggers that can induce potassium dissociation, thereby avoiding potential damage to the silica gel matrix caused by acidic conditions.

Thirdly, the synthesis chemistry and crown ether immobilization process require further in-depth study and optimization. Additionally, characterizing the synthesized materials in detail will provide a clearer understanding of the properties and behavior of CE-SG materials.

Overall, addressing these directions in future research endeavors will undoubtedly contribute to advancing the field and building upon the findings of this study.

4.6 REFERENCES

[1] Palmer, B. F. Regulation of Potassium Homeostasis. *Clinical Journal of the American Society of Nephrology* **2015**, *10* (6), 1050-1060. DOI: 10.2215/cjn.08580813.

[2] Allon, M. HYPERKALEMIA IN END-STAGE RENAL-DISEASE - MECHANISMS AND MANAGEMENT. *Journal of the American Society of Nephrology* **1995**, *6* (4), 1134-1142.

[3] Seliger, S. L. Hyperkalemia in patients with chronic renal failure. *Nephrology Dialysis Transplantation* **2019**, *34*, 12-18. DOI: 10.1093/ndt/gfz231.

[4] Takaichi, K.; Takemoto, F.; Ubara, Y.; Mori, Y. The clinically significant estimated glomerular filtration rate for hyperkalemia. *Internal Medicine* **2008**, *47* (14), 1315-1323. DOI: 10.2169/internalmedicine.47.0944.

[5] Lazich, L.; Bakris, G. L. Prediction and Management of Hyperkalemia Across the Spectrum of Chronic Kidney Disease. *Seminars in Nephrology* **2014**, *34* (3), 333-339. DOI: 10.1016/j.semnephrol.2014.04.008.

[6] United States Renal Data System. *2022 USRDS Annual Data Report: Epidemiology of kidney disease in the United States*; National Institutes of Health, National Institute of Diabetes and Digestive and Kidney Diseases, Bethesda, MD, https://adr.usrds.org/2022.

[7] Makar, M. S.; Pun, P. H. Sudden Cardiac Death Among Hemodialysis Patients. *American Journal of Kidney Diseases* **2017**, *69* (5), 684-695. DOI: 10.1053/j.ajkd.2016.12.006.

[8] Samanta, R.; Chan, C.; Chauhan, V. S. Arrhythmias and Sudden Cardiac Death in End Stage Renal Disease: Epidemiology, Risk Factors, and Management. *Canadian Journal of Cardiology* **2019**, *35* (9), 1228-1240. DOI: 10.1016/j.cjca.2019.05.005.

[9] Bleyer, A. J.; Hartman, J.; Brannon, P. C.; Reeves-Daniel, A.; Satko, S. G.; Russell, G. Characteristics of sudden death in hemodialysis patients. *Kidney International* **2006**, *69* (12), 2268-2273. DOI: 10.1038/sj.ki.5000446.

[10] Collins, A. J.; Pitt, B.; Reaven, N.; Funk, S.; McGaughey, K.; Wilson, D.; Bushinsky, D. A. Association of Serum Potassium with All-Cause Mortality in Patients with and without Heart Failure, Chronic Kidney Disease, and/or Diabetes. *American Journal of Nephrology* **2017**, *46* (3), 213-221. DOI: 10.1159/000479802.

[11] Mazzaferro, S.; de Martini, N.; Cannata-Andia, J.; Cozzolino, M.; Messa, P.; Rotondi, S.; Tartaglione, L.; Pasquali, M.; Grp, E.-E. C.-M. W. Focus on the Possible Role of Dietary Sodium, Potassium, Phosphate, Magnesium, and Calcium on CKD Progression. *Journal of Clinical Medicine* **2021**, *10* (5). DOI: 10.3390/jcm10050958.

[12] Morris, A.; Krishnan, N.; Kimani, P. K.; Lycett, D. Effect of Dietary Potassium Restriction on Serum Potassium, Disease Progression, and Mortality in Chronic Kidney Disease: A Systematic Review and Meta-Analysis (vol 30, pg 276, 2020). *J. Renal Nutr.* **2022**, *32* (1), E1-E10. DOI: 10.1053/j.jrn.2021.07.001.

[13] Sterns, R. H.; Grieff, M.; Bernstein, P. L. Treatment of hyperkalemia: something old, something new. *Kidney International* **2016**, *89* (3), 546-554. DOI: 10.1016/j.kint.2015.11.018.

[14] Palmer, B. F.; Carrero, J. J.; Clegg, D. J.; Colbert, G. B.; Emmett, M.; Fishbane, S.; Hain, D. J.; Lerma, E.; Onuigbo, M.; Rastogi, A.; et al. Clinical Management of Hyperkalemia. *Mayo Clinic Proceedings* **2021**, *96* (3), 744-762. DOI: 10.1016/j.mayocp.2020.06.014.

[15] Kovesdy, C. P. Management of Hyperkalemia: An Update for the Internist. *American Journal of Medicine* **2015**, *128* (12), 1281-1287. DOI: 10.1016/j.amjmed.2015.05.040.

[16] Ahmed, J.; Weisberg, L. S. Hyperkalemia in dialysis patients. *Seminars in Dialysis* **2001**, *14* (5), 348-356. DOI: 10.1046/j.1525-139X.2001.00087.x.

[17] Long, B.; Warix, J. R.; Koyfman, A. CONTROVERSIES IN MANAGEMENT OF HYPERKALEMIA. *Journal of Emergency Medicine* **2018**, *55* (2), 192-205. DOI: 10.1016/j.jemermed.2018.04.004.

[18] Bansal, S.; Pergola, P. E. Current Management of Hyperkalemia in Patients on Dialysis. *Kidney Int. Rep.* **2020**, *5* (6), 779-789, Review. DOI: 10.1016/j.ekir.2020.02.1028.

[19] Parks, M.; Grady, D. Sodium Polystyrene Sulfonate for Hyperkalemia. *Jama Internal Medicine* **2019**, *179* (8), 1023-1024. DOI: 10.1001/jamainternmed.2019.1291.

[20] Beccari, M. V.; Meaney, C. J. Clinical utility of patiromer, sodium zirconium cyclosilicate, and sodium polystyrene sulfonate for the treatment of hyperkalemia: an evidence-based review. *Core evidence* **2017**, *12*, 11-24. DOI: 10.2147/ce.s129555.

[21] Mistry, M.; Shea, A.; Giguere, P.; Nguyen, M. L. Evaluation of Sodium Polystyrene Sulfonate Dosing Strategies in the Inpatient Management of Hyperkalemia. *Annals of Pharmacotherapy* **2016**, *50* (6), 455-462. DOI: 10.1177/1060028016641427.

[22] Kessler, C.; Ng, J.; Valdez, K.; Xie, H.; Geiger, B. The Use of Sodium Polystyrene Sulfonate in the Inpatient Management of Hyperkalemia. *Journal of Hospital Medicine* **2011**, *6* (3), 136-140. DOI: 10.1002/jhm.834.

[23] Hunt, T. V.; DeMott, J. M.; Ackerbauer, K. A.; Whittier, W. L.; Peksa, G. D. Single-dose sodium polystyrene sulfonate for hyperkalemia in chronic kidney disease or end-stage renal disease. *Clinical Kidney Journal* **2019**, *12* (3), 408-413. DOI: 10.1093/ckj/sfy063.

[24] Lepage, L.; Dufour, A. C.; Doiron, J.; Handfield, K.; Desforges, K.; Bell, R.; Vallee, M.; Savoie, M.; Perreault, S.; Laurin, L. P.; et al. Randomized Clinical Trial of Sodium Polystyrene

Sulfonate for the Treatment of Mild Hyperkalemia in CKD. *Clinical Journal of the American Society of Nephrology* **2015**, *10* (12), 2136-2142. DOI: 10.2215/cjn.03640415.

[25] Harel, Z.; Harel, S.; Shah, P. S.; Wald, R.; Perl, J.; Bell, C. M. Gastrointestinal Adverse Events with Sodium Polystyrene Sulfonate (Kayexalate) Use: A Systematic Review. *American Journal of Medicine* **2013**, *126* (3). DOI: 10.1016/j.amjmed.2012.08.016.

[26] Nguyen, T.; Ondrik, D.; Zhufyak, O.; To, W.; He, S. Hyperkalemia and potential pitfalls of sodium polystyrene sulfonate. *Jaapa-Journal of the American Academy of Physician Assistants* **2015**, *28* (3), 41-45. DOI: 10.1097/01.JAA.0000458856.92020.1e.

[27] Sidhu, K.; Sanjanwala, R.; Zieroth, S. Hyperkalemia in heart failure. *Current Opinion in Cardiology* **2020**, *35* (2), 150-155. DOI: 10.1097/hco.0000000000000709.

[28] Chaitman, M.; Dixit, D.; Bridgeman, M. B. Potassium-Binding Agents for the Clinical Management of Hyperkalemia. *P & T : a peer-reviewed journal for formulary management* **2016**, *41* (1), 43-50.

[29] Rafique, Z.; Liu, M. Y.; Staggers, K. A.; Minard, C. G.; Peacock, W. F. Patiromer for Treatment of Hyperkalemia in the Emergency Department: A Pilot Study. *Academic Emergency Medicine* **2020**, *27* (1), 54-60. DOI: 10.1111/acem.13868.

[30] Weir, M. R.; Bakris, G. L.; Bushinsky, D. A.; Mayo, M. R.; Garza, D.; Stasiv, Y.; Wittes, J.; Christ-Schmidt, H.; Berman, L.; Pitt, B.; et al. Patiromer in Patients with Kidney Disease and Hyperkalemia Receiving RAAS Inhibitors. *New England Journal of Medicine* **2015**, *372* (3), 211-221. DOI: 10.1056/NEJMoa1410853.

[31] Bakris, G. L.; Pitt, B.; Weir, M. R.; Freeman, M. W.; Mayo, M. R.; Garza, D.; Stasiv, Y.; Zawadzki, R.; Berman, L.; Bushinsky, D. A.; et al. Effect of Patiromer on Serum Potassium Level in Patients With Hyperkalemia and Diabetic Kidney Disease The AMETHYST-DN Randomized

Clinical Trial. *Jama-Journal of the American Medical Association* **2015**, *314* (2), 151-161. DOI: 10.1001/jama.2015.7446.

[32] Pitt, B.; Bakris, G. L.; Bushinsky, D. A.; Garza, D.; Mayo, M. R.; Stasiv, Y.; Christ-Schmidt, H.; Berman, L.; Weir, M. R. Effect of patiromer on reducing serum potassium and preventing recurrent hyperkalaemia in patients with heart failure and chronic kidney disease on RAAS inhibitors. *European Journal of Heart Failure* **2015**, *17* (10), 1057-1065. DOI: 10.1002/ejhf.402.

[33] Li, L. Y.; Harrison, S. D.; Cope, M. J.; Park, C.; Lee, L.; Salaymeh, F.; Madsen, D.; Benton, W. W.; Berman, L.; Buysse, J. Mechanism of Action and Pharmacology of Patiromer, a Nonabsorbed Cross-Linked Polymer That Lowers Serum Potassium Concentration in Patients With Hyperkalemia. *Journal of Cardiovascular Pharmacology and Therapeutics* **2016**, *21* (5), 456-465. DOI: 10.1177/1074248416629549.

[34] al., F. S. e. Sodium zirconium cyclosilicate. (2023, March 4). Wikipedia: Wikipedia, 2014.

[35] Stavros, F.; Yang, A.; Leon, A.; Nuttall, M.; Rasmussen, H. S. Characterization of Structure and Function of ZS-9, alpha K+ Selective Ion Trap. *PLoS One* **2014**, *9* (12). DOI: 10.1371/journal.pone.0114686.

[36] Gras, J. SODIUM ZIRCONIUM CYCLOSILICATE Potassium (K+) ion trap Treatment for hyperkalemia. *Drugs of the Future* **2015**, *40* (7), 437-441. DOI: 10.1358/dof.2015.40.7.2319756.

[37] Hoy, S. M. Sodium Zirconium Cyclosilicate: A Review in Hyperkalaemia. *Drugs* **2018**, *78* (15), 1605-1613. DOI: 10.1007/s40265-018-0991-6.

[38] Anker, S. D.; Kosiborod, M.; Zannad, F.; Pina, I. L.; McCullough, P. A.; Filippatos, G.; van der Meer, P.; Ponikowski, P.; Rasmussen, H. S.; Lavin, P. T.; et al. Maintenance of serum

potassium with sodium zirconium cyclosilicate (ZS-9) in heart failure patients: results from a phase 3 randomized, double-blind, placebo-controlled trial. *European Journal of Heart Failure* **2015**, *17* (10), 1050-1056. DOI: 10.1002/ejhf.300.

[39] Spinowitz, B. S.; Fishbane, S.; Pergola, P. E.; Roger, S. D.; Lerma, E. V.; Butler, J.; von Haehling, S.; Adler, S. H.; Zhao, J. E.; Singh, B.; et al. Sodium Zirconium Cyclosilicate among Individuals with Hyperkalemia A 12-Month Phase 3 Study. *Clinical Journal of the American Society of Nephrology* **2019**, *14* (6), 798-809. DOI: 10.2215/cjn.12651018.

[40] Kosiborod, M.; Rasmussen, H. S.; Lavin, P.; Qunibi, W. Y.; Spinowitz, B.; Packham, D.; Roger, S. D.; Yang, A.; Lerma, E.; Singh, B. Effect of Sodium Zirconium Cyclosilicate on Potassium Lowering for 28 Days Among Outpatients With Hyperkalemia The HARMONIZE Randomized Clinical Trial. *Jama-Journal of the American Medical Association* **2014**, *312* (21), 2223-2233. DOI: 10.1001/jama.2014.15688.

[41] Packham, D. K.; Rasmussen, H. S.; Lavin, P. T.; El-Shahawy, M. A.; Roger, S. D.; Block, G.; Qunibi, W.; Pergola, P.; Singh, B. Sodium zirconium cyclosilicate in hyperkalemia. *New England Journal of Medicine* **2015**, *372* (3), 222-231.

[42] Database of Zeolite Structures. http://www.iza-structure.org/databases/ (accessed Aug 2023).

[43] Baile, P.; Fernandez, E.; Vidal, L.; Canals, A. Zeolites and zeolite-based materials in extraction and microextraction techniques. *Analyst* **2019**, *144* (2), 366-387. DOI: 10.1039/c8an01194j.

[44] Tosheva, L.; Valtchev, V. P. Nanozeolites: Synthesis, crystallization mechanism, and applications. *Chem. Mat.* **2005**, *17* (10), 2494-2513. DOI: 10.1021/cm047908z.

[45] Sun, L. Y.; Zhang, Y. F.; Gong, Y. J. Structural Features and Application of Micro-Microporous Composite Zeolites. *Acta Physico-Chimica Sinica* **2016**, *32* (5), 1105-1122. DOI: 10.3866/pku.whxb201603015.

[46] Xu, X. W.; Wang, J.; Long, Y. C. Zeolite-based materials for gas sensors. *Sensors* **2006**, *6* (12), 1751-1764. DOI: 10.3390/s6121751.

[47] Semmens, M. J.; Martin, W. P. THE INFLUENCE OF PRETREATMENT ON THE CAPACITY AND SELECTIVITY OF CLINOPTILOLITE FOR METAL-IONS. *Water Research* **1988**, *22* (5), 537-542. DOI: 10.1016/0043-1354(88)90052-8.

[48] Martin-Kleiner, I.; Flegar-Mestric, Z.; Zadro, R.; Breljak, D.; Janda, S. S.; Stojkovic, R.; Marusic, M.; Radacic, M.; Boranic, M. The effect of the zeolite clinoptilolite on serum chemistry and hematopoiesis in mice. *Food and Chemical Toxicology* **2001**, *39* (7), 717-727. DOI: 10.1016/s0278-6915(01)00004-7.

[49] Weatherley, L. R.; Miladinovic, N. D. Comparison of the ion exchange uptake of ammonium ion onto New Zealand clinoptilolite and mordenite. *Water Research* **2004**, *38* (20), 4305-4312. DOI: 10.1016/j.watres.2004.08.026.

[50] Guo, X.; Zeng, L.; Li, X. M.; Park, H. S. Ammonium and potassium removal for anaerobically digested wastewater using natural clinoptilolite followed by membrane pretreatment. *Journal of Hazardous Materials* **2008**, *151* (1), 125-133. DOI: 10.1016/j.jhazmat.2007.05.066.

[51] Pavelic, S. K.; Medica, J. S.; Gumbarevic, D.; Filosevic, A.; Przulj, N.; Pavelic, K. Critical Review on Zeolite Clinoptilolite Safety and Medical Applications in vivo. *Frontiers in Pharmacology* **2018**, *9*. DOI: 10.3389/fphar.2018.01350.

[52] Wang, D. J.; Liu, Z. N.; Li, X. L.; Xie, Z. K. Mesoporous zeolite materials. *Progress in Chemistry* **2008**, *20* (5), 637-643.

[53] Pan, T.; Wu, Z. J.; Yip, A. C. K. Advances in the Green Synthesis of Microporous and Hierarchical Zeolites: A Short Review. *Catalysts* **2019**, *9* (3). DOI: 10.3390/catal9030274.

[54] Valtchev, V.; Mintova, S. Hierarchical zeolites. *Mrs Bulletin* **2016**, *41* (9), 689-693. DOI: 10.1557/mrs.2016.171.

[55] Davis, M. E. Ordered porous materials for emerging applications. *Nature* **2002**, *417* (6891), 813-821. DOI: 10.1038/nature00785.

[56] Liu, Z. H.; Hua, Y. J.; Wang, J. J.; Dong, X. L.; Tian, Q. W.; Han, Y. Recent progress in the direct synthesis of hierarchical zeolites: synthetic strategies and characterization methods. *Materials Chemistry Frontiers* **2017**, *1* (11), 2195-2212. DOI: 10.1039/c7qm00168a.

[57] Davis, M. E. Zeolites from a Materials Chemistry Perspective. *Chem. Mat.* **2014**, *26* (1), 239-245. DOI: 10.1021/cm401914u.

[58] Furukawa, H.; Cordova, K. E.; O'Keeffe, M.; Yaghi, O. M. The chemistry and applications of metal-organic frameworks. *Science* **2013**, *341* (6149), 1230444.

[59] Ding, S.-Y.; Wang, W. Covalent organic frameworks (COFs): from design to applications. *Chem. Soc. Rev.* **2013**, *42* (2), 548-568.

[60] Furukawa, H.; Ko, N.; Go, Y. B.; Aratani, N.; Choi, S. B.; Choi, E.; Yazaydin, A. O.; Snurr, R. Q.; O'Keeffe, M.; Kim, J.; et al. Ultrahigh Porosity in Metal-Organic Frameworks. *Science* **2010**, *329* (5990), 424-428. DOI: 10.1126/science.1192160.

[61] Qin, J. S.; Yuan, S.; Wang, Q.; Alsalme, A.; Zhou, H. C. Mixed-linker strategy for the construction of multifunctional metal-organic frameworks. *Journal of Materials Chemistry A* **2017**, *5* (9), 4280-4291. DOI: 10.1039/c6ta10281f.

[62] Lu, W. G.; Wei, Z. W.; Gu, Z. Y.; Liu, T. F.; Park, J.; Tian, J.; Zhang, M. W.; Zhang, Q.; Gentle, T.; Bosch, M.; et al. Tuning the structure and function of metal-organic frameworks via linker design. *Chem. Soc. Rev.* **2014**, *43* (16), 5561-5593. DOI: 10.1039/c4cs00003j.

[63] Yuan, S.; Feng, L.; Wang, K. C.; Pang, J. D.; Bosch, M.; Lollar, C.; Sun, Y. J.; Qin, J. S.; Yang, X. Y.; Zhang, P.; et al. Stable Metal-Organic Frameworks: Design, Synthesis, and Applications. *Adv. Mater.* **2018**, *30* (37). DOI: 10.1002/adma.201704303.

[64] Li, J. R.; Kuppler, R. J.; Zhou, H. C. Selective gas adsorption and separation in metal-organic frameworks. *Chem. Soc. Rev.* **2009**, *38* (5), 1477-1504. DOI: 10.1039/b802426j.

[65] Ferey, G. Hybrid porous solids: past, present, future. *Chem. Soc. Rev.* **2008**, *37* (1), 191-214. DOI: 10.1039/b618320b.

[66] Xu, T. T.; Shehzad, M. A.; Yu, D. B.; Li, Q. H.; Wu, B.; Ren, X. M.; Ge, L.; Xu, T. W. Highly Cation Permselective Metal-Organic Framework Membranes with Leaf-Like Morphology. *Chemsuschem* **2019**, *12* (12), 2593-2597. DOI: 10.1002/cssc.201900706.

[67] Carboni, M.; Abney, C. W.; Liu, S. B.; Lin, W. B. Highly porous and stable metal-organic frameworks for uranium extraction. *Chem. Sci.* **2013**, *4* (6), 2396-2402. DOI: 10.1039/c3sc50230a.

[68] Goyal, P.; Tiwary, C. S.; Misra, S. K. Ion exchange based approach for rapid and selective Pb(II) removal using iron oxide decorated metal organic framework hybrid. *Journal of Environmental Management* **2021**, *277*. DOI: 10.1016/j.jenvman.2020.111469.

[69] Yaghi, O. M.; Li, G. M.; Li, H. L. SELECTIVE BINDING AND REMOVAL OF GUESTS IN A MICROPOROUS METAL-ORGANIC FRAMEWORK. *Nature* **1995**, *378* (6558), 703-706. DOI: 10.1038/378703a0.

[70] Han, L.; Zhou, J.; Li, X.; Sun, C. Y.; Zhao, L.; Zhang, Y. T.; Zhu, M.; Wang, X. L.; Su, Z. M. Recognition of harmful fused aromatic hydrocarbons via a metal-organic framework with

hydrophobic pores. *Inorganic Chemistry Communications* **2017**, *86*, 200-203. DOI: 10.1016/j.inoche.2017.10.015.

[71] Hench, L. L.; West, J. K. THE SOL-GEL PROCESS. *Chem. Rev.* **1990**, *90* (1), 33-72, Review. DOI: 10.1021/cr00099a003.

[72] Livage, J.; Sanchez, C. SOL-GEL CHEMISTRY. *J. Non-Cryst. Solids* **1992**, *145* (1-3), 11-19, Article; Proceedings Paper. DOI: 10.1016/s0022-3093(05)80422-3.

[73] Bryans, T. R.; Brawner, V. L.; Quitevis, E. L. Microstructure and porosity of silica xerogel monoliths prepared by the fast sol-gel method. *J. Sol-Gel Sci. Technol.* **2000**, *17* (3), 211-217, Article. DOI: 10.1023/a:1008711921746.

[74] Assink, R. A.; Kay, B. D. SOL-GEL KINETICS .1. FUNCTIONAL-GROUP KINETICS. *J. Non-Cryst. Solids* **1988**, *99* (2-3), 359-370, Article. DOI: 10.1016/0022-3093(88)90441-3.

[75] Danks, A. E.; Hall, S. R.; Schnepp, Z. The evolution of 'sol-gel' chemistry as a technique for materials synthesis. *Materials Horizons* **2016**, *3* (2), 91-112. DOI: 10.1039/c5mh00260e.

[76] Alothman, Z. A. A Review: Fundamental Aspects of Silicate Mesoporous Materials. *Materials* **2012**, *5* (12), 2874-2902. DOI: 10.3390/ma5122874.

[77] Esposito, S. "Traditional" Sol-Gel Chemistry as a Powerful Tool for the Preparation of Supported Metal and Metal Oxide Catalysts. *Materials* **2019**, *12* (4). DOI: 10.3390/ma12040668.

[78] Kaplan, J. H. Biochemistry of na, K-ATPase. *Annual review of biochemistry* **2002**, *71* (1), 511-535.

[79] Suhail, M. Na, K-ATPase: Ubiquitous Multifunctional Transmembrane Protein and its Relevance to Various Pathophysiological Conditions. *Journal of clinical medicine research* **2010**, *2* (1), 1-17. DOI: 10.4021/jocmr2010.02.263w.

[80] Lupfert, C.; Grell, E.; Pintschovius, V.; Apell, H. J.; Cornelius, F.; Clarke, R. J. Rate limitation of the Na+,K+-ATPase pump cycle. *Biophys. J.* **2001**, *81* (4), 2069-2081, Article. DOI: 10.1016/s0006-3495(01)75856-0.

[81] Pedersen, C. J. CYCLIC POLYETHERS AND THEIR COMPLEXES WITH METAL SALTS. *J. Am. Chem. Soc.* **1967**, *89* (10), 2495-&. DOI: 10.1021/ja00986a052.

[82] Izatt, R. M.; Terry, R. E.; Haymore, B. L.; Hansen, L. D.; Dalley, N. K.; Avondet, A. G.; Christensen, J. J. Calorimetric titration study of the interaction of several uni- and bivalent cations with 15-crown-5, 18-crown-6, and two isomers of dicyclohexo-18-crown-6 in aqueous solution at 25.degree.C and .mu. = 0.1. *J. Am. Chem. Soc.* **1976**, *98* (24), 7620-7626. DOI: 10.1021/ja00440a028.

[83] Lamb, J.; Izatt, R.; Swain, C.; Christensen, J. A systematic study of the effect of macrocycle ring size and donor atom type on the log K,. DELTA. H, and T. DELTA. S of reactions at 25. degree. C in methanol of mono-and divalent cations with crown ethers. *J. Am. Chem. Soc.* **1980**, *102* (2), 475-479.

[84] Frensdorff, H. K. STABILITY CONSTANTS OF CYCLIC POLYETHER COMPLEXES WITH UNIVALENT CATIONS. *J. Am. Chem. Soc.* **1971**, *93* (3), 600-+. DOI: 10.1021/ja00732a007.

[85] Dang, L. X. MECHANISM AND THERMODYNAMICS OF ION SELECTIVITY IN AQUEOUS-SOLUTIONS OF 18-CROWN-6 ETHER - A MOLECULAR-DYNAMICS STUDY. *J. Am. Chem. Soc.* **1995**, *117* (26), 6954-6960, Article. DOI: 10.1021/ja00131a018.

[86] Jing, Z. F.; Wang, G. G.; Zhou, Y. Q.; Pang, D. K.; Zhu, F. Y.; Liu, H. Y. Selectivity of 18-crown-6 ether to alkali ions by density functional theory and molecular dynamics simulation. *Journal of Molecular Liquids* **2020**, *311*. DOI: 10.1016/j.molliq.2020.113305.

[87] Thunhorst, K. L.; Noble, R. D.; Bowman, C. N. Properties of the transport of alkali metal salts through polymeric membranes containing benzo-18-crown-6 crown ether functional groups. *J. Membr. Sci.* **1999**, *156* (2), 293-302. DOI: 10.1016/s0376-7388(98)00358-5.

[88] Zhang, H. X.; Huang, Z. X.; Zhao, P. Y.; Hou, Y.; Guo, J. J.; Wu, Y. C. Crown ether functionalized graphene oxide as ultrasensitive electrochemical sensor for detection of potassium ions. *Mater. Res. Express* **2019**, *6* (12), 6, Article. DOI: 10.1088/2053-1591/ab5d65.

[89] Acar, E. T.; Buchsbaum, S. F.; Combs, C.; Fornasiero, F.; Siwy, Z. S. Biomimetic potassium-selective nanopores. *Science Advances* **2019**, *5* (2). DOI: 10.1126/sciadv.aav2568.

[90] Slampova, A.; Kuban, P.; Bocek, P. Fine-tuning of electromembrane extraction selectivity using 18-crown-6 ethers as supported liquid membrane modifiers. *Electrophoresis* **2014**, *35* (23), 3317-3320. DOI: 10.1002/elps.201400372.

[91] Tamura, H.; Kimura, K.; Shono, T. COATED WIRE SODIUM-SELECTIVE AND POTASSIUM-SELECTIVE ELECTRODES BASED ON BIS(CROWN ETHER) COMPOUNDS. *Anal. Chem.* **1982**, *54* (7), 1224-1227. DOI: 10.1021/ac00244a055.

[92] Yost, T. L.; Fagan, B. C.; Allain, L. R.; Barnes, C. E.; Dai, S.; Sepaniak, M. J.; Xue, Z. L. Crown ether-doped sol-gel materials for strontium(II) separation. *Anal. Chem.* **2000**, *72* (21), 5516-5519, Article. DOI: 10.1021/ac0005518.

[93] Vendilo, A. G.; Djigailo, D. I.; Smirnova, S. V.; Torocheshnikova, II; Popov, K. I.; Krasovsky, V. G.; Pletnev, I. V. 18-Crown-6 and Dibenzo-18-crown-6 Assisted Extraction of Cesium from Water into Room Temperature Ionic Liquids and Its Correlation with Stability Constants for Cesium Complexes. *Molecules* **2009**, *14* (12), 5001-5016. DOI: 10.3390/molecules14125001.

[94] Tsurubou, S.; Mizutani, M.; Kadota, Y.; Yamamoto, T.; Umetani, S.; Sasaki, T.; Le, Q. T. H.; Matsui, M. IMPROVED EXTRACTION SEPARATION OF ALKALINE-EARTHS AND LANTHANIDES USING CROWN-ETHERS AS ION SIZE-SELECTIVE MASKING REAGENTS - A NOVEL MACROCYCLE APPLICATION. *Anal. Chem.* **1995**, *67* (8), 1465-1469, Article. DOI: 10.1021/ac00104a025.

[95] You, N.; Song, Y. X.; Wang, H. R.; Kang, L. X.; Fan, H. T.; Yao, H. Sol-Gel Derived Benzo-Crown Ether-Functionalized Silica Gel for Selective Adsorption of Ca2+ Ions. *J. Chem. Eng. Data* **2019**, *64* (4), 1378-1384, Article. DOI: 10.1021/acs.jced.8b00955.

[96] Badheka, R.; Johnson, A.; Perry, C. C.; Sermon, P. A.; Taylor, A.; Vong, M. S. W. Synergy in macrocycle/SiO2 sol gel nano-composites. *J. Mater. Chem.* **2002**, *12* (11), 3278-3284. DOI: 10.1039/b204428p.

[97] Sui, Z. J.; Hanan, N. J.; Phimphivong, S.; Wysocki, R. J.; Saavedra, S. S. Synthesis, characterization and sol-gel entrapment of a crown ether-styryl fluoroionophore. *Luminescence* **2009**, *24* (4), 236-242. DOI: 10.1002/bio.1106.

[98] Kim, D. W.; Kang, B. M.; Jeon, B. K.; Ryu, H. Adsorption and isotope effects by ion exchange with aqueous-2-aminomethyl-18-crown-6 bonded Merrifield resin. *Journal of Colloid and Interface Science* **2002**, *254* (1), 190-194. DOI: 10.1006/jcis.2002.8411.

[99] Kim, D. W.; Jeon, B. K.; Kang, B. M.; Chi, K. Y.; Ryu, H. I. Lithium isotope separation by chemical exchange using polymer-bound azacrown compounds. *Main Group Metal Chemistry* **2001**, *24* (11), 751-755.

[100] Da, S. L.; Feng, Y. Q.; Da, H. N.; Gong, Y. H.; Zhang, Y. W. Preparation and characterization of 3-(aza-18-crown-6) propylsilyl bonded phase for reversed-phase liquid

chromatography. *Journal of Chromatographic Science* **1999**, *37* (5), 137-144. DOI: 10.1093/chromsci/37.5.137.

[101] Escobar, E. C.; Sio, J. E. L.; Bendoy, A. P.; Torrejos, R. E. C.; Fissaha, H. T.; Kim, H.; Chung, W. J.; Nisola, G. M. Removal of Cs+ in water by dibenzo-18-crown-6 ether tethered on mesoporous SBA-15 as a reusable and efficient adsorbent. *J. Water Process. Eng.* **2021**, *39*, 13, Article. DOI: 10.1016/j.jwpe.2020.101716.

[102] Ye, G.; Bai, F. F.; Wei, J. C.; Wang, J. C.; Chen, J. Novel polysiloxane resin functionalized with dicyclohexano-18-crown-6 (DCH18C6): Synthesis, characterization and extraction of Sr(II) in high acidity HNO3 medium. *Journal of Hazardous Materials* **2012**, *225*, 8-14. DOI: 10.1016/j.jhazmat.2012.04.020.

[103] van de Water, L. G. A.; Driessen, W. L.; Reedijk, J.; Sherrington, D. C. Metal-ion extraction by immobilised aza crown ethers. *European Journal of Inorganic Chemistry* **2002**, (1), 221-229.

[104] Innocenzi, P.; Kidchob, T.; Yoko, T. Hybrid organic-inorganic sol-gel materials based on epoxy-amine systems. *J. Sol-Gel Sci. Technol.* **2005**, *35* (3), 225-235. DOI: 10.1007/s10971-005-2290-4.

[105] Takeuchi, T.; Tokunaga, K.; Lim, L. W. Separation of Inorganic Anions on a Chemically Bonded 18-Crown-6 Ether Stationary Phase in Capillary Ion Chromatography. *Analytical Sciences* **2013**, *29* (4), 423-427. DOI: 10.2116/analsci.29.423.

[106] Lim, L. W.; Tokunaga, K.; Takeuchi, T. Development of chemically bonded crown ether stationary phases in capillary ion chromatography. *Chromatography* **2014**, *35* (2), 95-101.

[107] Siriviriyanun, A.; Imae, T. Anti-fingerprint properties of non-fluorinated organosiloxane self-assembled monolayer-coated glass surfaces. *Chem. Eng. J.* **2014**, *246*, 254-259. DOI: 10.1016/j.cej.2014.02.066.

[108] Menaa, B.; Takahashi, M.; Innocenzi, P.; Yoko, T. Crystallization in hybrid organic-inorganic materials induced by self-organization in basic conditions. *Chem. Mat.* **2007**, *19* (8), 1946-1953. DOI: 10.1021/cm062660u.

[109] Celzard, A.; Mareche, J. F. Applications of the sol-gel process using well-tested recipes. *J. Chem. Educ.* **2002**, *79* (7), 854-859, Article. DOI: 10.1021/ed079p854.

[110] Supplements, N. I. o. H. O. o. D. *Potassium Fact Sheet for Health Professionals*. 2022. https://ods.od.nih.gov/factsheets/Potassium-HealthProfessional/ (accessed.

[111] Kraft, M. D.; Btaiche, I. F.; Sacks, G. S.; Kudsk, K. A. Treatment of electrolyte disorders in adult patients in the intensive care unit. *Am. J. Health-Syst. Pharm.* **2005**, *62* (16), 1663-1682, Review. DOI: 10.2146/ajhp040300.

[112] Shibata, S.; Uchida, S. Hyperkalemia in patients undergoing hemodialysis: Its pathophysiology and management. *Ther. Apher. Dial.* **2022**, *26* (1), 3-14. DOI: 10.1111/1744-9987.13721.

[113] Peiris, D. M.; Yang, Y. J.; Ramanathan, R.; Williams, K. R.; Watson, C. H.; Eyler, J. R. Infrared multiphoton dissociation of electrosprayed crown ether complexes. *International Journal of Mass Spectrometry and Ion Processes* **1996**, *157*, 365-378. DOI: 10.1016/s0168-1176(96)04462-x.

[114] Arabzadeh, H. Excursions in Molecular Simulations and Thermodynamics of Lanthanides with Crown Ethers.

Chapter 5. VISUALIZING ELECTROOSMOSIS: SYNTHESIS AND APPLICATION OF ROBUST CARBON NANOTUBE MEMBRANES FOR EFFICIENT MOLECULE TRANSPORT

5.1 INTRODUCTION

Carbon nanotubes (CNT) have attracted attention from various fields since their discovery by Sumio Iijima in 1991. This discovery was described as coaxial tubes of graphitic sheets with the hexagonal unit of graphite lining up in a helical arrangement about the tube axis. [1] The substances found were later referred to as multi-walled carbon nanotubes (MWCNTs) with 2-50 walls. Later, in 1993, the same lab reported the synthesis of single-walled carbon nanotubes (SWCNTs). [2] Although carbon nanotubes exhibit unparalleled performance in various properties such as mechanical strength, thermal conductivity, and electrical conductivity, the focus of this chapter will be solely on their simplest application scenario, serving as tubes.

Simulation and experiment-based calculations indicate that the liquid flow rate within carbon nanotubes is exceptionally fast. Simulation of water transport through a single-walled carbon nanotube of 8.1 Å was found to occur at a rate of 51×10^{-14} cm^3/s (or 99 cm/s) or higher due to an unexpected formation of a 1-D water chain. [3] Other simulation works predicts flow rate of water range from approximately 1-200 m/s. [4-6] Experimental observation of liquid transport through CNTs, on the other hand, is challenging compared to simulation due to difficulties in measurement and robust apparatus fabrication. Although challenging, numerous designs have successfully demonstrated the measurement of liquid flow velocities within carbon nanotubes. Examples include encupsulating vertically aligned carbon nanotube arrays with polymers or other materials to fabricate thin films, [7-10] synthesizing carbon nanotubes within specific membrane templates,

[11] stabilizing individual carbon nanotubes within bilayer lipid membranes, [4, 12-15] and integrating carbon nanotubes with microfluidic and microelectrode systems. [16, 17] Reported flow rates span a significant range, from 10's of μm/s to 10's of cm/s, owing to variations in fabricated device and measurement methods. Even though, thus far, experimental results of fluid velocity within the CNT core are lower than simulation, it should be noted that these results are still significantly higher than conventional Hagen-Poiseuille flow predictions by ~3 orders of magnitude. Hagen-Poiseuille flow is based on the assumption of zero velocity on the pore wall and a parabolically increasing flow to the maximum at the pore center. The zero velocity at the pore wall is generally set by the fact that random scattering off of an atomically rough surface will have equal probability of forward or backward motion.

The unexpectedly high velocity observed in carbon nanotubes can be attributed to multiple factors, with the ultrasmooth surface of the CNT core, down to the atomic scale, being foremost among them. It is important to note that the very large (3angstrom) van der Wall's distance of graphene due to perpendicular π-bonds makes the surface even smoother than single crystal surfaces. In contrast to fluid modeled under the Hagen-Poiseuille description, the smooth interior surface of the CNT conduit is expected to have limited or no interaction with water or other fluids. Therefore, at the interior surface of the CNT conduit, the axial velocity of the fluid is nonzero, and the velocity profile along the radial direction is described as "plug-like". [5, 18] For the flow of water, the hydrophobicity of the CNT surface further contributes to reducing the friction to water flow, i.e., the water-CNT interaction at the wall of the CNT. [8, 19, 20] In this sense, intentionally induced roughness in the core of CNT was found to cause significant disturbance of liquid flow. [21] The weakened fluid-CNT interaction was later quantified by analyzing the flow slip length, which was always found magnitudes larger than the diameter of carbon nanotubes. [6, 8, 22-24] Therefore, flow

within CNT conduits was often regarded as frictionless. The ordering of water within the core of CNT is another phenomenon associated with fast fluid transport. Under the extreme confinement of an 8 Å CNT, a 1-D water chain is formed by hydrogen bonding. [3] For nanotubes with larger diameters, an increased concentration of water molecules, compared to the bulk solution, was observed at the interface between water and the tube wall. [5] This increase in water molecule concentration, or density, has introduced a novel 'ice-like' phase of water. Various simulation studies have predicted more intricate water structures within nanotubes, including square, pentagonal, hexagonal, and heptagonal ice nanotubes. [25-29] These structures are influenced by factors such as nanotube size, chirality, temperature, and pressure. Several analytical techniques, including IR and NMR spectroscopy, have been employed to confirm the proposed water molecule structures. [30-32] Other factors such a chirality, tube geometry and charge were also studied. [33-37] But our current understanding of water molecules intercalated in CNTs remains limited.

The exploration of carbon nanotube applications has not ceased due to the gap of knowledge in nanofluidics. Combining size-based exclusion and electrostatic interactions, carbon nanotubes are naturally studied for ion sieving. [38] The regulation of ion transport, both positive and negative, through CNTs has been achieved through functionalization at the tips of nanopores and the tuning of environmental pH. [4, 12, 39-41] This has subsequently led to the proposal of water desalination and more refined ion distinction based on similar mechanisms. [41-45] Utilizing controlled electroosmotic flow or electrophoretic motion of charged molecules through CNT nanopores, active cross-membrane transfer of larger molecules has been enabled, expanding the potential applications of CNT platforms in drug delivery. [46-48] Applications in other fields like sensors, energy, etc. was also explored by pilot studies. [49]

As discussed earlier, previous studies suggest that several factors play crucial roles in fast liquid transport within CNT conduits, including the frictionless surface of CNTs and the nanoconfinement-induced ordering of water molecules, which is predicted to reduce the system's energy and favor liquid transport. To examine the effects of these phenomena, the velocity of electroosmotic water flow was utilized as a measure.

Calculated from the transport of marker molecules, the velocity of water transfer through CNTs was found to be orders of magnitude faster than transfer through nanopores of anodic aluminum oxide, even when coated with amorphous carbon. [20] This observation underscores the importance of the smoothness of the CNT tube surface. Another intriguing finding pertains to the influence of entrance charge on mass transfer during electrophoresis. It was discovered that the electrophoretic transfer of charged nicotine molecules promoted the motion of uncharged caffeine molecules. Additionally, an effective surface was found to favor the electroosmotic motion of markers, likely due to the screening effect of anion transfer. [4, 46]

However, all of the aforementioned studies relied on ionic current or marker transfer for electroosmotic velocity calculations. This was primarily because CNT membranes are delicate, challenging to scale up, and exhibit limited stability over extended periods. But visual observation of electroosmosis (EO) liquid transfer is still more desirable and conclusive.

Hence, this chapter is dedicated to further exploring nanofluidic phenomena under the nanoconfinement of sub-2 nm CNTs. Electroosmotic behavior was examined with electrolyte solutions containing different solute species, solute concentrations, and solvent mixtures to evaluate the potential of the CNT platform as a nanofluidic device for delicate separations. The influence of CNT surface smoothness was examined by placing aromatic compound at the CNT surface. Hydrogen-bonded (H-bond) water ordering was also investigated by intentionally

disturbing H-bonds using alcohol molecules or the chaotropic agent NaSCN. To enable this study, a robust CNT composite membrane and a sensitive measurement setup were meticulously engineered.

5.2 EXPERIMENTAL

5.2.1 *Materials and Chemicals*

Chemicals used for this study were obtained from Sigma-Aldrich (St. Louis MO USA) and used without further process unless otherwise stated. Acrylic sheets were acquired from McMaster Carr.

5.2.2 *Synthesis and Decoration of Carbon Nanotube Membranes*

Following the previously developed method, DWCNTs (1.3–2 nm inner diameter, 50 μm length, Sigma Aldrich, St. Louis, MO, USA.) were sonicated for 1 h in methanol with Triton-X100 to open the bundles. [50] Then a series of filtration was done to obtain CNTs of the desired size (1 μm < length < 38 μm). Obtained dry CNTs were transferred to a glass vail and mixed with Epon 862 epoxy resin (Miller Stephenson Chemical Company), methyl hexahydro phthalic anhydride as hardener (Broadview Tech. Inc.), and 2-ethyl-4-methyl-1-H-imidazole-1-propaneneitrile as catalyst using a Thinky™ mixer. The CNT composite mixture was made with resin: hardener: catalyst (1.1:0.45:0.009) composition ratio while the CNT load was kept at about 1 wt%. After curing at 120 °C for 2 hr, the yielded cylindrical composite was microtomed into membranes with a thickness of 5-10 μm and stored in isopropanol. CNT Membranes were then epoxy sealed onto supports made from acrylic or polycarbonate with the center cut open to a diameter of 4.5 mm (acrylic support) or 4.0 mm (polycarbonate support) as shown in Figure 5.1.

The as-made CNT membrane was voltage oxidized to open the CNT pores. Pt wires electrodes were used to oxidize the membrane at 10 V transmembrane potential. AgCl wires electrodes were used to monitor the ionic current with 0.6 V transmembrane potential applied as a reference of porosity. The electrolyte used for oxidation was 0.1 M KCl. Post-oxidation current at 10x μA was regarded as successful while lower current implies insufficient oxidation and higher current normally indicates damaged membrane.

Chemical decoration of the membrane was done with the u-tube setup mentioned in previously published studies. In general, the chemical decoration was limited to the desired surface of the CNT membrane by hydraulic pressure induce flow. A conductive layer of gold, which is < 5 nm, was deposited on the CNT membrane surface as an electrode.

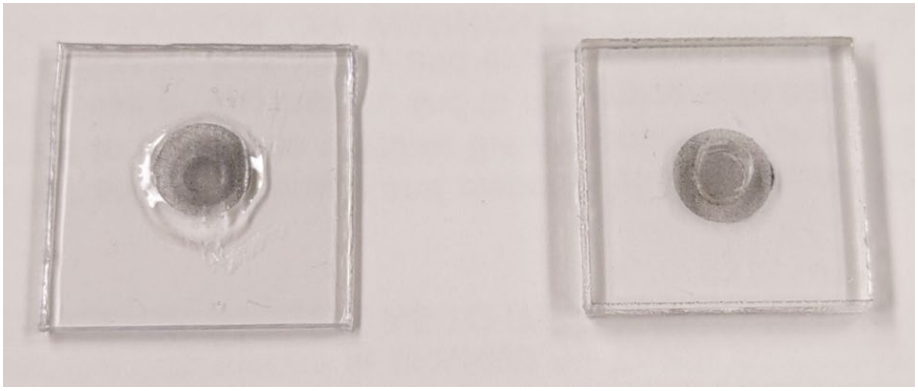

Figure 5.1. Picture of CNT membrane secured on polycarbonate support (left) and sandwiched in laser cut acrylic support (right).

5.2.3 *Synthesis of Silver Chloride Electrodes*

The silver chloride electrodes employed in the electrochemical tests were prepared by oxidizing pure silver wires (diameter: 0.5 mm, purity: 99.9% or 99.99%, sourced from Sigma Aldrich). Initially, the silver wire was cut to a length of 5 cm, with 3.5 cm of it coiled and securely placed in an acrylic support using epoxy sealing, as depicted in Figure 5.2. Subsequently, a solution consisting of 0.25 M FeCl3 and 0.2 M HCl in water was used to oxidize the sealed silver wire for

a minimum of 15 minutes. The resulting silver chloride electrodes, identifiable by their gray-brownish color, were then thoroughly rinsed with deionized water and stored in an argon (Ar) atmosphere prior to use.

Figure 5.2. Picture of silver wire electrode (left) and synthesized silver chloride electrode (right).

5.2.4 *Diffusion and Active Pumping Tests*

Static diffusion tests with marker molecules were performed to prove the integrity of the CNT membranes and to determine the porosity. Direct blue 71 (DB71), with a molecular weight of about 1kDa, was selected as a marker molecule for the detection of cracks and pinholes on the membrane. Solutions of equal osmotic pressure were set on both sides of the membrane while the feed side contains DB 71. The DB 71 concentration in permeate solution after set time was determined by Uv-vis spectroscopy. A membrane with DB 71 flux at 10^{-10} mol/cm^2·hr level or lower was regarded as defect free.

The porosity of the CNT membrane was determined by a cross membrane static diffusion test of smaller marker molecules such as caffeine, nicotine, and urea with setup shown in Figure 5.3. The porosity was calculated using the equation shown:

$$A_p = {J \times \Delta x}/{D \times \Delta C} \qquad (5.4)$$

$$\text{And: } porosity = {A_p}/{A_{total}} \qquad (5.5)$$

Where A_p and A_{total} are the areas of CNT pore and membrane, J is the flux of the marker molecule, Δx is the thickness of the membrane, D is the diffusion coefficient of the marker molecule and ΔC is the concentration of marker molecule of the feed side solution.

Active electroosmotic pumping of marker molecule was demonstrated in the sme diffusion setup as well, employing an additional wire electrode placed across the membrane to apply an electric potential. Continuous EO pumping was observed as a marker-free solution was pumped through needle injection and outlet. The concentration of the marker in the permeate solution was quantified using UV-Vis spectroscopy.

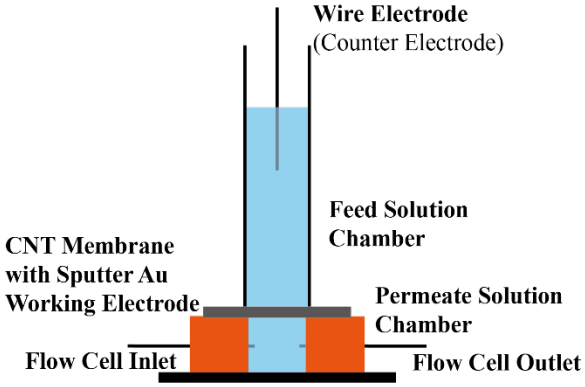

Figure 5.3. Scheme of diffusion/electroosmotic marker pumping test setup.

5.2.5 *Electroosmosis Setup and Test*

Electroosmosis (EO) tests were conducted to demonstrate the electric potential-induced transmembrane flux of water. First, a carbon nanotube (CNT) membrane was assembled between two AgCl electrodes as shown in Figure 5.4. Subsequently, this assembly was placed within capillary U-tubes with an inner diameter of 0.6 mm. A galvanostatic setting was applied across the membrane at 10 μA, while the applied potential was continuously monitored to ensure that no electro-hydrolysis events occurred. The motion of cross-membrane liquid transport was recorded

with a video camera (Dino-Lite Premier Digital Microscope) to measure liquid velocity. Using equation:

$$Velocity = \frac{[(L_{WE}-L_{CE})-(L_{WE}'-L_{CE}')]\cdot A_t}{2\cdot\Delta t\cdot A_p} \qquad (5.6)$$

Where Δt is time required to observe length between the liquid front and a marked position to change from L_{WE} to L_{WE}' in the working electrode cell or from L_{CE} to L_{CE}' in the counter electrode cell. At and Ap denotes the cross-section area of the tube and carbon nanotube pore area of the tested membrane. Then the calculated velocity was normalized with respect to the applied potential. Calculated velocity and velocity per volt applied was averaged for tabulation.

EO tests were also employed to calculate the separation capacity and turnover rate of the CNT membranes.

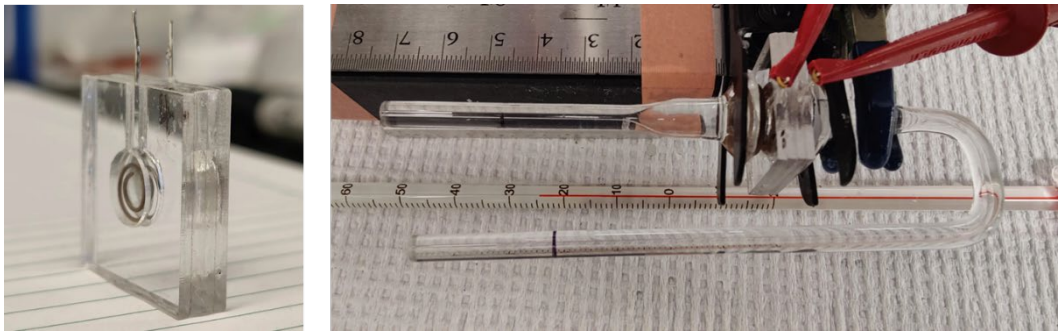

Figure 5.4. Picture of CNT membrane electrode assembly (left) and electroosmosis setup (right).

5.3 Result and Discussion

5.3.1 *Porosity Determination*

The investigation of applying carbon nanotube membrane platforms begins with a fundamental understanding of membrane properties. Among these properties, porosity stands out as a crucial factor. Through static diffusion tests with marker molecules, such as tris(bipyridine)ruthenium chloride ($Ru(bpy)_3Cl_2$), potassium ferricyanide (K_3FeCN_6), caffeine, nicotine and urea, the

porosity of membranes were determined by quantitative analysis of cross membrane transfer of makers.

Table 5.9. Calculated Porosity of Selected CNT Membranes. Membranes 10.2 and 10.3 were functionalized with DB 71 and a 5nm gold layer, while membranes 10.4 and 10.8 featured open pores without functionality.

		Porosity of CNT Membranes			
Marker M.W.	Membrane / Marker	10.2	10.3	10.4	10.8
569.63	$Ru(bpy)_3Cl_2$	1.5E-05	6.5E-05	1.043E-04	3.140E-05
212.35	$K_3Fe(CN)_6$	4.9E-05	9.1E-05	5.044E-05	2.243E-04
194.194	**Caffeine**	**2.9E-06**	**6.0E-06**	**8.4E-06**	**1.143E-05**
162.236	Nicotine (+)	1.0E-05	4.5E-05	2.6E-05	8.042E-05
60.6	Urea	3.2E-05	1.3E-04	7.2E-05	1.8E-04

As can be seen from the result summarized in Table 5.1, the porosity of was found to be in the range of $2x10^{-4}$ to $3x10^{-6}$ level of screened CNT membranes, which is in good agreement with the previous publication, regardless of type of marker. Porosity found with charged markers, in general, is greater than the results that turned out with neutral markers. This was believed to be caused by electrostatic interaction between marker molecules and the entrance of CNT porins with oxidized (-COOH) entrances. The dye grafting and gold depositing process reduced the effective pore size due to spatial hindrance. Therefore, the calculated porosity with the functionalized membranes was in general smaller. The porosity measured by caffeine was chosen as a reference because the diffusion of caffeine is not disturbed by electrostatic interaction between the membrane surface and the marker. More of the caffeine tested membranes were found to have porosity at 10^{-4} level. However, those membranes were more susceptible to leakage of large dyes (direct blue 71) in our screening process.

5.3.2 *Electroosmosis Pumping with Monovalent Cation and Hydrogen Bond Interruption*

Membranes with established porosity were subsequently subjected to electroosmosis (EO) pumping tests. In such tests, a CNT membrane, along with AgCl electrode sets, was securely positioned between capillary tubes containing an electrolyte solution. Under continuous video surveillance, the membrane setup underwent an electroosmosis pumping test conducted in a galvanostatic setting. Analysis of recorded videos allowed for the calculation of liquid flux velocity based on the motion of the liquid front. The successful observation of liquid motion under a galvanostatic setting of 10 μA serves as an indicator of the examined CNT membrane's integrity. Because any significant defects would have allowed the free passage of ionic current without liquid motion. As shown in Figure 5.5, which are pictures taken from EO pumping test with 33.3 mM $CaCl_2$, the motion of water EO flux was monitored by camera and analyzed by calculation of liquid velocity through the CNT porins. As can be indicated by the difference between the solid lines and the dotted lines in the pictures, after the EO pumping tests, even with equal forward and backward pumping time, the liquid position did not return to the initial position. This phenomenon was attributed to liquid evaporation and differences in charge density between the working electrode side and the counter electrode side of the CNT membrane, which then led to difference in pumping velocity. The influence of liquid evaporation was mitigated by measuring the liquid position, denoted as 'length,' on both sides of the CNT membrane and then utilizing the change in this length difference for liquid velocity calculations. The calculated result was then plotted to demonstrated the electroosmosis motion of water in response to applied electric field as shown in Figure 5.5 (bottom).

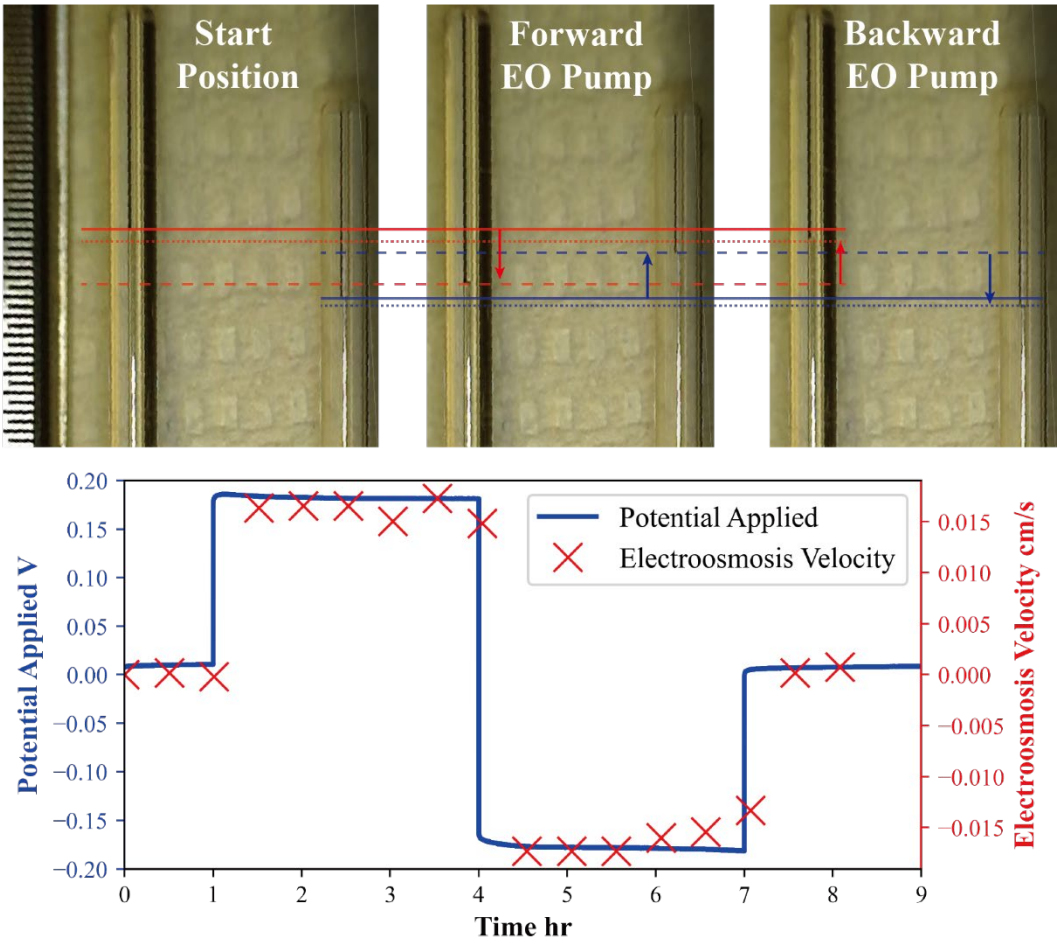

Figure 5.5. Visualization of water flux motion resulting from electroosmotic pumping at 10 μA with 33 mM $CaCl_2$ solution. Top: Pictures of liquid motion from EO pumping. Arrows indicate the pumping direction, while lines delineate the liquid front position. The working electrode side liquid motion is depicted in red, while the counter electrode side is represented in blue. Solid lines are start positions, dashed line after forward pumping, dotted line after backward pumping. Bottom: Visualization of corresponding potential applied and electroosmosis velocity observed.

The results of electroosmosis tests on an unfunctionalized CNT membrane (AS68) are depicted in Figure 5.6. Initially, proton conduction across the CNT membranes was assessed using an EO pump test with 0.1 M HCl (aq). However, no significant EO motion was observed due to the entrance $-COO^-$ being protonated therefore losing the anion screening effect. This confirmed the

previously reported observation of decreased ionic current through CNT pores because of protonating the surface group. Another factor might also contribute to the lack of EO flux is the interference of acid-etched epoxy matrix. Fortunately, after repeated EO pumping tests with a 0.1 M KCl solution, the CNT membrane exhibited recovered EO performance, as indicated by the blue bar in Figure 5.6, achieving an average performance of approximately 0.0098 ± 0.00087 cm/s or 0.12 ± 0.022 cm/sV with applied potential normalized. The data calculated here is in alignment with previous observations. [20]

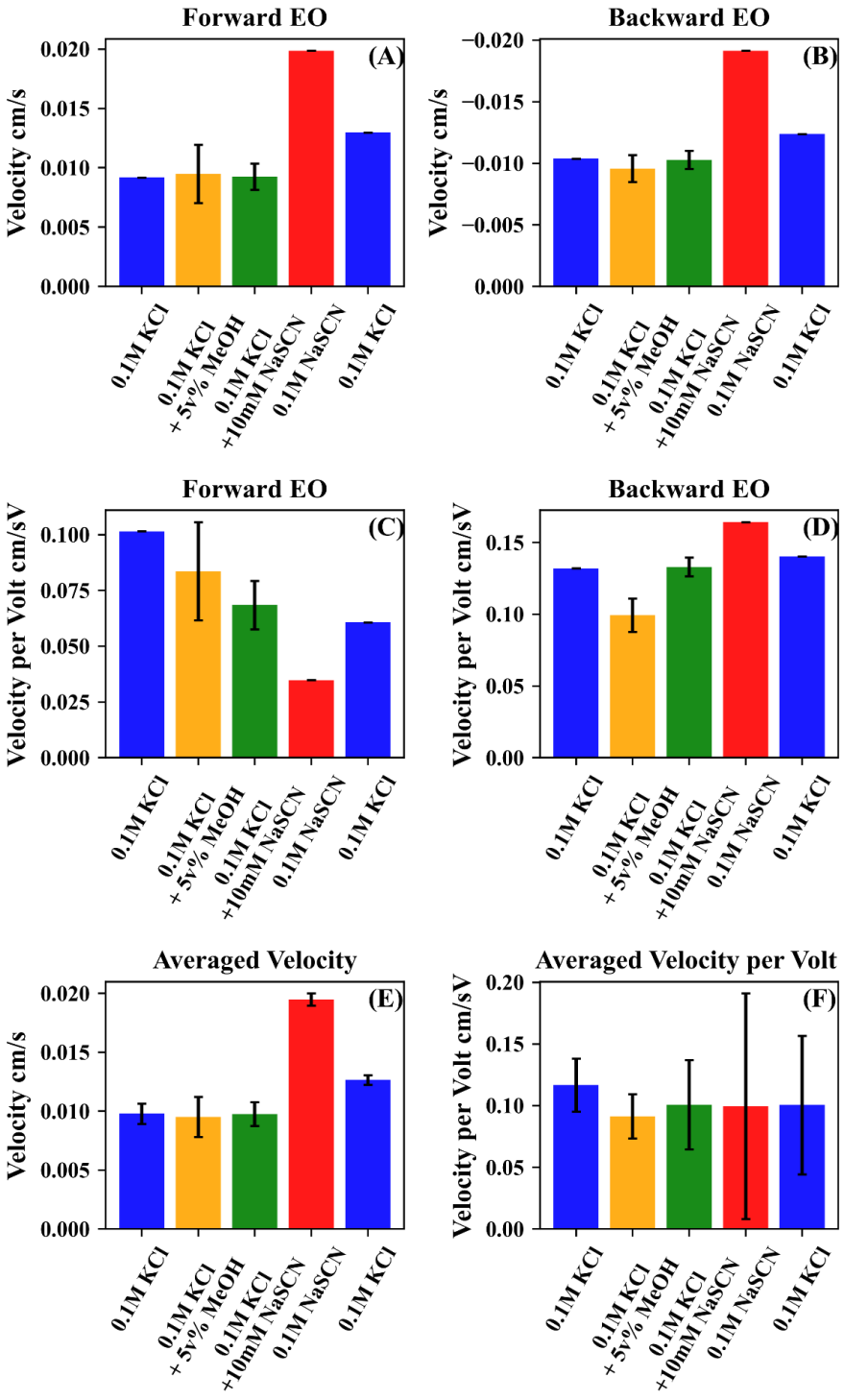

Figure 5.6. Calculated electroosmosis velocity of liquid through CNT porins of different solutions. For first 0.1 M KCl data n=1, 0.1 M KCl + 5v% MeOH n=3, 0.1 M KCl + 10 mM NaSCN n=3, 0.1M NaSCN n=1, last 0.1 M KCl n=1, for (A)-(D). For (E) and (F), n is doubled to respective set.

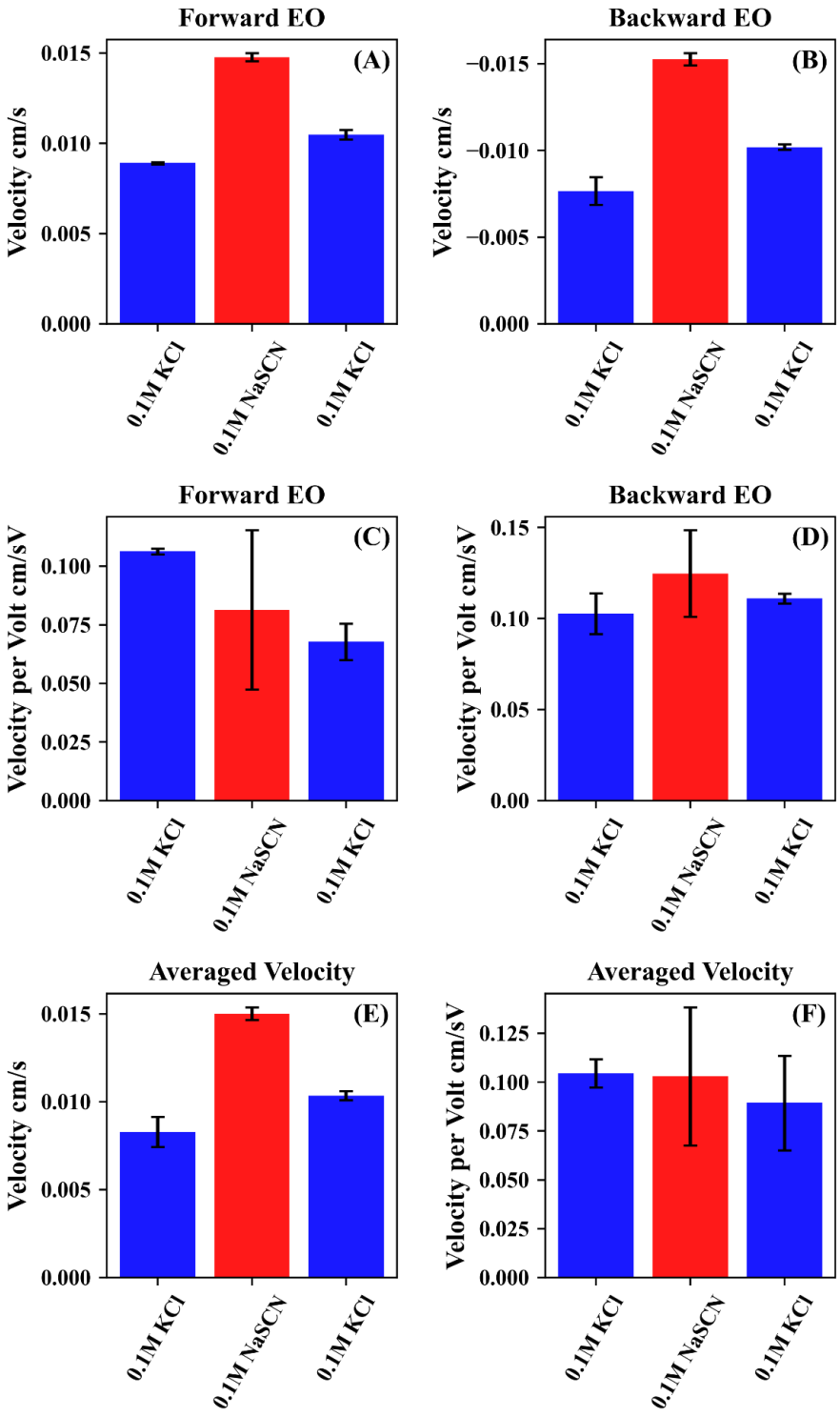

Figure 5.7. Calculated electroosmosis velocity of liquid through CNT porins of 0.1 M KCl and 0.1 M NaSCN after replacing AgCl electrode. For all the data shown n=3 for (A)-(D), while n=6 for (E) and (F).

As suggested by simulation works discussed previously, ordered water structure was expected promote water transfer through the core of CNTs. [3, 28, 32] To intentionally disrupt the ordering of water, methanol and sodium thiocyanate (NaSCN) were added to 0.1 M KCl solutions. [51, 52] However, the observed velocities of MeOH (0.095 ± 0.0017 cm/s or 0.091 ± 0.018 cm/sV) and NaSCN (0.0098 ± 0.0010 cm/s or 0.0 ± 0.036 cm/sV) mixtures, depicted as yellow and green bars in Figure 5.6, were not significantly different from the velocity of the simple 0.1 M KCl solution. More counterintuitively, the velocity observed with 0.1 M NaSCN, 0.019 ± 0.0005 cm/s, was almost twice that of the EO performance of the KCl solution, as indicated by the red bars in Figure 5.6 (A) and (B). This high flux velocity was driven by an increased cross-membrane potential. Thus, after accounting for the applied potential, the EO velocity of the 0.1 M NaSCN solution was calculated to be 0.10 ± 0.09 cm/sV, comparable to the EO velocity of the 0.1 M KCl. It should be noted that the large deviation in velocity resulted from the difference between forward and backward EO potential operated in a galvanic mode with 10 μA current. Given the critical role of AgCl electrode reactions, as depicted in Figure 5.8, in maintaining electroneutrality across the membrane, the wear and deterioration of the AgCl electrodes became evident over the course of the experiment. This deterioration resulted in an increase in applied potential due to the disruption of the reaction balance caused by the absence of Cl^- ions in the solution. After replacing Ag electrodes, another set of experiments involving KCl and NaSCN electroosmosis pumping was conducted in triplets and summarized in Figure 5.7 to eliminate the influence of electrode wear. It is clear that the observed EO velocity for NaSCN is indeed faster than the velocity for KCl, measuring at 0.015±0.00037 cm/s. Additionally, the potential-normalized velocity, averaging 0.10±0.035 cm/sV, aligns with the previous measurements. Overall, the observation suggests that

the interruption of hydrogen bonds, and thus the disruption of the predicted structural water, did not significantly obstruct the water flow within the core of the CNT.

Because the electroosmosis flux direction aligns with the electric field direction, it was believed that the electrophoretic motion of cations was responsible for the electroosmosis flux. However, it should be noted that both cations and anions contribute to the cross-membrane ionic current while moving in opposite directions, as illustrated in Figure 5.8. The electroosmotic motion of water can be analogized as a piston of cations pushing the water molecules along the cylinder of a carbon nanotube. Since all tests were performed under a galvanostatic setting of 10 μA, the transfer rate (charge/unit time) of "pistons" remain the same for all tests.

This model can be then employed to interpret the velocity behavior of the 0.1 M NaSCN solution. In this case, the cation, sodium ion, has the same charge and a larger hydrated radius compared to the potassium ion (3.58 Å and 3.31 Å for hydrated Na^+ and K^+). [53] Furthermore, the anion thiocyanate is also larger than chloride (2.42 Å and 2.24 Å for hydrated SCN^- and Cl^-). [54] Therefore, a larger electric force is required to drive the motion of the ion pair with a larger size. Simultaneously, more water molecules are transferred through the CNT conduit due to the increased electric field force. This, in turn, results in a higher observed flux velocity, but there is no significant difference in velocity when the field effect is normalized.

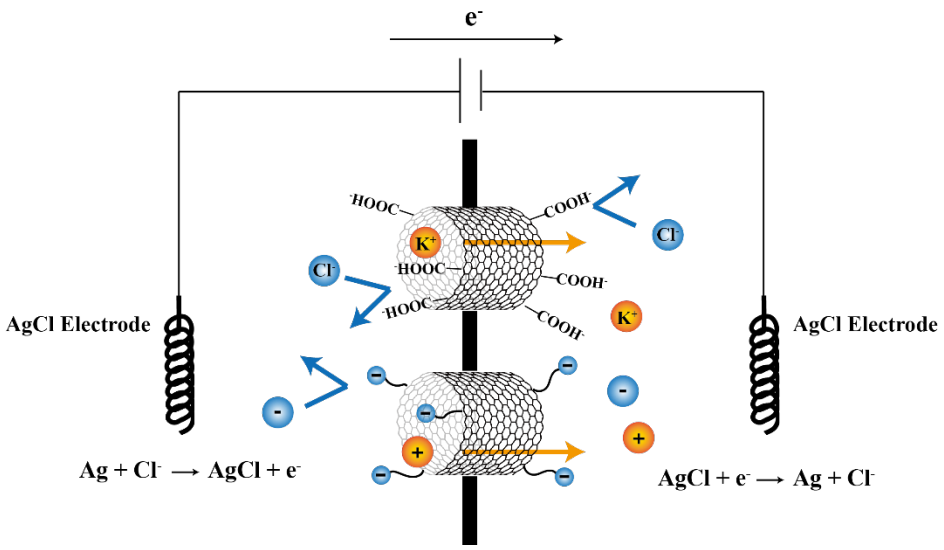

Figure 5.8. Schematic demonstration of electric cell setup with ion motion direction denoted by arrows and electrode reaction expected for chloride solution.

5.3.3 *Electroosmosis Pumping with Divalent Cations*

Divalent cations carry more charge compared to monovalent cations and are generally larger in size. The radius of hydrated calcium ion (Ca^{2+}) and tris(bipyridine) ruthenium ion ($Ru(bpy)_3^{2+}$) is 4.1 Å and 5.5 Å, respectively. [20, 53] Considering the DWCNT used for this study has an inner diameter of 13-20 Å and the predicted "depletion region" near the wall of CNT, only one of these selected cation will fit into the core of CNT at one time. Therefore, it can be expected that the electroosmosis pumping of these larger ion pairs requires a higher applied potential, which is in line with experimental observations.

As shown in Figure 5.9 (green bar) with freshly reset electrodes, the observed electroosmosis velocity of the 33.3 mM $CaCl_2$ solution is measured at 0.016±0.00032 cm/s or 0.089±0.0024 cm/sV with applied potential normalized. The higher velocity was believed to result from a tighter fit between the cation and the CNT conduit. This matching in size eliminated the chance for water molecules to slip through the gap between the cation "piston" and CNT "cylinder," thus making the EO pump more efficient. However, a larger amount of energy is also required to fit Ca^{2+} into

the CNT conduit due to the larger ion size and less number, halved, of cation carrying the charge compared to monovalent cation. Therefore, after accounting for the greater applied potential across the CNT membrane, the calculated EO velocity did not significantly differ from the performance of the 0.1 M KCl solution, which has the same ionic strength. But it should be noted that, since less cation of calcium was involved with the electroosmosis transfer of water, the real transfer efficiency, or the number of water molecules being pumped by a single cation, was doubled.

As for the other divalent cation, $Ru(bpy)_3^{2+}$, the EO performance is shown as the red bar in Figure 5.9. The observed electroosmosis velocity for the 33.3 mM $Ru(bpy)_3Cl_2$ solution was found to be 0.0065±0.0028 cm/s or 0.033±0.013 cm/sV. Unlike $CaCl_2$, the larger size of $Ru(bpy)_3^{2+}$ did not positively influence the electroosmosis flux. The proposed hypothesis explaining this phenomenon is that the $Ru(bpy)_3^{2+}$ ion is too large to allow the passage of the counter ion in the opposite direction without significant disruption of water molecules being transferred along. Therefore, both the observed and potential-normalized EO velocity of $Ru(bpy)_3Cl_2$ was found to be lower than that of the KCl solution with the same ionic strength, even with a higher applied potential. Another factor that might contribute to the slower than expected EO flux is that the aromatic pyridine ligand may impose π-bond interactions with the CNT conduit and slow down the transport. Considering that the molecule orientation required for π-bond stacking is not favored for fluidics, the influence of this factor was considered minor.

It should also be noted that since galvanostatic settings govern the number of charge transfers per unit time, and divalent cations carry more charge, the actual number of water molecules being transported per cation should be doubled. According to this hypothesis, the estimation of EO efficiency by larger divalent cations should be increased.

5.3.4 *Electroosmosis Pump with π-bond Interaction*

Benzyl alcohol (PhMeOH), at a concentration of 3 vol %, was added to water to create a 0.1 M KCl solution mixture for electroosmosis pumping tests. The EO velocity of this mixture is presented as the gray bar in Figure 5.9. More than a *tenfold* decrease in EO velocity was observed with the addition of PhMeOH, measuring at 0.0044±0.00044 cm/s or 0.0083±0.0031 cm/sV. The applied potential across the membrane during the EO test with this 0.1 M KCl water-PhMeOH mixture solution is comparable to a simple 0.1 M KCl aqueous solution. This implies that the energy required for K^+ to enter and transfer through the CNT conduit remains the same. Furthermore, since the galvanostatic setting dictates the same cation transfer rate, the slower electroosmosis flow of water cannot be attributed to a lower "piston," K^+, velocity.

The molecular structure of Ph-MeOH can influence water flow through two possible mechanisms, corresponding to the alcohol and aromatic part of the molecule. Alcohol interaction with water through hydrogen bonding was believed to interrupt the ordering of the water structure and potentially slow the transfer velocity. However, previous discussions with MeOH addition demonstrated a negligible influence. Then the aromatic portion of the PhMeOH was naturally suspected to be the reason for the reduced EO velocity. Since CNTs are made of hexagonally arranged carbon atoms, they inherently possess a shared π orbital parallel to their surface. Such a π orbital or π bond has a high affinity for aromatic compounds through π-bond stacking. [55] Thus, PhMeOH is expected to adhere to the inner surface of the CNT conduit. The adhered PhMeOH molecules would then disrupt the atomic-level smoothness of the CNT inner surface. As the near ‘frictionless’ surface is critically important for liquid transport through the CNT conduit, the "roughened" surface leads to a significantly decreased electroosmosis velocity. Other studies that

intentionally disrupt the smooth surface also demonstrated decreased liquid transfer velocity. [21, 56]

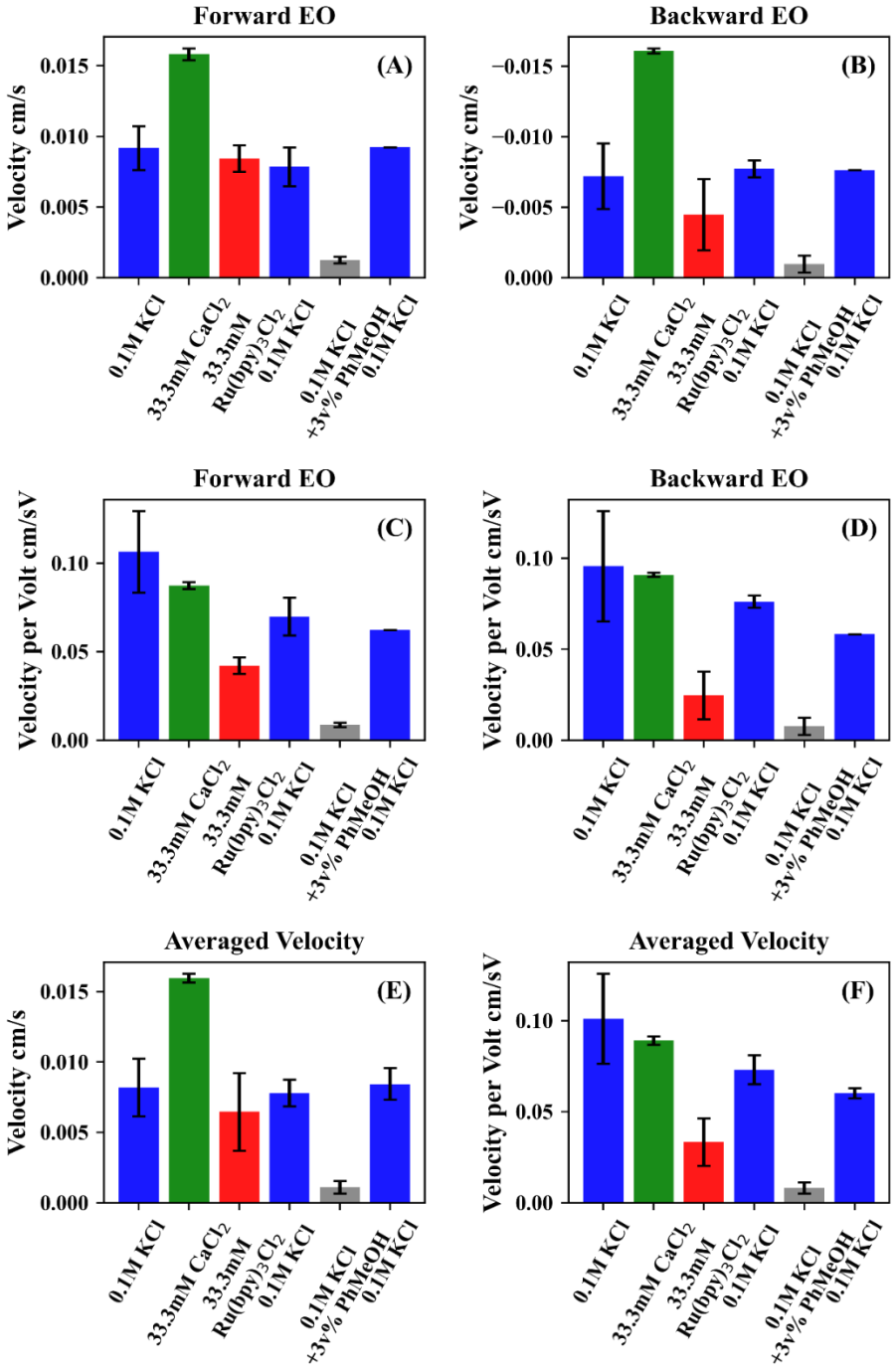

Figure 5.9. Calculated electroosmosis velocity of liquid through CNT porins of different solutions after replacing AgCl electrode. For all data shown n=3 for (A)-(D) and n=6 for (E) and (F), except the last 0.1 M KCl n=1 for (A)-(D) and n=2 for (E) and (F).

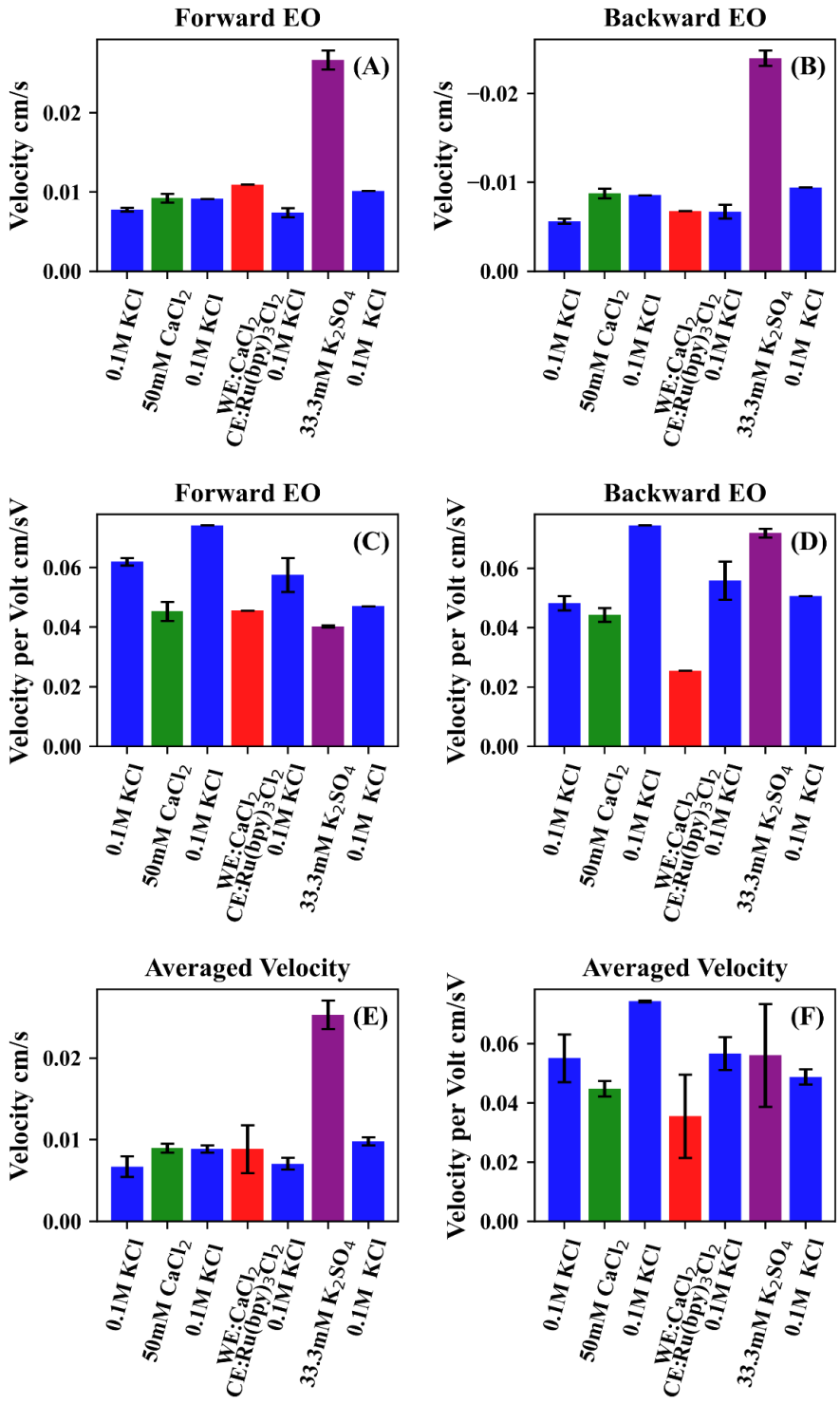

Figure 5.10. Calculated electroosmosis velocity of liquid through CNT porins of different solutions after replacing AgCl electrode. For all data shown n=3 for (A)-(D) and n=6 for (E) and (F), except the second and last 0.1 M KCl test n=1 for (A)-(D) and n=2 for (E) and (F).

5.3.5 *Electroosmosis Pump with Asymmetric Solution*

Another set of electroosmosis pumping tests was conducted after resetting the cell with fresh electrodes, as shown in Figure 5.10 and Figure 5.11. An asymmetric pumping test, shown as red bars, was performed with the working electrode (WE) side solution containing 33 mM $CaCl_2$ and the counter electrode (CE) side solution containing 33 mM $Ru(bpy)_3Cl_2$. As demonstrated previously, Ca^{2+} has a positive impact on the electroosmosis flux while $Ru(bpy)_3^{2+}$ has a negative influence on the EO phenomenon. By placing both solution sides next to each other for the test, the pumping difference is again demonstrated by EO tests under forward and backward pumping bias, as shown in Figure 5.10 (A) and (B). Upon repeating the same EO pumping test as shown in Figure 5.11, the velocity difference was sustained.

Cyclic voltammetry was employed to examine the difference in electrophoretic motion of these divalent cations. The higher current value (24 μA) at 0.5 V, compared to the value (18 μA) at -0.5 V, suggests that the forward pumping bias, involving the transfer of Ca^{2+} ions, is favorable over the backward pumping bias, involving the transfer of $Ru(bpy)_3^{2+}$. This indicates that the energy required for Ca^{2+} to enter the CNT conduit is smaller than the energy required for $Ru(bpy)_3^{2+}$, confirming the discussion in section 5.3.3.

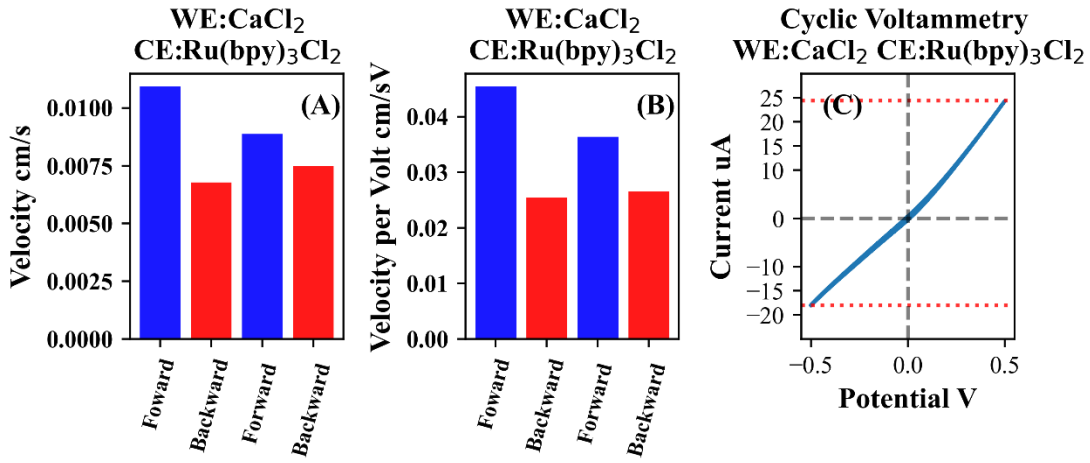

Figure 5.11. Bar charts of velocity value (A) and potential-normalized velocity value (B) of electroosmosis pumping with working electrode side solution $CaCl_2$ and counter electrode side solution $Ru(bpy)_3Cl_2$ and cyclic voltammetry scan with same electrode-solution setting (C).

Furthermore, since the $CaCl_2$ solution (at WE) is colorless, the transfer of $Ru(bpy)_3Cl_2$ (from CE) under backward EO pumping bias was quantified by measuring the $Ru(bpy)_3Cl_2$ concentration in the WE cell after the test with UV-vis spectroscopy. Assuming the galvanostatic current was carried by the motion of cation, $Ru(bpy)_3^{2+}$, with a charge of 2, the accumulation of cation can be calculated by converting the current to charge transfer per unit time then factor in the electroosmosis pumping time with following equation:

$$C = \frac{I \cdot e \cdot t}{z \cdot V \cdot N_a} \qquad (5.7)$$

Where C is the calculated concentration, I is the ionic current, e is the elementary charge, t is EO pump time, z is the cation charge number, V is the volume of electrode cell, and N_a is the Avogadro's constant The calculated concentration and observed concentration of $Ru(bpy)_3Cl_2$ in the WE cell were summarized in table 5.2.

Overall, the observed concentration of $Ru(bpy)_3Cl_2$ is in good agreement with the estimation. The matching of current and cation transfer further strengthens the association of electroosmosis

flux with cation electrophoresis motion. The reason for the less observed $Ru(bpy)_3Cl_2$ transfer was attributed to the combined effect of a small electrode cell, polarization of $Ru(bpy)_3Cl_2$ concentration near the CNT membrane, and depleted concentration of $Ru(bpy)_3Cl_2$ in the counter electrode cell.

Table 5.10. Average potassium adsorption capacity of CE silica gel with different CE:Si ratio.

Potassium Adsorption Capacity (mmol K^+/g adsorbent)						
Adsorption Capacity (mmol/g)	Control Gel	1:4.0 CE:Si Gel	1:7.9 CE:Si Gel	**1:10.6 CE:Si Gel**	1:15.9 CE:Si Gel	1:23.8 CE:Si Gel
Average	0.037	0.050	0.079	**0.109**	0.089	0.085
Std	0.008	0.020	0.025	**0.016**	0.014	NA

5.3.6 *Electroosmosis Pump with Divalent Anion*

Similar to the case of divalent cations, the influence of anion size and valence was studied by electroosmosis pumping 0.33 mM K_2SO_4 across the CNT membrane. The larger anion of $SO4^{2-}$, with a hydrated diameter of 5.46 Å, was generally thought to impose a bigger interruption of the electroosmosis flux of water. [54] However, because the cation, K^+, used for this test is only about 3.3 Å, this ion pair was expected to have a higher chance of escaping the screening of entrance charge group and pass in opposite directions through the core of CNT (13-20 Å).

The observed EO velocity of 0.33 mM K_2SO_4 was found to be 0.025±0.0017 cm/s, which is almost 4 times the observed EO velocity of 0.1 M KCl in the same set of experiments. This increase in observed EO velocity was accompanied by an increased applied potential, 4 times compared to the potential applied for the 0.1 M KCl solution. Such higher potential was suspected to be the result of lack of chlorine ion similar to the case of NaSCN test. Therefore, the increase in the observed EO velocity was attributed to the combined effect of an increased electric field and fewer

anions transferred per unit time. As can be expected, after normalizing the applied potential, the EO velocity of K_2SO_4 was found to be 0.056±0.017 cm/sV, which is similar to the velocity found with 0.1 M KCl within the same group.

5.3.7 *Normalized Electroosmosis Velocity*

Due to the delicate nature of the fabricated carbon nanotube membrane and the wear experienced by the AgCl electrode sets, it becomes challenging to directly utilize the obtained velocity values for a quantitative comparison of electroosmotic behavior across different CNT membranes and various experimental setups. To mitigate these challenges, we adopted a normalization approach.

Considering that the initial measurement conducted with freshly prepared AgCl electrodes is anticipated to be the least affected by electrode wear, we designated the first set of measurements of electroosmotic velocity in a 0.1 M KCl solution as our reference dataset. This reference dataset serves as a baseline against which we compare and normalize the electroosmotic velocities observed in different solutions and under varying experimental conditions. This normalization strategy allows us to effectively bring together electroosmotic velocity data from different experiments, enabling meaningful comparisons across the studied variables.

As summarized in Figure 5.12 (A) and Table 5.3, NaSCN, $CaCl_2$, and K_2SO_4 significantly improved the observed EO velocity. This improved EO velocity was attributed to the increased potential applied. The decreased EO flux in the presence of $Ru(bpy)_3Cl_2$ is thought to be due to the spatial hindrance of large cations, which limits the passage of anions. Additionally, PhMeOH was found to significantly obstruct the EO flux by inducing friction between the CNT surface and the fluid. Notably, no significant difference was observed with the addition of a small fraction of MeOH and NaSCN to the KCl solution system.

Remarkably, when examining the potential-normalized velocity comparison, as illustrated in Figure 5.12 (B) and Table 5.3, it becomes apparent that NaSCN, $CaCl_2$, and K_2SO_4 did not yield such significant improvements in EO velocity. In fact, the electroosmotic pumping of KCl, NaSCN, and K_2SO_4 exhibited nearly identical behaviors. $CaCl_2$, on the other hand, exerted a negative influence on the EO flux, albeit not statistically significant. A negative influence of a similar magnitude was also observed upon the addition of MeOH and NaSCN, likely due to their affinity with the CNT surface. The stronger π-interaction between PhMeOH and the CNT surface resulted in a noteworthy reduction in EO velocity. A similar mechanism can be invoked to interpret the low EO velocity observed with the $Ru(bpy)_3Cl_2$ solution.

Through the normalization analysis, it was found that the valence difference of cation and anion are diminished with potential-normalized velocity comparison. And the solvent or solute affinity to the CNT surface poses a more dominant influence on the electroosmosis flow.

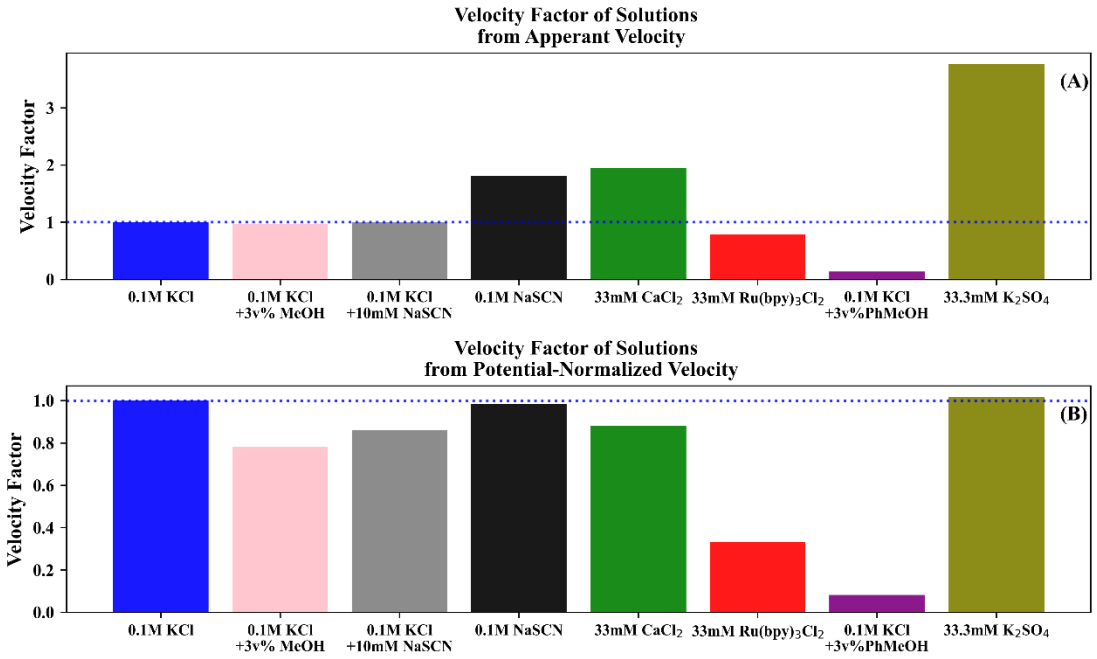

Figure 5.12. Visualization of normalized electroosmosis velocity of solutions of same ionic strength

Table 5.11. Normalized electroosmosis velocity factor of solutions of same ionic strength.

		Solution of 100 mM Ionic Strength							
		KCl	KCl + 3v% MeOH	KCl+ 10% NaSCN	NaSCN	$CaCl_2$	$Ru(bpy)_3Cl_2$	KCl + 3v% Benzyl Alcohol	K_2SO_4
Velocity Factor	Observed	1.00	0.97	1.00	1.81	1.95	0.79	0.14	3.77
	Potential Normalized	1.00	0.78	0.86	0.99	0.88	0.33	0.08	1.02

5.3.8 *Electroosmosis Pump with Solution of Different Ionic Strength*

As the preceding discussion primarily focused on electroosmosis pumping using solutions of identical ionic strength, we conducted a preliminary examination of the influence of ionic strength. The results of this exploration are summarized in Table 5. 4, where the velocity readings obtained with different solutions were normalized with respect to the velocity measured in the 0.1 M KCl solution.

Counterintuitively, it appears that lower solution concentrations yielded higher electroosmosis velocities. Even when accounting for the effect of applied potential, we observed a 30% increase in EO velocity for the 30 mM KCl solution and a 70% increase for the 10 mM KCl solution when compared to the 100 mM KCl solution. The 33 mM CaCl2 solution possesses the same ionic strength as the 100 mM KCl solution. Increasing the concentration of CaCl2 to 50 mM actually led to a reduction in EO velocity, approximately by 10%.

The observed trends may suggest the presence of an optimal electroosmotic ionic strength for carbon nanotubes with diameters ranging from 13 to 20 Å. This optimal ionic strength likely arises from the intricate interplay among various factors, including the Debye screening length, the scarcity of cations and anions, disparities in energy barriers for cations and anions entering the CNT pores, differences in electrophoretic mobility between cations and anions, and potential interruptions in anion transport, among others. However, it is important to note that due to limitations in our research capacity, further exploration in this specific direction has not been pursued. Additionally, the use of higher solution concentrations was necessitated in order to prolong the lifespan of the AgCl electrodes.

Table 5.12. Velocity Factor of Solution of Different Concentrations. a: test done with CNT membrane AS10, b: test done with CNT membrane AS68.

		KCl[a]			**$CaCl_2$[b]**	
	Concentration (mM)	10	30	100	33.3	50
Velocity Factor	Observed	8.01	4.13	1.00	1.95	1.34
	Potential-Normalized	1.77	1.39	1.00	0.88	0.81

5.3.9 *Electroosmosis Pumping for Drug Delivery*

Given that the electroosmosis velocity reached levels as high as 0.1 cm/sV, and the successful demonstration of molecule transfer across the membrane using $Ru(bpy)_3Cl_2$, we had high expectations for achieving efficient cross-membrane transfer of selected molecules through electroosmosis pumping. The carbon nanotube membranes employed in this study have thicknesses of 5 or 10 μm. When we compare the EO flux at the 0.1 cm/sV level to the membrane thickness, it becomes evident that the membrane thickness constitutes less than 0.1% of the flow length for a period of 1 second. Consequently, we anticipated that the cross-membrane delivery of marker molecule would not be significantly influenced by differences in CNT thickness.

While caffeine molecules are generally considered to be electrically neutral and, therefore, unaffected by external electric fields, an intriguing phenomenon emerged when 0.1 M caffeine was mixed with 0.1 M KCl. Remarkably, significant cross-membrane transfer of caffeine was observed, occurring in the direction of the applied electric field. This phenomenon is illustrated in Figure 5.13 (A), where all examined CNT membranes displayed a substantial increase, up to 10 times, in caffeine flux compared to simple diffusion without the assistance of an electroosmotic pump. This observation provides direct evidence of cross-membrane drug delivery facilitated by the electroosmotic flux of water.

However, upon a quantitative analysis of the transfer of potassium ions and caffeine, it became apparent that, under the influence of the applied potential, the ratio of K^+ to caffeine transferred across the membrane was approximately 100:1. The substantial amount of potassium ions required for caffeine transfer is suspected to be associated with the aromatic nature of caffeine, a characteristic previously discussed as a potential impediment to the electroosmotic flow.

Unlike caffeine, nicotine molecules carry a charge and are therefore susceptible to the influence of an electric field. When subjected to an applied cross-membrane potential, nicotine serves as a charge carrier, contributing to the overall ionic current. Consequently, the electroosmotic pumping of nicotine solution at a concentration of 0.7 M, which is positively charged at pH 8, was found to be notably more efficient. As illustrated in Figure 5.13 (B), the nicotine flux under the influence of applied potential exceeded 300 μmol/cm2hr, while the diffusion signal remained below 30 μmol/cm2hr. This substantial increase in nicotine flux, over tenfold, when aided by electroosmosis pumping aligns closely with our earlier findings in the caffeine study, confirming the effectiveness of EO induce molecule transfer and showcasing promising potential in drug delivery application. It is noteworthy that during the nicotine pumping tests, no significant differences in nicotine flux were observed with CNT membranes of varying thicknesses. This consistency can be attributed to the high electroosmotic velocity.

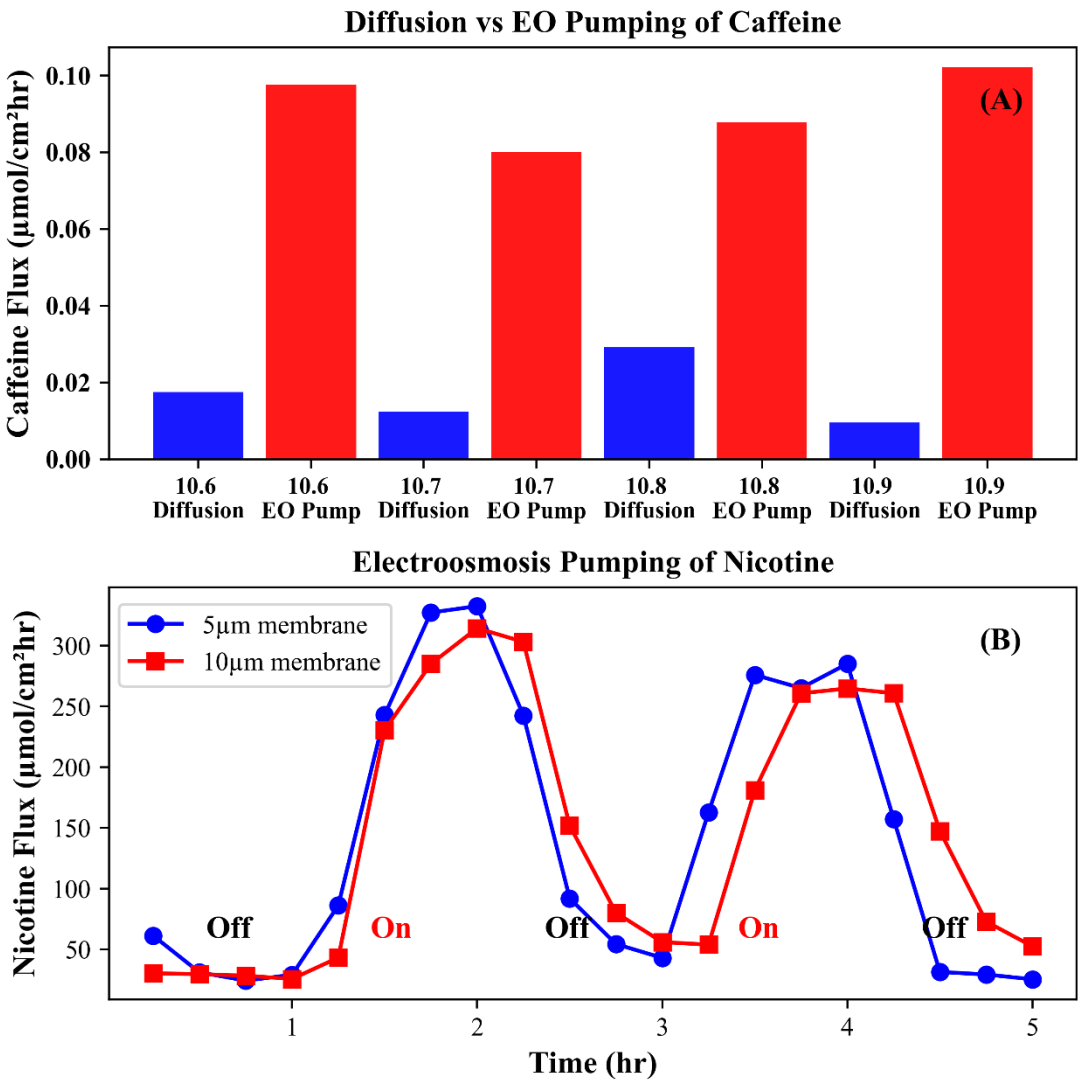

Figure 5.13. Bar chart comparison between static diffusion versus electroosmosis pumping of caffeine on 4 CNT membranes (A) and nicotine flux under external electric field in on/off cycles (B). All membranes shown were functionalized with direct blue 71.

Overall, it is evident that the high electroosmotic velocity enables the CNT platform to achieve high-efficiency transfer of selected marker molecules. Notably, the enhanced molecule transfer due to electroosmosis remained consistent irrespective of the membrane thickness. This demonstrates the robustness of the approach. Furthermore, the response of electroosmotic

molecule transfer to external electric potential was found to be significant, underscoring the versatility and potential of this method.

5.4 CONCLUSION

In this chapter, we presented the synthesis and fabrication of robust carbon nanotube (CNT) membranes with attached electrodes for the exploration of electroosmosis phenomena. All synthesized CNT membranes were observed to possess porosities ranging from the 10^{-6} to 10^{-4} level, as determined through the diffusion of marker molecules. While higher porosity is advantageous for observing transmembrane flux, it also comes with an increased risk of leakage due to the delicate nature of the fabricated membranes.

Subsequently, we set up capillary U-tubes using the membrane-electrode cell we created to investigate electroosmosis phenomena. This setup allowed for the visual observation of water transfer across CNT membranes driven by electroosmosis. We calculated the observed electroosmotic (EO) velocity of water through the CNT conduit by monitoring the volume change of water in both capillary tubes on either side of the CNT membrane. The EO flux of a 0.1 M KCl solution was found to have a velocity as high as 0.0098 ± 0.00086 cm/s or 0.12 ± 0.022 cm/sV when normalized for applied potential. This observation is consistent with previous studies.

We also examined the influence of solutes and additives on the system. The addition of 3 vol% MeOH and 10 mM NaSCN to a 0.1 M KCl solution was expected to disrupt the hydrogen bonding of water molecules within the CNT cores. Both of these agents were found to have a negative effect on EO flow, although not as significant as initially anticipated. Moreover, the test with 0.1 M NaSCN showed a significant increase in EO velocity at 0.020 ± 0.0005 cm/s. This increase was attributed to the higher applied cross-membrane potential. Consequently, after normalizing for the

effect of applied potential, the EO velocity of the 0.1 M NaSCN solution was determined to be 0.10 ± 0.091 cm/sV, which is comparable to the performance of the 0.1 M KCl solution.

Additionally, due to the increased applied potential, the electroosmosis velocity observed with 33 mM $CaCl_2$ and K_2SO_4 solutions exhibited a significant increase to 0.016 ± 0.00032 cm/s and 0.025 ± 0.0018 cm/s, respectively. Similarly, after normalizing for applied potential, both $CaCl_2$ and K_2SO_4 solutions exhibited normalized EO velocities comparable to the 0.1 M KCl solution. This increase in applied potential was associated with the larger size of the cation or anion in the ion pair, which in turn increased the energy required for entry into the CNT conduit.

Negative influences on electroosmosis flow were introduced by aromatic compounds. The addition of 3 vol% benzyl alcohol resulted in a tenfold decrease in EO velocity to 0.0011 ± 0.00044 cm/s or 0.0083 ± 0.0031 cm/sV. The interruption of the smoothness of the CNT surface due to the adhered aromatic molecules was believed to be the primary reason for this phenomenon. The divalent cation $Ru(bpy)_3^{2+}$ was also found to reduce electroosmosis velocity, presumably due to similar mechanisms, although the effect was less pronounced when compared to PhMeOH.

By normalizing the acquired velocity data with respect to the performance of the 0.1 M KCl solution, we were able to systematically compare the electroosmosis velocity behavior across different carbon nanotube membranes and electrode sets. Our analysis revealed that the smoothness of the CNT core is the most dominant factor influencing the electroosmotic flow through the CNT conduit. The effect of ion size and valence was found to be diminished when potential normalization was applied. Additionally, we observed that the concentration or ionic strength of the solution exerted an intriguing influence on the electroosmosis flow. Lower ionic strength was associated with higher EO velocity, even after compensating for the applied potential.

The electroosmosis flow was harnessed as a means to actively transport marker molecules across the membrane. With the application of an external potential, the flux of these marker molecules increased by over tenfold compared to the flux achieved through simple diffusion. It was observed that uncharged caffeine molecules exhibited a lower overall flux in comparison to nicotine, which carries a positive charge. This discrepancy in flux suggests differences in pumping efficiency attributable to the distinct charge carriers. Furthermore, we quantified the pumping of $Ru(bpy)_3Cl_2$ using UV-vis spectroscopy, which revealed a notable alignment between the observed transfer of $Ru(bpy)_3Cl_2$ and estimations based on the ionic current measurements.

In brief, a robust carbon nanotube membrane platform was created to study electroosmosis. Experiments with different solutions and additives showed potential for efficient molecule transfer across the membrane, which is the fundamental of chemical separation and drug delivery applications.

5.5 Future Outlooks

There are several promising directions for future work that are expected to enhance the investigation of electroosmosis phenomena within nanoconfinement.

Firstly, enhancing the porosity of the fabricated nanofluidic cell will not only improve observation accuracy but also increase the efficiency of mass transfer. This improvement will have wide-ranging applications across various fields.

Secondly, delving into the modeling of ion and molecule transfer through the CNT conduit will not only provide a better understanding of the enhanced flow velocity but also contribute to the design of more efficient nanofluidic devices.

Thirdly, for applications involving active transfer, the development of selective chemistry tailored to the species of interest is highly desirable. Such selectivity can greatly expand the utility of nanofluidic systems.

Lastly, improving the mechanical strength of the fabricated nanofluidic device is crucial for long-term and robust studies in this field.

5.6 REFERENCES

[1] Iijima, S. HELICAL MICROTUBULES OF GRAPHITIC CARBON. *Nature* **1991**, *354* (6348), 56-58. DOI: 10.1038/354056a0.

[2] Iijima, S.; Ichihashi, T. SINGLE-SHELL CARBON NANOTUBES OF 1-NM DIAMETER. *Nature* **1993**, *363* (6430), 603-605, Article. DOI: 10.1038/363603a0.

[3] Hummer, G.; Rasaiah, J. C.; Noworyta, J. P. Water conduction through the hydrophobic channel of a carbon nanotube. *Nature* **2001**, *414* (6860), 188-190, Article. DOI: 10.1038/35102535.

[4] Yao, Y. C.; Taqieddin, A.; Alibakhshi, M. A.; Wanunu, M.; Aluru, N. R.; Noy, A. Strong Electroosmotic Coupling Dominates Ion Conductance of 1.5 nm Diameter Carbon Nanotube Porins. *ACS Nano* **2019**, *13* (11), 12851-12859. DOI: 10.1021/acsnano.9b05118.

[5] Joseph, S.; Aluru, N. R. Why are carbon nanotubes fast transporters of water? *Nano Lett.* **2008**, *8* (2), 452-458, Article. DOI: 10.1021/nl072385q.

[6] Guo, S. R.; Meshot, E. R.; Kuykendall, T.; Cabrini, S.; Fornasiero, F. Nanofluidic Transport through Isolated Carbon Nanotube Channels: Advances, Controversies, and Challenges. *Adv. Mater.* **2015**, *27* (38), 5726-5737. DOI: 10.1002/adma.201500372.

[7] Holt, J. K.; Park, H. G.; Wang, Y. M.; Stadermann, M.; Artyukhin, A. B.; Grigoropoulos, C. P.; Noy, A.; Bakajin, O. Fast mass transport through sub-2-nanometer carbon nanotubes. *Science* **2006**, *312* (5776), 1034-1037, Article. DOI: 10.1126/science.1126298.

[8] Majumder, M.; Chopra, N.; Andrews, R.; Hinds, B. J. Nanoscale hydrodynamics - Enhanced flow in carbon nanotubes. *Nature* **2005**, *438* (7064), 44-44, Editorial Material. DOI: 10.1038/43844a.

[9] Wu, J.; Gerstandt, K.; Zhang, H. B.; Liu, J.; Hinds, B. J. Electrophoretically induced aqueous flow through single-walled carbon nanotube membranes. *Nat. Nanotechnol.* **2012**, *7* (2), 133-139. DOI: 10.1038/nnano.2011.240.

[10] Hinds, B. J.; Chopra, N.; Rantell, T.; Andrews, R.; Gavalas, V.; Bachas, L. G. Aligned multiwalled carbon nanotube membranes. *Science* **2004**, *303* (5654), 62-65. DOI: 10.1126/science.1092048.

[11] Miller, S. A.; Young, V. Y.; Martin, C. R. Electroosmotic flow in template-prepared carbon nanotube membranes. *J. Am. Chem. Soc.* **2001**, *123* (49), 12335-12342. DOI: 10.1021/ja011926p.

[12] Tunuguntla, R. H.; Henley, R. Y.; Yao, Y. C.; Pham, T. A.; Wanunu, M.; Noy, A. Enhanced water permeability and tunable ion selectivity in subnanometer carbon nanotube porins. *Science* **2017**, *357* (6353), 792-796, Article. DOI: 10.1126/science.aan2438.

[13] Geng, J.; Kim, K.; Zhang, J. F.; Escalada, A.; Tunuguntla, R.; Comolli, L. R.; Allen, F. I.; Shnyrova, A. V.; Cho, K. R.; Munoz, D.; et al. Stochastic transport through carbon nanotubes in lipid bilayers and live cell membranes. *Nature* **2014**, *514* (7524), 612-+. DOI: 10.1038/nature13817.

[14] Tunuguntla, R. H.; Allen, F. I.; Kim, K.; Belliveau, A.; Noy, A. Ultrafast proton transport in sub-1-nm diameter carbon nanotube porins. *Nat. Nanotechnol.* **2016**, *11* (7), 639-+. DOI: 10.1038/nnano.2016.43.

[15] Tunuguntla, R. H.; Escalada, A.; Frolov, V. A.; Noy, A. Synthesis, lipid membrane incorporation, and ion permeability testing of carbon nanotube porins. *Nature Protocols* **2016**, *11* (10), 2029-2047. DOI: 10.1038/nprot.2016.119.

[16] Qin, X. C.; Yuan, Q. Z.; Zhao, Y. P.; Xie, S. B.; Liu, Z. F. Measurement of the Rate of Water Translocation through Carbon Nanotubes. *Nano Lett.* **2011**, *11* (5), 2173-2177. DOI: 10.1021/nl200843g.

[17] Pang, P.; He, J.; Park, J. H.; Krstic, P. S.; Lindsay, S. Origin of Giant Ionic Currents in Carbon Nanotube Channels. *ACS Nano* **2011**, *5* (9), 7277-7283. DOI: 10.1021/nn202115s.

[18] Mattia, D.; Calabro, F. Explaining high flow rate of water in carbon nanotubes via solid-liquid molecular interactions. *Microfluidics and Nanofluidics* **2012**, *13* (1), 125-130. DOI: 10.1007/s10404-012-0949-z.

[19] Duan, C. H.; Majumdar, A. Anomalous ion transport in 2-nm hydrophilic nanochannels. *Nat. Nanotechnol.* **2010**, *5* (12), 848-852. DOI: 10.1038/nnano.2010.233.

[20] Wu, J.; Gerstandt, K.; Majumder, M.; Zhan, X.; Hinds, B. J. Highly efficient electroosmotic flow through functionalized carbon nanotube membranes. *Nanoscale* **2011**, *3* (8), 3321-3328. DOI: 10.1039/c1nr10303b.

[21] Majumder, M.; Corry, B. Anomalous decline of water transport in covalently modified carbon nanotube membranes. *Chem. Commun.* **2011**, *47* (27), 7683-7685. DOI: 10.1039/c1cc11134e.

[22] Buchsbaum, S. F.; Jue, M. L.; Sawvel, A. M.; Chen, C. T.; Meshot, E. R.; Park, S. J.; Wood, M.; Wu, K. J.; Bilodeau, C. L.; Aydin, F.; et al. Fast Permeation of Small Ions in Carbon Nanotubes. *Adv. Sci.* **2021**, *8* (3), 7, Article. DOI: 10.1002/advs.202001802.

[23] Kannam, S. K.; Todd, B. D.; Hansen, J. S.; Daivis, P. J. How fast does water flow in carbon nanotubes? *J. Chem. Phys.* **2013**, *138* (9). DOI: 10.1063/1.4793396.

[24] Myers, T. G. Why are slip lengths so large in carbon nanotubes? *Microfluidics and Nanofluidics* **2011**, *10* (5), 1141-1145. DOI: 10.1007/s10404-010-0752-7.

[25] Bai, J. E.; Wang, J.; Zeng, X. C. Multiwalled ice helixes and ice nanotubes. *Proceedings of the National Academy of Sciences of the United States of America* **2006**, *103* (52), 19664-19667. DOI: 10.1073/pnas.0608401104.

[26] Koga, K.; Gao, G. T.; Tanaka, H.; Zeng, X. C. Formation of ordered ice nanotubes inside carbon nanotubes. *Nature* **2001**, *412* (6849), 802-805. DOI: 10.1038/35090532.

[27] He, Z. J.; Zhou, J.; Lu, X. H.; Corry, B. Ice-like Water Structure in Carbon Nanotube (8,8) Induces Cationic Hydration Enhancement. *J. Phys. Chem. C* **2013**, *117* (21), 11412-11420, Article. DOI: 10.1021/jp4025206.

[28] Kohler, M. H.; da Silva, L. B. Size effects and the role of density on the viscosity of water confined in carbon nanotubes. *Chemical Physics Letters* **2016**, *645*, 38-41. DOI: 10.1016/j.cplett.2015.12.020.

[29] Farimani, A. B.; Aluru, N. R. Existence of Multiple Phases of Water at Nanotube Interfaces. *J. Phys. Chem. C* **2016**, *120* (41), 23763-23771. DOI: 10.1021/acs.jpcc.6b06156.

[30] Bernardina, S. D.; Paineau, E.; Brubach, J. B.; Judeinstein, P.; Rouziere, S.; Launois, P.; Roy, P. Water in Carbon Nanotubes: The Peculiar Hydrogen Bond Network Revealed by Infrared Spectroscopy. *J. Am. Chem. Soc.* **2016**, *138* (33), 10437-10443. DOI: 10.1021/jacs.6b02635.

[31] Hassan, J.; Diamantopoulos, G.; Homouz, D.; Papavassiliou, G. Water inside carbon nanotubes: Structure and dynamics. *Nanotechnology Reviews* **2016**, *5* (3), 341-354.

[32] Chatzichristos, A.; Hassan, J. Current Understanding of Water Properties inside Carbon Nanotubes. *Nanomaterials* **2022**, *12* (1). DOI: 10.3390/nano12010174.

[33] Sam, A.; Prasad, K. V.; Sathian, S. P. Water flow in carbon nanotubes: the role of tube chirality. *Physical Chemistry Chemical Physics* **2019**, *21* (12), 6566-6573. DOI: 10.1039/c9cp00429g.

[34] Qiao, R.; Aluru, N. R. Atypical dependence of electroosmotic transport on surface charge in a single-wall carbon nanotube. *Nano Lett.* **2003**, *3* (8), 1013-1017. DOI: 10.1021/nl034236n.

[35] Wang, J.; Zhu, Y.; Zhou, J.; Lu, X. H. Diameter and helicity effects on static properties of water molecules confined in carbon nanotubes. *Physical Chemistry Chemical Physics* **2004**, *6* (4), 829-835. DOI: 10.1039/b313307a.

[36] Wei, X. F.; Luo, T. F. Effects of Electrostatic Interaction and Chirality on the Friction Coefficient of Water Flow Inside Single-Walled Carbon Nanotubes and Boron Nitride Nanotubes. *J. Phys. Chem. C* **2018**, *122* (9), 5131-5140. DOI: 10.1021/acs.jpcc.7b11657.

[37] Falk, K.; Sedlmeier, F.; Joly, L.; Netz, R. R.; Bocquet, L. Molecular Origin of Fast Water Transport in Carbon Nanotube Membranes: Superlubricity versus Curvature Dependent Friction. *Nano Lett.* **2010**, *10* (10), 4067-4073. DOI: 10.1021/nl1021046.

[38] Fornasiero, F.; Park, H. G.; Holt, J. K.; Stadermann, M.; Grigoropoulos, C. P.; Noy, A.; Bakajin, O. Ion exclusion by sub-2-nm carbon nanotube pores. *Proceedings of the National Academy of Sciences of the United States of America* **2008**, *105* (45), 17250-17255. DOI: 10.1073/pnas.0710437105.

[39] Li, Z. W.; Li, Y. H.; Yao, Y. C.; Aydin, F.; Zhan, C.; Chen, Y. F.; Elimelech, M.; Pham, T. A.; Noy, A. Strong Differential Monovalent Anion Selectivity in Narrow Diameter Carbon Nanotube Porins. *ACS Nano* **2020**, *14* (5), 6269-6275. DOI: 10.1021/acsnano.0c02423.

[40] Fornasiero, F.; Bin In, J.; Kim, S.; Park, H. G.; Wang, Y.; Grigoropoulos, C. P.; Noy, A.; Bakajin, O. pH-Tunable Ion Selectivity in Carbon Nanotube Pores. *Langmuir* **2010**, *26* (18), 14848-14853. DOI: 10.1021/la101943h.

[41] Corry, B. Water and ion transport through functionalised carbon nanotubes: implications for desalination technology. *Energy & Environmental Science* **2011**, *4* (3), 751-759. DOI: 10.1039/c0ee00481b.

[42] Li, J.; Gao, S.; Long, R.; Liu, W.; Liu, Z. C. Self-pumped evaporation for ultra-fast water desalination and power generation. *Nano Energy* **2019**, *65*. DOI: 10.1016/j.nanoen.2019.104059.

[43] Das, R.; Ali, M. E.; Abd Hamid, S. B.; Ramakrishna, S.; Chowdhury, Z. Z. Carbon nanotube membranes for water purification: A bright future in water desalination. *Desalination* **2014**, *336*, 97-109. DOI: 10.1016/j.desal.2013.12.026.

[44] Song, W.; Kumar, M. Artificial water channels: toward and beyond desalination. *Current Opinion in Chemical Engineering* **2019**, *25*, 9-17. DOI: 10.1016/j.coche.2019.06.007.

[45] Wang, Q.; Song, J. S.; Gao, X. C.; Liu, L.; Liu, C. Carbon nanotube membranes for the separation of Li+ and Mg2+ ions: Effect of functional groups with charges. *Desalination* **2022**, *540*. DOI: 10.1016/j.desal.2022.115996.

[46] Gulati, G. K.; Hinds, B. J. Electrically controlled nicotine delivery through Carbon nanotube membranes via electrochemical oxidation and nanofluidically enhanced electroosmotic flow. *Biomed. Microdevices* **2021**, *23* (4), 14, Article. DOI: 10.1007/s10544-021-00580-1.

[47] Wu, J.; Paudel, K. S.; Strasinger, C.; Hammell, D.; Stinchcomb, A. L.; Hinds, B. J. Programmable transdermal drug delivery of nicotine using carbon nanotube membranes. *Proceedings of the National Academy of Sciences of the United States of America* **2010**, *107* (26), 11698-11702. DOI: 10.1073/pnas.1004714107.

[48] Sun, X. H.; Su, X.; Wu, J.; Hinds, B. J. Electrophoretic Transport of Biomolecules through Carbon Nanotube Membranes. *Langmuir* **2011**, *27* (6), 3150-3156. DOI: 10.1021/la104242p.

[49] Wang, J. Carbon-nanotube based electrochemical biosensors: A review. *Electroanalysis* **2005**, *17* (1), 7-14. DOI: 10.1002/elan.200403113.

[50] Majumder, M.; Chopra, N.; Hinds, B. J. Effect of tip functionalization on transport through vertically oriented carbon nanotube membranes. *J. Am. Chem. Soc.* **2005**, *127* (25), 9062-9070, Article. DOI: 10.1021/ja043013b.

[51] Finneran, I. A.; Carroll, P. B.; Allodi, M. A.; Blake, G. A. Hydrogen bonding in the ethanol-water dimer. *Physical Chemistry Chemical Physics* **2015**, *17* (37), 24210-24214. DOI: 10.1039/c5cp03589a.

[52] Fileti, E. E.; Chaudhuri, P.; Canuto, S. Relative strength of hydrogen bond interaction in alcohol-water complexes. *Chemical Physics Letters* **2004**, *400* (4-6), 494-499. DOI: 10.1016/j.cplett.2004.10.149.

[53] Nightingale, E. R. PHENOMENOLOGICAL THEORY OF ION SOLVATION - EFFECTIVE RADII OF HYDRATED IONS. *J. Phys. Chem.* **1959**, *63* (9), 1381-1387. DOI: 10.1021/j150579a011.

[54] Marcus, Y. Thermodynamics of solvation of ions. Part 5.—Gibbs free energy of hydration at 298.15 K. *Journal of the Chemical Society, Faraday Transactions* **1991**, *87* (18), 2995-2999.

[55] Tournus, F.; Charlier, J. C. Ab initio study of benzene adsorption on carbon nanotubes. *Physical Review B* **2005**, *71* (16). DOI: 10.1103/PhysRevB.71.165421.

[56] Majumder, M.; Chopra, N.; Hinds, B. J. Mass Transport through Carbon Nanotube Membranes in Three Different Regimes: Ionic Diffusion and Gas and Liquid Flow. *ACS Nano* **2011**, *5* (5), 3867-3877. DOI: 10.1021/nn200222g.

Chapter 6. CATALYTIC REDUCTION OF GRAPHENE OXIDE MEMBRANES AND WATER SELECTIVE CHANNEL FORMATION IN WATER–ALCOHOL SEPARATIONS

Adapted from previous open access publication: Yushi Zang, Alex Peek, Yongsoon Shin, David Gotthold and Bruce J. Hinds "Catalytic Reduction of Graphene Oxide Membranes and Water Selective Channel Formation in Water-Alcohol Separations". Membranes 2021, 11,317. https://doi.org/10.3390/membranes11050317 [1]

6.1 INTRODUCTION

Graphene oxide (GO) is a promising membrane system for applications in chemical separations due to enhanced 2-D nanofluidics properties and an ability to control inter-planar spacing for size-based chemical exclusion. Dramatic flow rate enhancements of 3–4 orders of magnitude have been experimentally seen through carbon nanotube (CNT) membranes with the atomically smooth surface of the graphitic planes making the tube walls. [2,3] Molecular dynamics simulations show that in addition to atomic smoothness,[4] water molecules can be structured to a single-chain conformation connected by two hydrogen bonds, giving flow rates greater than aquaporin water channels. [5] A similar phenomenon was also observed in 2-D atomically flat channels of graphene with near-frictionless fast transport of liquid molecule [6,7] and, similarly, large slip length for graphene nanochannels.[6,8] Water molecules confined in 2-D channels of graphene were also observed to have an ordered structure different from bulk water, including "square ice" 2-D ordering. [9–11] Simulations of H-bonding of water within GO membranes pre-dict slow water diffusion, [12] adding complexity to this system for determining the dom-inant

transport mechanisms. Additionally, nano-confinement effects give selectivity to-wards different chemical species. [7,10,13–15] However, the fabrication of mechanically robust membranes with 2-D channels and high porosity over large surface areas remains a challenge and is required for systematic chemical transport and selectivity studies.

Graphene oxide is produced by an industrially scalable process of chemically oxidizing bulk graphite, which is readily dispersed in aqueous solutions, thereby allowing for membrane fabrication by simple filtration. The hydrophilicity of GO is due to oxidation product moieties, such as hydroxyl, carbonyl, carboxyl, and epoxide groups covering roughly 18–36% of total carbon sites. [16] It is important to note that such oxygen-containing moieties are not evenly distributed across the GO surface and play a complex role in determining the properties of GO nanochannels. [16,17] For instance, stronger interaction between water molecules and oxidized region of GO can cause greater hindrance of transmembrane flux. [11,18–20] Others proposed a mechanism in which the oxygen-containing groups on the entrance of GO nanochannels disrupt the hydrogen bonding of bulk water, thereby lowering entrance enthalpy and reducing flow. [21] Although the true flow dynamic inside the GO nanochannel is yet to be revealed, an ap-proximation where the fast water flow was allowed by pristine graphene region formed "frictionless channels" was proposed with good agreement with experiment permeance observations. [19,22] Aside from the chemical condition of graphene oxide sheet, the separation performance of a GO membrane is also greatly affected by its fabrication process. Common GO membrane fabrication processes include direct drop-casting, [23] filtering, [10,24] slip-casting [25,26] of GO dispersion, and mixing the GO flakes into another matrix but have widely varying reported permeances. Permeability is defined as "membrane thickness × permeance of solvent" and is more appropriate for comparison of membranes produced by different methods resulting in significantly

different thicknesses. [13,27] The membrane community commonly uses a permeance nomenclature of LMH/bar, which is liters of permeate per m^2 of membrane area per hour per bar pressure applied. For instance, one study showed that pressure-assisted filtered GO membrane could have a permeance (permeability) performance of about 2.5 kg/m^2·h (0.59 μm × liter/(m^2·h·bar) or μm × LMH/bar) with a water–alcohol (1:9) mixture, while the drop-casted membranes only show 0.9 kg/m^2·h (0.41 μm × LMH/bar). A vacuum-assisted filtered membrane shows 2.4 kg/m^2·h (0.91 μm × LMH/bar) under the same condition, demonstrating the importance of the membrane synthesis methods to give ordered laminate nanochannel structures. [24] The slip-casting process was systematically optimized for GO membrane fabrication to improve the microstructure by shear-aligning GO flakes. Such membranes were found with water permeance as high as 71 LMH/bar (10.65 μm × LMH/bar), which is over 7 times the permeance of common filtered GO membranes. [25] The fabrication processes mentioned above also influence the interlayer space, or d-space, of the GO membrane, normally about 0.8 nm at dry state. [24,26] Due to high hydrophilicity, the membrane can expand as large as 6 nm and even redisperse into a suspension when wetted with water over an extended time. [16,18] Cations stabilize the GO membrane through electrostatic screening of anions of carboxyl groups of adjacent GO sheets and can tune the d-spacing. [28] In general, GO membranes require ~10 mM salt concentration in water to prevent the membrane's dissolution, limiting its applications. Forming chemical bonds between neighboring GO sheets with a designed crosslinking chemical is another elegant way to control the d-space of GO. [29–31] Larger spacers, such as engineered nanoparticles, car-bon nanotubes, and polymers, can be intercalated in GO membranes to promote higher trans-membrane flux with larger interlayer spacing. [27,32–35]

Energy-efficient water–alcohol separation is an unmet technical challenge for bio-mass-derived sustainable energy fuels. Particularly challenging is the tight control of channel size to give water selectivity over large membrane areas. Recent advances in slip-casting have led to using an optimized shear rate to align the GO grains in 5 μm thick GO membranes for ethanol dehydration via pervaporation. [26] Studies have purposed a concept of critical thickness, which is the required GO membrane thickness to avoid defect like pinholes that goes across the membrane, with 5 μm being a usable thickness. [13,14,23] Interestingly, in the pervaporation study, fluxes dropped dramatically for water–alcohol mixture, but not for individual components. [26] A similar flux decrease phenomenon was also observed in an attempt to separate water from ethanol and isopropyl alcohol. [23,36] Proposed mechanisms include forming a water–GO complex at the GO channel entrance that reduces the effective hydrodynamic pore size of GO, excluding alcohol. [26,36] Others propose that alcohol molecules disrupt the entrance of water molecules into the GO plane.[20,37–39]

Aside from applying chemical separation, GO was also considered a strong candidate for catalyzing a wide range of reactions. As a solid catalyst, free-standing GO powder was demonstrated to convert benzylic alcohols to corresponding aldehyde and ketone at the cost of GO being partially reduced. [40] Other reactions, such as ring-opening of epoxides, can also be catalyzed by GO with a good conversion rate and product selectivity. [41] GO was also made into membranes for efficient catalyst recovery after the reaction. Another GO-based membrane system, consisting of nitrogen-doped GO synthesized via chemical vapor deposition of NH_3 and CH_4 gas, demonstrated catalytic activity toward oxygen reduction in alkaline fuel cells for the first time. [42] Applications for GO-based catalytic membrane in other fields, such as biodiesel production and organic pollutants degradation, have also been developed. [43,44]

Reported here is a study of pressure-driven liquid mass transport behavior through GO membranes fabricated by a carefully engineered slip-casting process. The permeance (permeability) of single solvents of H2O, methanol (MeOH) and isopropyl alcohol (IPA) (all with 10 mM, mmol/L, NaCl stabilizer) were 0.38 ± 0.15, 0.33 ± 0.16 and 0.42 ± 0.31 LMH/bar (1.90 ± 0.77, 1.65 ± 0.8 and 2.09 ± 1.54 μm × LMH/bar), respectively. However, after wetting the membrane with a water–alcohol mixture, the permeating flux reduced by more than tenfold. A similar flux decrease phenomenon was also observed in osmotic pressure-driven fluxes when a water–alcohol mixture was present on the feed side of the membrane. The osmotic flux can be recovered when using single component solvents. Osmosis experiments demonstrated rejection of salt and the selectivity of water over alcohol through GO membranes. This occurred with membrane color change to dark black and reduction in interplanar d-spacing by 0.2 nm. A newly proposed GO reduction mechanism by alcohol mediated by water is consistent with experiment and literature observations. [16,19,45,46] The reduction process of the GO membrane can be reversed with the addition of oxidant to restore permeance.

6.2 MATERIALS AND METHODS

Units: The units used in this study include: L for liter; mL for milliliter; g for gram; mg for milligram; rpm for revolutions per minute; h for hour; mol for mole; M for mol/L; mM for millimol/L; mm for millimeter; μm for micrometer; nm for nanometer; °C for degree Celsius; LMH for $L/m^2 \cdot h$; LMH/bar for $L/m^2 \cdot h \cdot bar$.

Chemicals: Chemicals used for this study were obtained from Sigma-Aldrich and used without further process unless otherwise stated.

6.2.1 *GO Membrane Preparation*

The GO membrane was prepared by PNNL following a previous report. [26] An amount of 5.0 g graphite powder (Asbury, cat #3763, 500 μm flakes) was added to previously mixed H_2SO_4 (200 mL) and H_3PO_4 (40 mL). Then, 24.0 g of $KMnO_4$ was slowly added to the mixture while constantly stirring, followed by 5 h of reaction. The mixture was then poured into 1.0 L of ice water with 5.0 mL of H_2O_2 (30 wt.%) to remove $KMnO_4$ residue. After centrifuging the suspension for 5 min at 4000 rpm, the residual solid was then added to 1 M (mol/L) H_2SO_4 solution to remove the excess metal ion. The yielded mixture was again centrifuged for 10 min at 4000 rpm, followed by decanting the supernatant. The residual was continuously washed by deionized (DI) water and centrifuged at 9000 rpm for 30 min till a two-layer structure was formed, while the top layer was jelly-like and containing mostly exfoliated GO sheets. The top layer was collected and added to 1 L for centrifuge at 4000 rpm for 3 min to remove residue unexfoliated GO particles. Then, the remaining GO suspension was centrifuged to concentrate the exfoliated GO flakes. A brown slurry of GO suspension containing about 1 wt.% of GO was obtained by centrifuging at 10,000 rpm for 40 min and decanting the supernatant. Obtained GO slurry was poured onto a PES supporting membrane and slip-casted by a glass rod, then subsequently dried. It is important to physically secure the GO membrane for it to maintain its structure under pressure. Thus, supporting structures were employed. A 1.5875 mm (1/16 inch) thick Delrin sheet was laser cut into 25.4 mm × 25.4 mm squares with an 8 mm circular opening in the center as support for the GO membrane. 400 mesh stainless steel mesh from Ted Pella, Inc. was used to provide support as well. Medical-grade Loctite M31-CL epoxy was used to glue the GO membrane and form liquid-tight seals to the supports according to the sequence in Figure 6.1.

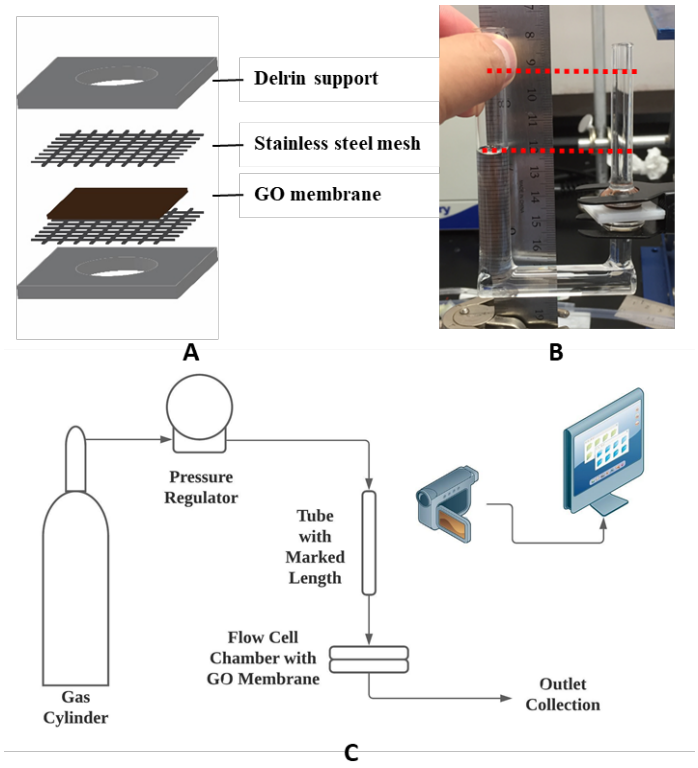

Figure 6.1. Schematic of graphene oxide (GO) membrane supports(**A**); photograph of u-tube test setup in osmosis test (**B**); schematic of the pressure-driven permeance test setup (**C**). Adapted from [1] with permission. Copyright 2021, by the authors.

6.2.2 *Chemical Modification*

Surface modifications were made to the GO membrane to accelerate the permeation of water. Chemical treatments of GO membranes were performed in a u-tube setup (Figure 6.1B) adapted from a previous study, [49] except the treatment with concentrated sulfuric acid. After the GO membrane was secured between tubes, DI water was filled into the long u-tube as feed solution, while the chemical solution (0.076 mM, mmol/L, for the two diazonium chemistries as described below) was filled into the other tube (draw tube). The liquid level in the feed tube was intentionally kept higher than the drawtube to induce a cross membrane flux towards the drawtube. Therefore, the chemical treatment was limited to only one side of the membrane. Such treatments were maintained overnight in a dark cabinet due to the light sensitivity of diazonium.

For sulfuric acid treatment, the GO membrane was secured between a glass slide and a glass tube by spring-loaded clamp and tub filled (~0.5 mL) with concentrated sulfuric acid for 60 s followed by a rinse with DI water.

6.2.3 *Aryl Diazonium Salt Synthesis*

The diazonium synthesis process used in this study were modified procedures of the diazotization process accommodating the nature of chemicals used.

p-carboxyl terminated: An amount of 0.02 mol 4-amino benzoic acid was added into 20 mL of water at 50 °C while stirring, followed by the addition of 0.044 mol of concentrated hydrochloric acid. The mixture was cooled to −3 °C. After cooling, a solution of 0.022 mol of $NaNO_2$ in 10 mL of water at 0 °C was slowly added to the mixture to initiate a reaction for 1 h. With the addition of 0.022 mol $NaBF_4$, while stirring, a suspension was made. The suspension was filtered after cooling to −3 °C. Ice cold water and ether were used to rinse the yielded light-yellow solid. The product was subsequently dried in a vacuum and stored in a desiccator at 4 °C.

p-Sulfo terminated: An amount of 2.0 g 4-sulfo aniline was dissolved into 25 mL water solution with 0.58 g Na_2CO_3 while heating and stirring. Then, the solution was cooled down to room temperature, and 0.75 g $NaNO_2$ was added. A solution made of 2.5 mL concentrated hydrochloric acid and 16 mL of water was made in advance and cooled in an ice bath before adding to the sulfo aniline-containing solution while stirring. The suspension yielded was filtered to yield white solid. Ice cold water was used to rinse the yield product, followed by vacuum drying and storage in a desiccator at 4 °C.

6.2.4 *Solution Preparation*

Water solution: An amount of 29.2 mg NaCl (EMD Chemicals Inc.) was added into 10 mL DI water to make 10 mM NaCl water solution. *MeOH solution*: 29.2 mg of NaCl was added to 10 mL HPLC grade MeOH obtained from Fisher Scientific with extended vortex mixing. IPA solution was made in the same fashion, while NaCl was added to saturation. *Water–alcohol Mixture*: water–alcohol mixture was made by mixing prepared water and alcohol solutions. The mixing ratio varies between tests. *Peroxide–alcohol mixture*: 30% (9.77 M) hydrogen peroxide aqueous solution (EMD Millipore) was slowly added into dry MeOH to the required mixing ratio. NaCl was added with gentle stirring.

6.2.5 *Permeance test*

Permeance tests of GO membrane were performed in a flow cell setup made with chemically inert tubes (Tygon 2375, 3/16 inch o.d., 1/16 inch i.d.) and chambers. Tubes of the flow cell setup were secured along a ruler as a reference to liquid flow. The flow cell chamber was machined from solid Delrin (polyoxymethylene-based) block and tapped with tread for tube fittings (Delrin and polypropylene) and screws assembly. Silicone rubber gaskets were used to seal and secure the GO membrane in the flow cell setup. Compressed Ar gas was used to provide constant pressure (10 psi). Solvents were injected and exchanged slowly by syringe before applying pressure on both sides of the stabilized GO membrane. Between tests, the flow cell was carefully rinsed with the solution to be tested by syringe to eliminate the residue solution from previous tests. The flow cell system's liquid flow was monitored by a video camera (Dino-lite digital microscope) and recorded by VideoVelocity for a time-lapse video. Pictures were taken from the time-lapse video with a same time interval and analyzed with *ImageJ* to identify the velocity of the liquid front moving along the tube. Then the transmembrane flux is calculated, as shown in the following equation:

$$Flux = {A_{tube} \times V_{liquid}}/{A_{membrane}} \quad (6.8)$$

where A_{tube} is the cross-section area of tube used, the V_{liquid} is the velocity of liquid front calculated from the distance liquid front moved during the set time interval, and the $A_{membrane}$ is the surface area of the membrane defined by the opening of the Delrin support. The calculated flux was presented in the unit of liter/m^2·h or LMH. The permeance of the solution was then calculated by the following equation, as shown:

$$Permeance = {Flux}/{P} \quad (6.9)$$

where P is the pressure applied by a compressed Ar tank as mentioned above. The permeance was presented in a commonly used unit of liter/m^2·h·bar, or LMH/bar.

6.2.6 *Osmosis test*

The osmotic behavior of the GO membrane was examined to study the water selectivity of the membrane. Osmosis tests were performed with mechanically secured GO membrane and custom-made glass U-tubes (Figure 6.1B), a short straight tube (i.d. 4.2 mm), and a longer U-shaped tube (i.d. 9.3 mm). After the GO membrane was secured with spring clamps between glass tubes and sealed by o-rings, different solutions were filled into glass tubes on each side of the GO membrane to equal heights without air bubbles. Then, both tubes were covered with parafilm to minimize the evaporation of the solutions. Between tests, the setup and membrane were rinsed with DI water to remove residue solution from previous tests. The osmotic flow was monitored and recorded using the same method mentioned in the previous section. The osmotic flux was calculated using Equation (6.1) by the same method described above. The result osmotic flux was presented in LMH.

Average permeance and flux calculation: The permeance measured by pressure-driven tests and measured osmotic flux shows a substantial decrease during the test period. (Figures 6.2 and 6.3 scatter plot). Due to this decrease, an average value during the sampling time interval is not representative of the GO membrane's best performance. To calculate initial permeance and osmotic flux, data collected within the initial 10 h was modeled with a linear fit:

$$Y = AX + B \tag{6.10}$$

where Y represents the pressure-driven permeance or osmotic flux, X represents test time, A is a negative constant revealing the decay rate of permeance or flux over time under the best fitting condition, and the intercept of the y-axis, B, giving the initial value of permeance or osmotic flux. The average and standard deviation of such initial values of permeance and osmotic flux from different tests were calculated and plotted in a column chart format. (Figures 6.2 and 6.3 column chart).

6.2.7 *The X-ray diffraction (XRD)*

The X-ray diffraction (XRD) patterns of GO membranes were obtained on a Rigaku desktop X-ray diffractometer using Cu Kα (1.54059 Å) radiation with the X-ray generator operating at 20 kV and 30 mA. Data were collected for a 2θ range of 5.0° to 20.0° at an angular resolution of 0.01°/s. The deconvolution of diffraction peaks was conducted by multipoint nonlinear curve fir (Lorentz) in origin. Then d-space was calculated using Bragg's law.

6.2.8 *Fourier-Transform Infrared (FT-IR) spectra*

FT-IR spectra were recorded over a range from 400 cm^{-1} to 4000 cm^{-1} with a resolution of 4.0 cm^{-1} using a point ATR mode of Nicolet iS10 FT-IR spectrometer (Thermo Fisher Scientific). A piece of GO membrane was soaked in 10 mM NaCl water solution for about 10 min then removed

from solution for measurement. The same GO membrane was re-soaked in 10 mM NaCl water–alcohol mixture solution for about 10 min and recorded spectra using the same technique.

6.3 Results and Discussion

There is a wide variety of reported permeability values reported in the literature, largely due to membrane fabrication and testing methods. The reported permeability of water ranges from 0.007 to 33 μm × LMH/bar, as shown in Table 6.1. Generally, higher fluxes or permeances are seen for thinner membranes, which are more prone to defects. GO membrane should exceed a critical thickness, which is dominated by its fabrication process, for example, at least 8 nm for a filtered membrane, to be considered as defect-free theoretically. [13,23] Aside from the thickness of the membrane, the microstructure of the GO membrane is another dictating factor of the membrane performance. [24] The graphene oxide membrane used in this study was fabricated through a slip-cast process with an optimal shear rate of non-Newtonian suspension results in highly oriented GO flakes compared to membranes made by common filtration or drop-casting process. [26] It is important to note that these GO membranes were unstable with pure solvents and required 10 mM (mmol/L) salt added, presumably to screen the charge of anionic oxide groups on the surface of GO flakes. For example, within 3 h, the membranes can swell from their initial thickness of 5 μm to about 1 mm when immersed in pure water. With extended time, the GO eventually redispersed into the solution. Such a phenomenon is consistent with previous reports and attributes to the hydrophilicity of graphene oxide. [16] It is also important to note that the handling of GO membranes while mounting in a flow cell or changing solvents can introduce defects and artificially induce high permeance. Hence a procedure to mount GO membranes between metal wire mesh and introduction of solvents via syringe through rubber gasket was developed to have consistent flux measurements. Direct blue 71 added to feed solutions in pressure-driven permeance

tests was not found in permeate solution, demonstrating the integrity of GO membrane was maintained during experiments.

Table 6.13. Literature reports of GO membrane permeabilities. Adapted from [1] with permission. Copyright 2021, by the authors.

Source	Test Method	Feed Solution	Thickness (μm)	Permeability μm × LMH/bar	Comment
This report	Pressure-driven	Water	5	1.895	The osmotic pressure generated by 1 mol/L NaCl and 10 mmol/L NaCl across the membrane was 49.58 bar
		MeOH		1.67	
		IPA		2.085	
	Osmosis	Water	5	0.034	
9	Pressure-driven	Water	5	16–33	
12	Pressure-driven	Water	0.15	0.045–0.225	
13	Pressure-driven	IPA	0.018	0.432	
		MeOH	0.018	1.355	
		Water	0.018	1.62	
18	Pressure-driven	Water	0.016	0.08–0.096	EDA crosslinked
				0.192–0.24	EDA crosslinked + reduction
22	Pressure-driven	Water	0.048	0.178	
		IPA	0.048	0.965	
		IPA:water 9:1	0.048	0.077	
24	Pressure-driven	Water	0.15	10.65	Slip-casted membrane
			0.17	1.7	Vacuum-filtered membrane
30	Pressure-driven	Water	0.07	0.56	
			0.7	19.32	
33	Pressure-driven	Water	0.04	0.190–0.485	
34	Pressure-driven	Water	0.6	18.9	
35	Pressure-driven	Water	0.1	9.2	
		IPA	0.1	13	
		EtOH	0.1	18	
23	Pervaporation	BuOH:water 9:1	0.231	0.587	Pressure-filtered membrane
			0.384	0.909	Vacuum-filtered membrane

			0.447	0.412	Evaporation-made membrane
25	Pervaporation	Water	5	6.733	
		EtOH:water 9:1	5	1.485	
28	Pervaporation	Alcohol:water 85:15	0.5	0.99	
29	Pervaporation	EtOH:water 9:1	0.412	0.546	
46	Pervaporation	EtOH:water 85:15	2	30.378	
47	Pervaporation	IPA:water 7:3	0.231	0.473	30 °C
			0.231	0.956	70 °C
14	Osmosis	Water	1	0.008	
27	Osmosis	Water	0.28	0.021	
			0.28	0.009	KCl intercalated
			0.55	0.023	
			0.55	0.011	KCl intercalated
			0.75	0.011	
			0.75	0.007	KCl intercalated

Table 6.1 continued.

The average initial permeance of single solvents H_2O, MeOH, and IPA (10 mM NaCl as GO stabilizer) were found to be 0.379 ± 0.153, 0.334 ± 0.160 and 0.417 ± 0.308 LMH/bar. It is important to note that the average initial permeance is defined by values of the y-axis intercept of a linear fit of data from corresponding tests. Thus, the value of the average initial permeance is expected to be higher than the observed values shown in the scatter plot. Considering the reported permeance of solvents was measured differently with membranes of different thickness from different groups, it is essential to normalize the permeance into permeability, which was defined as "membrane thickness × permeance" for practical comparisons. With our 5 μm thickness, the corresponding average permeability of water, MeOH and IPA are 1.90 ± 0.77, 1.67 ± 0.80, and 2.09 ± 1.54 μm × LMH/bar. The reported water permeability values in Table 1 have a large range of 0.007 to 33 μm × LMH/bar, with our slip-cast GO membranes in the higher range of permeance

performance. It is important to note that this is a relatively thick membrane avoiding defects that can dominate the observed permeance of thinner membranes. Thus, we consider this is a reliable report of permeability through GO membranes of ordered microstructure via slip-casting. It is also important to note that dry membrane thickness is used in the permeance calculation compared to the literature reports. This value can be adjusted proportionately by the observed d-spacing swelling described later in this report but is not tabulated here.

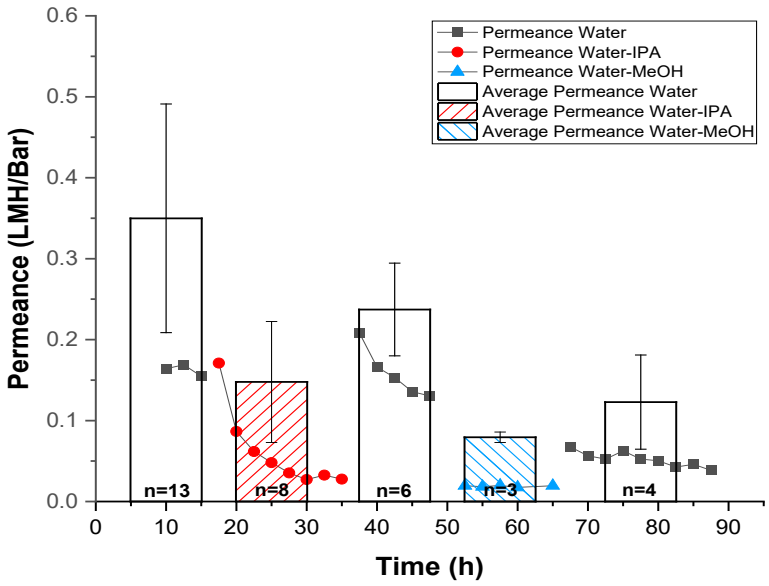

Figure 6.2. Pressure-driven permeance vs. time trend of the same GO membrane with different solvent mixtures (scatter plot, left axis) and average *initial* permeance calculated from tests on different membranes (columns, right axis). Water–alcohol (IPA or MeOH) mixtures are 1:1 *v/v*. The pressure applied was 10 psi. Each set of dots from the scatter plot shows the behavior of permeance in one continuous test with the solution mixture indicated by the legend. Between tests, solution mixtures were exchanged via syringes into the flow cell. The average permeance was calculated from "n" repeated tests under the same condition as described in the Experimental section. The number of tests, n, was labeled inside the corresponding columns. Adapted from [1] with permission. Copyright 2021, by the authors.

However, the permeance of water–alcohol mixtures was significantly lowered by a factor of 5–10, consistent with pervaporation results where the permeation flux dropped from 1.36 kg/m^{2}h with pure water to 0.3 kg/m^{2}h with 90 wt % EtOH. [26] Each set of dots from the scatter plot in Figure 6.2 shows the permeation drop trends on the same membrane in a continuous (~20 h) test. Between tests, solutions were exchanged via syringe to avoid mechanically disturbing the membranes or inducing defects. Upon addition of water–alcohol mixtures, the permeance dropped 10-fold (from over 0.15 LMH/bar to ~0.03 LMH/bar in the presented test) over 8 h for IPA and more rapidly with MeOH (quickly stabilized at ~0.02 LMH/bar in the presented test). Importantly, the fluxes could be recovered when switched back to pure water, indicating a reversible change in the membrane took place. For instance, in the shown test, the reduced flux of water–IPA immediately recovered from ~0.03 LMH/bar to over 0.15 LMH/bar. The observed permeance of water-MeOH stabilized ~0.02 LMH/bar, which was lower than the observed permeance of water–IPA stabilized at ~0.03 LMH/bar (Figure 6.2 scatter plot). This difference in decreased permeability is likely due to the difference in molecular sizes of the alcohols. Differences in mixture viscosity, surface tension, and other factors may also contribute to the difference in permeability decrease but cannot be quantified here. Normally, after replacing the water–alcohol mixed with water (10 mM NaCl stabilizer), the permeance would recover to its initial level immediately. However, after exchanging from the Water-MeOH mixture to water, the permeance stabilized at ~0.05 LMH/bar rather than the observed initial water permeance value of over 0.15 LHM/Bar in this test. Because the MeOH is smaller in molecular size and has a higher molar concentration (12.4 M, or mol/L) than IPA (6.5 M) in the corresponding water–alcohol mixture, it is expected that MeOH molecules enter the GO interlayer more readily compared to the IPA. In addition, it was reported that MeOH has a higher affinity to GO compared to water and other

alcohols. [22] Therefore, the ability to restore original water flux was reduced after MeOH exposure, presumably due to residue MeOH trapped in GO interlayer space. The average initial permeance value also agrees with the phenomenon where the water–alcohol mixture induced a reversible decay of permeance. The average initial permeance of water-MeOH and water–IPA was found to be 0.086 ± 0.007 and 0.160 ± 0.081 LMH/bar, which is lower than the initial permeance of water at 0.379 ± 0.153 LMH/bar (Figure 6.2 column chart). This can be explained by considering an assumed reversible reaction on the GO membrane that is not instantaneous, while the calculated average initial permeance was defined by the permeance at starting moment of tests. Even though the water permeance failed to recover to its initial value after extended exposure to alcohols, the recovery of permeance is still significant, indicating the reduction of water permeance is reversible.

Ion rejection by GO membranes is demonstrated by the osmotic flux 0.31 LMH observed with 10 mM NaCl and 1 M (mol/L) NaCl water solution opposite the membrane. The flux decreased about 20% from 0.31 LMH to 0.25 LMH over 20 h period (Figure 6.3 test A scatter plot). Since the osmotic pressure is directly proportional to the concentration of draw solute, a 20% decrease should correspond to a 20% change in draw solute concentration, which would require the addition of 0.175 mL solvent to the draw solution (0.7 mL initial). However, the volume increase of the draw solution was found to be about 0.24 mL, which should cause more than a 20% drop in flux. Likely, the decrease in flux was induced by a localized high concentration of solution near the GO membrane at the permeate side. The maintained osmotic flux (pressure) over time is direct evidence of ion rejection and the GO membrane's water selectivity. The average of initial osmotic flux was found to be 0.338 ± 0.087 LMH. (Figure 6.3, test A column)

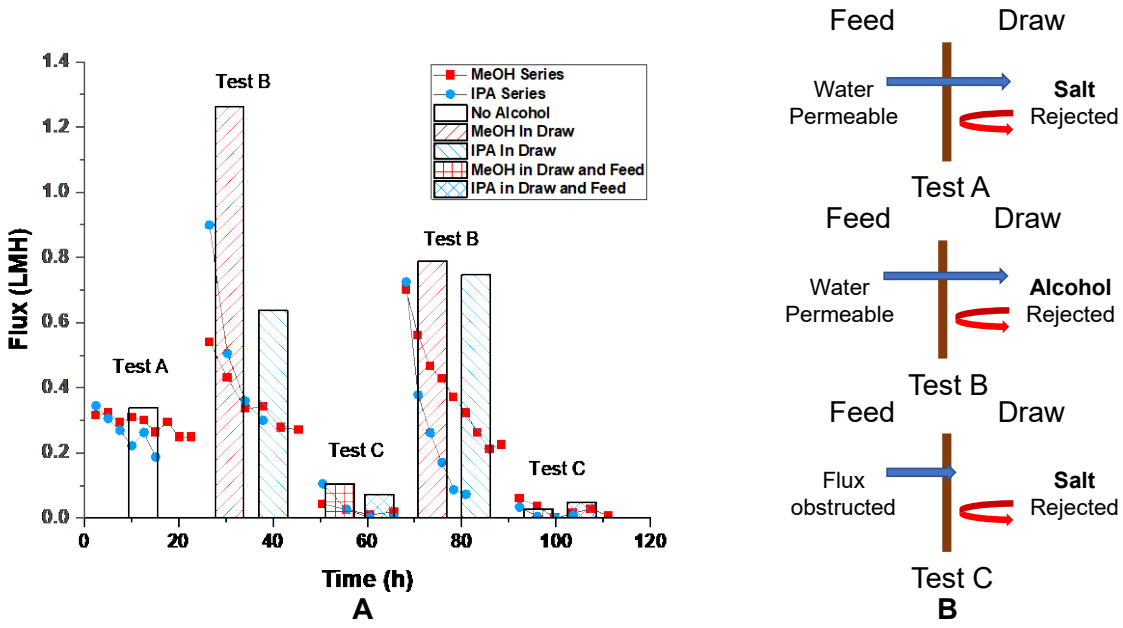

Figure 6.3 Observed osmotic flux vs. time trend on the same GO membrane under different test conditions (scatter plot) and average extrapolated initial flux of different GO membranes under various test conditions (columns) (**A**); schemes of cross-membrane flux under different test conditions (**B**). Test A: feed: 10 mM (mmol/L) NaCl in water, draw: 1 M (mol/L) NaCl in water, n = 7; test B: feed: 10 mM NaCl in water, draw: 10 mM NaCl in water–alcohol mixture, n = 1 for MeOH and 4 for IPA at the first test, n = 2 for MeOH and 3 for IPA at the repeat test; test C: feed: 10 mM NaCl in water–alcohol mixture, draw: 1 M NaCl in water–alcohol mixture n = 2 for MeOH and 3 for IPA at the first test, n = 2 for MeOH and 2 for IPA at the repeat test. Test B and C were repeated under the same condition. The number "n" is the number of tests used to calculate the average flux under the same condition specified by the corresponding legend (columns). The water–alcohol mixture is made by mixing 1:1 *v/v* water and alcohol (MeOH or IPA). Adapted from [1] with permission. Copyright 2021, by the authors.

Interestingly, osmotic flux was also observed with 1:1 water–alcohol mixture being a draw solution and water being feed solution (both with 10 mM NaCl added), as shown in Figure 6.3 test B. This is a clear indication of selectivity of water over water–alcohol mixture. The high value of initial osmotic flux, 1.263 LMH and 0.637 LMH for water-MeOH and water–IPA drawing

solution, at the beginning of the test is caused by higher molarity of solute (alcohol) in draw solution at 50 vol% (12.4 M and 6.5 M for MeOH and IPA). This is surprising since the permeance of pure IPA was found comparable to the permeance of pure water. This indicates that, in the presence of water, GO membranes form selective water channels excluding alcohol flow, whereas the GO is permeable to pure alcohols. This is the first observation of GO membranes becoming water selective in the presence of water–alcohol mixtures in an osmotic setup.

To make a more direct comparison to test A in Figure 6.3, test C in the same figure has water–alcohol mixtures on both sides and has a 0.99 M salt concentration difference across the membrane. The key distinction is that with alcohol in the feed solution, we expect a flux decrease similar to what was observed from pressure-driven permeance experiments (Figure 6.2). Consistent with our hypothesis, the osmotic flow was found to be less than 0.1 LMH at first and dropped to less than 0.02 LMH over the course of 20 h. (Figure 6.3 test C scatter plot) The averaged value of *initial* osmotic flux was 0.106 and 0.074 LMH for the case of MeOH and IPA being in the solvent. (Figure 6.3 test C column) This is significantly lower than the flux found under the conditions of Figure 6.3 test A, 0.338 ± 0.087 LMH, where no alcohol was presented in the feed solution. Presumably, with alcohol on the feed side, the osmotic flow would draw alcohol into the GO membrane. However, in the case of alcohol only on the draw side, alcohol was driven away from the membrane by osmotic flux. When the solution pair of 10 mM and 1 M NaCl in 1:1 water–alcohol (test C) was changed back to 10 mM NaCl in water, and 1:1 water–alcohol (repeat of test B), the osmotic flux recovered to its initial value at about 0.55 LMH, as shown in the scatter plot for repeated test B in Figure 6.3. The recovered average initial flux was found to be 0.788 LMH for MeOH and 0.747 LMH for IPA. Such recovery of osmotic flux (from 0.1 LMH level to greater

than 0.7 LMH) further confirmed the reversible nature of the osmotic flux reduction phenomenon induced by water–alcohol mixtures chemically reducing GO membranes.

Chemical modification of the GO membrane was performed to prevent flux decrease caused by water–alcohol mixtures. The hypothesis was that by having high charge density on GO surfaces and GO nanochannels' entrances, water would be favored over the less polar and more sterically hindered solvents like IPA. Concentrated sulfuric acid, 4-sulfo benzene diazonium, and direct blue 71 (coupled with 4-carboxyl benzene diazonium) were grafted onto the GO surface by the method used in prior work with CNT membrane.[49] Among the chemical modification tested, 4-sulfo benzene diazonium most significantly promoted osmotic flux of water (to 0.90 LHM from 0.27 LMH of pristine GO membrane), possibly due to stronger ion rejection. The contact angles were 72.5°, 70.0°, 73.3° concerning pristine, concentrated sulfuric acid-treated and 4-sulfo benzene diazonium treated GO membranes, indicating modest differences in hydrophilicity after treatment. However, when the feed solution had alcohol present, a dramatic drop in osmotic flux was seen (Figure 6.4 test A, test C). This indicates the modification of GO charge density is insufficient to counter the alcohol-induced hindrance of water transport. Figure 6.4 further shows the consistency of the alcohol interference phenomena with different surface chemistries. Therefore, the decreased trans-membrane flux, induced by the presence of water–alcohol in the feed side of the GO membrane, is not simply due to surface charge or hydrophobicity effects.

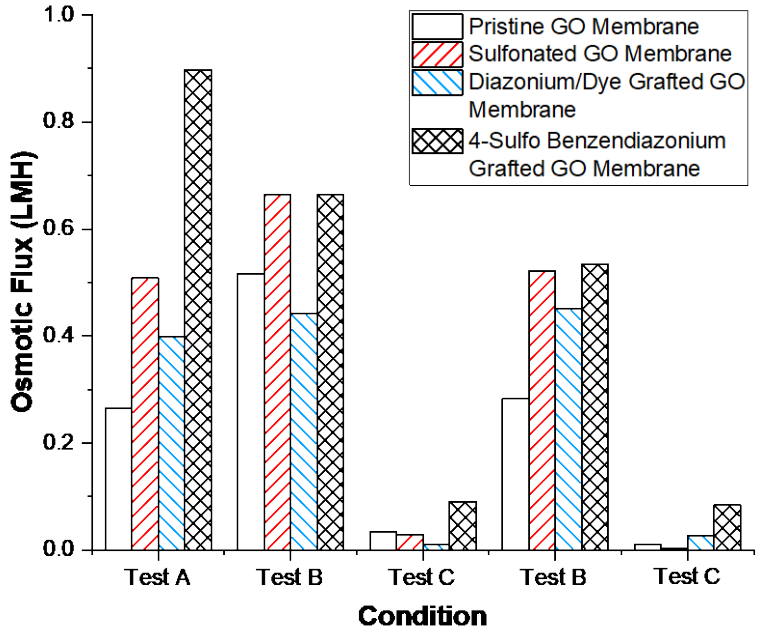

Figure 6.4 Column Chart of Osmotic flux of different chemical-treated GO membranes under different sequential test conditions. Test A: feed: 10 mM NaCl in water, draw: 1 M NaCl in water; test B: feed: 10 mM NaCl in water, draw: 10 mM NaCl in water–IPA mixture; test C: feed: 10 mM NaCl in water–IPA mixture, draw: 1 M NaCl in water–IPA mixture. The water–IPA mixture is 1:1 *v/v* water and IPA. Adapted from [1] with permission. Copyright 2021, by the authors.

To study GO membranes' structure, we used X-ray diffraction (XRD) to monitor the spacing change between 2-D planes of GO treated with different solvents and mixtures. Air-dried GO membrane has a d-spacing of 8.515 Å, which is comparable with previous studies, with a sharp XRD peak indicating a well-packed laminated structure of GO. [13,15,26] As expected, the d-spacing increased with the intercalation of large solvent molecules from 12.188 Å. 13.262 Å and 16.202 Å when the membrane was immersed in water, MeOH and IPA, respectively. The expansion in d-space is in good agreement with the increasing size of intercalated molecules.

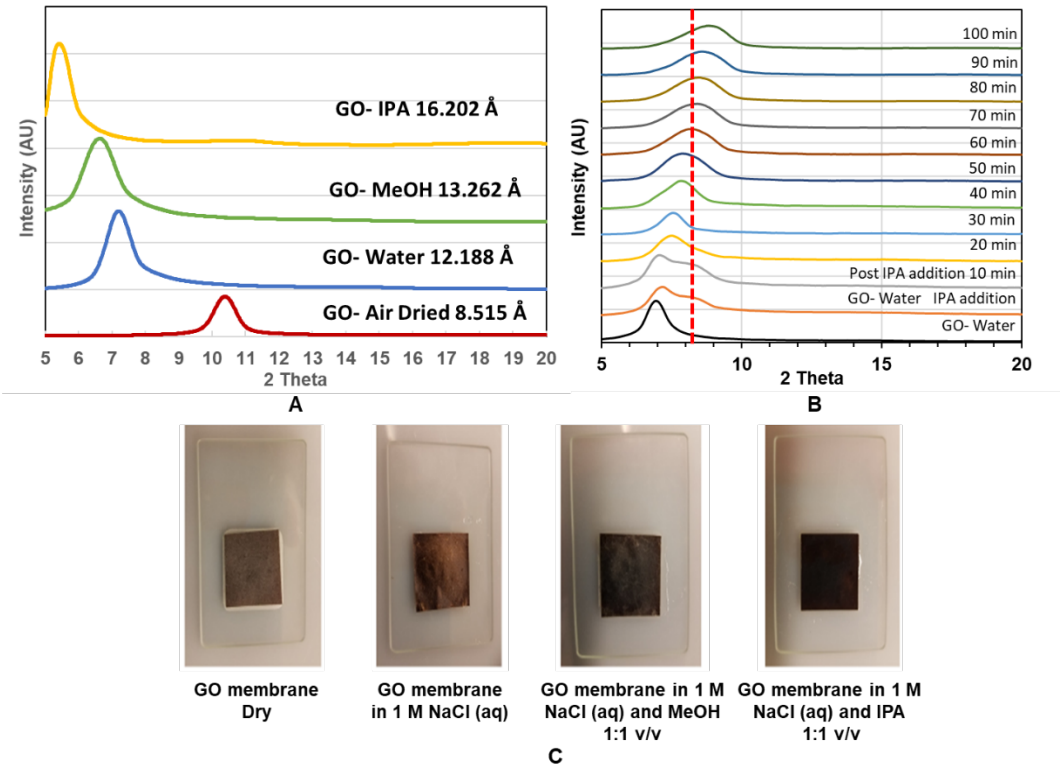

Figure 6.5 A: XRD of GO immersed in indicated solvents; B: XRD as a function of time for GO immersed in water and peak shift after addition of IPA; C: Color change observed when the GO membrane was immersed in different solution. Adapted from [1] with permission. Copyright 2021, by the authors.

However, the mixture of water–IPA, as shown in Figure 6.5 B, gave an unexpected decrease in d-spacing compared to the GO-water case. Upon the addition of IPA, a shoulder (at ~9.9 Å) is seen, and the main peak gradually shrinking from 12.875 Å to 9.927 Å during the 100 min period. This behavior is very different from the simple intercalation of molecules, such as IPA, which alone increased the d-spacing to 16.202 Å. Similarly, it is not likely that the cluster of alcohol–water molecules would enter the interlayer space of the GO membrane as it would cause expansion of the d-space rather than observed shrinkage. Interestingly, contraction in d-space is about 2 Å, which is similar to the size of removed–COOH groups for a GO reduction reaction. A similar d-space decrease with an alcohol–water mixture solvent was also observed in another study. [20]

However, different from our observation, they found alcohol molecules induce less expansion in GO d-spacing compared to water when intercalated in their GO membrane. Nevertheless, a decrease in GO d-spacing is expected to decrease trans-membrane flux.

Another important experimental observation is that the color of the GO membrane changed from brown to black by the addition of alcohol into water-wetted GO membranes Figure 6.5 C. This suggests a partial reduction reaction of GO to r–GO with the presence of water and alcohol. The initial brown color can be recovered by drying the membrane (not shown). Similar reduction/oxidation reaction induced color change of GO was also reported by another study. [19]

To investigate chemical reaction with water–alcohol mixtures, infrared spectra with corresponding XRD were done, as shown in Figure 6.6. Pristine GO membranes (black curve) show characteristic peaks at 1725 cm^{-1} (C=O), 1619 cm^{-1} (C=C), and a very broad O-H peak at 3300 cm^{-1}. With the addition of water (blue) and water–alcohol (red) mixture, the C=O peak at 1725 cm^{-1} disappeared. This reversible result is likely due to the formation of hemiacetals or hydrates (gem-diols) of carbonyl moieties in the presence of water or alcohol. Those are typically unstable so that they are completely reversible. The formation of hemiacetals or hydrates typically needs a negligible amount of acid or base catalyst. [46,50,51] Furthermore, of note is that the O-H stretch at 3200 cm^{-1} sharpens and increases to 3300 cm^{-1} for both water and mixture, indicating a more ordered system. In the case of water–alcohol mixtures, small peaks at 2900 cm^{-1} of C-H stretch and multiples 1500–900 cm^{-1} indicate the incorporation of alcohol. The IR spectra returned to the same as pristine GO with drying with C=O peak returning.

The corresponding XRD with solvent treatment is shown in Figure 6.6 B and D. The GO d-spacing increases with the addition of water (from 8.598 Å to over 13.18 Å), as expected. With the addition of MeOH, there is a small decrease in d-spacing to 12.65 Å, but the formation of a

shoulder-peak at 10.54 Å. A shoulder would indicate a mixture of sample states, compared to Figure 6.6 shifting of the entire peak. The deconvoluted peaks show, with the addition of MeOH and IPA, the d-space of regions of the GO membrane decreased ~2.1 Å and ~2.4 Å accordingly. Therefore, the d-space change cannot be attributed to the molecular size of a larger solvent but a reaction that removes chemical groups on the GO, particularly reducing carboxylate groups. Interestingly, GO has recently been found to be catalytically active for the oxidation of alcohols. [40,46,52]

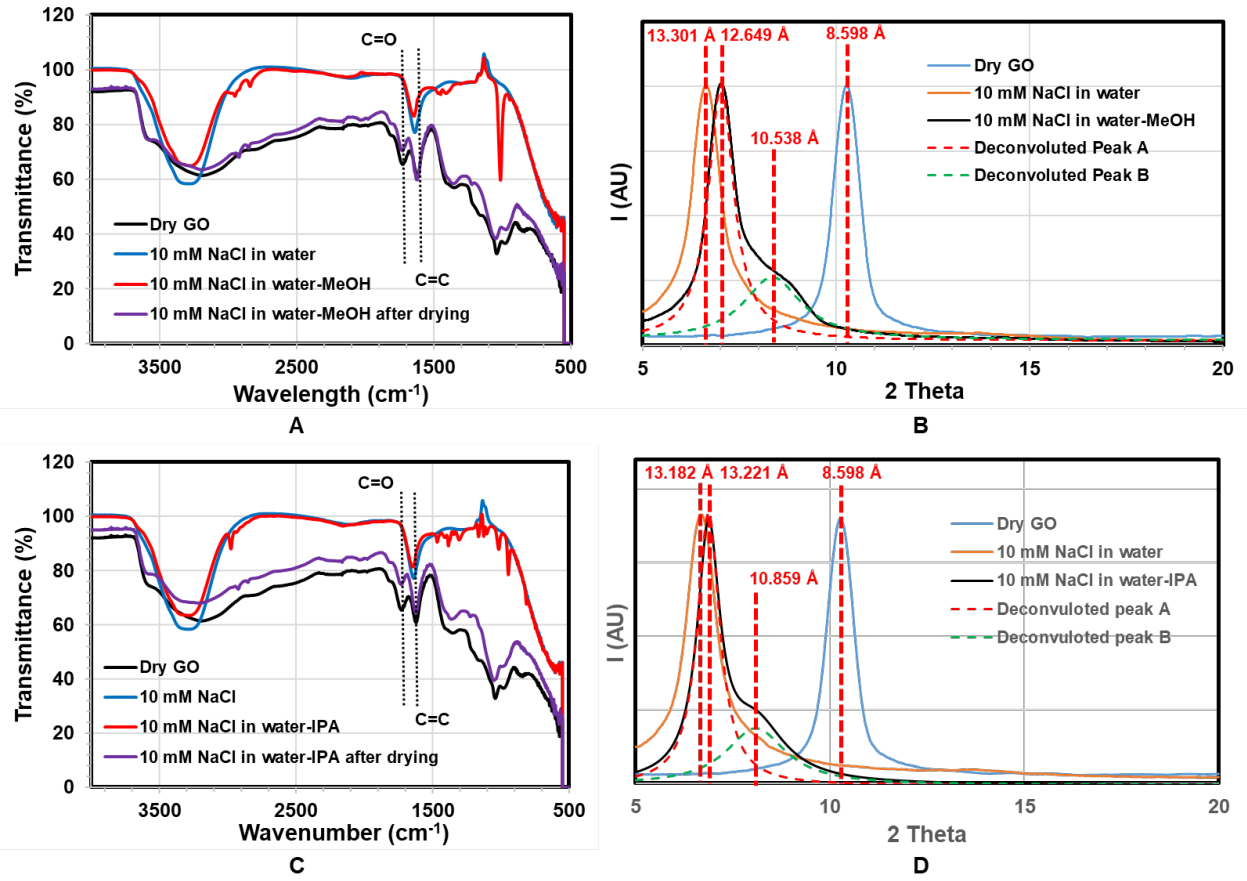

Figure 6.6 ATR-IR and corresponding XRD data on the same membrane. (**A**) ATR-IR of GO membrane immersed in water and water-MeOH; (**B**) corresponding XRD data of GO membrane immersed in water and water-MeOH; (**C**) ATR-IR of GO membrane immersed in water and water-IPA; (**D**) corresponding XRD data of GO membrane immersed in water and water-IPA. Adapted from [1] with permission. Copyright 2021, by the authors.

The proposed mechanism shown in Figure 6.7 A involves a catalytic cycle that oxidizes alcohol to its aldehyde and carboxylic acid form and causing a reduction of GO at the same time. [40,46,52] Once reduced, GO has less or no reaction activity and contracts in d-spacing with loss of carboxylates. This, in turn, dramatically slows the permeation of solvents. Hypothetically, once the reduced GO membrane was re-oxidized, the d-spacing can be recovered, restoring its reactivity and solvent permeability. This would be consistent with the observation of the reversibility of flow phenomena observed during drying. However, the flow cell and the osmosis test tubes were sealed from the air to prevent the evaporation of the solution. Thus, with limited oxidant from the air and excessive alcohol as reductant, the GO membrane remained at a reduced state, and the flux of solvent was limited by the reduced d-space. To test the catalytic cycle hypothesis, stoichiometric amounts of oxidant were added to the mixture with the expectation to recover flow rates. Figure 6.7 B shows water permeance at approximately 0.5 LMH/bar. With the addition of 10% MeOH (*v/v*) in water, the permeance dropped to approximately 0.16 LMH/bar, which is about 1/3 of the value of water permeance. Subsequently, H_2O_2 was introduced to restore the oxidation state and d-space of the GO membrane. With the addition of 10% MeOH (2.47 M)—90% H_2O_2 (8.79 M) mixture and proper compensation of bubble generated during reaction, the permeance of mixture solution recovered to approximately 0.6 LMH/bar. The recovery of flux with added oxidant is in a good alignment to our hypothesis and purposed catalytic reaction. With abundant oxidant supply, the water–alcohol-reduced rGO was oxidized to its initial state. Thus, the d-space of the GO membrane was recovered, allowing the initial fast transmembrane flux. Similarly, potassium permanganate was also tested as an oxidant added to the alcohol–water mixture and yielded similar results.

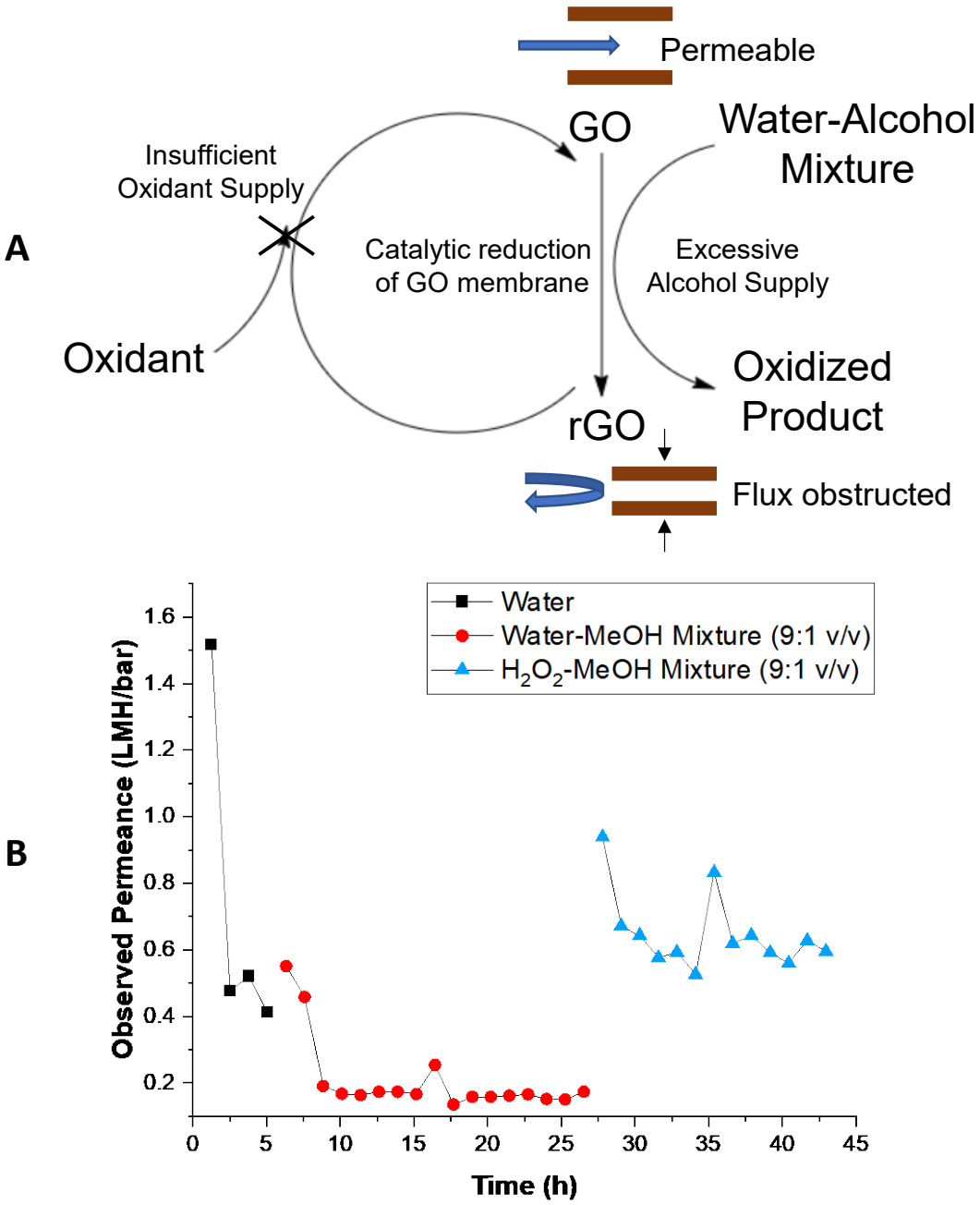

Figure 6.7 Scheme of purposed catalytic reduction of GO membrane by alcohols (**A**); pressure-driven permeance vs. time trend with added oxidant reversing the catalytic reduction of GO membrane (**B**). Figure also shows reduced d-space of GO membrane obstructing cross-membrane flux at reduced state. Adapted from [1] with permission. Copyright 2021, by the authors.

6.4 CONCLUSION

With proper stabilization methods, both chemically and mechanically, shear-aligned graphene oxide-based membranes were able to show steady and repeatable performance. The permeance of water, MeOH and IPA was observed to be 0.379 ± 0.153, 0.334 ± 0.160, and 0.417 ± 0.308 LMH/bar, respectively. Considering the membrane used here has a higher thickness (~5 μm) compared to membranes used by other researchers (commonly 10–50 nm), the permeance value was normalized with the thickness of the membrane yielding water permeability of 1.32 μm × LMH/bar. Knowing that various studies of GO membranes showing the water permeability range in a wide spectrum of 7×10^{-2} to 3.3×10^{1} μm × LMH/bar as the fabrication methods of membranes vary (Table 1), the water permeability performance of our GO membrane lays in the high end of the spectrum, thanks to aligned GO grains. We believe this observation is accurate since dye permeation control experiments excluded any significant role of defects larger than 2 nm. A similar slip-casted GO membrane with precise control of the fabrication process from Majumders' group showed a slightly better performance of 10.7 μm × LMH/bar, but with a lower thickness of 150 nm. [25] This indicates, with proper optimization, the permeance of our current GO-based membrane can be improved while maintaining defect-free 2-D nanochannels.

Although individual solvents show fast permeance through the GO membrane, a dramatic flux reduction over a magnitude (to 1/10 of its initial strength) was observed when the GO was approached by a mixture of water–alcohol solution. Note that the reduced permeance of the mixture solution is lower than the permeance of any individual of the component of the solution. This indicates the reduction of the flux was not caused by a simple single "slow" molecule species but through a more complicated mechanism. In addition, the permeance of a single solvent solution

can be recovered upon removal of the mixture solution, which indicates a non-permanent effect on the GO membrane.

Osmosis experiments provided more insight into the liquid transportation behavior within the GO membranes. The osmotic flow between water solutions of different salt concentrations indicated the GO membrane's nanochannels are water selective and can effectively reject salt ions. When testing with draw/feed pair of water–alcohol mixture/water, the osmotic flow was observed as well. Knowing that previous tests show that alcohols by themselves can permeate through the GO membrane, such phenomenon indicates that the GO membrane favors water over alcohol in a water–alcohol mixture and forms selective water channels. Consistent with the pressure-driven permeance tests, reduction of osmotic flux was also observed when water–alcohol mixtures are introduced into the feed side of the GO membrane during osmosis tests. Surface chemical modifications were made in an attempt to alter the selectivity of the molecule at the entrance of the GO membrane in the hope that polarized groups on the surface will ease the entrance energy barrier of the water molecule, therefore, eliminate the flux reduction with mixture solution. A significant increase of osmotic flux (to about 4 times of initial value after treatment with 4-sulfo benzene diazonium) was observed, but the phenomena of dramatic flux reduction with water–alcohol mixtures was still observed, suggesting a different mechanism other than chemical selectivity at the GO plane entrances.

The observation of color change of the GO membrane leads to the hypothesis of reduction of the GO, which was supported by FTIR characterization. In the water–alcohol mixture, the C=O peak disappeared than GO at the dry state or dried water–alcohol mixture treated GO. XRD data shows that upon the exposure of water–alcohol mixtures, the d-spacing of GO deceased by ~2.2 Å, which is in good agreement with the size of a carboxyl group. Combining these FTIR and XRD

data, we were led to believe that the GO was reduced by the water–alcohol mixture reversibly losing its carboxyl groups. As reported by Bielawski and Yang's group, the GO can catalytically oxidize alcohols at the cost of itself being reduced. [40,46,52] We also found the reduced GO can be re-oxidized to recover its catalytic activity. Our observation of reversible transmembrane flux reduction upon exposure to the water–alcohol mixture can be explained by the proposed catalytic reaction cycle. In the presence of excessive alcohol in an aqueous solution as reductant, the GO membrane was reduced, causing a d-space shortening, which leads to a reduction in transmembrane flux. Once the excessive alcohol reductant was removed, the reduced GO membrane will be re-oxidized by environmental oxidants, such as oxygen in the air. The reduced d-space of the GO membrane was thus expanded, allowing the recovery of transmembrane flux. To further prove the purposed catalytic reaction cycle, H_2O_2, as the oxidizer, was added into the MeOH containing mixture solvent and successfully prevented the reduction of permeation flux. This observation supports the mechanism of GO reduction being responsible for the observed GO d-spacing decrease and a significant decrease in permeability of water–alcohol mixtures. In short, the water–alcohol mixture-induced d-space reduction of GO membranes was demonstrated to be reversible and explained by a catalytic GO reduction reaction cycle. The selectivity of water, as well as rejection of alcohol and salt ions, was also demonstrated in mixtures. This insight is needed for the GO membrane's application in the biofuel production field, where one must carefully control the oxidation environment to ensure stable fluxes and productivity.

6.5 REFERENCES

[1] Zang, Y.; Peek, A.; Shin, Y.; Gotthold, D.; Hinds, B.J. Catalytic Reduction of Graphene Oxide Membranes and Water Selective Channel Formation in Water–Alcohol Separations. Membranes 2021, 11, 317.

[2] Majumder, M.; Chopra, N.; Andrews, R.; Hinds, B.J. Nanoscale hydrodynamics: Enhanced flow in carbon nanotubes. *Nature* **2005**, *438*, 44–44.

[3] Holt, J.K.; Park, H.G.; Wang, Y.M.; Stadermann, M.; Artyukhin, A.B.; Grigoropoulos, C.P.; Noy, A.; Bakajin, O. Fast mass transport through sub-2-nanometer carbon nanotubes. *Science* **2006**, *312*, 1034–1037.

[4] Joseph, S.; Aluru, N.R. Why are carbon nanotubes fast transporters of water? *Nano Lett.* **2008**, *8*, 452–458.

[5] Hummer, G.; Rasaiah, J.C.; Noworyta, J.P. Water conduction through the hydrophobic channel of a carbon nanotube. *Nature* **2001**, *414*, 188–190.

[6] Radha, B.; Esfandiar, A.; Wang, F.C.; Rooney, A.P.; Gopinadhan, K.; Keerthi, A.; Mishchenko, A.; Janardanan, A.; Blake, P.; Fumagalli, L.; et al. Molecular transport through capillaries made with atomic-scale precision. *Nature* **2016,** *538*, 222–+.

[7] Nair, R.R.; Wu, H.A.; Jayaram, P.N.; Grigorieva, I.V.; Geim, A.K. Unimpeded Permeation of Water Through Helium-Leak-Tight Graphene-Based Membranes. *Science* **2012**, *335*, 442–444.

[8] Kannam, S.K.; Todd, B.D.; Hansen, J.S.; Daivis, P.J. Slip length of water on graphene: Limitations of non-equilibrium molecular dynamics simulations. *J. Chem. Phys.* **2012**, *136*, 9.

[9] Algara-Siller, G.; Lehtinen, O.; Wang, F.C.; Nair, R.R.; Kaiser, U.; Wu, H.A.; Geim, A.K.; Grigorieva, I.V. Square ice in graphene nanocapillaries. *Nature* **2015,** *519*, 443–445.

[10] Abraham, J.; Vasu, K.S.; Williams, C.D.; Gopinadhan, K.; Su, Y.; Cherian, C.T.; Dix, J.; Prestat, E.; Haigh, S.J.; Grigorieva, I.V.; et al. Tunable sieving of ions using graphene oxide membranes. *Nat. Nanotechnol.* **2017,** *12*, 546.

[11] Wei, N.; Peng, X.S.; Xu, Z.P. Understanding Water Permeation in Graphene Oxide Membranes. *ACS Appl. Mater. Interfaces* **2014**, *6*, 5877–5883.

[12] Devanathan, R.; Chase-Woods, D.; Shin, Y.; Gotthold, D.W. Molecular Dynamics Simulations Reveal that Water Diffusion between Graphene Oxide Layers is Slow. *Sci. Rep.* **2016**, *6*, 8.

[13] Yang, Q.; Su, Y.; Chi, C.; Cherian, C.T.; Huang, K.; Kravets, V.G.; Wang, F.C.; Zhang, J.C.; Pratt, A.; Grigorenko, A.N.; et al. Ultrathin graphene-based membrane with precise molecular sieving and ultrafast solvent permeation. *Nat. Mater.* **2017,** *16*, 1198–1202.

[14] Huang, L.; Chen, J.; Gao, T.T.; Zhang, M.; Li, Y.R.; Dai, L.M.; Qu, L.T.; Shi, G.Q. Reduced Graphene Oxide Membranes for Ultrafast Organic Solvent Nanofi ltration. *Adv. Mater.* **2016**, *28*, 8669–8674.

[15] Joshi, R.K.; Carbone, P.; Wang, F.C.; Kravets, V.G.; Su, Y.; Grigorieva, I.V.; Wu, H.A.; Geim, A.K.; Nair, R.R. Precise and Ultrafast Molecular Sieving Through Graphene Oxide Membranes. *Science* **2014**, *343*, 752–754.

[16] Dreyer, D.R.; Park, S.; Bielawski, C.W.; Ruoff, R.S. The chemistry of graphene oxide. *Chem. Soc. Rev.* **2010**, *39*, 228–240.

[17] Liu, Z.L.; Norgaard, K.; Overgaard, M.H.; Ceccato, M.; Mackenzie, D.M.A.; Stenger, N.; Stipp, S.L.S.; Hassenkam, T. Direct observation of oxygen configuration on individual graphene oxide sheets. *Carbon* **2018**, *127*, 141–148.

[18] Zheng, S.X.; Tu, Q.S.; Urban, J.J.; Li, S.F.; Mi, B.X. Swelling of Graphene Oxide Membranes in Aqueous Solution: Characterization of Interlayer Spacing and Insight into Water Transport Mechanisms. *Acs Nano* **2017**, *11*, 6440–6450.

[19] Mi, B.X.; Zheng, S.X.; Tu, Q.S. 2D graphene oxide channel for water transport. *Faraday Discuss.* **2018**, *209*, 329–340.

[20] Talyzin, A.V.; Hausmaninger, T.; You, S.J.; Szabo, T. The structure of graphene oxide membranes in liquid water, ethanol and water-ethanol mixtures. *Nanoscale* **2014**, *6*, 272–281.

[21] Deng, J.J.; You, Y.; Bustamante, H.; Sahajwalla, V.; Joshi, R.K. Mechanism of water transport in graphene oxide laminates. *Chem. Sci.* **2017**, *8*, 1701–1704.

[22] Borges, D.D.; Woellner, C.F.; Autreto, P.A.S.; Galvao, D.S. Insights on the mechanism of water-alcohol separation in multilayer graphene oxide membranes: Entropic versus enthalpic factors. *Carbon* **2018**, *127*, 280–286.

[23] Aher, A.; Cai, Y.G.; Majumder, M.; Bhattacharyya, D. Synthesis of graphene oxide membranes and their behavior in water and isopropanol. *Carbon* **2017**, *116*, 145–153.

[24] Tsou, C.H.; An, Q.F.; Lo, S.C.; De Guzman, M.; Hung, W.S.; Hu, C.C.; Lee, K.R.; Lai, J.Y. Effect of microstructure of graphene oxide fabricated through different self-assembly techniques on 1-butanol dehydration. *J. Membr. Sci.* **2015**, *477*, 93–100.

[25] Akbari, A.; Sheath, P.; Martin, S.T.; Shinde, D.B.; Shaibani, M.; Banerjee, P.C.; Tkacz, R.; Bhattacharyya, D.; Majumder, M. Large-area graphene-based nanofiltration membranes by shear alignment of discotic nematic liquid crystals of graphene oxide. *Nat. Commun.* **2016**, *7*, 12.

[26] Shin, Y.; Taufique, M.F.N.; Devanathan, R.; Cutsforth, E.C.; Lee, J.; Liu, W.; Fifield, L.S.; Gotthold, D.W. Highly Selective Supported Graphene Oxide Membranes for Water-Ethanol Separation. *Sci. Rep.* **2019**, *9*, 11.

[27] Boffa, V.; Etmimi, H.; Mallon, P.E.; Tao, H.Z.; Magnacca, G.; Yue, Y.Z. Carbon-based building blocks for alcohol dehydration membranes with disorder-enhanced water permeability. *Carbon* **2017**, *118*, 458–466.

[28] Chen, L.; Shi, G.S.; Shen, J.; Peng, B.Q.; Zhang, B.W.; Wang, Y.Z.; Bian, F.G.; Wang, J.J.; Li, D.Y.; Qian, Z.; et al. Ion sieving in graphene oxide membranes via cationic control of interlayer spacing. *Nature* **2017**, *550*, 415–418.

[29] Hua, D.; Rai, R.K.; Zhang, Y.; Chung, T.S. Aldehyde functionalized graphene oxide frameworks as robust membrane materials for pervaporative alcohol dehydration. *Chem. Eng. Sci.* **2017**, *161*, 341–349.

[30] Hung, W.S.; Tsou, C.H.; De Guzman, M.; An, Q.F.; Liu, Y.L.; Zhang, Y.M.; Hu, C.C.; Lee, K.R.; Lai, J.Y. Cross-Linking with Diamine Monomers To Prepare Composite Graphene Oxide-Framework Membranes with Varying d-Spacing. *Chem. Mater.* **2014**, *26*, 2983–2990.

[31] Hu, M.; Mi, B.X. Enabling Graphene Oxide Nanosheets as Water Separation Membranes. *Environ. Sci. Technol.* **2013**, *47*, 3715–3723.

[32] Chen, L.; Li, N.; Wen, Z.Y.; Zhang, L.; Chen, Q.; Chen, L.N.; Si, P.C.; Feng, J.K.; Li, Y.H.; Lou, J.; et al. Graphene oxide based membrane intercalated by nanoparticles for high performance nanofiltration application. *Chem. Eng. J.* **2018**, *347*, 12–18.

[33] Jia, M.M.; Feng, Y.; Liu, S.C.; Qiu, J.H.; Yao, J.F. Graphene oxide gas separation membranes intercalated by UiO-66-NH2 with enhanced hydrogen separation performance. *J. Membr. Sci.* **2017**, *539*, 172–177.

[34] Han, Y.; Jiang, Y.Q.; Gao, C. High-Flux Graphene Oxide Nanofiltration Membrane Intercalated by Carbon Nanotubes. *ACS Appl. Mater. Interfaces* **2015**, *7*, 8147–8155.

[35] Chen, X.F.; Qiu, M.H.; Ding, H.; Fu, K.Y.; Fan, Y.Q. A reduced graphene oxide nanofiltration membrane intercalated by well-dispersed carbon nanotubes for drinking water purification. *Nanoscale* **2016**, *8*, 5696–5705.

[36] Akbari, A.; Meragawi, S.E.; Martin, S.T.; Corry, B.; Shamsaei, E.; Easton, C.D.; Bhattacharyya, D.; Majumder, M. Solvent Transport Behavior of Shear Aligned Graphene Oxide Membranes and Implications in Organic Solvent Nanofiltration. *ACS Appl. Mater. Interfaces* **2018**, *10*, 2067–2074.

[37] Gravelle, S.; Yoshida, H.; Joly, L.; Ybert, C.; Bocquet, L. Carbon membranes for efficient water-ethanol separation. *J. Chem. Phys.* **2016**, *145*, 8.

[38] You, S.J.; Yu, J.C.; Sundqvist, B.; Belyaeva, L.A.; Avramenko, N.V.; Korobov, M.V.; Talyzin, A.V. Selective Intercalation of Graphite Oxide by Methanol in Water/Methanol Mixtures. *J. Phys. Chem. C* **2013**, *117*, 1963–1968.

[39] Dharupaneedi, S.P.; Anjanapura, R.V.; Han, J.M.; Aminabhavi, T.M. Functionalized Graphene Sheets Embedded in Chitosan Nanocomposite Membranes for Ethanol and Isopropanol Dehydration via Pervaporation. *Ind. Eng. Chem. Res.* **2014**, *53*, 14474–14484.

[40] Dreyer, D.R.; Jia, H.P.; Bielawski, C.W. Graphene Oxide: A Convenient Carbocatalyst for Facilitating Oxidation and Hydration Reactions. *Angew. Chem.-Int. Ed.* **2010**, *49*, 6813–6816.

[41] Dhakshinamoorthy, A.; Alvaro, M.; Concepcion, P.; Fornes, V.; Garcia, H. Graphene oxide as an acid catalyst for the room temperature ring opening of epoxides. *Chem. Commun.* **2012**, *48*, 5443–5445.

[42] Qu, L.T.; Liu, Y.; Baek, J.B.; Dai, L.M. Nitrogen-Doped Graphene as Efficient Metal-Free Electrocatalyst for Oxygen Reduction in Fuel Cells. *ACS Nano* **2010**, *4*, 1321–1326.

[43] Tian, F.Y.; Xu, B.Q.; Li, Y.J.; Deng, J.; Zhang, H.L.; Peng, R.C. A Highly Active, Readily Synthesized and Easily Separated Graphene Oxide (GO)/Polyethersulfone (PES) Catalytic Membrane for Biodiesel Production. *Chemistryselect* **2020**, *5*, 1676–1682.

[44] Pedrosa, M.; Drazic, G.; Tavares, P.B.; Figueiredo, J.L.; Silva, A.M.T. Metal-free graphene-based catalytic membrane for degradation of organic contaminants by persulfate activation. *Chem. Eng. J.* **2019**, *369*, 223–232.

[45] Huang, K.; Liu, G.P.; Lou, Y.Y.; Dong, Z.Y.; Shen, J.; Jin, W.Q. A Graphene Oxide Membrane with Highly Selective Molecular Separation of Aqueous Organic Solution. *Angew. Chem.-Int. Ed.* **2014**, *53*, 6929–6932.

[46] Dreyer, D.R.; Murali, S.; Zhu, Y.W.; Ruoff, R.S.; Bielawski, C.W. Reduction of graphite oxide using alcohols. *J. Mater. Chem.* **2011**, *21*, 3443–3447.

[47] Tang, Y.P.; Paul, D.R.; Chung, T.S. Free-standing graphene oxide thin films assembled by a pressurized ultrafiltration method for dehydration of ethanol. *J. Membr. Sci.* **2014**, *458*, 199–208.

[48] Hung, W.S.; An, Q.F.; De Guzman, M.; Lin, H.Y.; Huang, S.H.; Liu, W.R.; Hu, C.C.; Lee, K.R.; Lai, J.Y. Pressure-assisted self-assembly technique for fabricating composite membranes consisting of highly ordered selective laminate layers of amphiphilic graphene oxide. *Carbon* **2014**, *68*, 670–677.

[49] Gulati, G.K.; Chen, T.; Hinds, B.J. Programmable carbon nanotube membrane-based transdermal nicotine delivery with microdialysis validation assay. *Nanomed.-Nanotechnol. Biol. Med.* **2017**, *13*, 1–9.

[50] Greenzaid, P. *A Nuclear Magnetic Resonance Study of the Reversible Hydration of Aliphatic Aldehydes and Ketones. I. Oxygen-17 and Proton Spectra and Equilibrium Constants*;

Samuel, Z.L., Ed.; American Chemical Society: Journal of the American Chemical Society, 1967; Volume 89, pp 749–756.

[51] Guthrie, J.P. C*arbonyl Addition Reactions: Factors Affecting the Hydrate–Hemiacetal and Hemiacetal–Acetal Equilibrium Constants*; Canadian Sicence Publishing:Canadian Journal of Chemistry, 1975; Volume 53, pp 898–906.

[52] Cui, Y.; Lee, Y.H.; Yang, J.W. Impact of Carboxyl Groups in Graphene Oxide on Chemoselective Alcohol Oxidation with Ultra-Low Carbocatalyst Loading. *Sci. Rep.* **2017**, *7*, 9.

Chapter 7. CONCLUSIONS

The overarching theme of this dissertation has been to explore and draw inspiration from nature's design in the realm of chemical separation and transfer, with the ultimate goal of applying these insights to solve real-world challenges. Our journey began with an extensive review of prevailing industrial chemical separation techniques, including distillation, filtration, and extraction, which revealed the staggering energy demands and the unfortunate waste of unrecoverable energy. This observation prompted us to look to nature's elegant solutions, particularly exemplified by the cell membrane's remarkable ability to discriminate among thousands of different compounds using a seemingly simple design.

Cell membranes in living organisms are equipped with an array of delicate membrane proteins, each dedicated to specific functions or capabilities that support the life of the cell. At a higher level, the functioning of organs involves the collaboration of millions of individual cells, a complexity that we, as humans, are still striving to fully comprehend. However, despite its relative immaturity in comparison to nature's solutions, human intelligence has led to notable attempts to mimic nature's design, and the dialysis machine stands out as an exemplary case. This machine operates on a fundamentally simple principle, employing precision-controlled transmembrane separation through hollow fiber membranes with a high surface area and specific pore size, supplemented by mechanical pumps and dialysate. Essentially, it functions as an artificial kidney, separating metabolic toxins through artificially created "renal tubules." Despite its simplicity, this technology continues to be a lifeline for patients awaiting kidney transplants. Yet, the long-term survival rates of these patients remain less than optimistic.

From the standpoint of materials science, the key to enhancing these aforementioned technologies, including dialysis, lies in the development of better functional materials. For dialysis,

this translates to improved management of pore size distribution and porosity, a path we have been following in the development of hollow fiber membranes. However, regardless of how clever and precise the design and manufacture of dialysis membranes may become, the inherent nature of passive diffusion limits the technology's evolution, preventing it from reaching the level of active recognition and separation seen in living organisms. It is reasonable to speculate that biomimetic active high-selectivity functionalization may be the path to overcoming this limitation in materials science.

As a result, we embarked on a journey to design, propose, synthesize, and validate selective surface chemistry modifications for serum albumin. This surface chemistry modification enabled the adsorption and desorption cycling of albumin while simultaneously removing protein-bound uremic toxins, which are challenging to eliminate using conventional dialysis processes. It is worth noting that during our study of the desorption process, we discovered a non-toxic and biocompatible eluent, allowing for the reuse of desorbed albumin. Following small-scale experiments and testing under physiological conditions, we initiated the scaling-up of this technology. Throughout this process, we systematically implemented the design and criteria for the scaled-up system, continuously refining it as we applied theoretical computational models to create real prototype instruments.

Similarly, in our pursuit of advancing dialysis technology, we focused on modifying highly selective functional groups, such as 18-crown-6 ether, onto low-cost silica adsorbents to remove potassium ions enriched in the dialysate during the development of mobile dialysis techniques. While we reviewed and discussed many existing adsorbents and natural adsorbent materials, we chose silica adsorbents due to their stability, affordability, and ease of preparation. The modified crown ether-silica adsorbents exhibited over three times the potassium ion adsorption capacity

compared to unmodified silica adsorbents. Furthermore, we confirmed the desorption of potassium ions under acidic conditions, offering the potential for the reuse of the synthesized potassium-selective adsorbent. However, improving the stability of the crown ether-modified silica adsorbent for repeated use remains a challenge. Regrettably, due to limitations in research time and resources, subsequent stability studies were not conducted after confirming the efficient adsorption and desorption of potassium ions.

Beyond our advancements in dialysis technology, we directed our efforts toward carbon material-based membranes, including carbon nanotube membranes and reduced graphene oxide membranes. These materials held promise because they can effectively address the limitations of membrane structure surface area. Under nanoscale confinement conditions, high-speed transmembrane transport of fluids becomes feasible, allowing for multiple uses of a unit surface area within a given time. Moreover, the membrane structure itself can carry selective functional groups, and, due to the efficiency of transmembrane separation, it can outperform conventional adsorbent-based separation methods. Therefore, the combination of both high selectivity and high-speed transmembrane transport holds the potential to effectively separate a wide array of high-value compounds.

In our research on carbon nanotube membranes, we achieved a significant milestone by directly observing high-speed transmembrane electroosmotic transport of aqueous solutions using a camera for the first time. Prior to this, despite numerous simulations and calculations based on the movement of marker molecules to verify the rapid flow of liquids within carbon nanotubes, visual observation remained unprecedented. In this study, we discovered that the observed electroosmotic fluid velocity across carbon nanotubes could reach up to 0.02 cm/s (in a 33 mM K_2SO_4 aqueous solution), with the flow rate essentially at the level of 0.1 cm/sV after accounting

for the influence of the electric field strength. In the presence of a 0.1 M KCl aqueous solution, stable fluid flow rates at the level of 0.1 cm/sV could be observed.

Notably, in electroosmotic experiments involving solutions of various ionic strengths, the observed electroosmotic fluid velocities remained almost constant until the addition of 3% (by volume) of benzyl alcohol to the system. After the addition of benzyl alcohol, the electroosmotic velocity decreased by more than tenfold. This reduction occurred because the interaction between the benzene ring and the carbon nanotube wall caused benzyl alcohol to adsorb onto the tube wall, thereby affecting the smooth surface characteristics of the carbon nanotubes. This smooth surface proved critical in supporting the high-speed flow of fluids through carbon nanotubes.

Our research on the influence of hydrogen bonding revealed that the addition of methanol or NaSCN indeed slowed down the fluid velocity by approximately 20%, although the effect was not as pronounced as that of benzyl alcohol. We also observed that low-concentration salt solutions were more effective in increasing electroosmotic fluid velocity. This occurred because low ionic strength, resulting from low concentration, enhanced the charge screening effect at the carbon nanotube mouths. Consequently, the movement of anions encountered greater resistance, while cations more effectively drove electroosmotic fluid flow.

The observations from this study strongly suggest that the development of carbon nanotube membranes holds significant promise, especially when they are functionalized with high-selectivity functional groups, for the extraction of high-value compounds. We further validated the concept of transmembrane drug delivery on negatively modified carbon nanotube membranes, effectively transporting caffeine and nicotine through the channels formed by electroosmosis.

In our exploration of graphene oxide membranes, we stumbled upon an intriguing catalytic reaction. In this reaction, alcohol substances underwent oxidation in the presence of water

molecules, leading to the reduction of graphene oxide and a decrease in its interlayer spacing. This phenomenon posed a challenge for the application of graphene oxide membranes in alcohol dehydration.

However, our experiments involving pressure-driven membrane permeation and osmotic pressure revealed that graphene oxide membranes could effectively block the passage of salt solution ions and hinder the passage of alcohol substances in alcohol-water mixtures. Yet, they did not impede pure alcohol or water from passing through. This selectivity held significant promise, particularly for alcohol dehydration applications. Nevertheless, the reduced interlayer spacing resulting from the catalytic reaction limited the transmembrane separation rate, presenting a formidable challenge.

To address this challenge, we leveraged the mechanism of the catalytic reaction itself and selectively introduced a certain amount of hydrogen peroxide or potassium permanganate to achieve the reverse reaction: the re-oxidation of reduced graphene. This reopened the interlayer spacing, allowing for high-speed fluid passage. Therefore, we proposed a solution to salvage the application of graphene oxide membranes in alcohol dehydration applications, despite the limitations imposed by the catalytic reaction.

In conclusion, the extensive exploration undertaken in the fields of materials science and biomimetic high-selectivity surface chemistry modification has borne fruit. Our research has provided validation for numerous scientific theories and has surmounted many engineering constraints. As we draw inspiration from nature's design, we find ourselves at the threshold of significant advancements in separation technologies. The possibilities for solving real-world challenges through biomimicry are boundless and hold great promise for the future.

VITA

Education:

Material Science & Engineering, Ph.D.	University of Washington 2018-2023
Material Science & Engineering, M.S.	University of Washington 2015-2017
Material Chemistry, B.S.	Northwest University 2011-2015
International Exchange Student	UNIVERSITY OF CENTRAL OKLAHOMA 2014-2015

Publication:

- Bruce J. Hinds, **Yushi Zang** "SYSTEM FOR REMOVING PROTEIN BOUND UREMIC TOXINS DURING HEMODIALYSIS" *Provisional Patent*
- **Yushi Zang**, Jeremy L. Fredricks, Yuehan Chen, Dan Shea, Bruce J Hinds "Protein bound uremic toxin removal with albumin regeneration" *Submitted* to ASC BioMaterials
- **Yushi Zang**, Alex Peek, Yongsoon Shin, David Gotthold, Bruce J Hinds "Catalytic Reduction of Graphene Oxide Membranes and Water Selective Channel Formation in Water–Alcohol Separations" *Membranes* DOI: 10.3390/membranes11050317
- Guozheng Shao, **Yushi Zang**, and Bruce J. Hinds "TiO2 Nanowires for Urea Photodecomposition and Dialysate Regeneration" *ACS Applied Nano Materials* DOI: 10.1021/acsanm.9b00709
- Meng Sun, Lekai Hou, Xiangxiang Chen, Xiaojuan Yang, Wei Sun, **Yushi Zang** "Palladium-Catalyzed Regioselective ortho-Acylation of Azoxybenzenes with Aldehyde Derivatives" *Advanced Synthesis & Catalysis* DOI: 10.1002/adsc.201400594

- Meng Sun, **Yushi Zang**, Lekai Hou, Xiangxiang Chen, Wei Sun, Shangdong Yang “Convenient Formation of Triarylphosphines by Nickel Catalyzed C–P Cross Coupling with Aryl Chlorides” *European Journal of Organic Chemistry* DOI: 10.1002/ejoc.201402660
- Tanaka, Rikki, Takuya Mabuchi, **Yushi Zang**, Bruce Hinds, and Takashi Tokumasu. "Molecular Dynamics Study of Proton Conductivity at an Interface between Nafion and Graphene Sheet." *ECS Transactions* 104, no. 8 (2021): 309. DOI 10.1149/10408.0309ecst